

**EXCHANGE-CORRELATION KERNELS WITHIN
TIME-DEPENDENT DENSITY FUNCTIONAL
THEORY FOR GROUND-STATE AND
EXCITED-STATE PROPERTIES**

A Dissertation
Submitted to
the Temple University Graduate Board

in Partial Fulfillment
of the Requirements for the Degree of
DOCTOR OF PHILOSOPHY

by

Niraj Kumar Nepal
December 2020

Examining Committee Members:

Adrienn Ruzsinszky, Advisory Committee Chair, Dept. of Physics
John P. Perdew, Examining Committee Chair, Dept. of Physics
Qimin Yan, Examining Committee member, Dept. of Physics
Vincenzo Carnevale, External member of Examining Committee, Dept. of
Biology

ABSTRACT

Exchange-correlation kernel within time-dependent density functional theory for ground-state and excited-state properties

by

Niraj Kumar Nepal

Chair: Adrienn Ruzsinszky

The exact exchange-correlation kernel is a functional derivative of the exact time-dependent exchange-correlation (XC) potential with respect to the time-dependent density, evaluated at the ground-state density. As the XC potential is not known, the exact kernel is also unavailable. Therefore, it must be modeled either using many-body perturbation theory or by satisfying the exact constraints for various prototype systems such as the paradigm uniform electron gas (UEG). The random phase approximation (RPA) neglects the kernel, therefore, fails to provide the accurate ground- and excited-state properties for various systems from a simple uniform electron gas to more complex periodic ones. There are numerous corrections to RPA available, including kernel-corrected RPA, often called the beyond-RPA (bRPA) methods.

In this work, we employed various bRPA methods for a diverse set of systems together with RPA. At first, we applied RPA based methods to study the phase stability of the cesium halides. Cesium halides phase stability is one of the stringent tests for a density functional approximation to assess its accuracy for dispersion interaction. Experimentally, CsF prefers the rocksalt (B1) phase, while the other halides CsCl, CsBr, and CsI prefer the cesium chloride (B2) phase. Without dispersion interaction, PBE and PBE0 predict all halides to prefer the B1 phase. However, all RPA based methods predict the experimental observations. The bRPA methods usually improve the quantitative prediction over RPA for the ground-state equilibrium properties of cesium halides. Next, we explored binary

intermetallic alloys, where we showed that RPA successfully predicts the accurate formation energies of weakly bonded alloys. However, a kernel corrected RPA is needed when dealing with strongly bonded alloys with partially filled d-band metals. We utilized the renormalized ALDA (rALDA) and rAPBE kernel as bRPA methods.

Exact constraints and appropriate norms such as the uniform electron gas are very useful to construct various approximations for the exchange-correlation potentials in the ground-state, and the exchange-correlation kernel in the linear-response theory within the TDDFT. These mathematical formulations not only guide us to formulate more robust nonempirical methods, but they also have more predictive power. We showed the importance of these constraints by calculating plasmon dispersion of the uniform electron gas using the non-local, energy-optimized (NEO) kernel using only a few constraints. More predictive power comes with more constraint satisfaction. As a result, we developed a new wavevector- and frequency-dependent exchange-correlation kernel that satisfies all the constraints that it should satisfy with a real frequency. It gives accurate ground-state correlation energy and describes the charge density wave in low-density UEG. It also predicts an accurate plasmon dispersion with a finite lifetime at wavevectors less than the critical one, where the plasmon dispersion meets the electron-hole continuum.

Dedicated to my family, friends, and well-wishers

ACKNOWLEDGEMENTS

First of all, I would like to extend my gratitude towards my advisor Prof. Adrienn Ruzsinszky, for her constant support during my Ph.D. journey. I also acknowledge Prof. John P. Perdew and Prof. Qimin Yan for their immense help. They supported me as my graduate committee members, and also mentored me as collaborators. I am also grateful to Prof. Jefferson E. Bates, Prof. Liping Yu, Prof. Jose M. Pitarke, and Dr. Aleksandr V Terentjev for their guidance in various projects. A huge thanks to my faculty oversight committee (FOC) members, Prof. Andreas Metz, and Prof. Maria Iavarone, for their concerns about my progress towards the degree. I would like to thank my group members Santosh Adhikari, Bimal Neupane, Santosh Neupane, and Shiqi Ruan for their assistance in various projects. My sincere thanks go to Puskar Bhattarai, Kamal Wagle, and Dr. Biswajit Santra for exchanging their ideas during the collaborations. Similarly, I would like to acknowledge all other co-authors and professors in the department for teaching me all the valuable knowledge and skills. I am very grateful to all my friends within Temple University and outside for making my life full of joy during this arduous journey. I owe all the successes to my family. Thanks, mom and dad! you always show faith in me. Your love and sacrifice always give me hope and energy to fight any difficulties. I would like to express my deep gratitude to my brothers Susheel, Chandra, Nishan, and Nischal, for filling all the positive vibes in my life. A special thanks go to Dr. Chandra Shahi and Priya Shahi for their immense love and care. Finally, I would like to acknowledge the Department of Physics, Graduate School of Temple University, and the National Science Foundation (NSF) for providing me the necessary financial assistantship.

TABLE OF CONTENTS

ABSTRACT	ii
DEDICATION	iv
ACKNOWLEDGEMENTS	v
LIST OF FIGURES	ix
LIST OF TABLES	xii
CHAPTER	
1. GROUND-STATE DENSITY FUNCTIONAL THEORY (DFT)	1
1.1 Kohn-Sham Formalism:	5
1.2 Exchange-correlation functional:	6
1.2.1 Local density approximation (LDA):	7
1.2.2 Generalized-gradient approximations (GGA):	8
1.2.3 Meta-generalized gradient approximations (MGGA):	9
1.2.4 Errors in semilocal approximations:	10
1.2.5 Hybrid functionals:	11
1.2.6 Random phase approximation (RPA):	11
2. TIME-DEPENDENT DENSITY FUNCTIONAL THEORY (TDDFT)	13
2.1 Introduction	13
2.2 Runge-Gross Theorem	16
2.3 Kohn-Sham equations in TDDFT	19
2.4 Linear-response theory	20
2.4.1 Interacting density-density response function	21
2.4.2 Exchange-correlation kernel	24
2.5 Adiabatic-connection fluctuation-dissipation theory (ACFDT) for the ground-state exchange-correlation energy	31
2.5.1 RPA correlation energy	36
2.5.2 Semi- and non-local corrections to RPA (RPA+)	38
2.5.3 RPA renormalization (RPA _r) scheme	39
2.6 Linear response theory for the excited-states properties	40
2.6.1 XC kernels for optical spectra	42
2.6.2 Absorption spectra of solids with the NEO kernel	45

3. ROCKSALT OR CESIUM CHLORIDE: INVESTIGATING THE RELATIVE STABILITY OF THE CESIUM HALIDE STRUCTURES WITH RANDOM PHASE APPROXIMATION BASED METHODS	49
3.1 Abstract	49
3.2 Introduction	51
3.3 Methods	53
3.4 Computational Details	58
3.5 Results	60
3.5.1 Equilibrium Structural Parameters	60
3.5.2 Cohesive Energies	60
3.6 Discussion & Conclusion	66
3.7 Acknowledgements	67
4. TREATING DIFFERENT BONDING SITUATIONS: REVISITING AU-CU ALLOYS USING THE RANDOM PHASE APPROXIMATION	70
4.1 Abstract	70
4.2 Introduction	71
4.3 Computational details	74
4.4 Results	75
4.4.1 Lattice constants	75
4.4.2 Bulk Moduli	76
4.4.3 Formation Energy	77
4.5 Conclusions	81
4.6 Acknowledgements	82
5. FORMATION ENERGY PUZZLE IN INTERMETALLIC ALLOYS: RANDOM PHASE APPROXIMATION FAILS TO PREDICT ACCURATE FORMATION ENERGIES	85
5.1 Abstract	85
5.2 Introduction	86
5.3 Computational details	88
5.4 Results and Discussions	89
5.4.1 CF-CF combination	91
5.4.2 CF-PF combination	95
5.4.3 PF-PF combination	99
5.5 Failure of RPA and beyond RPA correction	102
5.6 Conclusions	105
5.7 Acknowledgements	106

6. UNDERSTANDING PLASMON DISPERSION IN NEARLY-FREE-ELECTRON METALS: THE RELEVANCE OF EXACT CONSTRAINTS FOR NOVEL EXCHANGE-CORRELATION KERNELS WITHIN TIME-DEPENDENT DENSITY FUNCTIONAL THEORY	115
6.1 Abstract	115
6.2 Introduction	116
6.3 Methodology: Exchange-correlation kernels within linear response TDDFT	119
6.4 Plasmon dispersion with spatially nonlocal exchange-correlation kernels in nearly-free-electron metals	122
6.5 The dynamic structure factor within and beyond-RPA	130
6.6 Conclusion	133
6.7 Acknowledgment	135
7. CONSTRAINT-BASED WAVEVECTOR- AND FREQUENCY-DEPENDENT EXCHANGE-CORRELATION KERNEL OF THE UNIFORM ELECTRON GAS	136
7.1 Abstract	136
7.2 Introduction	137
7.3 Density dependence of constraint-based kernels	141
7.4 Modified CP07 static kernel	142
7.5 Static charge-density wave in jellium	145
7.6 Frequency-dependent local kernel of Gross and Kohn	147
7.7 Combining the wavevector dependence of MCP07 with the frequency dependence of the Gross-Kohn kernel	150
7.8 Plasmon in jellium	151
7.9 Correlation energy per electron in jellium	155
7.10 Conclusions	156
7.11 Acknowledgments	158
8. CONCLUSIONS	159
BIBLIOGRAPHY	160
APPENDIX	187

LIST OF FIGURES

Figure

2.1	Schematic of a linear-response mechanism.	20
2.2	Optical absorption spectra calculated using $ABS = \text{Im } \epsilon_M(\mathbf{q} \rightarrow 0, \omega)$	48
3.1	Bar diagram representing $\Delta E_{\text{coh}} = E_{\text{coh}}^{\text{B1}} - E_{\text{coh}}^{\text{B2}}$ obtained with various DFT methods.....	63
3.2	Bar diagram representing $\Delta E_{\text{coh}} = E_{\text{coh}}^{\text{B1}} - E_{\text{coh}}^{\text{B2}}$ obtained with beyond RPA methods using rALDA kernel.....	65
4.1	Mean absolute percentage error (MAPE) for both lattice constants and the bulk moduli.....	76
4.2	Formation energy (eV) versus volume (\AA^3).....	81
4.3	Convex hull of Au-Cu alloys.....	82
5.1	Computed formation energies compared with experimental values.	91
5.2	Formation energies with respect to three distinct classes.	92
5.3	The estimated valence d-band density of states with completely-filled d configuration compared with valence d-band ranges extracted from experimental X-ray photoemission spectra or ultraviolet photoemission spectra (denoted by horizontal solid line). References are given in sub-captions. ϵ_f is the Fermi-level.	96
5.4	The estimated valence d-band density of states of alloys with metals having completely-filled/completely-filled d-band configuration compared with valence d-band ranges extracted from experimental X-ray photoemission spectra or ultraviolet photoemission spectra (denoted by horizontal solid line). References are given in sub-captions. ϵ_f is the Fermi-level.	97
5.5	The estimated valence d-band density of states with partially-filled d configuration compared with valence d-band ranges extracted from experimental X-ray photoemission spectra or ultraviolet photoemission spectra (denoted by horizontal solid line). References are given in sub-captions. ϵ_f is the Fermi-level.	100
5.6	The estimated valence d-band density of states of alloys with metals having completely-filled / partially-filled d-band configuration compared with valence d-band ranges extracted from experimental X-ray photoemission spectra or ultraviolet photoemission spectra (denoted by horizontal solid line). References are given in sub-captions. ϵ_f is the Fermi-level.	101
5.7	The estimated valence d-band density of states of alloys with metals having partially-filled/partially-filled d-band configuration compared with valence d-band ranges extracted from experimental X-ray photoemission spectra or ultraviolet photoemission spectra (denoted by horizontal solid line). References are given in sub-captions. ϵ_f is the Fermi-level.	103

5.8	Schematic diagram for estimating the d-band range and FWHM from X-ray or ultraviolet photoemission spectra.	112
6.1	The Hartree kernel, ALDAXc kernel, and standard NEO xc kernel with $\tilde{c} = 0.264$ vs $Q = q/k_F$ for the uniform electron gas at $r_s = (\frac{3}{4\pi n})^{1/3} = 4$. For ease of comparison, it is actually minus the Hartree kernel ($-4\pi/q^2$) that is plotted here.	123
6.2	The plasmon dispersion for Al (modeled as jellium with $r_s = 2.07$) up to the critical wavevector. The left panel shows the dispersion obtained with RPA and beyond-RPA with ALDAX, ALDAXc, rALDAX and rALDAXc approximations. The right panel shows the dispersion from RPA and the three NEO approximations with the \tilde{c} parameters corresponding to different choices.	126
6.3	The plasmon dispersion for Na (modeled as jellium with $r_s = 3.93$), up to the critical wavevector. The left panel shows the dispersion obtained with RPA and beyond-RPA with ALDAX, ALDAXc, rALDAX and rALDAXc approximations. The right panel shows the dispersion from RPA and the three NEO approximations with the \tilde{c} parameters corresponding to different choices.	127
6.4	The plasmon dispersion for Cs (modeled as jellium with $r_s = 5.62$) up to the critical wavevector. The left panel shows the dispersion obtained with RPA and beyond-RPA with ALDAX, ALDAXc, rALDAX and rALDAXc approximations. The right panel shows the dispersion from RPA and the three NEO approximations with the \tilde{c} parameters corresponding to different choices.	128
6.5	The long wavelength behavior of all approximations considered in this work.	129
6.6	The plasmon dispersion of Na (left) and Cs (right) with RPA and some exchange-correlation kernels within the jellium model.....	129
6.7	a: The jellium spectral functions for RPA and NEO $\tilde{c} = 0.264$ at $r_s = 4$. b: the spectral functions for three NEO kernels at $r_s=4$. c: the jellium spectral functions for three NEO kernels at $r_s=5.62$ corresponding to Cs. To make it more visible, the plasmon peak has been unphysically broadened. At $q = 0.1k_F$, we see only the plasmon peak and it is barely visible. At $q = k_F$, the plasmon peak is overlapped with the continuum of single particle-hole excitations.	131
6.8	Wavevector analysis of the ground state correlation-only energy of jellium from the dynamic structure factor for reduced wavevector $K = \frac{q}{2k_F}$. The area under each curve is proportional to the correlation energy. The left figure shows the correlation-only energy for RPA, ALDA and NEO with the three choices for \tilde{c} , for $r_s=4$. The right figure shows the same for $r_s=5.62$ corresponding to Cs.	134
7.1	Modified CP07 (MCP07) static kernels for jellium with density parameter $r_s = 4$ at the exchange-only and exchange-correlation levels, versus reduced wavevector.	145

7.2	Critical Fermi wavevector for the appearance of a static charge-density wave in a low-density jellium, from the adiabatic local density approximation ($f_{xc} = f_{xc}(0,0)$) and MCP07 static ($f_{xc} = f_{xc}(q,0)$) exchange-correlation kernels, versus reduced wavevector.	146
7.3	Imaginary part of the Gross-Kohn $q = 0$ dynamic kernel for jellium with density parameter $r_s = 4$, at the exchange-only and exchange-correlation levels, versus real frequency.	148
7.4	Real part of the Gross-Kohn $q = 0$ dynamic kernel for jellium with density parameter $r_s = 4$, at the exchange-only and exchange-correlation levels, versus real frequency. (From the Kramers-Kronig relation of Eq. (20) and from the model of Eq. (22).)	149
7.5	The purely-real Gross-Kohn $q = 0$ dynamic kernel for jellium with density parameter $r_s = 4$, at the exchange-only and exchange-correlation levels, versus imaginary frequency. (From the Cauchy integral of Eq. (23) and the model of Eq. (22).)	150
7.6	Imaginary part of the exchange-correlation kernel of Eq. (24) for jellium with density parameter $r_s = 4$, for five different real frequencies, versus reduced wavevector.	151
7.7	Real part of the exchange-correlation kernel of Eq. (24) for jellium with density parameter $r_s = 4$, for five different real frequencies, versus reduced wavevector. (From the model of Eq. (22).)	152
7.8	Plasmon dispersion for jellium with density parameter $r_s = 4$, from the kernel of Eq. (24), versus reduced wavevector. The real part of the plasmon frequency is plotted.	153
7.9	Plasmon damping for jellium with density parameter $r_s = 4$, from the kernel of Eq. (24), versus reduced wavevector. The imaginary part of the plasmon frequency is plotted.	154
7.10	Plasmon dispersion for jellium with density parameter $r_s = 69$, from the kernel of Eq. (24), versus reduced wavevector. The softened plasmon mode may lead to the static charge-density wave.	154
7.11	Correlation energy per electron for jellium from various kernels, and the essentially-exact Perdew-Wang 1992 (PW92) parametrization, versus density parameter r_s . The RPA has no kernel ($f_{xc} = 0$). The adiabatic local density approximation ($f_{xc} = f_{xc}(0,0)$), the static MCP07 kernel of Eq. (13) ($f_{xc} = f_{xc}(q,0)$), and the full dynamic kernel of Eq. (24) ($f_{xc} = f_{xc}(q,\omega)$) are also tested here. The wavevector dependence and frequency dependence make the kernel $f_{xc}(q, \omega)$ less negative (Figs. 1 and 5), which moves the kernel-corrected correlation energy closer to RPA, in which the kernel is zero.	156

LIST OF TABLES

Table

3.1	Equilibrium volumes per CsX functional unit in \AA^3	61
3.2	Computed bulk moduli (GPa) from the equation of state fits	61
3.3	Computed cohesive energies (eV per formula unit) for the stable phases of the cesium halides.....	63
3.4	Comparison of equilibrium volumes for CsCl obtained using rAPBE with other RPA-based methods.	65
3.5	Beyond RPA results for equilibrium energy difference ($\Delta E_{\text{coh}} = E_{\text{coh}}^{\text{B1}} - E_{\text{coh}}^{\text{B2}}$) with rAPBE, CDOP, and CP07 kernels.....	65
3.6	Difference in cohesive energies between the two phases in eV per formula unit. Negative sign indicates the stability of the B2 phase.....	68
3.7	Difference in cohesive energies (B2-B1) of CsCl in eV per formula unit with respect to different cutoffs along with the results of extrapolated values which show the fast convergence of the relative energy with cutoff for rALDA.	69
3.8	Extension of Table ?? to beyond-RPA methods within the rALDA formalism.	69
3.9	Zero Point Energy (ZPE) per formula unit using PBE. We have not calculated ZPE for CsI.	69
4.1	Lattice constants (\AA) of Au-Cu alloys.....	76
4.2	Bulk moduli of Au-Cu alloys.....	77
4.3	The heat of formation (eV /atom) of Au-Cu alloys.....	80
4.4	Cohesive energy per atom (eV/atom) of Au-Cu alloys.....	80
4.5	Convergence parameters for RPA calculations; Bulk calculations: Energies for bulk calculations are converged within 1-2 meV; Atomic calculations: EXX energies are converged within 1-2 meV for both energy cutoff and cell volume. However for RPA, convergence was achieved within 1-5 meV for energy cutoff, while it is 15-20 meV for cell volume. We used PAW pseudopotentials such that the valence electron configuration includes $d^{10}s^1$ electrons for both copper and gold.	83
4.6	The equilibrium ground state properties of Au-Cu alloys using long-range dispersion corrected density functional theory (DFT), PBE+rVV10 and SCAN+rVV10. The inclusion of long-range dispersion in semilocal functionals does not significantly improve the results with respect to experiments. The rVV10 correction improves the lattice constants and bulk moduli for PBE while it slightly worsens for SCAN. However, it provides an insignificant correction to formation energies.	83

4.7	The equilibrium ground state properties of Au-Cu alloys using the spin-orbit coupling (SOC) in DFT calculations; PBE-SOC:- PBE with SOC; SCAN-SOC:- SCAN with SOC. As expected, SOC affects the results more for Au than that of Cu. Unlike thermal correction and long-range dispersion, SOC provides a reasonable correction to formation energies obtained with semilocal DFT results. However, it does not significantly improve the results compared to experiments.	84
5.1	Formation energy (eV) per atom of intermetallic alloys; the first column represents the alloys, while the second column shows the combination of the d-bands; CF is completely filled, PF is partially filled; All the compounds considered here crystallize in the B2 (CsCl) phase.	90
5.2	Formation energies (eV) per atom of alloys other than the B2 phase (CsCl, Pm-3m); CF is completely filled, PF is partially filled.	95
5.3	Formation energies (eV) from kernel-corrected RPA for PtSc and HfOs. Improving the short-range correlation in RPA can improve the formation energies of intermetallics where RPA fails severely.	104
5.4	Converged parameters for elemental bulk calculations. The kernel-corrected or beyond RPA calculations were performed at RPA Ecut and a fixed K-mesh of 16x16x16. Also, the response function is computed using only one cutoff of 300 eV without extrapolation.	108
5.5	Converged parameters for alloys. The kernel-corrected or beyond RPA calculations were performed at RPA Ecut and a fixed K-mesh of 16x16x16. Also, the response function is computed using only one cutoff of 300 eV without extrapolation.	109
5.6	Equilibrium volumes for constituent elemental bulk transition metals (\AA^3). 110	
5.7	Equilibrium volumes for alloys (\AA^3); Alloys are presented with an increasing experimental formation energies (see Table V); % Error means percentage error.	110
5.8	Bulk moduli for the constituent elemental bulk transition metals (GPa) . .	111
5.9	Bulk moduli for the alloys (GPa); The alloys are presented in order of increasing experimental formation energies (see Table V).	112
5.10	The d-band centroid and d-band ranges with respect to Fermi-level (or below Fermi-level) extracted from experimental photoemission spectra; unit eV.	114
7.1	Density (n) dependences of key ingredients (to be defined later) of the exchange-correlation kernel $f_{xc}(q, \omega)$ for a uniform electron gas.....	142

CHAPTER 1

GROUND-STATE DENSITY FUNCTIONAL THEORY (DFT)

The many-body wavefunction obtained by solving the time-independent Schrödinger's equation carries a plethora of information about the behavior of an electron in the presence of an external potential (nuclear potential in the ground-state). With the Born-Oppenheimer approximation [1], we assume the motion of nuclei can be neglected due to their heavy mass compared to that of electrons. Now, one can separate a time-independent non-relativistic Schrödinger's equation for N electrons within the nuclear potentials as

$$H\psi = \epsilon\psi. \quad (1.0-1)$$

Here, H is the non-relativistic spin-independent Hamiltonian that mainly consists of three terms, (a) the kinetic energy operator $-\sum_i^N \frac{\nabla_i^2}{2}$, (b) the external potential $\sum_i^N v(\mathbf{r}_i)$, and (c) the electron-electron interaction $\sum_{i<j}^N \frac{1}{|\mathbf{r}_i - \mathbf{r}_j|}$. $\psi = \psi(\mathbf{x}_1, \mathbf{x}_2, \dots, \mathbf{x}_N)$ is the many-particle wavefunction, where the \mathbf{x}_i 's represent a mixture of both spatial and spin coordinates. ϵ is an eigenvalue representing the total energy of the system. One can solve Eq. 1.0-1 exactly only for one electron hydrogen-like system (one nuclei with a single electron). However, solving it for many electron system is not an easy task due to connected motion of electrons.

Wavefunction theory can provide an effective way to decouple the correlated motion of electrons. Hartree devised a self-consistent-field method (SCF) of finding an effective interacting potential that an electron experiences in the presence of nuclei and other $N-1$

electrons [2]. Later, Fock (Hartree-Fock (HF) method) [3] included the Pauli's exclusion principle that a fermion must satisfy by utilizing a Slater determinant of spin orbitals as a many-body antisymmetrized wavefunction. These methods miss an important correlation part. Therefore various post-HF methods have been developed to incorporate the electron correlations in wavefunction theory such as configuration interaction (CI) [4], Møller-Plesset perturbation theory (MP2, MP3, MP4, etc.) [5], coupled-cluster (CC) method [6], etc. However, they are mostly feasible for finite systems such as atoms and molecules. They become inefficient and cumbersome for solids, as the computational costs can skyrocket as $(N^4 - N^6)$ with particle numbers increasing to Avogadro's number $N \sim 10^{28}$ [7]. An alternative approach that is simultaneously accurate as well as computationally efficient, can be achieved with the electronic density replacing the wavefunction. Similar to wavefunction theory that uses the wavefunction, this theory using the electronic density as its basic variable is called the density functional theory (DFT). Density functional theory (DFT) is a robust electronic-structure method, widely developed and used in different fields of science. It uses the three-dimensional electronic density $n(\mathbf{r})$ instead of $3N$ dimensional wave function $\psi(\mathbf{r}_1, \mathbf{r}_2, \dots, \mathbf{r}_N)$ to solve the quantum-mechanical many-body Schrödinger's equation.

The history of using the electron density as a variable in the quantum mechanical problem began a long time before the Hohenberg–Kohn (HK) theorems (will discuss later) around the 1920s by two theorists Llewellyn Thomas [8] and Enrico Fermi [9]. The work of Thomas laid out an assumption: “Electrons are distributed uniformly in the six-dimensional phase space for the motion of an electron at the rate of two for each h^3 of volume,” and that there is an effective potential field that “is itself determined by the nuclear charge and this distribution of electrons [8].” One can write the total energy of the system under the

assumption of a simpler Thomas-Fermi (TF) model as

$$E_{TF}[n(\mathbf{r})] = \frac{3}{5}(3\pi^2)^{5/3} \int d^3r n^{5/3}(\mathbf{r}) + \int d^3r n(\mathbf{r}) v(\mathbf{r}) + \frac{1}{2} \int d^3r \int d^3r' \frac{n(\mathbf{r})n(\mathbf{r}')}{|\mathbf{r}-\mathbf{r}'|}. \quad (1.0-2)$$

Here, the first term is the kinetic energy of independent particles under the influence of an external potential, which is given by the second term. The electron-electron interactions are simply represented by a classical Coulomb (or Hartree) interaction (the third term). This theory has two limitations [10]: (1) the kinetic energy is a crude approximation to the real one which is the largest source of error, and (2) it misses the important exchange-correlation energy, nature's glue, therefore, it does not bind atoms into the molecules. There were numerous attempts to overcome these limitations, but none of them were successful due to the oversimplified model of a complex real system.

DFT is based on two assumptions provided by Hohenberg and Kohn in 1964, also known as the Hohenberg–Kohn (HK) theorems [11]. One of the theorem establishes a one-to-one correspondence between one-body external potentials and one-body electron densities, whereas the other discusses the variational principle that leads to the minimum ground-state energy when an electron density becomes the exact ground-state density. Now, one can write the total energy of a many-body system as a functional of the ground-state density as

$$E[n(\mathbf{r})] = T[n(\mathbf{r})] + E_{ext}[n(\mathbf{r})] + E_{ee}[n(\mathbf{r})], \quad (1.0-3)$$

where $T[n]$ is an interacting kinetic energy. $E_{ext}[n] = \int d\mathbf{r} n(\mathbf{r}) v_{ext}(r)$ and $E_{ee}[n]$ are energies due to external potential and electron-electron interaction respectively. The electron density can be computed as

$$n(\mathbf{r}) = N \sum_{\sigma} \sum_{\sigma_2} \dots \sum_{\sigma_N} \int d\mathbf{r}_2 \int d\mathbf{r}_3 \dots \int d\mathbf{r}_N |\psi(\mathbf{r}, \sigma, \mathbf{r}_2, \sigma_2, \dots, \mathbf{r}_N, \sigma_N)|^2. \quad (1.0-4)$$

Now, $T[n(\mathbf{r})] + E_{ee}[n(\mathbf{r})]$ is independent of the external potential, and it is called a universal functional ($F_{HK}[n]$) of density $n(\mathbf{r})$. The application of the variational principle on Eq. 1.0-3 leads to the Euler-Lagrange's equation for the density $n(\mathbf{r})$ that minimizes $E[n(\mathbf{r})]$,

$$\mu = \frac{\delta E[n]}{\delta n(\mathbf{r})} = v(\mathbf{r}) + \frac{\delta F_{HK}[n]}{\delta n(\mathbf{r})}. \quad (1.0-5)$$

Here μ is the chemical potential and also the Lagrange's multiplier associated with the constraint $\int n(\mathbf{r})d\mathbf{r} = N$. If one has an exact form of the universal functional $F_{HK}[n]$, then Eqs. 1.0-3 and 1.0-5 would be the equations for the exact density. Unfortunately, it is difficult to realize these theorems in an application-perspective for real systems, as an explicit closed form of $F_{HK}[n]$ is not known yet or it is difficult to formulate. In addition, the HK theorems are only valid for the non-degenerate ground-state (HK 1st theorem) and v -representable densities (HK 2nd theorem). However, there are situations where the systems have degenerate ground-states. Also, there could be the density that is essentially non v -representable [12]. In those situations, one cannot obtain the ground-state properties as functionals of the electronic density as the HK theorem suggests. An alternative approach to circumvent the problem would be to satisfy a much weaker condition for the density that goes into both the functional as well as in the variational principle: N-representability. A density that can be obtained from an antisymmetric wavefunction satisfies this condition. For any N-representable density $n(\mathbf{r})$, the following conditions hold true:

$$n(\mathbf{r}) \geq 0, \quad \int n(\mathbf{r})d\mathbf{r} = N, \quad \int |\nabla n(\mathbf{r})^{1/2}|^2 d\mathbf{r} < \infty \quad (1.0-6)$$

The constrained-search method, devised by Levy in 1979 [13], eliminates the issues of v -representability of the HK theorem and provides the recipe to find the universal func-

tional

$$\begin{aligned}
F_{HK}[n_0] &= \langle \Psi_0 | \hat{T} + \hat{V}_{ee} | \Psi_0 \rangle \\
&= \underset{\Psi \rightarrow n_0}{\text{Min}} \langle \Psi | \hat{T} + \hat{V}_{ee} | \Psi \rangle .
\end{aligned} \tag{1.0-7}$$

Here, among all the wavefunctions that gives the same density n_0 , the ground-state wavefunction Ψ_0 minimizes the $F_{HK}[n_0]$.

1.1 Kohn-Sham Formalism:

Even though the HK theorem established a basis for DFT, it has still been impractical to be used for many-body calculations as it has not provided a recipe to calculate $F_{HK}[n]$. Later Kohn and Sham (KS), in 1965, provided a breakthrough to deal with the many-body interacting system by converting it to a simple one-body noninteracting system with the same density as that of the interacting one in the presence of one-body effective potential, called Kohn-Sham potential [14]. It is similar to HF, however, it explicitly includes many-body effects that the HF theory does not. In KS formalism, the total energy of the system given by Eq. 1.0-3 is rewritten as

$$E[n(\mathbf{r})] = T_s[n(\mathbf{r})] + E_{ext}[n(\mathbf{r})] + E_H[n(\mathbf{r})] + E_{XC}[n(\mathbf{r})], \tag{1.1-8}$$

where $T_s[n(\mathbf{r})] = -\frac{1}{2} \sum_i^N \langle \phi_i | \nabla^2 | \phi_i \rangle$ is a noninteracting kinetic energy evaluated using the KS orbitals $\{\phi_i\}$, $E_{ext}[n(\mathbf{r})]$ is the external energy, $E_H[n(\mathbf{r})] = \frac{1}{2} \int \int d\mathbf{r} d\mathbf{r}' \frac{n(\mathbf{r})n(\mathbf{r}')}{|\mathbf{r}-\mathbf{r}'|}$ is the classical Hartree energy, and $E_{XC}[n(\mathbf{r})] = T - T_s + E_{ee} - E_H$ is the exchange-correlation energy that contains all the quantum many-body effects. The Euler's equation becomes

$$\mu = v_{eff}(\mathbf{r}) + \frac{\delta T_s[n]}{\delta n(\mathbf{r})} \tag{1.1-9}$$

where the effective KS potential is given as

$$v_{eff}(\mathbf{r}) = v_{ext}(r) + \frac{\delta E_H[n]}{\delta n(\mathbf{r})} + \frac{\delta E_{XC}[n]}{\delta n(\mathbf{r})} = v_{ext}(r) + \frac{1}{2} \int d\mathbf{r}' \frac{n(\mathbf{r}')}{|\mathbf{r} - \mathbf{r}'|} + v_{xc}(\mathbf{r}) \quad (1.1-10)$$

Here $v_{xc}(\mathbf{r})$ is the exchange-correlation potential. Now, one can obtain the ground-state density $n(\mathbf{r})$ that satisfies Eq. 1.1-9 by simply solving N one-body equations

$$\left[-\frac{1}{2} \nabla^2 + v_{eff}(\mathbf{r}) \right] \phi_i(\mathbf{r}) = \epsilon_i \phi_i(\mathbf{r}), \quad (1.1-11)$$

with $n(\mathbf{r}) = \sum_i^N |\phi_i(\mathbf{r})|^2$. There are various scenarios when one has to take spin densities (n_σ , $\sigma = \uparrow$ or \downarrow) into account; (a) the external potential is spin-dependent, or (b) for the standard approximate density functional approximation, but not for the exact one. Here, Eq. 1.1-8 can be written as

$$E[n_\uparrow, n_\downarrow] = T_s[n_\uparrow, n_\downarrow] + E_{ext}[n_\uparrow, n_\downarrow] + E_H[n_\uparrow, n_\downarrow] + E_{XC}[n_\uparrow, n_\downarrow] \quad (1.1-12)$$

with $n_\uparrow + n_\downarrow = n$ (the total density). Similarly, one can write all other equations in terms of spin densities. The major portion of the total energy can be obtained by computing the first 3 terms in the right-hand side of Eq. 1.1-12, as they are exactly known. The last term called the exchange-correlation energy that has all the quantum many-body effects, comprises of a small portion of the total energy, but it is completely unknown. It is a small but important quantity, also known as nature's glue as it helps to bind atoms into molecules in DFT. In the next section, we will discuss this term and its several widely-used approximations.

1.2 Exchange-correlation functional:

We know that the exchange-correlation (XC) energy is defined as

$$E_{XC} = T - T_s + E_{ee} - E_H, \quad (1.2-13)$$

where $T - T_s$ gives the kinetic-correlation contribution, and the remaining terms include a nonclassical part of E_{ee} . In principle, one can obtain an exact expression of the XC-energy using the adiabatic-connection fluctuation-dissipation theorem (ACFDT) within time-dependent DFT [15, 16]. However, in practice, we need to approximate the XC-functionals by satisfying exact constraints and appropriate norms such as uniform electron gas (UEG). Apart from constructing functionals from exact constraints and appropriate norms, there are other kinds, empirical or semi-empirical ones, that are fitted to some real systems. We may list them, but we won't discuss them in detail. Now, we discuss various approximations within an approximate ground-state DFT starting from a simpler local density approximation (LDA) [14].

1.2.1 Local density approximation (LDA):

It is the simplest form of the XC-functionals purposed by Kohn and Sham (1965). Assuming a slowly varying density, one can obtain the LDA exchange-correlation energy as

$$E_{XC}^{\text{LDA}}[n(\mathbf{r})] = \int d\mathbf{r} n(\mathbf{r}) \epsilon_{xc}(n(\mathbf{r})), \quad (1.2-14)$$

where $\epsilon_{xc}(n(\mathbf{r}))$ is the exchange-correlation energy per particle of uniform electron gas (UEG), computed only with the electron density. Further, ϵ_{xc} can be decomposed into a separate exchange (ϵ_x) and the correlation part (ϵ_c). The exchange part ϵ_x of UEG is defined exactly as $-(3/4)(3/\pi)^{1/3}n^{1/3}$, whereas there is no exact analytical form for the correlation. There are three most popular parametrization of LDA correlation, namely VWN5 [17], PZ81 [18], and PW92 [19], and these correlations combined with the exchange give slightly different LDA (or LSDA) functionals. A corresponding LDA XC-potential ($v_{xc}^{\text{LDA}}[n](\mathbf{r})$) is a functional derivative of XC-energy with respect to the density ($\frac{\delta E_{XC}^{\text{LDA}}[n]}{\delta n(\mathbf{r})}$). The KS single-particle equations can be solved using this potential in Eqs. 1.1-10 and 1.1-11 to obtain the LDA orbitals and energies. Finally, one can calculate the electron density and the total energy of the system. The spin-polarized version of LDA is

known as the local spin density approximation (LSDA) [14, 19] in which the XC-energy takes a form

$$E_{XC}^{\text{LSDA}}[n_{\uparrow}, n_{\downarrow}] = \int d\mathbf{r} n(\mathbf{r}) \varepsilon_{xc}(n_{\uparrow}(\mathbf{r}), n_{\downarrow}(\mathbf{r})), \quad (1.2-15)$$

where $\varepsilon_{xc}(n_{\uparrow}(\mathbf{r}), n_{\downarrow}(\mathbf{r}))$ is the same exchange-correlation energy per particle of UEG, but computed with spin densities $n_{\uparrow}, n_{\downarrow}$. The LDA functionals are essentially exact for infinite UEG, but are highly inaccurate for inhomogeneous densities. Unlike the Thomas-Fermi model, LDA does bind the atoms into a molecule. However, it typically overbinds a molecule, predicts too short bond lengths, severely underestimates the energy barriers, etc [20].

1.2.2 Generalized-gradient approximations (GGA):

The systematic improvement over LSDA can be achieved at the GGA level with the inclusion of gradient of density (∇n) along with the density. GGAs reduce the overestimation of atomization energies of molecules in LSDA by about a factor of 4, improving underestimation of energy barrier by $\sim 30\%$, etc [20]. In generalized-gradient approximations (GGAs), the exchange-correlation energy is defined as

$$E_{XC}^{\text{GGA}}[n_{\uparrow}, n_{\downarrow}] = \int d\mathbf{r} n(\mathbf{r}) f(n_{\uparrow}(\mathbf{r}), n_{\downarrow}(\mathbf{r}), \nabla n_{\uparrow}(\mathbf{r}), \nabla n_{\downarrow}(\mathbf{r})). \quad (1.2-16)$$

Here, the function $f(n_{\uparrow}(\mathbf{r}), n_{\downarrow}(\mathbf{r}), \nabla n_{\uparrow}(\mathbf{r}), \nabla n_{\downarrow}(\mathbf{r}))$ is devised to recover the second-order gradient expansion for slowly-varying density using the ε_{xc} of UEG by satisfying more exact constraints of the exchange-correlation energy than the LDA does. A highly successful GGA functional by Perdew-Burke-Ernzerhof (PBE) satisfies 11 exact constraints, which has PBE exchange combined with the PBE correlation [21]. Some of the other GGA functionals can be constructed with the combination of different GGA exchange and GGA correlation. For example, GGA exchange may include PW91, revPBE [22], PBEsol [23], RPBE [24], B88 [25], while GGA correlations can be PW91, PBEsol [23], P86 [26], LYP

[27, 28], etc. Some popular GGAs are BP86 (B88 + P86), BLYP (B88 + LYP), RPBE (RPBE + PBE) [24], PBEsol (PBEsol + PBEsol) [23], etc. Though there is a systematic improvement of GGAs over LSDA, they are not accurate enough compared to experiments or higher level wavefunction calculations. The bond lengths are mostly overestimated. The error in energy barriers of the reaction and atomization energies of molecules still remains intact. Furthermore, they do not provide an accurate description of dispersion interactions, and also fail to describe strongly-correlated systems [29]. GGAs underestimate the band-gap of semiconductors and insulators [30, 31].

1.2.3 Meta-generalized gradient approximations (MGGA):

The errors in LDA and GGAs can be systematically reduced with the inclusion of the meta-GGA (MGGA) ingredients such as the kinetic energy density ($\tau(\mathbf{r}) = \sum_i^N |\nabla\phi_i|^2$) or Laplacian of the density ($\nabla^2 n(\mathbf{r})$). More exact constraints need to be satisfied with the addition of these ingredients that make MGGA functionals more useful for a diverse set of material's properties. The MGGA exchange-correlation energy is obtained as

$$E_{XC}^{\text{MGGA}}[n_{\uparrow}, n_{\downarrow}] = \int d\mathbf{r} n(\mathbf{r}) f(n_{\uparrow}(\mathbf{r}), n_{\downarrow}(\mathbf{r}), \nabla n_{\uparrow}(\mathbf{r}), \nabla n_{\downarrow}(\mathbf{r}), \tau_{\uparrow}, \tau_{\downarrow}, \nabla^2 n_{\uparrow}, \nabla^2 n_{\downarrow}). \quad (1.2-17)$$

Some commonly used MGGA functionals are TPSS [32], revTPSS [33, 34], made simple (MS) functionals (MS0, MS1, MS2) [35, 36], PKZB [37], MO6-L [38], SCAN [39], etc. Among these functionals, the strongly constrained and appropriately normed (SCAN) MGGA is more successful in predicting a diverse set of properties as it can describe different bonding situations [40–42]. It satisfies 17 exact constraints that a meta-GGA can satisfy, and also incorporates an intermediate range of dispersion. It is able to describe a weak hydrogen bond and the dispersion interaction in some materials [40]. The SCAN-calculated equilibrium bond-lengths of molecules and the lattice constants of solids are highly accurate [39]. Meta-GGAs also improve the bandgap of various semiconductors

and insulators beyond GGAs [43, 44] and also describe some of the strongly-correlated systems [45–47]. We have utilized the SCAN functional to predict the ground-state equilibrium properties of monolayer transition metal dichalcogenides (TMDs) [48]. It predicts the accurate lattice constants and the phase stability of these two dimensional materials. In addition, we have also explored the effect of mechanical bending on these materials using thin-plate bending method. Interested reader can consult Ref. [48] for more details.

1.2.4 Errors in semilocal approximations:

Though a meta-GGA at the semilocal level can improve a wide range of properties, two types of the major source of errors remain uneliminated, (a) absence of a full nonlocality (or a long-range part), and (b) the self-interaction error. Several attempts have been made to include the missing nonlocality in semilocal approximation with an additional semi-empirical dispersion correction to DFT including GGAs. For examples, Grimme’s DFT+D methods [49–52], vdW-DF [53], VV10 [54], SCAN+rVV10 [55], etc. They can be combined with various DFT methods with a few parameters that can be determined with the fitting to give an accurate binding energy curve of some basic non-bonded molecules of inert gases such as He₂, Kr₂, etc. Sometimes, a benchmark S22 dataset of noncovalent complexes is also utilized to obtain the optimal parameters for the dispersion-corrected DFT methods. Surprisingly, these simple methods work qualitatively well for some systems, but not always [56]. However, to get the accurate quantitative prediction, we need full nonlocality as in the case of RPA.

Regarding the second source of the error, Perdew and Zunger in 1981 devised a way (self-interaction correction (SIC)) to subtract the self-interaction error (SIE) from the total energy on an orbital-by-orbital basis [18]. Since then, there have been numerous attempts to improve the performance of the SIC methods [57–63]. Another way to incorporate

SIC corrections in the DFT is to mix the exact exchange with semilocal exchange and correlation, giving hybrid functionals within the generalized KS scheme [64].

1.2.5 Hybrid functionals:

The hybrid functionals are another group of density functionals that systematically improve on many properties such as bandgap, properties related to strong correlation, etc. over semilocal approximations. Some fraction of the exact exchange (or Hartree-Fock exchange) is mixed with the DFT exchange and correlation, thereby incorporating some non-locality to balance the self-interaction error in the nonlocal Hartree energy. The simplest form of the hybrid exchange-correlation energy can be written as

$$E_{xc}^{hyb} = E_x^{exact} + (1 - a)(E_x^{DFT} - E_x^{exact}) + E_c^{DFT}, \quad (1.2-18)$$

where E_x^{exact} and E_x^{DFT} are the HF exact-exchange and DFT exchange energy respectively, while E_c^{DFT} is the DFT correlation energy. “ a ” is the mixing parameter. The GGAs are usually taken as the DFT part [65–67], while some meta-GGAs [68] also have been utilized to construct hybrid functionals. The simplest form is PBE0 which is formulated by mixing 25 % ($a = 0.25$) of exact exchange with the remaining PBE exchange and correlation [65]. Some other popular hybrid functionals are HSE06 [66, 67], B3LYP [69], SCAN0 [68], etc.

1.2.6 Random phase approximation (RPA):

So far, we have discussed the DFT functionals that use occupied orbitals only to construct the key ingredient, the electron density. On the other hand, the density-density response function χ is the key quantity in the linear response theory. It uses both occupied and virtual (unoccupied) orbitals from ground-state calculations. The total energy in RPA is defined as

$$E = E^{EXX} + E_c^{RPA}, \quad (1.2-19)$$

with $E^{EXX} = T_s + E_{ext} + E_H + E_x^{Exact}$ called the EXX energy, and E_c^{RPA} is the RPA correlation energy. E_x^{Exact} is the HF exchange energy, evaluated using the KS occupied orbitals, whereas, E_c^{RPA} is evaluated using the ACFDT within linear-response theory. RPA is widely applicable for the ground-state properties, where the proper description of a long-range interaction is needed. However, due to a neglect of the dynamic exchange-correlation kernel, it often fails to describe the short-range correlation in the ground-state and the electron-hole interactions in the excitation processes. We will discuss the RPA-based methods within linear-response theory in detail in the next chapter “Time-dependent density functional theory (TDDFT)”.

CHAPTER 2

TIME-DEPENDENT DENSITY FUNCTIONAL THEORY (TDDFT)

2.1 Introduction

Time-dependent density functional theory (TDDFT) is the time-dependent extension of ground-state density functional theory (DFT) which, in principle, offers the solutions to the time-dependent quantum-mechanical many-body problem using the one-body density $n(\mathbf{r}, t)$. Suppose that a system (atom, molecule, or solid) is perturbed by a time-dependent perturbation such as a laser probe, the behavior of electrons within the system can be described by the exact solution of the time-dependent Schrödinger equation [70]. Constructing the exact Hamiltonian and obtaining its solutions for the many-body interacting system is not an easy task, even for the ground-state. Therefore using the Hohenberg-Kohn [11] in a static ground-state and Runge-Gross theorems [71] for a time-dependent state, one can map the one-to-one correspondence between the one-body densities ($n(\mathbf{r})$, $n(\mathbf{r}, t)$) and the one-body external potentials ($v_{ext}(r)$, $v_{ext}(r, t)$). Similar to the ground-state, one can define a fictitious system of non-interacting particles in the time-dependent effective one-body potential, known as the time-dependent Kohn-Sham potential. It consists of an external part, the Hartree part, and the exchange-correlation part $v_{xc}(\mathbf{r}, t)$. The exchange-correlation part is a functional of the initial interacting wavefunctions $\psi(0)$, the initial Kohn-Sham wavefunctions $\phi(0)$, and the entire history of the density ($n(\mathbf{r}, t)$), which make it more complicated to deal with [72]. A simpler quantity would be the one that depends only on instantaneous density, not on the entire history of the density. This approximation is called

the adiabatic approximation [73].

When an external time-dependent perturbation is applied to the system of electrons in its ground-state, it evolves with time. One can describe the effect of the external perturbation in the system in terms of variations of observables. In the context of DFT, we are interested in density-variations. If the perturbation is weak enough, the density-variation depends linearly on the applied perturbation ($\delta n = \chi \delta v_{ext}$), and it can be treated using many-body perturbation theory. The underlying principle that describes such phenomena is linear-response theory. Many spectroscopic experiments work within the linear-response regime. However, there are other spectroscopic studies that use strong perturbation such as strong laser field, and the response beyond linear-regime is necessary, which is out of the scope for the present work.

The basic approximation within linear-response theory for both ground- and excited-state systems is the random phase approximation (RPA) [74, 75]. In RPA, the effective interaction between particles can be approximated with collective excitation of independent particles that are in the same phase plus the screened Coulomb interactions. All out-of-phase components of random excitations cancel each other, justifying the name “random phase approximation (RPA)”. RPA can effectively describe various bonding situations such as covalent [76–82], metallic [83, 84], and van der Waals interactions [85–89] within solids. However, due to neglect of the dynamic exchange–correlation kernel, it can severely fail in those situations, where the accurate description of short-range electron–electron correlation is necessary such as atomization energies of molecules [90], transition metal atoms, formation energies of strongly-bonded intermetallic alloys [91], and equilibrium properties of cesium halides [92], etc. On the other hand, RPA can qualitatively describe excited-state properties such as absorption spectra, electron-energy-loss-spectra (EELS), and plasmon dispersion of various models and real systems. For an accurate description of these proper-

ties, we need a frequency- and wavevector- dependent exchange-correlation kernel that can capture all the dynamic effects within the electron density due to time-dependent external perturbation [93–104].

The main objective of our work is to discuss the construction and the applications of various exchange-correlation kernels. The exact exchange-correlation kernel is the functional-derivative of the exact ground-state exchange-correlation potential with respect to the density. Since the latter is unknown, so is the former. However, one can approximate them either using many-body perturbation theory or by satisfying exact-constraints and appropriate norms. The simplest form is the adiabatic local density approximation or time-dependent LDA, which is local in both space and time [72].

In this work, we assessed the constructions and applications of various exchange- correlation kernels. We identified different cases, where RPA does not provide accurate results, and show that the kernel-corrected RPA methods improve various ground- and excited-state properties. At first, we gave a brief introduction about the ground-state density functional theory in Chapter 1. Then, we discuss time-dependent DFT in detail in this section (Chapter 2). We also discuss an application of a model kernel to calculate the optical spectra of various solids in this chapter. Chapters 3-5 cover the applications of RPA and kernel-corrected RPA for real solids. Chapter 6 is dedicated to ground- and excited-state applications of TDDFT for uniform electron gas, especially the plasmonic excitations. We discuss a newly developed constraint-based wavevector- and frequency-dependent exchange-correlation kernel using the uniform electron gas as an appropriate norm in Chapter 7. Finally, overall conclusions are presented in Chapter 8, followed by references.

2.2 Runge-Gross Theorem

The Runge-Gross theorem is the time-dependent analogue of the HK theorem of the ground-state theory. It establishes a one-to-one correspondence between the one-body time-dependent density and the one-body time-dependent potential. However, no variational principle exists in terms of the total energy, as it is not a conserved quantity in TDDFT. Suppose, there is system with N electrons interacting with each other and with a time-dependent external potential $v(\mathbf{r}, t)$. Let v and v' be two time-dependent one-body potentials corresponding to densities n and n' , respectively. The Runge-Gross theorem states that

$$v(\mathbf{r}, t) \neq v'(\mathbf{r}, t) + c(t) \rightarrow n(\mathbf{r}, t) \neq n'(\mathbf{r}, t), \quad (2.2-1)$$

where $c(t)$ is purely time-dependent constant. Eq. 2.2-1 implies a one-to-one correspondence between time-dependent densities and potentials.

Proof:

Let us assume that the potential $v(\mathbf{r}, t)$ is Taylor expandable with respect to initial time t_0 as

$$v(\mathbf{r}, t) = \sum_{k=0}^{\infty} C_k(\mathbf{r})(t - t_0)^k, \quad (2.2-2)$$

with $C_k(\mathbf{r}) = \frac{1}{k!} \frac{\partial^k}{\partial t^k} v(\mathbf{r}, t) |_{t=t_0}$. We also define

$$u_k(\mathbf{r}) = \frac{\partial^k}{\partial t^k} [v(\mathbf{r}, t) - v'(\mathbf{r}, t)] |_{t=t_0} = k! [C_k(\mathbf{r}) - C'_k(\mathbf{r})]. \quad (2.2-3)$$

If the two potentials differ by more than a purely time-dependent function, there should be at least one $u_k(\mathbf{r})$ that differ by more than a constant. Now, we proceed with the proof in two parts. At first, if the left part of the Eq. 2.2-1 holds true, then the current densities generated by these potentials also differ with each other. Secondly, we show a one-to-one

correspondence between the current densities and the one-body electron densities.

Let us define a current density operator $\hat{\mathbf{j}}$,

$$\hat{\mathbf{j}}(\mathbf{r}) = -\frac{1}{2i} \{ [\nabla \hat{\psi}^\dagger(\mathbf{r})] \hat{\psi}(\mathbf{r}) - \hat{\psi}^\dagger(\mathbf{r}) [\nabla \hat{\psi}(\mathbf{r})] \}. \quad (2.2-4)$$

Now, the current density $j(\mathbf{r}, t)$ is simply obtained from the expectation value of this operator:

$$\mathbf{j}(\mathbf{r}, t) = \langle \psi(t) | \hat{\mathbf{j}}(\mathbf{r}) | \psi(t) \rangle. \quad (2.2-5)$$

The evolution of current densities j and j' with respect to time is given by the equations of motion

$$i \frac{d}{dt} \mathbf{j}(\mathbf{r}, t) = \langle \psi(t) | [\hat{\mathbf{j}}(\mathbf{r}), \hat{H}] | \psi(t) \rangle \quad (2.2-6)$$

$$i \frac{d}{dt} \mathbf{j}'(\mathbf{r}, t) = \langle \psi'(t) | [\hat{\mathbf{j}}(\mathbf{r}), \hat{H}'] | \psi'(t) \rangle \quad (2.2-7)$$

Subtracting Eq. 2.2-7 from Eq. 2.2-6, using the same initial conditions for the wavefunction, density, and the current density at $t = t_0$, we get

$$i \frac{d}{dt} [\mathbf{j}(\mathbf{r}, t) - \mathbf{j}'(\mathbf{r}, t)]_{t=t_0} = \langle \psi_0 | [\hat{\mathbf{j}}(\mathbf{r}), H(t_0) - H'(t_0)] | \psi_0 \rangle \quad (2.2-8)$$

$$= in_0(r) \nabla [v(\mathbf{r}, t_0) - v'(\mathbf{r}, t_0)] \quad (2.2-9)$$

where initial values of $(\psi_0, n_0, \mathbf{j}_0)$ are given to each of the wavefunction, density, and the current density respectively. Applying the equation of motion $k + 1$ times leads to

$$i \frac{d^{k+1}}{dt^{k+1}} [\mathbf{j}(\mathbf{r}, t) - \mathbf{j}'(\mathbf{r}, t)]_{t=t_0} = in_0(r) \nabla u_k(\mathbf{r}) \quad (2.2-10)$$

The right side of Eq. 2.2-10 is nonzero, therefore, the current densities \mathbf{j} and \mathbf{j}' are not equal to each other. Now, the next part is to establish a one-to-one correspondence between the

current densities and the electron densities. For that, we utilize the continuity equation

$$\frac{\partial}{\partial t}n(\mathbf{r},t) = -\nabla \cdot \mathbf{j}(\mathbf{r},t) \quad (2.2-11)$$

We can write the continuity equation for both primed and unprimed systems. After taking the time-derivative $k + 1$ times for both systems and taking difference leads to

$$\frac{\partial^{k+2}}{\partial t^{k+2}}[n(\mathbf{r},t) - n'(\mathbf{r},t)] = -\nabla \cdot \frac{\partial^{k+1}}{\partial t^{k+1}}[\mathbf{j}(\mathbf{r},t) - \mathbf{j}'(\mathbf{r},t)] \quad (2.2-12)$$

$$= -\nabla \cdot [n_0(r)\nabla u_k(\mathbf{r})] \quad (2.2-13)$$

For some k , $u_k(\mathbf{r}) \neq \text{constant}$. If we show $\nabla \cdot [n_0(r)\nabla u_k(\mathbf{r})] \neq 0$, then we can prove $n \neq n'$. Runge and Gross show this using *reductio ad absurdum*. Let us assume $\nabla \cdot [n_0(r)\nabla u_k(\mathbf{r})] = 0$ with $u_k(\mathbf{r}) \neq \text{constant}$. The Green's first identity for two scalars Ψ and ϕ gives us

$$\int_V (\Psi \nabla^2 \phi + \nabla \Psi \cdot \nabla \phi) dV = \oint_S \Psi \nabla \phi \cdot d\mathbf{S}. \quad (2.2-14)$$

Substituting $\Psi = u_k(\mathbf{r})$ and $\phi = n_0(r)u_k(\mathbf{r})$, we get following identity.

$$\int_V n_0(\mathbf{r})|\nabla u_k(\mathbf{r})|^2 dV = - \int_V u_k(\mathbf{r})\nabla \cdot [n_0(r)\nabla u_k(\mathbf{r})] + \oint_S n_0(\mathbf{r})u_k(\mathbf{r})\nabla u_k(\mathbf{r}) \cdot d\mathbf{S} \quad (2.2-15)$$

Here, the first term on R.H.S of Eq. 2.2-15 is zero by assumption. The second term also vanishes for infinite surface as $r \rightarrow \infty$. However, the term on the L.H.S is positive and becomes zero only if $u_k(\mathbf{r})$ is just a constant. This clearly violates our assumptions. Therefore, $\nabla \cdot [n_0(r)\nabla u_k(\mathbf{r})] \neq 0$ proving $n \neq n'$ if $\mathbf{j} \neq \mathbf{j}'$. This completes the proof of the RG theorem.

2.3 Kohn-Sham equations in TDDFT

The Kohn-Sham equation for the interacting electrons in the presence of time-dependent potential is given by

$$i\frac{\partial}{\partial t}\phi_i(\mathbf{r},t) = \left[-\frac{\nabla^2}{2} + v_{KS}(\mathbf{r},t) \right] \phi_i(\mathbf{r},t), \quad (2.3-16)$$

with the density $n(\mathbf{r},t) = \sum_i^{occupied} |\phi_i(\mathbf{r},t)|^2$. The $v_{KS}(\mathbf{r},t)$ is the time-dependent KS potential defined similarly as in Eq. 1.1-10, but with both spatial and time dependences. Similar to the static case, the most important and complex part in the KS potential is the exchange-correlation potential which now depends on initial states ψ_0, ϕ_0 and also on the entire history of the density (i.e. memory dependence). The static form of v_{xc} is simply the functional derivative of the XC-energy. Though its exact form is unknown, several good approximations exist for the static case. Also, there are various ways of constructing a time-dependent exchange-correlation potential such as adiabatic approximation, time-dependent optimized effective potential (TDOEP) [105–107], or some memory dependent functionals [106]. The kernels we used basically come from the first category, an adiabatic approximation. Therefore, we will discuss this particular approach more in details.

Adiabatic approximation

In this approximation, we evaluate an exchange-correlation potential simply as a function of the instantaneous density, instead of using the entire history of the density. Therefore, the resulting functionals are local in time. This approximation works well in those scenarios where the effect of temporal dependence is negligible. In common practice, we simply take various approximations within the static ground-state (GS) and evaluate it using instantaneous density to obtain a time-dependent XC potential as

$$v_{xc}^{adiabatic}(\mathbf{r},t) = v_{xc}^{GS}[n](\mathbf{r}) \big|_{n=n(t)} \quad (2.3-17)$$

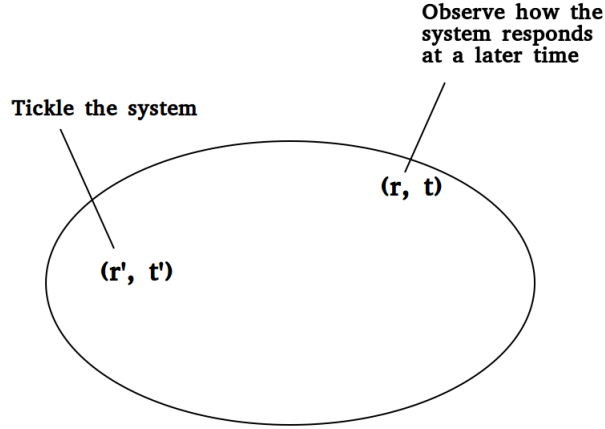


Figure 2.1: Schematic of a linear-response mechanism.

Here $v_{xc}^{GS}[n](\mathbf{r})$ is simply the static ground-state XC potential. If use LDA XC potential, then we get adiabatic LDA (ALDA) approximation which is the simplest approximation available in TDDFT,

$$v_{xc}^{ALDA}(\mathbf{r}, t) = v_{xc}^{HEG}(n) |_{n=n(\mathbf{r}, t)}. \quad (2.3-18)$$

$v_{xc}^{HEG}(n)$ is simply the static XC potential of homogeneous electron gas (HEG). Similarly, one can use GGAs and meta-GGAs ground-state XC-potentials to construct their time-dependent counterpart. We will discuss their performances on various properties in details in next section of the dynamic exchange-correlation kernel within the linear response theory. They provide the accurate results for many properties, however, the error in static ground-state XC potential also transfers to the TDDFT approximations.

2.4 Linear-response theory

The linear-response theory provides an alternative way other than to solve a full time-dependent KS equations to deal with system of electrons under the influence of the time-dependent perturbation. However, It works well only when the external time-dependent potential is small as in the case of many spectroscopic experiments. We assume that our system remains in the vicinity of the ground-state after the application of a weak time-

dependent perturbation. Suppose $\delta v_{ext}(\mathbf{r}', t')$ be the external perturbation applied to the system at \mathbf{r}', t' , then the density fluctuation $\delta n(\mathbf{r}, t)$ at \mathbf{r}, t is defined as

$$\delta n(\mathbf{r}, t) = \chi(\mathbf{r}, \mathbf{r}', t - t') \delta v_{ext}(\mathbf{r}', t'). \quad (2.4-19)$$

Where χ is called an interacting density-density response function, which describe the response of the system under the influence of the external perturbation. Here, we have drop the necessary spatial and frequency integration, and we will follow the same throughout the text. In frequency space, the relation is given as

$$\delta n(\mathbf{r}, \omega) = \chi(\mathbf{r}, \mathbf{r}', \omega) \delta v_{ext}(\mathbf{r}', \omega). \quad (2.4-20)$$

The Eqs. 2.4-19 and 2.4-20 show a linear relationship between the perturbation and the density fluctuation. However, there can be processes [108, 109] that require the nonlinear response or nonperturbative theory.

2.4.1 Interacting density-density response function

Interacting density-density response function χ is a key quantity in the linear-response TDDFT, as it can describe various ground-state and excited-state properties related to different phenomenon. For example, static screening, collective plasmon modes, electron-energy-loss spectra, absorption spectra, Raman spectra, etc. The χ can computed using noninteracting density response function χ_0 of a fictitious system, also known as the Kohn-Sham response function. The relation between interacting and noninteracting response function is given by a Dyson-like equation

$$\chi = \chi_0 + \chi_0 f_{Hxc} \chi, \quad (2.4-21)$$

where f_{Hxc} is known as the Hartree exchange-correlation kernel. χ_0 is the noninteracting response function. Similarly, one can obtain the density fluctuation using the Kohn-Sham effective potential as

$$\delta n(\mathbf{r}, \omega) = \chi_0(\mathbf{r}, \mathbf{r}', \omega) \delta v_{KS}(\mathbf{r}', \omega). \quad (2.4-22)$$

The KS potential $\delta v_{KS}(\mathbf{r}', \omega)$ is defined as

$$\delta v_{KS}(\mathbf{r}, \omega) = \delta v_{ext}(\mathbf{r}, \omega) + \delta v_{Hartree}(\mathbf{r}, \omega) + \delta v_{xc}(\mathbf{r}, \omega), \quad (2.4-23)$$

where δv_{ext} is the same external potential defined in the case of interacting response function. The $\delta v_{Hartree}$ is the linear part of the change in the Hartree potential, whereas the last term $\delta v_{xc}(\mathbf{r}, \omega)$ present the change in the exchange-correlation part. Now applying the chain rule,

$$\begin{aligned} \chi(\mathbf{r}, \mathbf{r}', \omega) &= \frac{\delta n(\mathbf{r}, \omega)}{\delta v_{ext}(\mathbf{r}', \omega)} \\ &= \frac{\delta n(\mathbf{r}, \omega)}{\delta v_{KS}(\mathbf{r}_1, \omega)} \times \frac{\delta v_{KS}(\mathbf{r}_1, \omega)}{\delta v_{ext}(\mathbf{r}', \omega)} \\ &= \chi_0(\mathbf{r}, \mathbf{r}_1, \omega) \times \frac{\delta v_{ext}(\mathbf{r}_1, \omega) + \delta v_H(\mathbf{r}_1, \omega) + \delta v_{xc}(\mathbf{r}_1, \omega)}{\delta v_{ext}(\mathbf{r}', \omega)} \\ &= \chi_0(\mathbf{r}, \mathbf{r}_1, \omega) \times \left[\frac{\delta v_{ext}(\mathbf{r}_1, \omega)}{\delta v_{ext}(\mathbf{r}', \omega)} + \frac{\delta v_H(\mathbf{r}_1, \omega)}{\delta v_{ext}(\mathbf{r}', \omega)} + \frac{\delta v_{xc}(\mathbf{r}_1, \omega)}{\delta v_{ext}(\mathbf{r}', \omega)} \right] \\ &= \chi_0(\mathbf{r}, \mathbf{r}_1, \omega) \times \left[\delta(\mathbf{r}_1 - \mathbf{r}') + \frac{\delta v_H(\mathbf{r}_1, \omega)}{\delta n(\mathbf{r}_2, \omega)} \times \frac{\delta n(\mathbf{r}_2, \omega)}{\delta v_{ext}(\mathbf{r}', \omega)} + \frac{\delta v_{xc}(\mathbf{r}_1, \omega)}{\delta n(\mathbf{r}_2, \omega)} \times \frac{\delta n(\mathbf{r}_2, \omega)}{\delta v_{ext}(\mathbf{r}', \omega)} \right] \\ \therefore \chi(\mathbf{r}, \mathbf{r}', \omega) &= \chi_0(\mathbf{r}, \mathbf{r}_1, \omega) \times \left[\delta(\mathbf{r}_1 - \mathbf{r}') + \frac{1}{|\mathbf{r}_1 - \mathbf{r}_2|} \chi(\mathbf{r}_2, \mathbf{r}', \omega) + f_{xc}(\mathbf{r}_1, \mathbf{r}_2, \omega) \chi(\mathbf{r}_2, \mathbf{r}', \omega) \right] \end{aligned} \quad (2.4-24)$$

Here, we use $\frac{\delta v_H(\mathbf{r}_1, \omega)}{\delta n(\mathbf{r}_2, \omega)} = \frac{1}{|\mathbf{r}_1 - \mathbf{r}_2|}$, $\frac{\delta n(\mathbf{r}_2, \omega)}{\delta v_{ext}(\mathbf{r}', \omega)} = \chi(\mathbf{r}_2, \mathbf{r}', \omega)$, and $\frac{\delta v_{xc}(\mathbf{r}_1, \omega)}{\delta n(\mathbf{r}_2, \omega)} = f_{xc}(\mathbf{r}_1, \mathbf{r}_2, \omega)$. The $f_{xc}(\mathbf{r}_1, \mathbf{r}_2, \omega)$ is an exchange-correlation kernel and the term f_{Hxc} in Eq. 2.4-21 is simply the sum of this kernel with the Hartree kernel defined by $\frac{1}{|\mathbf{r}_1 - \mathbf{r}_2|}$, also represent the effective interaction within the system. The kernel is set to zero ($f_{xc} = 0$) for the RPA,

while it should be restored to include other local-field effects beyond a mean-field like interaction in RPA. Here, again we drop the necessary frequency and spatial integration in the derivation. A complete form would be

$$\chi(\mathbf{r}, \mathbf{r}', \omega) = \chi_0(\mathbf{r}, \mathbf{r}_1, \omega) + \int \int d^3 r_1 d^3 r_2 \chi_0(\mathbf{r}, \mathbf{r}_1, \omega) \left[\frac{1}{|\mathbf{r}_1 - \mathbf{r}_2|} + f_{xc}(\mathbf{r}_1, \mathbf{r}_2, \omega) \right] \chi(\mathbf{r}_2, \mathbf{r}', \omega). \quad (2.4-25)$$

Both Eq. 2.4-24 and Eq. 2.4-21 are the same and called the Dyson's equation. Furthermore, in the wavevector and frequency space, it has a form

$$\chi(q, \omega) = \chi_0(q, \omega) + \chi_0(q, \omega) \left[\frac{4\pi}{q^2} + f_{xc}(q, \omega) \right] \chi(q, \omega). \quad (2.4-26)$$

The uniform electron gas (UEG or HEG) is a paradigm model system, used to construct the density functionals for both static and the excited-state properties. Approximations to the exchange-correlation energy in the static ground-state and the dynamic exchange-correlation kernel within TDDFT obtained using HEG are also highly applicable for many properties of real systems. Therefore, it is intuitive to discuss Eq. 2.4-25 for UEG. Noninteracting response function (χ_0) for UEG can be calculated using an exact expression given by Lindhard [110]. Alternatively, the noninteracting response function can be constructed using Kohn-Sham ground-state eigenstates $\{\phi\}$ and eigenvalues $\{\epsilon\}$.

$$\chi_0(\mathbf{r}, \mathbf{r}', \omega) = \lim_{\eta \rightarrow 0^+} \sum_{ij}^{\infty} (f_i - f_j) \left[\frac{\phi_j(\mathbf{r}) \phi_j^*(\mathbf{r}') \phi_i(\mathbf{r}') \phi_i^*(\mathbf{r})}{\omega - (\epsilon_j - \epsilon_i) + i\eta} \right] \quad (2.4-27)$$

Also, the exchange-correlation kernel can be constructed from UEG by satisfying exact-constraints which is governed by the exact properties of the interacting response function. For UEG, some of them are listed below.

- A complex quantity
- Stability condition, $\chi(q, \omega = 0) \leq 0$.

- It has poles in a lower half of the complex-frequency plane.
- It is an analytic function of complex frequency along the imaginary-frequency axis.
- It follows the symmetry relations: $\chi(q, \omega) = \chi(-q, \omega)$, $\text{Re}\chi(q, -\omega) = \text{Re}\chi(q, \omega)$, and $\text{Im}\chi(q, -\omega) = -\text{Im}\chi(q, \omega)$.
- High-frequency behavior: $\text{Re} \chi(\mathbf{q}, \omega) \xrightarrow{\omega \rightarrow \infty} \frac{M^1(\mathbf{q})}{\omega^2} + \frac{M^3(\mathbf{q})}{\omega^4}$,
where $M^i(\mathbf{q}) = -\frac{2}{\pi} \int_0^\infty \omega^i \text{Im}\chi(\mathbf{q}, \omega) d\omega$ is the i^{th} moment of the density-density fluctuation satisfying the sum rules.
- The f-sum rule: $-\frac{1}{\pi} \int_0^\infty \omega \text{Im}\chi(\mathbf{q}, \omega) d\omega = \frac{nq^2}{2}$
- The third-moment sum rule:
$$-\frac{1}{\pi} \int_0^\infty \omega^3 \text{Im}\chi(\mathbf{q}, \omega) d\omega = \frac{nq^2}{2} \left\{ \frac{q^4}{4} + nq^2 v_q + \frac{6q^2}{d} t + n \sum_{\mathbf{k} \neq \mathbf{q}, \mathbf{k} > 0} v_k \left(\frac{\mathbf{k} \cdot \mathbf{q}}{q} \right)^2 [S(\mathbf{q} - \mathbf{k}) - S(\mathbf{k})] \right\}$$
. Here, $S(q) = \frac{M^0(\mathbf{q})}{2n}$ is the static structure factor, d is the number of dimensions, t is the average kinetic energy per particle in the ground-state, and $v_q = \frac{4\pi}{q^2}$ is the Fourier transform of the Coulomb interaction.

2.4.2 Exchange-correlation kernel

The exchange-correlation kernel is simply defined as the functional derivative of the time-dependent exchange-correlation potential with respect to the density, evaluated using the ground-state density $n_0(r)$.

$$f_{xc}(\mathbf{r}t, \mathbf{r}'t') = \left. \frac{\delta v_{xc}(\mathbf{r}, t)}{\delta n(\mathbf{r}', t')} \right|_{n=n_0(\mathbf{r})} \quad (2.4-28)$$

The kernel has different role in various kind of problems. It refers to as a “local field correction” while evaluating the correlation energy of an uniform electron gas. In the Landau’s Fermi-liquid theory, the combination of kernel and the bare Coulomb’s interaction gives the effective interaction. It also represents the effective electron-hole interaction when used to

describe the excitonic effects in the semiconductors and insulators.

The exact exchange-correlation is not known due to an absence of an exact static exchange-correlation potential. Therefore, it is either constructed by satisfying exact-constraints and appropriate norms or by using many-body perturbation theory. There are several attempts to construct the kernel either only with wavevector-dependence, or only with frequency-dependence, or both. As previously mentioned, the simplest kernel is ALDA. Using the potential given by Eq. 2.3-18, ALDA kernel can be defined as,

$$f_{xc}^{ALDA}(\mathbf{r}t, \mathbf{r}'t') = \delta(\mathbf{r} - \mathbf{r}')\delta(t - t')f_{xc}^{UEG}(n)|_{n=n(\mathbf{r},t)} \quad (2.4-29)$$

$$= \delta(\mathbf{r} - \mathbf{r}')\delta(t - t')\frac{d}{dn}v_{xc}^{UEG}(n)|_{n=n(\mathbf{r},t)} \quad (2.4-30)$$

$$= \delta(\mathbf{r} - \mathbf{r}')\delta(t - t')\frac{d^2}{dn^2}E_{xc}^{UEG}(n)|_{n=n(\mathbf{r},t)}, \quad (2.4-31)$$

where $E_{xc}^{UEG}(n)$ and $v_{xc}^{UEG}(n)$ are the exchange-correlation energy and potential respectively of an uniform electron gas. It is a kernel, local in both space and time. More advance kernel can be constructed for the UEG, using more exact-constraints listed below.

- Compressibility sum rule

$$\lim_{q \rightarrow 0} f_{xc}^{UEG}(q, \omega = 0; n) = \frac{d^2}{dn^2} [n\epsilon_{xc}(n)] = f_0[n] \quad (2.4-32)$$

- Third frequency moment rule

$$\lim_{q \rightarrow \infty} f_{xc}^{UEG}(q, \omega = 0; n) = -\frac{4}{5}n^{2/3}\frac{d}{dn}\left(\frac{\epsilon_{xc}(n)}{n^{2/3}}\right) + 6n^{1/3}\frac{d}{dn}\left(\frac{\epsilon_{xc}(n)}{n^{1/3}}\right) = f_\infty[n] \quad (2.4-33)$$

- $f_0[n] < f_\infty[n] < 0$
- $f_{xc}^{UEG}(q, \omega)$ is a complex-valued function. Its real and imaginary parts respectively

are even and odd function of frequency.

- $f_{xc}^{UEG}(q, \omega)$ is an analytic function of ω in the upper half of the complex frequency plane, with a real high-frequency limit $f_{xc}^{UEG}(q, \infty)$. Therefore, the following Kramers-Kronig relations hold.

$$\text{Re}f_{xc}^{UEG}(q, \omega) - f_{xc}^{UEG}(q, \infty) = P \int_{\infty}^{\infty} \frac{d\omega'}{\pi} \frac{\text{Im}f_{xc}^{UEG}(q, \omega')}{\omega' - \omega} \quad (2.4-34)$$

$$\text{Im}f_{xc}^{UEG}(q, \omega) = -P \int_{\infty}^{\infty} \frac{d\omega'}{\pi} \frac{\text{Re}f_{xc}^{UEG}(q, \omega') - f_{xc}^{UEG}(q, \infty)}{\omega' - \omega} \quad (2.4-35)$$

- $\text{Im}f_{xc}^{UEG}(q=0, \omega \rightarrow \infty) = -\frac{23\pi}{15\omega^{3/2}}$. This result comes from the second-order perturbation expansion of the irreducible polarization operator. It becomes exact at high densities.
- $\text{Re}f_{xc}^{UEG}(q=0, \omega \rightarrow \infty) = f_{\infty} + \frac{23\pi}{15\omega^{3/2}}$.

However, the construction of the kernel for properties of an inhomogeneous real system is somehow complicated. The most important properties of the kernel for the real solids is its optical limit, *i.e.*, $f_{xc} \sim \frac{\alpha(\omega)}{q^2}|_{q \rightarrow 0}$, where $\alpha(\omega)$ is the some frequency-dependent function [111]. Here are some commonly used exchange-correlation kernels for an inhomogeneous system that can be found in the literature, beside ALDA kernel.

(I) Richardson and Ashcroft (RA) kernel

It is a wavevector- and frequency- dependent exchange-correlation kernel. This kernel is developed using the numerical data calculated by RA [112] and it also satisfies more exact constraints. The RA kernel for imaginary frequency iu can be expressed in terms of local-field factors

$$f_{xc}^{RA}(\mathbf{q}, iu) = -\frac{4\pi e^2}{q^2} [G_s(Q, iU) + G_n(Q, iU)], \quad (2.4-36)$$

with $Q = \frac{q}{2k_F}$, and $U = \frac{u}{4\omega_F}$. Also, the local-field factors G_n and G_s can be obtained from the on-top pair distribution function $g(0)$. More details can be explored from Ref. [112].

(II) PGG kernel

It was derived by Petersilka, Gossmann, and Gross in 1996 [95], in the context of the time-dependent OEP method. The PGG kernel is exchange-only, frequency-independent and its real-space version is given by

$$f_x^{PGG}(\mathbf{r}, \mathbf{r}', \omega) = -\frac{2e^2}{|\mathbf{r} - \mathbf{r}'|} \frac{|\sum_k f_k \phi_k(\mathbf{r}) \phi_k^*(\mathbf{r}')|^2}{n(\mathbf{r})n(\mathbf{r}')}, \quad (2.4-37)$$

whereas, its q-space version is defined as

$$f_x^{PGG}(\mathbf{q}, \omega) = -\frac{3\pi e^2}{10k_F^2} \left\{ \left(\frac{2}{Q} - 10Q \right) \ln \frac{1+Q}{|1-Q|} + (2Q^4 - 10Q^2) \ln \left[\left(1 + \frac{1}{Q} \right) \left| 1 - \frac{1}{Q} \right| \right] + 11 + 2Q^2 \right\}, \quad (2.4-38)$$

where $Q = \frac{q}{2k_F}$.

(III) Energy optimized XC kernels from Dobson and Wang

This kernel is parametrized for the interacting electron gas, provides accurate correlation energy when applied within the ACFDT framework. Dobson and Wang simply took the kernel given by Eq. 2.4-31, and employed two kind of scaling schemes with respect to Coulomb coupling strength λ . The kernel has a simple form of

$$f_{xc\lambda}(\mathbf{r}, \mathbf{r}', t - t') \approx f_{xc}(n, \lambda) \delta^3(\mathbf{r} - \mathbf{r}') \delta(t - t') \quad (2.4-39)$$

The first scaling scheme is defined as,

$$f_{xc}(n, \lambda) = \lambda f_{xc}^I(n). \quad (2.4-40)$$

Where, $f_{xc}^I(r_s) \approx -0.51887r_s^2 + 4.9359 \times 10^{-3}r_s^3 - 5.9603 \times 10^{-5}r_s^4$ is a function, parametrized to give an accurate correlation energy of UEG using the least-square fitting. Similarly, the second scheme is described as

$$f_{xc}^{II}(n, \lambda) = \lambda^{-1} F_{xc}^{II}(\lambda r_s), \quad (2.4-41)$$

where, $F_{xc}^{II}(r_s) \approx -0.50044r_s^2 + 4.9653 \times 10^{-3}r_s^3 - 3.366 \times 10^{-5}r_s^4$ is obtained using similar optimization procedure as that of scheme I.

CP07 kernel

It is a dynamic exchange-correlation kernel, developed by Constantin and Pitarke in 2007 [113]. It is defined as

$$f_{xc}^{CP07}(n; \mathbf{q}, \omega) = \frac{4\pi}{q^2} B(n) \left[e^{-k_n \omega q^2} - 1 \right] - \frac{4\pi}{k_F^2} \frac{c(n)}{1 + 1/q^2}. \quad (2.4-42)$$

Here, $B(n)$, $k_{n,\omega}$, and $C(n)$ are defined as follows:

$$k_F = (3\pi n)^{1/3} \quad (2.4-43)$$

$$B(n) = \frac{1 + a_1 x + a_2 x^3}{3 + b_1 x + b_2 x^3}; x = \sqrt{r_s}, a_1 = 2.15, a_2 = 0.435, b_1 = 1.57, b_2 = 0.409 \quad (2.4-44)$$

$$c(n) = -\frac{\pi}{2k_F} \frac{d(r_s \epsilon_c)}{dr_s} \quad (2.4-45)$$

$$a(n) = 6\sqrt{c(n)} \quad (2.4-46)$$

$$k_{n,iu} = -\frac{f_{xc}(n; \mathbf{q} \rightarrow 0, \omega = 0)}{4\pi B(n)} \frac{1 + a(n)u + c(n)u^2}{1 + u^2} \quad (2.4-47)$$

$$= -\frac{f_0}{4\pi B(n)} \frac{1 + a(n)u + c(n)u^2}{1 + u^2} \quad (2.4-48)$$

This kernel satisfies the compressibility sum rule and the third-frequency-moment sum rules. It also provides the correct asymptotic behavior at large q . We also have revised this kernel to get a modified-CP07 (MCP07) kernel, which is presented in section 7 in detail.

Renormalized XC kernels (rALDA and rAPBE)

Contrary to the RPA, the ALDA kernel predicts too high correlation energies for a wide range of densities and wavevectors, compared to the results from the exact parametrization of Perdew and Wang [19]. Also, the correlation energy from the ALDA kernel decays too slowly at large q . This is due to its locality in the approximation, as it is independent of q . To address this problem, Olsen and Thygesen proposed a renormalization scheme defined by truncating the ALDA kernel at $q = 2k_F$ as

$$f_{Hxc}^{rALDA}(\mathbf{q}) = \theta(2\mathbf{k}_F - \mathbf{q})f_{Hxc}^{ALDA}(\mathbf{q}). \quad (2.4-49)$$

Similarly, we can define renormalized adiabatic PBE (rAPBE) kernel. We can also include nonlocal exchange-correlation effects by replacing local density $n(\mathbf{r})$ by an average density $n^*(\mathbf{r}) = \int \phi(\mathbf{r} - \mathbf{r}')n(\mathbf{r}')d\mathbf{r}'$. The ϕ can be chosen as the Fourier transform of the step function $\theta(2\mathbf{k}_F - \mathbf{q})$. In real space, the kernel has the form:

$$f_{xc}^{rAX}[n](\mathbf{r}) = \frac{f_{xc}^{AX}[n]}{2\pi^2 r^3} [\sin(q_c[n]\mathbf{r}) - q_c[n]r\cos(q_c[n]\mathbf{r})] - \frac{1}{\mathbf{r}} \left[1 - \frac{2}{\pi} \int_0^{q_c[n]\mathbf{r}} \frac{\sin x}{x} dx \right], \quad (2.4-50)$$

with $q_c[n] = \sqrt{\frac{-4\pi}{f_{xc}^{AX}[n]}}$. X is either LDA or PBE. For inhomogeneous systems, following substitutions have been made.

$$\mathbf{r} \rightarrow |\mathbf{r} - \mathbf{r}'| \quad (2.4-51)$$

$$n \rightarrow \frac{n(\mathbf{r}) + n(\mathbf{r}')}{2} \quad (2.4-52)$$

$$\nabla n \rightarrow \frac{\nabla_{\mathbf{r}}n(\mathbf{r}) + \nabla_{\mathbf{r}'}n(\mathbf{r}')}{2} \quad (2.4-53)$$

More details about construction and applications of the renormalized kernels can be found in Refs. [79, 114, 115]

NEO kernels

The nonlocal energy-optimized (NEO) kernels are constructed for both uniform electron gas and for the jellium surface [116]. It is also a kernel having meta-GGA ingredients such as Z_σ and α , and are exchange-like kernels. There are mainly three forms of this kernel. The first form is called the NEO-I kernel [117]. It is designed to produce a correctly long-range exchange kernel for one and two electron systems, where $Z_\sigma = 1$. Also, it should not produce any second-order gradient correction to the RPA correlation energy in a slowly-varying high electron density, where $Z_\sigma \rightarrow 0 + O(\nabla^2)$. It is defined as

$$f_x^{NEO}([n], \mathbf{r}, \mathbf{r}') = -v(\mathbf{r}, \mathbf{r}') \sum_{\sigma} \left(\frac{n_{\sigma}}{n} \right)^2 \times \text{erfc}(a^{NEO-I} |\mathbf{r} - \mathbf{r}'|) \quad (2.4-54)$$

$$a^{NEO-I} = \sqrt{\tilde{c}(1 - Z_{\sigma}^2) k_{F\sigma}^2} \quad (2.4-55)$$

$$Z_{\sigma} = \frac{\tau_{\sigma}^W}{\tau_{\sigma}} \quad (2.4-56)$$

$$\tau_{\sigma}^W = \frac{|\nabla n_{\sigma}|^2}{8n_{\sigma}} \quad (2.4-57)$$

$$\tau_{\sigma} = \frac{1}{2} \sum_i^{\text{occup}} |\nabla \phi_{i\sigma}|^2 \quad (2.4-58)$$

In momentum space, the kernel becomes

$$f_x^{NEO}[n, z](\mathbf{q}) = -\frac{4\pi}{q^2} \sum_{\sigma} \left(\frac{n_{\sigma}}{n} \right)^2 \times \left[1 - \exp\left(-\frac{q^2}{4\tilde{c}(1 - Z_{\sigma}^2) k_{F\sigma}^2} \right) \right]. \quad (2.4-59)$$

The $\tilde{c} = 0.264$ parameter is taken to fit the exact second-order exchange contribution to the correlation energy of the UEG. The problem with this kernel is that it produces an unwanted long-ranged behavior in the tail of the electron density of a jellium surface where the RPA should be recovered. The second form has the similar expression as that of the NEO-I

kernel, but only differs in Eq. 2.4-55.

$$a^{NEO-II} = \sqrt{\tilde{c}(3\alpha_\sigma - 3\alpha_\sigma^2 + \alpha_\sigma^3)k_{F\sigma}^2} \quad (2.4-60)$$

$$\alpha_\sigma = \frac{\tau_\sigma - \tau_\sigma^W}{\tau_\sigma^{unif}} \quad (2.4-61)$$

$$\tau_\sigma^{unif} = (1/2)(3/10)(3\pi^2)^{(2/3)}(2n_\sigma)^{5/3} \quad (2.4-62)$$

It preserves all the good features of the first scheme, but also eliminates an unwanted kernel in the tail of the electron density far away from the surface ($\alpha_\sigma \rightarrow \infty$). Moreover, we can also tune the value of \tilde{c} by fitting with other exact constraints or by fitting with various parametrization of the ground-state correlation energy of the UEG [116, 118]. In chapter 6, we will discuss the various forms of these NEO kernels to describe the plasmonic excitation of the homogeneous interacting electron gas. We will also discuss various forms of the NEO kernels for the absorption spectra of various semiconductors and insulators in chapter 8.

2.5 Adiabatic-connection fluctuation-dissipation theory (ACFDT) for the ground-state exchange-correlation energy

The ACFDT formalism accurately describe the ground-state exchange-correlation (XC) energy within the linear response theory. Here, we provide a detail derivation of the XC energy using this formalism. The noninteracting and interacting Hamiltonian are connected adiabatically as

$$H(\lambda) = H_0 + \lambda H_1(\lambda). \quad (2.5-63)$$

Here, $H(\lambda = 0) = H_0$ and $H(\lambda = 1)$ are noninteracting and interacting Hamiltonian respectively.

$$H(\lambda) = \sum_{i=1}^N \left[-\frac{1}{2} \nabla_i^2 + v_{ext}^\lambda(\mathbf{r}_i) \right] + \sum_{i>j=1}^N \frac{\lambda}{|\mathbf{r}_i - \mathbf{r}_j|} \quad (2.5-64)$$

$$H_0 = \sum_{i=1}^N \left[-\frac{1}{2} \nabla_i^2 + v_{ext}^{\lambda=0}(\mathbf{r}_i) \right] \quad (2.5-65)$$

$$H_1(\lambda) = \sum_{i>j=1}^N \frac{1}{|\mathbf{r}_i - \mathbf{r}_j|} + \frac{1}{\lambda} \sum_{i=1}^N \left[v_{ext}^\lambda(\mathbf{r}_i) - v_{ext}^{\lambda=0}(\mathbf{r}_i) \right] \quad (2.5-66)$$

The λ is called the coupling strength with $0 \leq \lambda \leq 1$. The switching of the system is quite smooth in a adiabatic-connection path such that the total electronic densities of λ -dependent fictitious systems remain conserved and equal to that of interacting system.

$$n^\lambda(\mathbf{r}) = n^{\lambda=1}(\mathbf{r}) = n(\mathbf{r}) \quad (2.5-67)$$

Now, the total energy in AC connection is obtained by solving an eigenvalue problem.

$$H(\lambda)|\psi_\lambda\rangle = E(\lambda)|\psi_\lambda\rangle \quad (2.5-68)$$

$$\langle \psi_\lambda | \psi_\lambda \rangle = 1 \quad (2.5-69)$$

The Hellman-Feynman theorem states,

$$\frac{dE(\lambda)}{d\lambda} = \langle \psi_\lambda | \frac{dH(\lambda)}{d\lambda} | \psi_\lambda \rangle . \quad (2.5-70)$$

Therefore, the total ground-state energy is obtained as

$$E(\lambda = 1) = E_0 + \int_{\lambda=0}^{\lambda=1} d\lambda \langle \psi_\lambda | H_1(\lambda) + \lambda \frac{dH_1(\lambda)}{d\lambda} | \psi_\lambda \rangle \quad (2.5-71)$$

$$= E_0 + \int_0^1 d\lambda \langle \psi_\lambda | \frac{1}{2} \sum_{i \neq j=1}^N \frac{1}{|\mathbf{r}_i - \mathbf{r}_j|} | \psi_\lambda \rangle + \int_0^1 d\lambda \langle \psi_\lambda | \sum_{i=1}^N \frac{dv_{ext}^\lambda(\mathbf{r}_i)}{d\lambda} | \psi_\lambda \rangle \quad (2.5-72)$$

$$E = E_0 + \frac{1}{2} \int_0^1 d\lambda \iint d\mathbf{r} d\mathbf{r}' \times \langle \psi_\lambda | \frac{\hat{n}(\mathbf{r})[\hat{n}(\mathbf{r}') - \delta(\mathbf{r} - \mathbf{r}')] }{|\mathbf{r} - \mathbf{r}'|} | \psi_\lambda \rangle + \int d\mathbf{r} n(\mathbf{r}) [v_{ext}^{\lambda=1}(\mathbf{r}) - v_{ext}^{\lambda=0}(\mathbf{r})], \quad (2.5-73)$$

with $\hat{n}(\mathbf{r}) = \sum_i^N \delta(\mathbf{r} - \mathbf{r}_i)$ is the density operator, and gives $n(\mathbf{r}) = \langle \psi_\lambda | \hat{n}(\mathbf{r}) | \psi_\lambda \rangle$ for any λ . Also, substituting $E_0 = \langle \psi_0 | H_0 | \psi_0 \rangle$ in Eq. 2.5-73, we get

$$E = \langle \psi_0 | \sum_{i=1}^N \left[-\frac{1}{2} \nabla_i^2 + v_{ext}^{\lambda=0}(\mathbf{r}_i) \right] | \psi_0 \rangle + \frac{1}{2} \int_0^1 d\lambda \iint d\mathbf{r} d\mathbf{r}' \times \langle \psi_\lambda | \frac{\hat{n}(\mathbf{r})[\hat{n}(\mathbf{r}') - \delta(\mathbf{r} - \mathbf{r}')] }{|\mathbf{r} - \mathbf{r}'|} | \psi_\lambda \rangle + \int d\mathbf{r} n(\mathbf{r}) [v_{ext}^{\lambda=1}(\mathbf{r}) - v_{ext}^{\lambda=0}(\mathbf{r})] \quad (2.5-74)$$

$$\therefore E = T_s[\psi_i(\mathbf{r})] + \int d\mathbf{r} n(\mathbf{r}) v_{ext}^{\lambda=1}(\mathbf{r}) + \frac{1}{2} \int_0^1 d\lambda \iint d\mathbf{r} d\mathbf{r}' \times \langle \psi_\lambda | \frac{\hat{n}(\mathbf{r})[\hat{n}(\mathbf{r}') - \delta(\mathbf{r} - \mathbf{r}')] }{|\mathbf{r} - \mathbf{r}'|} | \psi_\lambda \rangle \quad (2.5-75)$$

Now, we define the “fluctuation” ($\delta\hat{n}(\mathbf{r})$) of the density operator ($\hat{n}(\mathbf{r})$) with respect to its expectation value $n(\mathbf{r})$ as

$$\delta\hat{n}(\mathbf{r}) = \hat{n}(\mathbf{r}) - n(\mathbf{r}) \quad (2.5-76)$$

Substituting Eq. 2.5-76 in Eq. 2.5-75 and comparing with Eq. 1.1-8, we get

$$E = T_s[\psi_i(\mathbf{r})] + E_{ext}[n(\mathbf{r})] + E_H[n(\mathbf{r})] + \frac{1}{2} \int_0^1 d\lambda \iint d\mathbf{r}d\mathbf{r}' \times \frac{\langle \psi_\lambda | \delta\hat{n}(\mathbf{r})\delta\hat{n}(\mathbf{r}') | \psi_\lambda \rangle - n(\mathbf{r})\delta(\mathbf{r}-\mathbf{r}')}{|\mathbf{r}-\mathbf{r}'|} \quad (2.5-77)$$

$$\therefore E_{xc} = \frac{1}{2} \int_0^1 d\lambda \iint d\mathbf{r}d\mathbf{r}' \times \frac{\langle \psi_\lambda | \delta\hat{n}(\mathbf{r})\delta\hat{n}(\mathbf{r}') | \psi_\lambda \rangle - n(\mathbf{r})\delta(\mathbf{r}-\mathbf{r}')}{|\mathbf{r}-\mathbf{r}'|} \quad (2.5-78)$$

The integrand in Eq. 2.5-78 divided by the density is an exact expression of the exchange-correlation hole. The quantity $\langle \psi_\lambda | \delta\hat{n}(r)\delta\hat{n}(r') | \psi_\lambda \rangle$ represents the density-density correlation (or fluctuations). It can be linked to the response of the system via the fluctuation-dissipation theorem as follows,

$$\langle \psi_\lambda | \delta\hat{n}(\mathbf{r})\delta\hat{n}(\mathbf{r}') | \psi_\lambda \rangle = -\frac{1}{\pi} \int_0^\infty d\omega \text{Im} \chi^\lambda(\mathbf{r}, \mathbf{r}', \omega), \quad (2.5-79)$$

where χ^λ is the interacting response function of the fictitious λ -dependent system. The Dyson's equation (Eq. 2.4-26) for such fictitious system also becomes λ -dependent as follows.

$$\chi^\lambda(\mathbf{q}, \omega) = \chi_{KS}(\mathbf{q}, \omega) + \chi_{KS}(\mathbf{q}, \omega) [v_c^\lambda(q) + f_{xc}^\lambda(\mathbf{q}, \omega)] \chi^\lambda(\mathbf{q}, \omega) \quad (2.5-80)$$

Also, the following scaling relation holds [119].

$$n \rightarrow \frac{n}{\lambda^3}, \quad q \rightarrow \frac{q}{\lambda}, \quad r_s \rightarrow \lambda r_s, \quad \omega \rightarrow \frac{\omega}{\lambda^2} \quad (2.5-81)$$

$$v_c^\lambda(q) = \frac{4\pi\lambda^2}{q^2} \quad (2.5-82)$$

$$f_{xc}^\lambda(q, \omega) = \lambda^{-1} f_{xc}^{\lambda=1}(q/\lambda, \omega/\lambda^2) \quad (2.5-83)$$

Substituting Eqs. 2.5-79 and 2.5-80 in Eq. 2.5-78, $v(r, r') = \frac{1}{|r-r'|}$, and using the scaling relations one can get the exact expression for the ground-state exchange-correlation energy

as,

$$\begin{aligned}
E_{xc} &= \frac{1}{2} \int_0^1 d\lambda \iint d\mathbf{r}d\mathbf{r}' v(\mathbf{r}, \mathbf{r}') \times [\langle \psi_\lambda | \delta \hat{n}(\mathbf{r}) \delta \hat{n}(\mathbf{r}') | \psi_\lambda \rangle - n(\mathbf{r}) \delta(\mathbf{r} - \mathbf{r}')] \\
&= \frac{1}{2} \int_0^1 d\lambda \iint d\mathbf{r}d\mathbf{r}' v(\mathbf{r}, \mathbf{r}') \times \left[-\frac{1}{\pi} \int_0^\infty d\omega \text{Im} \chi^\lambda(\mathbf{r}, \mathbf{r}', \omega) - n(\mathbf{r}) \delta(\mathbf{r} - \mathbf{r}') \right] \\
&= \frac{1}{2} \int_0^1 d\lambda \iint d\mathbf{r}d\mathbf{r}' v(\mathbf{r}, \mathbf{r}') \times \left[-\frac{1}{\pi} \int_0^\infty d\omega \chi^\lambda(\mathbf{r}, \mathbf{r}', i\omega) - n(\mathbf{r}) \delta(\mathbf{r} - \mathbf{r}') \right] \quad (2.5-84)
\end{aligned}$$

Here, we used the property of χ that it is analytic function of complex frequency along the imaginary-frequency axis. Also, in the q-space, it gives the wavevector-decomposition of the ground-state XC energy

$$E_{xc} = \int \frac{d^3q}{(2\pi)^3} \frac{1}{2} \int_0^1 d\lambda \frac{4\pi}{q^2} N[S^\lambda(\mathbf{q}) - 1], \quad (2.5-85)$$

with $S^\lambda(\mathbf{q})$ is the static structure factor obtained from the dynamic spectral function $S^\lambda(\mathbf{q}, \omega) = \left(-\frac{1}{\pi} \text{Im} \chi^\lambda(\mathbf{q}, \omega) \right)$ as

$$\begin{aligned}
S^\lambda(\mathbf{q}) &= \frac{1}{N} \int_0^\infty d\omega \left(-\frac{1}{\pi} \text{Im} \chi^\lambda(\mathbf{q}, \omega) \right) \\
\therefore S^\lambda(\mathbf{q}) &= \frac{1}{N} \int_0^\infty d\omega S^\lambda(\mathbf{q}, \omega) \quad (2.5-86)
\end{aligned}$$

We can obtain the exact exchange energy by substituting $\lambda = 0$ and evaluating Eqs. 2.5-85 as

$$E_x = \int \frac{d^3q}{(2\pi)^3} \frac{1}{2} \int_0^1 d\lambda \frac{4\pi}{q^2} N[S^{\lambda=0}(\mathbf{q}) - 1]. \quad (2.5-87)$$

Finally, the correlation energy is obtained as

$$E_c = E_{xc} - E_x. \quad (2.5-88)$$

When the kernel f_{xc} is zero, the correlation energy is called the RPA correlation energy, while it is called the beyond-RPA (bRPA) correlation energy when the kernel is restored.

2.5.1 RPA correlation energy

The interacting response function for the RPA is

$$\begin{aligned}\chi_{RPA}^\lambda &= \chi_0 + \chi_0 \lambda v \chi_{RPA}^\lambda \\ \therefore \chi_{RPA}^\lambda &= \frac{1}{\chi_0^{-1} - \lambda v}\end{aligned}\quad (2.5-89)$$

with $v = \frac{1}{|\mathbf{r}-\mathbf{r}'|}$ being the Hartree kernel, and χ_0 is given by Eq. 2.4-27. Now, the RPA correlation energy is defined as

$$\begin{aligned}E_c^{RPA} &= \frac{1}{2} \int_0^1 d\lambda \iint d\mathbf{r}d\mathbf{r}' v(\mathbf{r}, \mathbf{r}') \times \left[-\frac{1}{\pi} \int_0^\infty d\omega \chi_{RPA}^\lambda(\mathbf{r}, \mathbf{r}', i\omega) - n(\mathbf{r})\delta(\mathbf{r}-\mathbf{r}') \right] \\ &\quad - \frac{1}{2} \int_0^1 d\lambda \iint d\mathbf{r}d\mathbf{r}' v(\mathbf{r}, \mathbf{r}') \times \left[-\frac{1}{\pi} \int_0^\infty d\omega \chi_0(\mathbf{r}, \mathbf{r}', i\omega) - n(\mathbf{r})\delta(\mathbf{r}-\mathbf{r}') \right] \\ &= \frac{1}{2} \int_0^1 d\lambda \iint d\mathbf{r}d\mathbf{r}' v(\mathbf{r}, \mathbf{r}') \times -\frac{1}{\pi} \int_0^\infty d\omega [\chi_{RPA}^\lambda(\mathbf{r}, \mathbf{r}', i\omega) - \chi_0(\mathbf{r}, \mathbf{r}', i\omega)] \\ &= -\frac{1}{2\pi} \iint d\mathbf{r}d\mathbf{r}' v(\mathbf{r}, \mathbf{r}') \int_0^\infty d\omega \left[\int_0^1 d\lambda \chi_{RPA}^\lambda(\mathbf{r}, \mathbf{r}', i\omega) - \chi_0(\mathbf{r}, \mathbf{r}', i\omega) \right] \\ \therefore E_c^{RPA} &= \frac{1}{2\pi} \int_0^\infty d\omega Tr[\ln(1 - \chi_0(i\omega)v) - \chi_0(i\omega)v].\end{aligned}\quad (2.5-90)$$

Here Tr represents the trace of the matrix. To calculate the RPA correlation energy of a real solid, we estimate the noninteracting response function given by Eq. 2.4-27 as

$$\chi_0(\mathbf{r}, \mathbf{r}', \omega) = \sum_{\mathbf{k}, \mathbf{q}} \sum_{nm'}^{BZ} \frac{f_{n\mathbf{k}} - f_{n'(\mathbf{k}+\mathbf{q})}}{\omega + \varepsilon_{n\mathbf{k}} - \varepsilon_{n'(\mathbf{k}+\mathbf{q})} + i\eta} \psi_{n\mathbf{k}}^*(\mathbf{r}) \psi_{n'\mathbf{k}+\mathbf{q}}(\mathbf{r}) \psi_{n\mathbf{k}}(\mathbf{r}') \psi_{n'\mathbf{k}+\mathbf{q}}^*(\mathbf{r}'), \quad (2.5-91)$$

where, \mathbf{k}, \mathbf{q} are kpoint indices, and n, n' are the band indices. $\varepsilon_{n\mathbf{k}}$ and $\psi_{n\mathbf{k}}$ are the ground-state KS eigenvalues and eigenstates, which are normalized to 1 within the crystal volume Ω . The BZ represents the Brillouin zone in the reciprocal space. Now for solids, χ_0 can be expanded in planewave basis

$$\chi_0(\mathbf{r}, \mathbf{r}', \omega) = \frac{1}{\Omega} \sum_{\mathbf{q}} \sum_{GG'}^{BZ} e^{i((\mathbf{q}+\mathbf{G})\cdot\mathbf{r})} \chi_0^{GG'}(\mathbf{q}, \omega) e^{-i((\mathbf{q}+\mathbf{G})\cdot\mathbf{r}')}, \quad (2.5-92)$$

where the Fourier coefficients $\chi_0^{\mathbf{G}\mathbf{G}'}(\mathbf{q}, \omega)$ is defined as [120, 121]

$$\begin{aligned} \chi_0^{\mathbf{G}\mathbf{G}'}(\mathbf{q}, \omega) &= \frac{1}{\Omega} \sum_{\mathbf{q}} \sum_{nn'}^{BZ} \frac{f_{n\mathbf{k}} - f_{n'(\mathbf{k}+\mathbf{q})}}{\omega + \varepsilon_{n\mathbf{k}} - \varepsilon_{n'(\mathbf{k}+\mathbf{q})} + i\eta} \\ &\times \langle \psi_{n\mathbf{k}} | e^{-i((\mathbf{q}+\mathbf{G})\cdot\mathbf{r})} | \psi_{n'\mathbf{k}+\mathbf{q}} \rangle \langle \psi_{n\mathbf{k}} | e^{i((\mathbf{q}+\mathbf{G}')\cdot\mathbf{r}')} | \psi_{n'\mathbf{k}+\mathbf{q}} \rangle . \end{aligned} \quad (2.5-93)$$

Here, $\{\mathbf{G}\}$ are the reciprocal lattice vectors. Now the Dyson's equation in Fourier space becomes

$$\chi^{\mathbf{G}\mathbf{G}'}(\mathbf{q}, \omega) = \chi_0^{\mathbf{G}\mathbf{G}'}(\mathbf{q}, \omega) + \sum_{\mathbf{G}_1\mathbf{G}_2} \chi_0^{\mathbf{G}\mathbf{G}_1}(\mathbf{q}, \omega) \left(\frac{4\pi\delta_{\mathbf{G}_1\mathbf{G}_2}}{|\mathbf{q} + \mathbf{G}_1|^2} + f_{xc}^{\mathbf{G}_1\mathbf{G}_2}(\mathbf{q}, \omega) \right) \chi^{\mathbf{G}_2\mathbf{G}'}(\mathbf{q}, \omega) \quad (2.5-94)$$

The result for $\mathbf{G} = \mathbf{G}' = 0$ corresponds to the primitive cell. The inclusion of the reciprocal lattice vectors in the RPA correlation energy captures a more local-field effects, required for the periodic solids. The number of the reciprocal lattice vectors can be controlled by providing a cutoff energy which satisfies the relation, $\frac{|\mathbf{q}+\mathbf{G}|^2}{2} < E_{cut}$. However, a large number of plane waves or ($\{\mathbf{G}\}$) vectors should be used, as the RPA correlation energy has a slow convergence with respect to them. Therefore, an extrapolation scheme has been developed. The correlation energy is computed for various number of $\{\mathbf{G}\}$ vectors, and later extrapolated to an infinite number of G -vectors according to [85]

$$E_c(E_{cut}) = E_c^{RPA} + \frac{A}{E_{cut}^{3/2}}. \quad (2.5-95)$$

The correlation energy computed for the homogeneous electron gas from RPA shows a significant deviation from the exact correlation energies computed from a high level quantum Monte-Carlo method (QMC). The underestimation is up to ~ 0.5 eV per particle for a wide range of densities. It is due to the fact that RPA does have self-correlation error, though, it has the self-interaction-free exchange. There are various beyond-RPA methods developed to address this deficiency. Some of them are discussed below.

2.5.2 Semi- and non-local corrections to RPA (RPA+)

As we know, the RPA accurately describes the long-range electron electron interaction, while it suffers to capture the short-range correlation effects due to the absence of kernel. The correlations from semilocal DFT functionals such as LDA and GGA are utilized to improve the short-range correlation in RPA, and the resulting method is called RPA+ [122, 123] In the RPA+ method, the short-range correlation energy is defined as

$$E_{c,sr} = \int d^3r n(\mathbf{r}) \epsilon_{c,sr}. \quad (2.5-96)$$

The total correlation energy in RPA+ becomes

$$E_c = E_c^{RPA} + E_{c,sr} \quad (2.5-97)$$

Now, $\epsilon_{c,sr}$ is the short-range correlation energy per particle of the uniform electron gas, defined as

$$\epsilon_{c,sr}^{LDA} = \epsilon_c^{unif}(r_s) - \epsilon_c^{RPA}(r_s) \text{(LDA)} \quad (2.5-98)$$

$$\epsilon_{c,sr}^{GGA} = \epsilon_c^{unif}(r_s) - \epsilon_c^{RPA}(r_s) + H(r_s, t, \epsilon_c^{unif}(r_s)) - H(r_s, t, \epsilon_c^{RPA}(r_s)) \text{(GGA)}. \quad (2.5-99)$$

Here, $\epsilon_c^{unif}(r_s)$ and $\epsilon_c^{RPA}(r_s)$ are the correlation energy per particle of the uniform electron gas, parametrized using high-level QMC calculation [18, 19] and RPA calculation [17] respectively. H is a function of a gradient-correction term t , density, and the uniform electron gas correlation energy per particle. These methods are quite successful in improving the total energies, ionization energies, etc, over RPA, but fail to correct the RPA underestimation of molecular atomization energies. It may be due to missing middle-range multicenter non-locality in the molecule in the direct RPA and RPA+ with semilocal corrections. Therefore,

Ruzsinszky *et. al.* [123] proposed a nonlocal correction as

$$E_{c,sr}^{nonlocal} = \int d^3r n(\mathbf{r}) [\epsilon_c^{GGA}(\mathbf{r}) - \epsilon_c^{GGA-RPA}(\mathbf{r})] [1 - \alpha F(f(\mathbf{r}))], \quad (2.5-100)$$

$$F(f) = f[1 - 7.2f^2][1 + 14.4f^2] \exp(-7.2f^2), \text{ and} \quad (2.5-101)$$

$$f(\mathbf{r}) = \frac{\epsilon_x^{GGA}(\mathbf{r}) - \epsilon_x^{exact}(\mathbf{r})}{\epsilon_x^{GGA}(\mathbf{r})}, \quad (2.5-102)$$

$$(2.5-103)$$

with ϵ_x is an exchange energy per particle, and $\alpha = 9$ provides a good fit to the atomization energies of Furche [124].

A large part of the short-range correlation error cancels while calculating energy iso-electronic differences in RPA. The kernel corrections or the semilocal or nonlocal corrections such as in RPA+ methods greatly improve and give exact correlation energy for the uniform electron gas. RPA+ methods usually give accurate predictions for spin-unpolarized systems. However, they also break down while dealing with spin-polarized systems such as H_2^+ or other ions. Gould *et. al.* [125] proposed the gRPA+ method that changes RPA+ only for spin-polarized system, and developed by locally modifying RPA+ correlation energy density using various meta-GGA ingredients. The gRPA+ method is a self-interaction corrected version of RPA+, and it is exact for all one-electron densities.

2.5.3 RPA renormalization (RPA_r) scheme

The RPA renormalization is a scheme to present the beyond RPA correlation as the perturbative corrections to the RPA correlation energy. Note that, though, the term sounds similar as that of kernel renormalization in the cases of rALDA or rAPBE, they are different. Instead of evaluating the interacting response function using the KS response function,

it is expressed in terms of the RPA response function [117, 126].

$$\begin{aligned}
\chi &= \chi_0 + \chi_0(v + f_{xc})\chi \\
\chi &= \frac{1}{\chi_0^{-1} - (v + f_{xc})} \\
\chi &= \frac{1}{\chi_{RPA}^{-1} - f_{xc}} \\
\chi &= \chi_{RPA} (1 - f_{xc}\chi_{RPA})^{-1} \\
\chi &= \chi_{RPA} (1 + f_{xc}\chi_{RPA} + f_{xc}\chi_{RPA}f_{xc}\chi_{RPA} + \dots) \\
\therefore \chi &= \chi_{RPA} + \chi_{RPA}f_{xc}\chi_{RPA} + \chi_{RPA}f_{xc}\chi_{RPA}f_{xc}\chi_{RPA} + \dots \quad (2.5-104)
\end{aligned}$$

Here, $\chi_0^{-1} - v = \chi_{RPA}^{-1}$ and $(1 - x)^{-1} = 1 + x + x^2 + \dots$ are utilized. The first two terms give the RPAr1 approximation. If we replace one of the RPA response functions in RPAr1 by the noninteracting KS response function, we get the ACSOSEX approximation. Unlike the infinite-order method, these approximations avoid divergences of the single-reference perturbation theory due to small noninteracting gaps. Also, the computational cost is quite comparable to bare RPA. We have utilized this scheme with various kernels to calculate the ground-state equilibrium properties of cesium halide systems, as presented in chapter 3.

2.6 Linear response theory for the excited-states properties

Until now, we have discussed the linear response theory for its application in the ground-state theory. We derived an exact expression of the exchange-correlation energy within RPA and various beyond-RPA methods. We also discussed various exchange-correlation kernels developed using the uniform electron gas by satisfying exact constraints. These kernels are useful especially for the ground-state correlation energy by improving the short-range electron-electron correlation within the system. However, these kernels are not useful for the excited-state properties in real systems, as they miss an important ultranlocality $f_{xc} \sim \frac{\alpha(\omega)}{q^2}|_{q \rightarrow 0}$ behavior at the optical limit ($q \rightarrow 0$). In this section, we will explore

various kernels especially designed for the optical properties of solids by satisfying the optical-limit property. Before that, let's define the dielectric function for real solids within linear-response theory, which can be utilized to obtain various excited-state properties such as absorption spectra, electron-energy-loss spectra, etc.

When a time-dependent perturbation is applied to the many-electron system, the system polarizes. This polarization induces a potential that screens the original applied external perturbation. Therefore, the total potential becomes

$$\begin{aligned}
v_{tot}(\mathbf{r}, t) &= v_{ext}(\mathbf{r}, t) + v_{induced}(\mathbf{r}, t) \\
\int_{-\infty}^{\infty} dt' \int d^3 r' \epsilon^{-1}(\mathbf{r}, \mathbf{r}', t - t') v_{ext}(\mathbf{r}', t') &= v_{ext}(\mathbf{r}, t) \\
&\quad + \int_{-\infty}^{\infty} dt' \int d^3 r'' \int d^3 r' \frac{\chi(\mathbf{r}'', \mathbf{r}', t - t') v_{ext}(\mathbf{r}', t')}{|\mathbf{r} - \mathbf{r}''|} \\
\therefore \epsilon^{-1}(\mathbf{r}, \mathbf{r}', t - t') &= \delta(\mathbf{r} - \mathbf{r}') \delta(t - t') + \int d^3 r'' \frac{\chi(\mathbf{r}'', \mathbf{r}', t - t')}{|\mathbf{r} - \mathbf{r}''|}
\end{aligned} \tag{2.6-105}$$

This is the expression of the inverse dielectric function. The Fourier-transformation in reciprocal space gives,

$$\epsilon_{\mathbf{G}\mathbf{G}'}^{-1}(\mathbf{q}, \omega) = \delta_{\mathbf{G}\mathbf{G}'} + \sum_{\mathbf{G}''} \frac{4\pi \delta_{\mathbf{G}\mathbf{G}''}}{|\mathbf{q} + \mathbf{G}| |\mathbf{q} + \mathbf{G}''|} \chi_{\mathbf{G}''\mathbf{G}'}(\mathbf{q}, \omega) \tag{2.6-106}$$

This is a matrix of $G \times G'$ size. For the RPA approximation,

$$\epsilon_{\mathbf{G}\mathbf{G}'}^{RPA}(\mathbf{q}, \omega) = \delta_{\mathbf{G}\mathbf{G}'} - \sum_{\mathbf{G}''} \frac{4\pi \delta_{\mathbf{G}\mathbf{G}''}}{|\mathbf{q} + \mathbf{G}| |\mathbf{q} + \mathbf{G}''|} \chi_{\mathbf{G}''\mathbf{G}'}^0(\mathbf{q}, \omega) \tag{2.6-107}$$

The macroscopic dielectric function is defined as

$$\epsilon_M(\mathbf{q}, \omega) = \frac{1}{\epsilon_{\mathbf{G}=0, \mathbf{G}'=0}^{-1}(\mathbf{q}, \omega)} \tag{2.6-108}$$

Now, the optical absorption spectra can be obtained by $\text{Im}\epsilon_M(\mathbf{q} \rightarrow 0, \omega)$, whereas the electron-energy-loss spectra (EELS) is given by $-\text{Im}\frac{1}{\epsilon_M(\mathbf{q}, \omega)}$.

2.6.1 XC kernels for optical spectra

In order to obtain accurate optical spectra, one needs to predict accurate energy levels and also incorporate any excitonic effects (physics of bound electron-hole pair) present in the system. The first part is related to the electron-electron (e-e) correlation, while the second part arises from the electron-hole (e-h) interactions. Since we use the ground-state KS eigenvalues and eigenstates to compute the noninteracting KS response function, which raises the energy bands below the Fermi-level while lowering the levels above the Fermi-level, the bandgaps are underestimated. Therefore, any excitation processes within such inaccurate energy-levels are also unreliable. The accurate energy-levels can be obtained using the exact ground-state XC potential, but it is impossible to obtain it. However, an improved version of DFT functionals in meta-GGA levels such as TASK [44] and the hybrid functionals can provide more accurate bandgaps. The most accurate bandgaps can be obtained using *GW* methods from many-body Green's function theory [127], though they are more expensive than any DFT method. Once, we have accurate bandgaps from experiments or from the higher-level theoretical calculations then we can correct the e-e interactions in optical spectra by applying the Scissors shift [128, 129]. The Scissors shift can be defined as

$$\Delta_s = E_g^{exact} - E_g^{KS-DFT}, \quad (2.6-109)$$

where E_g^{exact} is an exact bandgap, either taken from the experiment or calculated from the higher-level methods. The E_g^{KS-DFT} is the KS bandgap. This shift simply raises the unoccupied orbitals. Without the bandgap correction, the optical spectra are usually red-shifted to the lower binding energies.

The next important thing to incorporate is the excitonic effects by improving the e-h interactions. RPA simply uses the Hartree kernel that cannot properly include the e-h interactions, therefore, the binding energies of the absorption spectra computed by RPA with the Scissors shift are often overestimated (or blue-shifted), compared to the experiment. Also, some of the features of the exact spectra can be missing. The many-body quantum theory provided by Hans Bethe and Edwin Salpeter, also known as Bethe-Salpeter equation (BSE) [130], in conjunction with the *GW* method (GW-BSE), can give the accurate optical spectra with correct binding energies, and also includes the exact features of the spectra. However, these methods are highly expensive in terms of both computational time and memory consumption. Alternatively, the dynamical exchange-correlation kernel can be restored to improve the RPA calculated optical spectra. Some of them are discussed as follows.

Long-range contribution (LRC) to XC kernel

This is also known as the long-range kernel. This kernel is developed just by satisfying an ultranonlocality property at the optical limit [111, 131]. In real space, it has a static form of

$$f_{xc}^{LRC}(\mathbf{r} - \mathbf{r}') = -\frac{\alpha}{4\pi|\mathbf{r} - \mathbf{r}'|}, \quad (2.6-110)$$

where α is some materials-dependent constant. If starting from *GW* bandstructures, it has values of 0.09, 0.05, and 0.15 for Silicon, GaAs, and AlAs respectively [131]. In reciprocal space, it has a form of

$$\left(f_{xc}^{LRC}(\mathbf{q}, \omega)\right)_{\mathbf{G}\mathbf{G}'} = -\frac{\alpha\delta_{\mathbf{G}\mathbf{G}'}}{|\mathbf{q} + \mathbf{G}|^2} \quad (2.6-111)$$

It also can be made frequency-dependent, simply changing static α to a ω -dependent α .

Bootstrap kernel

This kernel is obtained by solving together the Dyson's equation and the equation of the inverse dielectric function self-consistently. We have an expression for the inverse dielectric function as,

$$\varepsilon^{-1}(q, \omega) = 1 + \chi_0(q, \omega)v(q) [1 - \{v(q) + f_{xc}(q, \omega)\}\chi_0(q, \omega)]^{-1}. \quad (2.6-112)$$

Here, all quantities are matrices obtained using the basis of the reciprocal lattice vectors $\{\mathbf{G}\}$. The kernel $f_{xc}(q, \omega)$ is approximated by

$$f_{xc}(q, \omega) = -\frac{\varepsilon^{-1}(q, \omega = 0)v(q)}{\varepsilon_0^{00}(q, \omega = 0) - 1} = \frac{\varepsilon^{-1}(q, \omega = 0)}{\chi_0^{00}(q, \omega = 0)} \quad (2.6-113)$$

The RPA dielectric function is defined as $\varepsilon_0(q, \omega) = 1 - v(q)\chi_0(q, \omega)$. Only $\mathbf{G} = \mathbf{G}' = 0$ component has been used in the denominator.

The calculation starts by setting $f_{xc} = 0$ and obtain ε^{-1} using Eq. 2.6-112. Then, it is bootstrapped to Eq. 2.6-113 to obtain a new f_{xc} . This process is continuously carried out until the self-consistency at $\omega = 0$ is achieved. The resulting kernel has ultra-non-locality at the optical limit that is crucial to capture the excitonic peak within the fundamental gap. Also in the zero frequency limit ($\omega \rightarrow 0$), Eq. 2.6-112 yields the static dielectric constants close to RPA results.

Jellium with gap (JGM) model kernels

This is a static ($\omega = 0$) kernel based on the jellium-with-gap (JG) model [101]. Unlike other kernels described above, it is designed to obtain the accurate optical properties of the semiconductor and insulators. This kernel is extended form of the CP07 kernel for the JG

model. This kernel satisfies the following constraint at the optical limit,

$$f_{xc}^{JGM}(q \rightarrow 0; n, E_g) \simeq -\frac{E_g^2}{nq^2}, \quad (2.6-114)$$

where, E_g being the band gap. Now, the kernel itself is defined as,

$$f_{xc}^{JGM}(q; n, E_g) = \frac{4\pi}{q^2} B'(n, E_g) \left[e^{-k'_{n,E_g} q^2} - 1 \right] - \frac{4\pi}{k_F^2} \frac{c'(n, E_g)}{1 + 1/q^2}. \quad (2.6-115)$$

$$B'(n, E_g) = \frac{B(n) + E_g}{1 + E_g} \quad (2.6-116)$$

$$c'(n, E_g) = \frac{c(n)}{1 + E_g} \quad (2.6-117)$$

$$k'_{n,E_g} = k_n + \frac{1}{4\pi q^2} \frac{E_g^2}{nB'(n, E_g)} \quad (2.6-118)$$

Since, the second term in Eq. 2.6-115 does not describe the optical limit property at $q \rightarrow 0$, a different kernel has been purposed, known as JGMs [81] which is defined as:

$$f_{xc}^{JGMs}(\mathbf{q}; n, G) = \frac{4\pi}{q^2} \left[e^{-k_n q^2} e^{-G^2/(4\pi n)} - 1 \right], \quad (2.6-119)$$

where $G = E_g$. This kernel provides a proper description of UEG correlation energy, and improves the ground-state properties of bulk systems. It also satisfies the optical limit as that of JGM kernel. In addition, the gradient correction to JGM kernel (JGM-G) improves the optical spectra, as described in Ref. [102].

2.6.2 Absorption spectra of solids with the NEO kernel

Here, we explore various kernels including the NEO kernel to calculate the optical response, mainly absorption spectra, of the bulk solids. It is a simple model kernel, just satisfies a few constraints. For optical spectra, we use the NEO kernel of form

$$f_x^{NEO}(q, n; z) = \frac{4\pi}{q^2} \sum_{\sigma} \left(\frac{n_{\sigma}}{n} \right)^2 \left[(1 - x_{i\sigma}) \left(\exp \left[-c_n \frac{q^2}{F_{z\sigma}} \right] - 1 \right) - x_{i\sigma} \right], \quad (2.6-120)$$

where

$$F_{i\sigma} = 4\tilde{c}(1 - z_\sigma)^2 k_{F\sigma}^2 \quad (2.6-121)$$

$$z_\sigma = \frac{\tau_{vW}}{\tau_\sigma}, \quad (2.6-122)$$

$$\tau_{vW}(\mathbf{r}) = \frac{|\nabla n_\sigma(\mathbf{r})|^2}{8n_\sigma(\mathbf{r})}, \quad (2.6-123)$$

$$\tau_\sigma(\mathbf{r}) = \frac{1}{2} \sum_i |\nabla \phi_{i\sigma}(\mathbf{r})|^2, \quad (2.6-124)$$

and $k_{F\sigma} = (6\pi^2 n_\sigma)^{1/3}$ is the Fermi-wavevector, $\tilde{c} = 0.264$, and c_n is a fitting parameter. The $x_{i\sigma}$ is the screening parameter having values between 0 and 1, inclusive, which can be defined differently, based on constraint satisfaction. For example, when we chose optical-limit property of Eq. 2.6-114 at $q \rightarrow 0$ giving

$$-\frac{4\pi}{q^2} \sum_\sigma \left(\frac{n_\sigma}{n}\right)^2 x_{1\sigma} = -\frac{E_g^2}{nq^2}. \quad (2.6-125)$$

For spin-unpolarized systems $n_\sigma = \frac{n}{2}$, Eq 2.6-125 gives

$$x_{1\sigma} = \frac{E_g^2}{2\pi n}. \quad (2.6-126)$$

Here, E_g can be an experimental gap. It is an exchange only, frequency-independent kernel. Now, we utilize this kernel to calculate an optical spectra of various solids.

2.6.2.1 Computational details

The ground-state eigenstates and eigenvalues required to calculate noninteracting KS response function have been calculated using *ABINIT* software [132] with Troullier-Martins norm-conserving pseudopotentials. The PBE calculations have been performed using a planewave cutoff of ~ 250 eV, and the Brillouin-zone sampling of Monkhorst-Pack $16 \times 16 \times 16$ k-mesh. The total number of bands taken is ~ 40 -60 including the unoccupied ones. The di-

electric functions, and hence the absorption spectra are computed using the *YAMBO* [133] code. We performed beyond-RPA calculations using NEO kernel and JGMs kernel, and compared the results of the optical spectra from RPA and experiment. The unoccupied energy levels were shifted up using the Scissors shift, where the experimental bandgaps were used as the exact fundamental gap.

2.6.2.2 Results and Discussions

Here, we show the role of kernel-corrected TDDFT methods in the excited-state properties of real solids by calculating the optical absorption spectra (ABS), as shown in Fig. 2.2. Though the NEO kernel has different mathematical expression than that of JGMs kernel, the optical spectra from both methods are almost similar. The RPA often blue-shifted the ABS curve, compared to experiments. On the other hand, both kernel significantly improve the ABS spectra, where it is needed. However, these kernels still fail to capture the accurate excitonic effects in the case of more wide-gap insulators. Also, they could not revive the missing features in RPA spectra. Moreover, these kernels uses the experimental bandgaps, which makes them semi-empirical. All these discrepancies can be addressed with the correct optical limit at $\mathbf{q} \rightarrow 0$. Though our kernel does not provide the most accurate results under the present circumstances, it can be improved by using more sophisticated screening factor. Furthermore, it can include frequency-dependence as well.

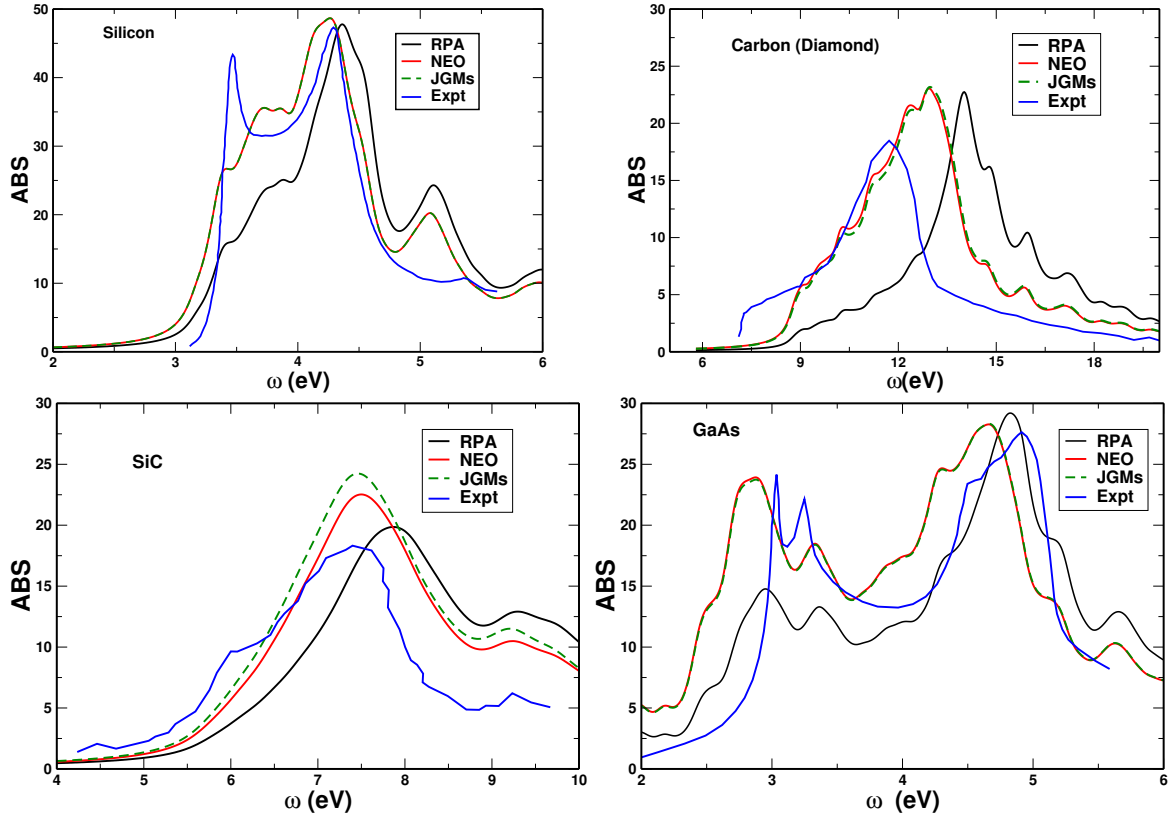


Figure 2.2: Optical absorption spectra calculated using $ABS = \text{Im } \epsilon_M(\mathbf{q} \rightarrow 0, \omega)$. The experimental bandgaps used are 1.17 eV, 5.50 eV, 2.42 eV, and 1.52 eV with the Scissors shifts of 0.55 eV, 3.64 eV, 1.4 eV, and 0.51 eV respectively for Si, C, SiC, and GaAs [134]. Lorentz broadening of 0.1-0.2 eV were used in the calculations. Experimental spectra are taken from Refs. [135–138].

CHAPTER 3

ROCKSALT OR CESIUM CHLORIDE: INVESTIGATING THE RELATIVE STABILITY OF THE CESIUM HALIDE STRUCTURES WITH RANDOM PHASE APPROXIMATION BASED METHODS

3.1 Abstract

The ground state structural and energetic properties for rocksalt and cesium chloride phases of the cesium halides were explored using the Random Phase Approximation (RPA) and beyond-RPA methods to benchmark the non-empirical SCAN meta-GGA and its empirical dispersion corrections. The importance of non-additivity and higher-order multipole moments of dispersion in these systems is discussed. RPA generally predicts the equilibrium volume for these halides within 2.4% of the experimental value, while beyond-RPA methods utilizing the renormalized adiabatic LDA (rALDA) exchange-correlation kernel are typically within 1.8%. The zero-point vibrational energy is small and shows that the stability of these halides is purely due to electronic correlation effects. The rAPBE kernel as a correction to RPA overestimates the equilibrium volume and could not predict the correct phase ordering in the case of cesium chloride, while the rALDA kernel consistently predicted results in agreement with the experiment for all of the halides. However, due to its reasonable accuracy with lower computational cost, SCAN+rVV10 proved to be a good alternative to the RPA-like methods for describing the properties of these ionic solids.

3.2 Introduction

Alkali halides provide a useful benchmark for new theoretical methods to test their performance in predicting equilibrium and non-equilibrium properties of ionic solids [139–145]. Among the alkali halides, cesium halides are of particular interest in terms of their phase stability and have been studied both experimentally as well as theoretically [141, 146–150]. CsF is experimentally stable in the B1 structure, while the Cl, Br, and I materials exist experimentally in the B2 structure. In Strukturbericht notation, B1 corresponds to the rocksalt (NaCl) phase, whereas B2 refers to the CsCl phase [151]. This difference in phase preference for the cesium halides can only be understood through the inclusion of dispersion interactions [141, 146–150].

The unexpected stability of an ionic B2 phase was explained by London [146] through the presence of relatively large van der Waals interactions between the heavy Cs^+ cation and the heavier halide anions (Cl^- , Br^- , and I^-). Since dispersion effects are proportional to the polarizability and number of electrons in the anion, they are expected to become more important as one moves down the halide column. Furthermore, the coordination number of Cs in the B2 phase is higher than that in the B1 phase so there are locally more halide anions with which to interact. Dispersion is a pure quantum mechanical effect due to instantaneous or induced electronic multipole moments and is therefore difficult to capture with classical models [152]. The simplest treatment of the dispersion interaction is modeled by simple pairwise-additive interactions between atoms, but this type of approximation completely ignores any nonadditive, nonlocal, and collective many-body effects [152, 153], which can be important in cases where screening effects modify electron-electron interactions.

Rather than rely on classical models, *ab initio* calculations can be readily used to study

the details of these systems. The development of accurate approximations to the exchange-correlation energy of density functional theory [11] (DFT) has enabled it to become the default electronic structure method for the computational molecular sciences. Approximations such as the local density approximation [14, 154] (LDA) and the Perdew, Burke, Ernzerhof [21] (PBE) generalized gradient approximation (GGA) have been applied to a wide range of systems, but they fail to deliver accurate results when non-local interactions are important. Global hybrid density functionals, such as PBE0 [65], often improve in situations with stretched bonds [155, 156], but do not have any impact on dispersion interactions. By constructing meta-GGA (MGGA) approximations that include the kinetic-energy density [35, 38, 39, 157, 157–160], part of the dispersion interaction can be directly included in a semilocal calculation, however the long-range part is still missing and must be included through other means. Incorporating the missing long-range dispersion interactions into semilocal DFT calculations by adding empirical pairwise-additive contributions has been an active topic of research for more than two decades [49, 50, 161–166]. More recent formulations of these corrections go beyond pairwise contributions and can include three-body terms [51] or even some non-locality [54, 167, 168].

The adiabatic-connection fluctuation-dissipation theorem (ACFDT) DFT formalism provides a non-empirical route to construct a nonlocal correlation energy that can be combined with the self-interaction free exact exchange (EXX) energy to compute the total ground state energy [169–172]. With improved algorithms [173–177] and ever increasing computational power, the Random Phase Approximation (RPA) has become an accessible alternative to semilocal DFT and is the simplest approximation within ACFDT-DFT. Naturally accounting for weak interactions, RPA has been demonstrated to yield accurate results for systems heavily influenced by van der Waals interactions (vdW) [85–89], as well as for covalently bound systems [76–82]. Since RPA is determined from a Dyson-type equation, it also naturally incorporates non-pairwise-additive dispersion contributions [178] that are

missing from simple empirical dispersion schemes [171, 179] and can be used as a benchmark for diverse physical and chemical properties involving both van der Waals and covalent interactions in the literature [77, 180–182]. However the absence of an exchange-correlation (xc) kernel in RPA leads to an inaccurate description of short-range correlation [90, 117, 124, 183]. Beyond-RPA (bRPA) methods including an approximate exchange-correlation kernel from time dependent DFT [117, 171, 172, 184, 185] (TDDFT) correct this deficiency of RPA while preserving the accurate description of long-range interactions.

In this work, we have assessed the performance of several semilocal functionals plus long-range dispersion corrections, as well as ACFDT-based methods to determine the relative stability of the cesium halides in comparison to experiment. The importance of non-additivity in these difficult ionic system was also tested. The impact of short-ranged interactions for these systems was explored with a comparative study of RPA and beyond RPA methods. The rest of the paper is organized as follows. The methods we used for this assessment are discussed in Sec. 3.3 and computational details are given in Sec. 3.4. The results are presented in Sec. 3.5, followed by a brief discussion and some conclusions in Sec. 3.6.

3.3 Methods

In this work, we have used several standard semilocal functionals to assess the ground state properties of the cesium halides. Analogous to previous works [42, 141], we have used the local density approximation [14] (LDA) and the generalized gradient approximation of Perdew, Burke, and Ernzerhof [21] (PBE) as a starting point for comparing the performance of more advanced methods. These two functionals do not explicitly include dispersion effects, though sometimes error cancellation in the exchange and correlation energies can simulate the effects of including these additional attractive forces [42]. Previous results reported with these functionals demonstrated that LDA predicts the correct phase

ordering while PBE does not, but adding a long-range dispersion correction to PBE corrects this fundamental failure [141]. In practice dispersion corrections work well with the PBE0 global hybrid functional. PBE0 itself has been effective in predicting the stability of hydrogen-bonded ice polymorphs [186]. Long-range dispersion corrections are, however, essential for an accurate prediction of structures for various systems. In this case PBE0 without dispersion correction does not necessarily deliver the desired accuracy as pointed out in Refs. [187–189]. In order to explicitly include some dispersion at the semilocal level, more advanced approximate functionals are needed, such as from the MGGA “rung” of DFT [157, 190, 191].

The strongly constrained and appropriately normed (SCAN) functional is one such approximation that incorporates intermediate-range dispersion interactions through its dependence on the kinetic energy density [39]. SCAN is one of the most advanced non-empirical semilocal functionals to date, satisfying all possible exact constraints that a MGGA can, and has proven to be accurate for diversely bonded systems [39, 42, 55, 192, 193]. Comparing the SCAN results to those of previous non-empirical functionals should show clearly the impact that including dispersion, if only partially, makes at the semilocal level for the ground state properties of ionic materials.

Though SCAN includes intermediate-range vdW effects, it does not capture long-range interactions which arise from electron density fluctuations. To incorporate these missing contributions to the energy, we have utilized two correction schemes based on approximate treatments of the dispersion interaction. The first route, Grimme *et al.*'s D3 [51, 52] method, improves upon the previous D2 approach by incorporating three-body interactions and treating effects from the local environment. We also tested the impact of including dispersion through the non-local rVV10 correction [54, 55, 168] in combination with SCAN [39]. The rVV10 correction naturally includes higher-order multipole moments, but does

not capture non-pairwise-additive effects [55]. Including the impact of these corrections is important since previous works used lower level approximations, such as D2, and found a large energy difference between the B1 and B2 phases [141].

In order to verify our semilocal results, we also utilized methods from the adiabatic-connection fluctuation-dissipation theorem (ACFDT) formulation of DFT [119, 169, 171, 184]. The most common approximation of ACFDT-DFT, known as the Random Phase Approximation (RPA), was originally developed in the 1950's [74, 75] for the uniform electron gas and has received renewed interest more recently due to increased computational power and more efficient algorithms [124, 173, 175, 176, 194–196]. The detailed mathematical description of the ACFDT formalism, as well as its implementations, can be found in the review articles Refs. [171, 172]. To summarize briefly, within the ACFDT-DFT the total energy is computed from the non-local, self-interaction-error-free exact exchange (EXX) energy and a non-local correlation energy,

$$E^{\text{ACFD}} = E_{\text{EXX}} + E_C^{\text{ACFD}}. \quad (3.3-1)$$

The total correlation energy itself can be exactly decomposed into two contributions [117],

$$E_C^{\text{ACFD}} = E_C^{\text{RPA}} + \Delta E_C^{\text{bRPA}}, \quad (3.3-2)$$

where the second term accounts for all of the many-body effects not captured by RPA. Within RPA, $\Delta E_C^{\text{bRPA}} = 0$ since the exchange-correlation kernel is explicitly neglected. The RPA correlation energy naturally includes long-range dispersion and is non-perturbative, meaning that it can be safely applied to zero-gap systems without diverging [197]. For this work, the non-perturbative nature is important not because the band gaps are small, but because non-perturbative methods capture non-pairwise-additive contributions to dispersion [153, 179]. Consequently, we can count on RPA to provide a quasi-benchmark with which

to compare the semilocal and dispersion-corrected results. However, if treating the short-ranged correlation accurately is important for these ionic materials, RPA may not provide the desired accuracy needed for a true benchmark, and more advanced methods beyond RPA are needed.

Due to neglect of the exchange-correlation kernel within RPA, the short-ranged correlation is not accurately described [90, 183]. To go beyond RPA, we have studied the impact of two approximate exchange-like kernels, rALDA [114, 198] and rAPBE [115]. These kernels are derived from electron gas model kernels and are spatially renormalized in order to avoid the divergence of the pair-density at the origin from adiabatic, local kernels in TDDFT [81, 184, 198]. These kernels have been demonstrated to improve upon RPA for non-isogyric processes, such as computing atomization or cohesive energies, while preserving the good performance of RPA for covalent and dispersion bound systems [115, 198, 199]. We have also used the CP07 [113] exchange-correlation kernel to determine if the exchange-like kernels are sufficiently accurate for predicting the energy difference between the B1 and B2 phases. We did not explore the structures with these exchange-correlation kernels since they are noticeably more computationally demanding and Ref. [81] demonstrated that their performance for lattice constants and bulk moduli of simple solids is only marginally different than that of rALDA and rAPBE.

Rather than compute the infinite-order response function including the kernel [119, 170, 184], we utilize RPA renormalization [15, 117, 185] (RPA_r) to compute ΔE_C^{bRPA} . To briefly describe these approximations, within RPA renormalization the infinite-order expression for the bRPA piece [117, 185] *for a given kernel* is

$$\Delta E_C^{\text{bRPA}}[f_{xc}] = -\text{Re} \int_0^1 d\lambda \int_0^\infty \frac{du}{2\pi} \left\langle V \hat{\chi}_\lambda(iu) f_{xc}^\lambda(iu) \chi_\lambda(iu) \right\rangle, \quad (3.3-3)$$

where V is the bare Coulomb interaction, χ_λ is the interacting density-density response function, $\hat{\chi}_\lambda$ is the RPA response function, f_{xc} is the exchange-correlation kernel, iu is an imaginary frequency, though we take the Re part of the integral, λ the adiabatic-connection coupling constant, and $\langle A \rangle$ indicates the trace of matrix A . For periodic boundary conditions, this trace involves an integration over the Brillouin zone and summation over the reciprocal lattice vectors.

RPA_r to first-order, RPA_r1, is obtained by replacing χ_λ with the RPA response function $\hat{\chi}_\lambda$

$$\Delta E_C^{\text{RPAr1}}[f_{xc}] = - \int_0^1 d\lambda \int_0^\infty \frac{du}{2\pi} \langle V \hat{\chi}_\lambda(iu) f_{xc}^\lambda(iu) \hat{\chi}_\lambda(iu) \rangle. \quad (3.3-4)$$

RPA renormaliation to first-order (RPA_r1) was previously demonstrated to account for $\sim 90\%$ of the total bRPA correlation energy, delivering a consistent performance in comparison to the traditional infinite-order approach [15, 117, 197]. In order to capture high-order correlation contributions, we have also utilized an approximate second-order RPA_r correction [185] which we call the higher-order terms (HOT) approximation [200]. This approximation makes up the difference between RPA_r1 and the infinite-order result

$$\Delta E_C^{\text{HOT}}[f_{xc}] = E_C^{\text{bRPA}} - E_C^{\text{RPAr1}} \approx - \frac{1}{2} \int_0^\infty \frac{du}{2\pi} \langle V \hat{\chi} f_{xc} \hat{\chi} f_{xc} \hat{\chi} \rangle, \quad (3.3-5)$$

typically recovering the total infinite-order correlation energy to within 1% when added to RPA_r1. We have also utilized an approximation to RPA_r1 called ACSOSEX [15, 16, 117, 185, 201, 202], which neglects a certain set of third and higher-order contributions to the correlation energy in comparison to RPA_r1 [15]. This approximation is obtained by replacing one $\hat{\chi}$ with χ_0 in the RPA_r1 correlation energy

$$\Delta E_C^{\text{ACSOSEX}}[f_{xc}] = - \int_0^1 d\lambda \int_0^\infty \frac{du}{2\pi} \langle V \hat{\chi}_\lambda(iu) f_{xc}^\lambda(iu) \chi_0(iu) \rangle, \quad (3.3-6)$$

and was shown to be less systematic than RPA_{r1} due to the reintroduction of the non-interacting KS response function [15, 117]. This is to be distinguished from the coupled-cluster doubles approximation known as second-order screened exchange [203–205] (SOSEX), however ACSOSEX and SOSEX have been shown to be analytically and numerically quite similar [15, 201]. The differences in these approximations hinge on the differences in the response functions used to evaluate the traces, which can be important for describing non-perturbative dispersion interactions, since we cannot expect χ_0 to contain any information beyond the mean-field level. By studying the relative performance of these three methods we can understand the impact that the partial resummations of the correlation energy makes on the ground state properties of these ionic materials.

3.4 Computational Details

Ground state LDA and PBE calculations were performed within the Projected Augmented Wave (PAW) formalism [206] as implemented in GPAW [207–209]. We used PBE input orbitals for all of the RPA and beyond-RPA calculations, since they are evaluated non-self-consistently. Calculations with the strongly constrained and appropriately normed (SCAN) functional [39] and its combination with the revised VV10 dispersion correction (SCAN+rVV10) [55] were obtained self-consistently with VASP [210]. A plane wave cutoff of 600 eV was used in conjunction with $6 \times 6 \times 6$ Gamma-centered Monkhorst-Pack [211] k-point meshes to sample the Brillouin zone for semilocal and hybrid functionals. A higher plane wave cutoff of 800 eV and Brillouin zone sampling of $8 \times 8 \times 8$ were used for the EXX and RPA correlation energy calculations. Fermi-Dirac occupations corresponding to a temperature of 0.01 eV were used throughout. GPAW calculations were performed using the 0.9.20000 datasets, while the VASP calculations utilized the `_sv` and simple PP for Cs and halogens respectively, modified to include kinetic energy density required for MGGA calculations [212].

The non-interacting density response function can be computed from a sum-over-states expression [213] which is truncated at the number of bands determined by the plane wave cutoff for the response function. Since the calculation of the response function converges slowly with respect to the sum over unoccupied states, an extrapolation is needed to obtain converged correlation energies from the adiabatic connection [85, 124]. We used a maximum cutoff for the response function of 400 eV, and 4 smaller cutoffs in 5% increments of the maximum to extrapolate the correlation energy according to Eq. (7) in Ref. [85]. The frequency integral was performed as in Ref. [85] using a 16 point Gauss-Legendre quadrature, and with a frequency scale of 2.0 for non-metallic systems as recommended in Ref. [79]. A Wigner-Seitz truncation scheme [214] was used for the EXX energy to treat the small wavevector divergence of the Coulomb interaction, while the perturbative approach suggested in Ref. [213] was used for the correlation energy. For the RPA correlation calculations we have used $8 \times 8 \times 8$ Gamma-centered k-point meshes, For the bRPA calculations we have used $6 \times 6 \times 6$ meshes for both phases because the kernel-corrected methods tend to converge faster than RPA with respect to the k-mesh size, much like the original SOSEX method [204]. We have used a 350 eV cutoff without extrapolation for these bRPA calculations. For the CP07 calculations, we used the same settings as for the rADFT kernels, but evaluated the energy difference at only a single volume for each phase near their respective minima as predicted by rALDA.

The atomic energies for the ACFD methods were computed using rectangular simulation cells of $6 \text{Å} \times 7 \text{Å} \times 8 \text{Å}$ for F and $7 \text{Å} \times 8 \text{Å} \times 9 \text{Å}$ for Cs, Cl, Br, and I. Two cutoffs, 300 and 350 eV, were used to extrapolate the atomic results, since these cutoffs were previously demonstrated to yield converged results for RPA [79]. Atomic EXX energies were computed using simulation cells of $12 \text{Å} \times 12 \text{Å} \times 12 \text{Å}$ and an 1000 eV plane wave cutoff. The atomic energies for SCAN and SCAN+rVV10 were calculated using a plane wave basis set with maximum kinetic energies of 250–400 eV and a $20 \text{Å} \times 20 \text{Å} \times 20 \text{Å}$ simulation cell.

We calculated the zero-point vibrational energy (ZPVE) from PBE using VASP and PHONOPY [215] to estimate thermal corrections to the ground state energy. The ZPVE calculation includes the effect of LO-TO splitting within a polar solid [216]. The equilibrium properties of the bulk materials were determined from a fit to the third-order Birch-Murnaghan equation of state using at least seven volume points around the minimum.

3.5 Results

3.5.1 Equilibrium Structural Parameters

The computed equilibrium volumes and bulk moduli are reported in Tables 3.1 and 3.2 respectively. Beyond-RPA results are computed using rALDA. Experimental volumes were obtained using the lattice constants reported in the literature [217]. PBE systematically overestimates the equilibrium volume while LDA underestimates it, and our results are in good agreement with those of Refs. [141, 150]. On the other hand, a global hybrid PBE0 does improve over PBE slightly, but still overestimates the equilibrium volume. In order to predict accurate equilibrium volumes, some level of dispersion must be included. The equilibrium volumes predicted by SCAN, SCAN+D3, and SCAN+rVV10 are much more accurate than PBE or LDA, and tend to be quite close to one another and to the RPA results. The beyond-RPA methods tend to be even more accurate than dispersion corrected SCAN or RPA in comparison to experiment. The accuracy of the various methods to estimate the bulk modulus follows essentially the same trends as for the equilibrium volumes.

3.5.2 Cohesive Energies

The cohesive energies per formula unit for the low-energy phases of the cesium halides are presented in Table 3.3. For the fluoride this corresponds to the B1 phase, while for the other salts B2 is the low-energy phase. LDA and SCAN tend to overestimate the cohesive energies for the fluoride and chloride salts and underestimate the cohesive energy

Table 3.1: Equilibrium volumes per CsX functional unit in \AA^3 . Experimental volumes correspond to room temperature. LDA underestimates the lattice constants whereas PBE always overestimates them. RPA along with SCAN (S), S+rVV10, and S+D3 are noticeably more accurate for predicting the equilibrium volumes than PBE and LDA, however the beyond-RPA methods using rALDA (RPAr1, HOT, and ACSOSEX) yield the most accurate results.

V_0	LDA	PBE	PBE0	SCAN	S+D3	S+rVV10	RPA	RPAr1	HOT	ACSOSEX	Expt.[217]
F-B1	49.299	58.096	55.844	53.783	53.443	52.849	53.566	54.118	53.959	54.027	54.270
F-B2	43.336	51.087	49.298	47.873	47.809	47.018	47.687	47.898	47.770	48.057	
Cl-B1	76.719	89.031	87.188	85.863	84.929	84.116	83.128	82.324	82.104	81.826	
Cl-B2	62.853	74.780	72.564	70.235	69.483	68.490	68.315	68.873	68.681	68.977	69.934
Br-B1	86.980	101.332	99.234	97.794	96.756	95.666	94.181	93.772	93.453	93.070	
Br-B2	71.270	84.980	82.464	79.887	78.922	77.892	77.321	78.154	78.888	78.164	78.954
I-B1	104.001	121.620	119.266	117.978	116.913	115.045	113.348	112.582	112.160	111.715	
I-B2	85.622	102.028	99.229	98.182	96.922	95.545	93.525	94.079	93.713	94.010	95.444

Table 3.2: Computed bulk moduli (GPa) from the equation of state fits. The experimental values of Ref. [218] are taken at 4.2 K, Ref. [149, 219] were measured around liquid nitrogen temperature, and the remaining were measured around room temperature. RPA and SCAN are quite accurate in predicting the bulk moduli of these halides, however SCAN+rVV10 and the kernel-corrected bRPA methods utilizing the rALDA kernel are still systematic improvements.

B	LDA	PBE	PBE0	SCAN	S+D3	S+rVV10	RPA	RPAr1	HOT	ACSOSEX	Expt.
F-B1	33.2	19.8	22.5	27.7	28.4	29.6	25.4	27.5	27.8	27.9	25.0 [220]
F-B2	41.2	23.7	26.4	33.3	29.1	34.7	28.1	31.6	31.9	31.2	
Cl-B1	19.3	12.2	13.0	15.0	15.6	16.2	15.6	17.3	17.5	18.1	
Cl-B2	24.7	14.3	15.7	19.4	19.7	21.4	20.4	20.6	20.8	20.9	22.9 [219]
Br-B1	16.5	10.3	11.0	12.7	13.2	13.7	13.3	14.5	14.7	15.3	
Br-B2	21.0	12.2	13.3	14.6	16.5	17.7	17.5	17.6	17.8	17.9	17.9 [149], 18.4 [218]
I-B1	13.3	8.2	8.7	10.0	10.4	11.0	10.8	11.8	11.9	12.4	
I-B2	16.9	9.9	10.7	13.4	12.8	13.7	13.8	14.3	14.5	14.6	13.5 [221], 14.4 [218]

for the iodide. The bromide tends to be the halide where these semilocal functionals are closest to the experiment. PBE universally underestimates the cohesive energies for all of the halide salts. PBE0 still underestimates the cohesive energy providing only a slight improvement over PBE. Adding dispersion to PBE improves the cohesive energies of these halides [141, 150]. Similarly, the D3 correction to PBE0 improves the equilibrium properties significantly, as presented in Table S5 of the supporting information. Adding long range dispersion from D3 or rVV10 to SCAN systematically increases the cohesive energies, resulting in larger overestimates for the fluoride and chloride, a little change for the bromide, and reducing the underestimation of the iodide salt. RPA and the bRPA methods also have varied performances, tending to yield overestimates for F and Cl, but underestimates for the Br and I salts. There is some difference amongst the bRPA methods themselves for the cohesive energies since a free atom is involved, and the different levels of RPA_r recover different amounts of bRPA correlation [185]. The short-ranged contributions captured by the bRPA corrections become important for the heavier halides since the CsX bond is more covalent than the lighter halides, based solely on electronegativity differences [222]. Thus RPA tends to be more accurate vs experiment for the fluoride and chloride and less accurate for the bromide and iodide salts, whereas the bRPA methods have the opposite trend.

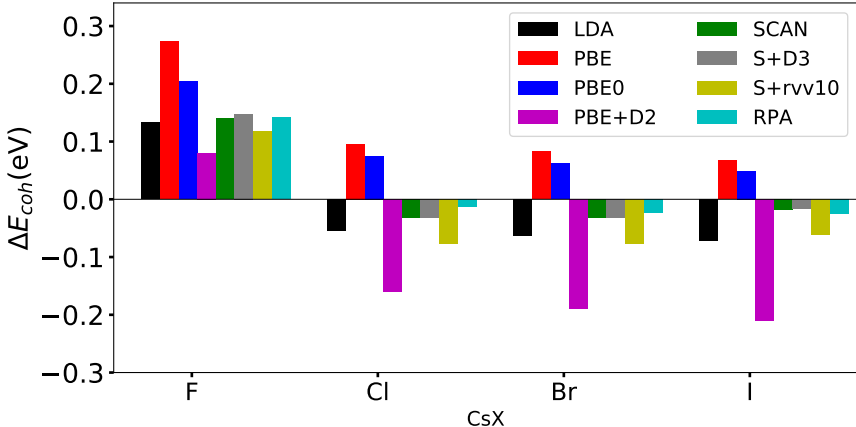
Comparing the semilocal results against the ACFDT results indicates that the incorporation of dispersion is crucial, as expected. The dispersion corrected SCAN results agree to a good extent with the higher level calculations, though whether they agree with RPA or bRPA methods depends on the halide. For the fluoride, the ACFDT methods are likely superior because they utilize the self-interaction error free exact exchange energy and correctly incorporate all ranges of dispersion, whereas the semilocal results (other than PBE) are too large already without dispersion and only become larger with the addition of D3 or rVV10. For the other halides, the difference between the dispersion corrected SCAN results and the bRPA methods is around 300 meV per functional unit ($\sim 3-5\%$) indicating

an adequate prediction by the lower-level methods. Though the magnitude of the cohesive energy is important to compare with experiment, the difference in predicted cohesive energies is also important for predicting the relative stability of the B1 and B2 phases.

Table 3.3: Computed cohesive energies (eV per formula unit) for the stable phases of the cesium halides. The columns are labeled as they were for Table 3.1. SCAN+D3 results were computed using "zero" damping. The experimental values given by Ref. [148] are taken at room temperature.

E_{coh}	LDA	PBE	PBE0	PBE+D2 [141]	SCAN	S+D3	S+rVV10	RPA	RPAr1	HOT	ACSOSEX	Expt. [148]
F-B1	8.28	7.19	6.91	7.94	8.09	8.14	8.24	7.51	7.68	7.81	7.82	7.48
Cl-B2	6.97	6.07	6.08	6.84	6.874	6.94	7.08	6.865	7.12	7.24	7.40	6.74
Br-B2	6.49	5.64	5.70	6.48	6.37	6.44	6.57	6.03	6.08	6.20	6.42	6.48
I-B2	5.92	5.12	5.20	6.02	5.73	5.80	5.94	5.56	5.59	5.70	5.93	6.18

Figure 3.1: Bar diagram representing $\Delta E_{coh} = E_{coh}^{B1} - E_{coh}^{B2}$ obtained with various DFT methods. PBE+D2 results are taken from Ref. [141]. Positive ΔE_{coh} corresponds to the B1 phase being preferred as the ground state, whereas negative values indicate the preferred stability of the B2 phase. PBE predicts all ground state cesium halides to be in the B1 phase whereas all other methods favor the B2 structure except in CsF. Data for energy differences between cohesive energies between two phases are presented by Table 3.6 in supplementary material.



The differences in the predicted cohesive energies between B1 and B2 phases, $\Delta E_{coh} = E_{coh}^{B1} - E_{coh}^{B2}$, are summarized in Figures 3.1 and 3.2. Figure 3.1 contains the dispersion-corrected semilocal results along with PBE0, and RPA. The bRPA results using rALDA are presented in Figure 3.2. As in Ref. [141], both PBE and PBE0 predict all of the cesium halides to prefer the B1 phase, whereas all the other methods predict CsF to prefer

the B1 phase and CsCl, CsBr, and CsI to prefer the B2 phase. LDA predicts the correct energetic orderings for all of the halides in addition to accurately predicting the structural parameters. The PBE+D2 results of Ref. [141] correct the failure of PBE, but result in a large difference in cohesive energies due to an inadequate description of dispersion effects in these ionic compounds. Both RPA and SCAN predict the correct phase ordering, but the difference in cohesive energies is noticeably smaller than that of PBE+D2. RPA yields a consistent trend of increasing ΔE_{coh} going down from Cl in the halide group, as do LDA and PBE+D2 [141], but SCAN does not yield the same trend, with the predicted energy difference for the iodide being smaller than that for Cl and Br. Beyond RPA methods follow the RPA trend, but yield consistently larger splittings between the phases. Since the bRPA methods contain proper short- and long-ranged correlation effects, as well as a self-interaction error free exchange energy, we prefer them for a benchmark in these systems. With that in mind, the SCAN and SCAN+dispersion results yield reasonable predictions for each of the salts, though the chemical trend is not reproduced. We found that the difference in ZPVE between the two phases is 5 meV for CsF, and decreases to 0.1 meV as we go towards the heavier anions. No imaginary vibrational modes were observed during phonon calculation. These thermal shifts are negligible compared to the electronic energy difference [141], thus the primary contribution to ΔE_{coh} comes from electronic correlation at 0 K and not from any temperature effects.

The beyond RPA results obtained with the rAPBE, CDOPs [223], and CP07 kernels for CsCl are reported in Tables 3.4 and 3.5. Results for rAPBE are obtained using the Birch–Murnaghan equation of state with an energy cutoff of 350 eV, while the others were calculated close to the RPA minimum. Table 3.4 shows that rAPBE significantly overestimates the equilibrium volume, while Table 3.5 shows that it predicts both phases to be iso-energetic, in contradiction to the experimental fact that CsCl prefers the B2 phase. Both CDOPs and CP07 predict that CsCl prefers the B2 phase by at least 15 meV per

Table 3.4: Comparison of equilibrium volumes for CsCl obtained using rAPBE with other RPA-based methods.

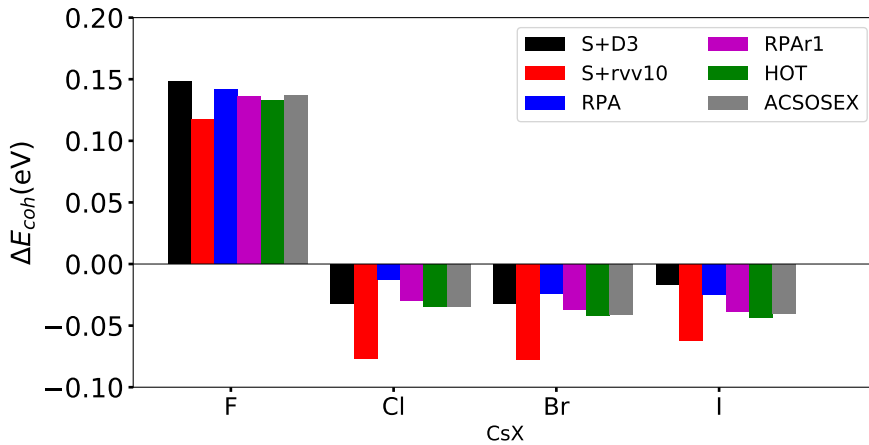
Vol(\AA^3)	rALDA				rAPBE		
	RPA	RPAr1	HOT	ACSOSEX	RPAr1	HOT	ACSOSEX
CsCl-B1	83.128	82.324	82.104	81.826	87.080	87.476	87.257
CsCl-B2	68.315	68.873	68.681	68.977	74.732	75.448	75.074

functional unit, supporting the assertion that the results obtained with the rALDA kernel are more reliable than those of rAPBE.

Table 3.5: Beyond RPA results for equilibrium energy difference ($\Delta E_{\text{coh}} = E_{\text{coh}}^{\text{B1}} - E_{\text{coh}}^{\text{B2}}$) with rAPBE, CDOP, and CP07 kernels. The Birch-Murnaghan equation of state was fit to get the rAPBE results, whereas the calculation was only done near the equilibrium volume obtained with RPA for the others. Only rAPBE fails to predict the correct phase ordering. The HOT approximation is not currently implemented for CP07 or CDOPs. RPA predicts a splitting of 0.0123 eV.

ΔE_{Coh} (eV/f.u.)	rAPBE	CPO7	CDOPs
RPAr1	0.003	-0.019	-0.035
HOT	0.001	—	—
ACSOSEX	0.001	-0.019	-0.040

Figure 3.2: Bar diagram representing $\Delta E_{\text{coh}} = E_{\text{coh}}^{\text{B1}} - E_{\text{coh}}^{\text{B2}}$ obtained with beyond RPA methods using rALDA kernel. Dispersion corrected results to SCAN (SCAN+D3 and SCAN+rVV10) and RPA results are presented alongside for the sake of comparison between various beyond rALDA approximations. Positive ΔE_{coh} indicates the B1 phase is the preferred ground state, whereas negative values indicate the preferred stability of the B2 phase. Data for energy differences between cohesive energies between two phases are presented by Table S3 in supplementary material.



3.6 Discussion & Conclusion

Due to the lack of explicit treatment of weak, but important, van der Waals interactions between the ions [141, 147, 150], PBE and PBE0 are inaccurate for determining the equilibrium ground state properties of the cesium halides. The correct ordering predicted by LDA, in addition to the accurate cohesive energies, is due to error cancellation between exchange and correlation, and is not reliable in general for novel ionic materials. SCAN is a reliable semilocal functional for these materials, since it incorporates some of the missing dispersion contributions absent in the other non-empirical functionals we tested. SCAN simultaneously provides an accurate prediction of the structural properties and cohesive energies, but is unable to completely capture the same trends as RPA with respect to the relative magnitudes of the cohesive energies. Adding the long-range dispersion shifts the magnitude of the SCAN result, but does not impact its underlying physical prediction. For the cesium halides, the rVV10 correction tends to be larger in magnitude, resulting in underestimated equilibrium volumes and overestimated cohesive energies, while the D3 correction is smaller and yields overall results in close agreement with the uncorrected SCAN.

The ACFDT-DFT methods delivered highly accurate structural results, though RPA is more accurate for the cohesive properties of the lighter halogens and bRPA methods only overtake RPA for the bromide and iodide. Since RPA naturally incorporates long-range dispersion and the lighter halogens contain more ionic interactions, incorporating additional short-ranged interactions through an xc kernel overestimates the cohesive energy difference between the B1 and B2 phases. For the heavier halogens, the kernel is more important since the interactions are less ionic. Of the kernels we tested, three indicated a clear preference for the B2 phase for Cl, Br, and I, further validating our RPA and semilocal results. Though rALDA and rAPBE both share very similar functional forms, the inability of rAPBE to predict the correct phase ordering is puzzling, and will require further tests to understand. Amongst the RPA methods there is little difference in overall performance, in-

dicating that any reasonable treatment of bRPA effects should improve the RPA result. We prefer RPA_{r1} to ACSOSEX since it is a completely screened perturbation theory [15, 117].

Overall, the splitting between B1 and B2 in cohesive energies predicted by LDA, RPA, SCAN, and SCAN+rVV10 ranges from 20 to 80 meV for the halogen series, whereas it ranges from 80 meV to 210 meV for PBE+D2 [141] (See Fig. 3.1). This large splitting in PBE+D2 is due to the fact that it describes dispersion only through 2-body attractive dispersion without taking effects from local environment into account and does not incorporate repulsive 3-body dispersion contributions to the cohesive energy in these halides [224]. The lower splitting in cohesive energy by RPA and SCAN can be attributed to the fact that RPA lacks a proper description of short ranged dispersion whereas SCAN does not include long ranged dispersion. The rALDA results are more accurate for the heavier halogens than RPA because short-ranged interactions are properly included through an exchange-like kernel. The SCAN+rVV10 results also show systematic improvement over SCAN by adding missing long-range dispersion, resulting in energy differences that closely mimic the bRPA results of rALDA. Results obtained with CP07 and CDOPs further support that the rALDA kernel is sufficiently accurate for explaining the phase stability of these ionic solids. Due to their lower computational cost, SCAN and dispersion-corrected SCAN methods can be a reliable alternative to the ACFD methods for ionic systems, where treating the various distance scales of electron-electron interactions are important. Benchmarking against RPA or bRPA is recommended though, if one is interested in chemical trends.

3.7 Acknowledgements

We thank Chandra Shahi and Haowei Peng for their assistance with some calculations. This work was supported by the National Science Foundation under Grant No. DMR-1553022. J.E.B. was also supported through start-up funds from the A. R. Smith Chemistry Department at Appalachian State University. Computational support was provided

by HPC of Temple University through the NSF major research instrumentation Grant No. CNS-09-58854. A portion of the calculations utilized resources from the Center for the Computational Design of Functional Layered Materials, an Energy Frontier Research Center (EFRC) funded by the US Department of Energy, Office of Science, Basic Energy Sciences, under Award No. DESC0012575. Figures were created using Matplotlib [225].

SUPPORTING INFORMATION

Tables ?? and 3.8 represent the cohesive energy differences data corresponding to FIG. 1 and FIG. 2 respectively in the paper. Table 3.7 demonstrates the faster convergence of the difference in the cohesive energy between the 2 phases of CsCl with increased energy cutoff obtained by the beyond-RPA method rALDA, as discussed in the main paper. It can be seen from Table 3.7 that the energy cutoff of 280 eV is sufficient to study the relative phase stability of Cesium halides. However, 350 eV was taken for a better convergence of other ground state equilibrium properties. Finally, the zero point energies are presented in Table 3.9.

Table 3.6: Difference in cohesive energies between the two phases in eV per formula unit. Negative sign indicates the stability of the B2 phase. PBE+D2 results are taken from Ref. [141]

CsX	LDA	PBE	PBE0	PBE+D2	SCAN	S+D3	S+rVV10	RPA
F	0.1331	0.2729	0.2043	0.0800	0.1398	0.1479	0.1173	0.1414
Cl	-0.0550	0.0960	0.0752	-0.1600	-0.0312	-0.0320	-0.0768	-0.0123
Br	-0.0630	0.0830	0.0619	-0.1900	-0.0312	-0.0320	-0.0773	-0.0238
I	-0.0720	0.0674	0.0486	-0.2100	-0.0183	-0.0168	-0.0622	-0.0247

Table 3.7: Difference in cohesive energies (B2-B1) of CsCl in eV per formula unit with respect to different cutoffs along with the results of extrapolated values which show the fast convergence of the relative energy with cutoff for rALDA.

E-Cut	RPAr1	HOT	ACSOSEX
280	-0.0294	-0.0343	-0.0348
297	-0.0294	-0.0341	-0.0346
315	-0.0300	-0.0347	-0.0350
332	-0.0298	-0.0345	-0.0348
350	-0.0295	-0.0342	-0.0345
Extrapolated	-0.0300	-0.0345	-0.0345

Table 3.8: Extension of Table ?? to beyond-RPA methods within the rALDA formalism.

CsX	RPAr1	HOT	ACSOSEX
F	0.1360	0.1330	0.1368
Cl	-0.0295	-0.0341	-0.0345
Br	-0.0371	-0.0417	-0.0408
I	-0.0385	-0.0433	-0.0405

Table 3.9: Zero Point Energy (ZPE) per formula unit using PBE. We have not calculated ZPE for CsI.

CsX	Zero-point(eV)
CsF-B1	0.0350
CsF-B2	0.0301
CsCl-B1	0.0259
CsCl-B2	0.0256
CsBr-B1	0.0190
CsBr-B2	0.0189

CHAPTER 4

TREATING DIFFERENT BONDING SITUATIONS: REVISITING AU-CU ALLOYS USING THE RANDOM PHASE APPROXIMATION

4.1 Abstract

The ground state equilibrium properties of copper-gold alloys have been explored with the state-of-the-art random phase approximation (RPA). Our estimated lattice constants agree with the experiment within a mean absolute percentage error (MAPE) of 1.4 percent. Semilocal functionals such as the generalized gradient approximation (GGA) of Perdew, Burke, and Ernzerhof (PBE) and strongly constrained and appropriately normed (SCAN) fail to provide accurate bulk moduli, which indicate their inability to describe the system in a stretched or compressed state with respect to the equilibrium geometry. The PBE, PBE revised for solids (PBEsol), and revised TPSS (revTPSS) by Perdew et. al. predict too low formation energies while the SCAN slightly overestimates it. The inclusion of thermal correction or the long-range dispersion provides negligible contribution to the formation energies estimated with semilocal density functional theory (DFT). The spin-orbit coupling (SOC) improves the formation energies of PBE only by 7-8 meV, while it intensifies the overestimation of SCAN. We found that the non-locality present in RPA is able to describe the transition between two delocalized electron densities (bulk elemental constituents to crystallized alloys), as required to provide accurate formation energies without any further corrections. Based on our results, we conclude that it is difficult to find a universal density functional which can give accurate results for a wide range of properties of inter-metallic alloys. However, RPA can capture different bonding situations, often better than other density functionals. It gives accurate results for a wide range of ground state properties for the

alloys, generated from metals with completely filled d-shells.

©2019 American Physical Society

4.2 Introduction

Inter-metallic alloys, the mixture of 2 or more metals in a solid form, manifest a defined stoichiometry and an ordered crystal structure [226]. The brittleness and high melting point with various electronic and magnetic properties of these solid compounds make them significantly useful in industrial applications. The heat of formation or formation energy of an alloy is the difference between the total binding energy of the system and its pure constituents, and its accurate prediction is extremely important in alloy theory. It governs the stability of the alloys with different compositions at different temperatures and pressures [226, 227].

Density functional theory (DFT) is a robust electronic structure method, applicable across numerous fields of science. Various forms of the approximation to the exchange-correlation (XC-) energy, a key but unknown quantity in DFT, afford different levels of accuracy and computational efficiency. These different forms constitute the different rungs of Perdew's Jacob's ladder [190]. The local density approximation (LDA) [14] and generalized gradient approximations (GGA) such as PBE [21], AM05 by Armiento and Mattsson [228], and PBE revised for solids (PBEsol) [23], though being highly accurate and efficient in many cases, often fail to provide an accurate description of the properties which require either self-interaction correction, at least a fraction of exact exchange, or an adequate description of many-body correlation [229]. Meta-GGAs such as TPSS [32] by Tao, Perdew, Staroverov, and Scuseria, the made-simple (MS) family [35, 230], and SCAN [39] provide significant improvement over LDA and GGAs, with the inclusion of kinetic energy density ($\tau(\mathbf{r})$) as an ingredient in addition to the density ($n(\mathbf{r})$) and its gradient ($\nabla n(\mathbf{r})$).

However, regarding the formation energy of inter-metallic alloys, semi-local functionals have a mixed performance [231–233]. To estimate an accurate formation energy, a functional should not only provide reliable energetics of an alloy but also simultaneously of its constituent elements. However, most semi-local functionals fail in that regard, leading to inaccurate predictions of the formation energy [234].

At high temperature, copper and gold form a continuous solid solution while they crystallize to form Au-Cu super-lattices at lower temperature [235]. The Au-Cu systems, AuCu_3 (or $\text{Au}_{0.25}\text{Cu}_{0.75}$), AuCu (or $\text{Au}_{0.5}\text{Cu}_{0.5}$), and CuAu_3 (or $\text{Au}_{0.75}\text{Cu}_{0.25}$), are the paradigms of inter-metallic alloys, and have been extensively studied with semi-local as well as non-local DFT methods [232–234]. Experimentally, the fully ordered AuCu_3 and CuAu_3 stabilize in the $L1_2$ phase while the ordered AuCu prefers the $L1_0$ phase at $T = 0$ K [226]. In addition to the distorted face-centered cubic (FCC) phase for AuCu ($L1_0$), we also have explored its FCC phase. Previous work clearly established that LDA could not predict the ground state of CuAu_3 as the $L1_2$ phase and also significantly underestimates the formation energies of all the Au-Cu alloys [233]. Similar to LDA, PBE also predicts CuAu_2 as the stable phase and CuAu_3 as the unstable one [232]. On the other hand, the screened hybrid XC-functional HSE06 (simply HSE by Heyd, Scuseria, and Ernzerhof) [66, 67] developed by mixing non-local exact exchange with semi-local exchange-correlation, is able to provide accurate geometries and formation energies of these compounds [232]. Moreover, HSE is designed to be nonlocal at short range, while the exact exchange is screened at long range. SCAN was demonstrated to capture medium-range weak interactions, while HSE is known to reduce the delocalization error in semilocal functionals. Inspired by these facts, we aim to climb even higher on the rungs of Jacob’s ladder to gain more understanding about any competition between weak interactions and free electron-like bonding in Cu-Au systems [83].

In this work, we have revisited the Au-Cu alloy systems using the random phase approximation (RPA) [74, 75, 236]. RPA is the simplest approximation within an adiabatic-connection fluctuation-dissipation theorem (ACFDT) formalism [169, 170]. It combines the non-local one electron self-interaction free exact exchange (EXX) energy with the non-local correlation energy (E_c^{RPA}) [171, 172]. Most importantly, it can provide accurate results for systems involving weak interactions such as van der Waals (vdW) interactions [85–87], as well as ionic [83, 92] and covalent interactions [76, 77, 79, 83]. The total energy in the ACFDT-DFT framework can be expressed as,

$$E = E_{EXX} + E_C^{RPA} \quad (4.2-1)$$

where, E_{EXX} is the Hartree-Fock (HF) total energy evaluated non-self-consistently using self-consistently-obtained Kohn-Sham DFT orbitals. E_C^{RPA} is the RPA correlation energy, which can be obtained using the interacting density-density response function (χ) which is related to the non-interacting response function (χ_0) via a Dyson-like equation [124, 171, 172]. The RPA correlation energy naturally incorporates long-range dispersion and is non-perturbative. For this work, the systems are heavy coinage metals which are largely influenced by dispersion interactions [237–239]. Furthermore, the systems have zero band gap. Due to its non-perturbative nature, RPA can be safely applied to zero-gap systems without divergence [197]. In both aspects, the application of RPA to these systems is justified.

For the sake of comparison, we also have assessed semi-local functionals such as PBE, PBEsol, the revised TPSS (revTPSS) [33, 34] and SCAN along with RPA. We also tested the impact of long-range dispersion through the nonlocal revised VV10 (rVV10) correction. We utilized PBE+rVV10 [56, 240] and SCAN+rVV10 [55] to check whether the discrepancies in semilocal DFT are due to the absence of long-range dispersion interac-

tions. The rest of the paper is organized as follows. Computational details are provided in section II, followed by results in section III. We will present our conclusions in section IV.

4.3 Computational details

All DFT calculations were carried out using a projector augmented wave (PAW) [206] method, as implemented in GPAW [207–209] and VASP [210]. We utilized VASP to perform semi-local calculations whereas RPA calculations were carried out using GPAW. Moreover, semi-local calculations were performed self-consistently while RPA calculations were carried out using a non-self-consistent approach. We used a plane-wave cutoff of 600 eV and Brillouin zone sampling of $20 \times 20 \times 20$ Gamma centered k-mesh to avoid the convergence test for semi-local DFT calculations. Ground state PBE calculations were performed as an input for the RPA calculations. Separate convergence tests for EXX and the RPA correlation energies were carried out to determine the plane-wave cutoffs and k-mesh sampling with less than 2 meV relative error (Supplementary Table 4.5). We used a maximum cutoff of 350 eV to compute the response function. All other parameters and procedure of the RPA calculations were kept similar to that of Ref. [92], except skipping the gamma point ($\mathbf{q} = 0$) to avoid the possible divergent contribution from metals as discussed in Ref. [76].

We calculated the zero-point vibrational energy (ZPVE) to estimate the thermal contribution to the formation energy. PBEsol [23] calculations were done with a $2 \times 2 \times 2$ supercell (32 atoms) using VASP [212, 241] and PHONOPY [215]. The estimated thermal corrections are less than or equal to 1 meV/atom, consistent with previous results [232]. Relativistic effects are included at the scalar level for each atom within the PAW potentials provided in VASP and GPAW. We further tested, at least for PBE and SCAN, an impact of the spin-orbit coupling [242] on semi-local DFT results. We have performed calculations for 7 volume points near the experimental equilibrium volume and fit the Birch-Murnaghan

equation of state [243] to evaluate the equilibrium properties. We have used the experimental structures from Ref. [235] and varied the lattice constants isotropically to generate structures with different volumes. In order to compute the cohesive energies, atomic energies were computed. We have performed spin polarized semi-local DFT calculations with VASP using a plane-wave cutoff of 600 eV and $23 \times 24 \times 25 \text{ \AA}^3$ simulation cell to avoid any interactions of an isolated atom with its periodic images. Separate convergence tests for atomic energies were performed with GPAW for both EXX and RPA (Supplementary Table 4.5).

4.4 Results

4.4.1 Lattice constants

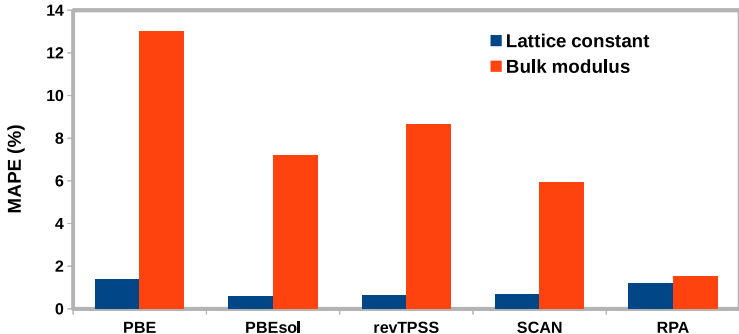
The equilibrium lattice constants of the ordered Au-Cu alloys are presented in Table 4.1. As expected, PBE overestimates the lattice constants and PBEsol yields reasonable lattice constants of the coinage metals such as Au and Cu [83]. The failure of PBE to estimate accurate lattice constants is related to the poor descriptions of exchange-correlation effects between completely filled d-shells in coinage metals [83]. RPA lattice constants are also overestimated which can be decreased by including the Pauli repulsion in SOSEX or adding a kernel correction to RPA [92, 117, 244], thereby improving the short-range correlations necessary to describe the systems with more filled d-shells. On the other hand, SCAN along with revTPSS show good performance in the prediction of equilibrium lattice constant. With the inclusion of kinetic energy density, both SCAN and revTPSS can distinguish different bonding regions relevant to lattice constants, and this becomes more effective as more d bands are filled in the transition metal [83]. Overall, all methods show a reasonable agreement with the experiment for the lattice constant with mean absolute percentage error (MAPE) less than 1.4%, as shown in Figure 4.1. Furthermore, the addition of long-range dispersion correction slightly improves the PBE lattice constants, while it slightly worsens

the SCAN results (Supplementary Table 4.6). The inclusion of spin-orbit coupling can change the PBE and SCAN lattice constants by 1 picometer (Supplementary Table 4.7).

Table 4.1: Lattice constants (\AA). The experimental lattice constants are taken from Reference [235]. Among the DFT functionals utilized, PBEsol shows the best performance in predicting the equilibrium lattice constant.

	PBE	PBEsol	revTPSS	SCAN	RPA	Experiment
Cu	3.64	3.57	3.57	3.57	3.63	3.62
Au	4.16	4.08	4.08	4.09	4.15	4.08
AuCu ₃	3.78	3.72	3.72	3.72	3.78	3.75
AuCu (FCC)	3.92	3.85	3.85	3.85	3.92	3.87
AuCu (P4/mmm)	2.84	2.79	2.79	2.79	2.83	2.80
CuAu ₃	4.05	3.97	3.98	3.98	4.05	3.95
MAE (\AA)	0.051	0.022	0.023	0.026	0.046	–
MAPE (%)	1.37	0.59	0.64	0.7	1.21	–

Figure 4.1: Mean absolute percentage error (MAPE) for both lattice constants and the bulk moduli. Overall, PBEsol is the most accurate method for lattice constants, while RPA predicts excellent bulk moduli compared to experiments.



4.4.2 Bulk Moduli

The bulk modulus measures the curvature of an energy-volume relation, and its accurate prediction indicates the ability of a DFT approximation to describe the system in a non-equilibrium state with respect to the equilibrium state. We calculated the bulk moduli of various Au-Cu systems and tabulated them in Table 4.2. PBE underestimates the bulk modulus, while PBEsol and revTPSS predict accurate bulk moduli for gold. However, the performance of these functionals worsens on increasing the concentration of copper. On the other hand, SCAN provides an improvement for the bulk modulus of copper, thereby

improving the bulk moduli of all alloys compared to PBEsol and revTPSS (Figure 4.1). The inability of semi-local functionals to give an accurate prediction of bulk moduli indicates their inability to describe the compressed or stretched electron densities with respect to the equilibrium ground state electron densities. One can see that the overall bulk moduli predicted by PBE for all the alloys are close to the experimental value of copper while those of other semi-local functionals are closer to gold. On the other hand, RPA provides accurate bulk moduli for both alloys and those of the constituent bulk elemental systems. This indicates that, contrary to the lattice constant, the description of short-range correlation is not crucial for the prediction of the bulk modulus. The inclusion of long-range dispersion via rVV10 provides a more significant correction to the bulk modulus for PBE than that for SCAN. On the other hand, spin-orbit coupling can increase the bulk moduli by 3-6 GPa with respect to DFT results without SOC (Supplementary Table 4.7).

Table 4.2: Bulk Moduli (GPa). Experimental bulk moduli are computed using $\frac{(C_{11}+2C_{12})}{3}$ (cubic lattice), where C_{ij} is the elastic moduli. Overall, RPA predicts the bulk moduli in close agreement with the experiment.

	PBE	PBEsol	revTPSS	SCAN	HSE [245]	RPA	Experiment
Cu	137.89	164.50	170.14	157.91	133.8	144.74	143.6 [246]
Au	139.03	174.34	176.01	166.95	146.6	176.71	177.6 [247], 180.53 [246]
AuCu ₃	139.49	168.05	171.09	164.84		155.25	151.83 [248]
AuCu (FCC)	139.99	171.02	173.12	169.47		163.77	162.97 [249]
AuCu (P4/mmm)	138.75	169.56	171.90	166.16		159.09	–
CuAu ₃	139.03	171.64	173.25	165.74		162.15	166.33 [250]
MAE (GPa)	21.71	11.04	13.19	9.31	–	2.42	
MAPE (%)	13.02	7.20	8.65	5.93	–	1.50	

4.4.3 Formation Energy

The formation energy of a Au-Cu alloy can be obtained using,

$$\Delta E_f(\text{Au}_x\text{Cu}_{1-x}) = \Delta E_{\text{coh}}(\text{Au}_x\text{Cu}_{1-x}) - x\Delta E_{\text{coh}}(\text{Au}) - (1-x)\Delta E_{\text{coh}}(\text{Cu}) \quad (4.4-2)$$

where $\Delta E_f(\text{Au}_x\text{Cu}_{1-x})$, $\Delta E_{\text{coh}}(\text{Au}_x\text{Cu}_{1-x})$, $\Delta E_{\text{coh}}(\text{Au})$, and $\Delta E_{\text{coh}}(\text{Cu})$ are the formation energy of the system, cohesive energy of the whole system, cohesive energy of gold, and

the cohesive energy of copper per atom respectively and x is the fraction of gold atoms in the alloys. We have computed the formation energy of a given alloy as a function of crystal volume, Figure 4.2. Experimental volumes are indicated by a '#', whereas the formation energies are represented by black dots. Positive formation energies imply instability of the alloy while negative formation energies imply stability with respect to their elemental bulk constituents.

Without any correlation, EXX predicts destabilized systems within the range of volumes considered. Contrary to EXX, PBE stabilizes the systems with the presence of both exchange and correlation energies (Figure 4.2). Formation energies obtained from PBE agree with RPA values either at the highly compressed state or at the highly stretched state. However, they start to deviate from RPA and even from the experimental value as the equilibrium geometry is approached. On the contrary, SCAN slightly overbinds the formation energies near the equilibrium geometries, and the overestimation gets larger as we deviate from the equilibrium. The formation energy vs volume calculated with PBEsol and revTPSS behave similarly to that of SCAN, however, they are slightly shifted upward along the direction of positive formation energy. Despite the fact that RPA overestimates the lattice constant, it accurately predicts the curvature and minima of the equation of state for these alloys.

The heats of formation of the Au-Cu system at equilibrium are presented in Table 4.3, whereas the stability of the alloys are represented by a convex hull as in Figure 4.3. As in the earlier studies [232, 234], PBE severely underestimates the formation energies. On restoring the second-order gradient expansion for the exchange over a wide range of densities at the GGA level, PBEsol slightly improves the results, but at the meta-GGA level revTPSS [251] worsens it. By satisfying more exact constraints and including more appropriate norms [39], SCAN shows a considerable improvement over revTPSS. However,

it still performs poorly for copper-rich alloys, while the error decreases on increasing the concentration of gold, as more filled 5d shells in Au are involved [83]. The deficiencies in semi-local PBE and SCAN could not be overcome simply by taking thermal correction, long-range dispersion correction, or spin-orbit coupling into account (Supplementary Tables 4.6 and 4.7). In contrast, non-local density functionals such as hybrid HSE and RPA consistently predict accurate formation energies of these alloys without any aforementioned corrections. In comparison, self-consistent HSE outperforms non-self-consistent RPA by only a little, but there can be room for improvement when RPA is also evaluated self-consistently [252].

In the present work, both alloys and the constituent metals are in the solid phase and hence possess delocalized electron densities. The reliable prediction of formation energies requires an accurate description of the transition from delocalized electron densities of constituent metals to delocalized electron densities of inter-metallic alloys. All semi-local functionals included herein fail to describe such a transition, while the non-locality present in HSE and RPA is able to effectively detect such changes. However, the transition from localized (atoms) to delocalized (solid metals and alloys) is not straightforward even for non-local functionals, as evident from the cohesive energies presented in Table 4.4. The best density functional for formation energies is the worst for cohesive energies. The hybrid HSE seriously underestimates the cohesive energies of Au-Cu system with a mean absolute error (MAE) of nearly 0.7 eV/atom. Surprisingly, semi-local functionals perform much better than HSE in the order of $\text{PBE} < \text{revTPSS} < \text{PBEsol} < \text{SCAN}$ with decreasing MAE and MAPE. RPA, on the other hand, provides reasonable cohesive energies for Cu-rich compounds, while it worsens on increasing the concentration of gold in the alloys. As the number of filled d bands increases, the short-range correlation becomes more crucial in describing the interactions within transition metal atoms as well as their alloys. Restoring the exchange-correlation kernel within the RPA can improve the cohesive energies of

transition metals up to 0.3 to 0.4 eV [79, 253].

The performance of various density functionals on Au-Cu alloys clearly depends on their ability to describe the less-delocalized “3d” electron density of copper as well as the more-delocalized “5d” electron density of gold. SCAN along with PBEsol and revTPSS can effectively describe the 5d bands of gold, thereby giving sensibly accurate lattice constants, bulk moduli, and cohesive energies for Au-rich alloys. However, RPA has the opposite trend that it can provide an accurate prediction for Cu-rich alloys, but falls short when describing Au-rich alloys. On the contrary, HSE fails to provide accurate bulk moduli and cohesive energies for both copper and gold, giving too low cohesive energies for both Au- and Cu- rich alloys. With that in mind, one can argue that the density functionals that can separately describe the constituents, can ultimately describe the weakly bonded alloys.

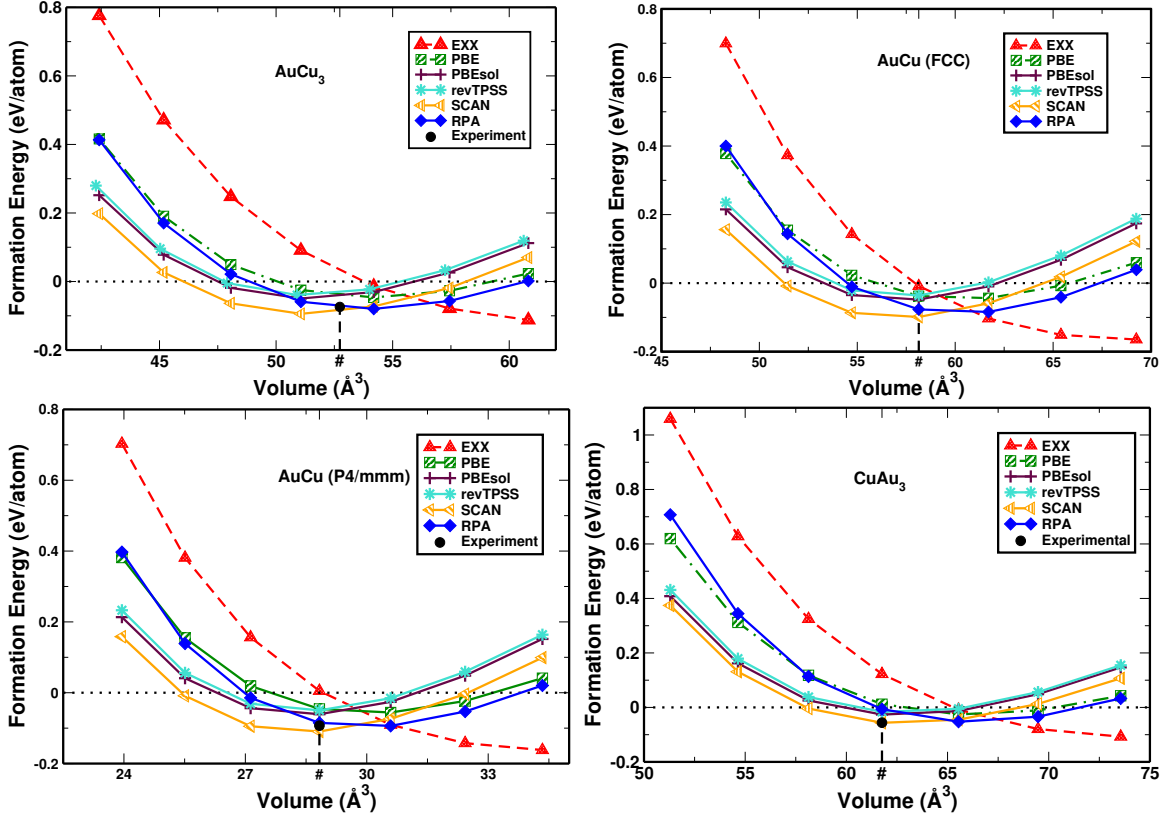
Table 4.3: The heat of formation (eV /atom). Note that the results for semi-local functionals and HSE are obtained self-consistently, while the RPA results are obtained non-self-consistently using PBE orbitals. Experimental results taken from Reference [226] are obtained at 320 K, whereas Reference [227] corresponds to 298.15 K; CuAu₃: The experimental structure taken in Reference [226] is not fully ordered structure. The heat of formation for a fully ordered CuAu₃ is estimated using cubic interpolation of composition (x)-Gibbs energy (ΔG)-entropy (ΔS) of formation data taken from Reference [227].

	PBE	PBEsol	revTPSS	SCAN	HSE [232]	RPA	Experiment [226]
AuCu ₃	-0.046	-0.050	-0.040	-0.093	-0.071	-0.080	-0.074 , -0.075 [227]
AuCu (FCC)	-0.047	-0.050	-0.037	-0.101		-0.088	
AuCu (P4/mmm)	-0.058	-0.062	-0.051	-0.111	-0.091	-0.096	-0.093
CuAu ₃	-0.026	-0.028	-0.019	-0.059	-0.053	-0.052	-0.039, -0.056 [227]

Table 4.4: Cohesive energy per atom (eV/atom). The cohesive energies for HSE are obtained using References [232, 245], while the experimental cohesive energies are obtained using References [226, 254] using Eq. 4.4-2. Among the functionals used, SCAN predicts most accurate cohesive energy as compared to the experiment.

	PBE	PBEsol	revTPSS	SCAN	HSE	RPA	Experiment
Cu	3.484	4.030	4.057	3.886	3.060 [245]	3.350	3.490 [254]
Au	3.035	3.720	3.627	3.555	2.880 [245]	3.395	3.810 [254]
AuCu ₃	3.419	4.003	3.990	3.896	3.086	3.441	3.644
AuCu (P4/mmm)	3.317	3.937	3.893	3.828	3.111	3.469	3.743
CuAu ₃	3.175	3.826	3.753	3.695	2.978	3.436	3.786
MAE (eV/atom)	0.409	0.245	0.256	0.216	0.672	0.276	–
MAPE (%)	10.84	6.78	7.08	5.93	18.05	7.41	–

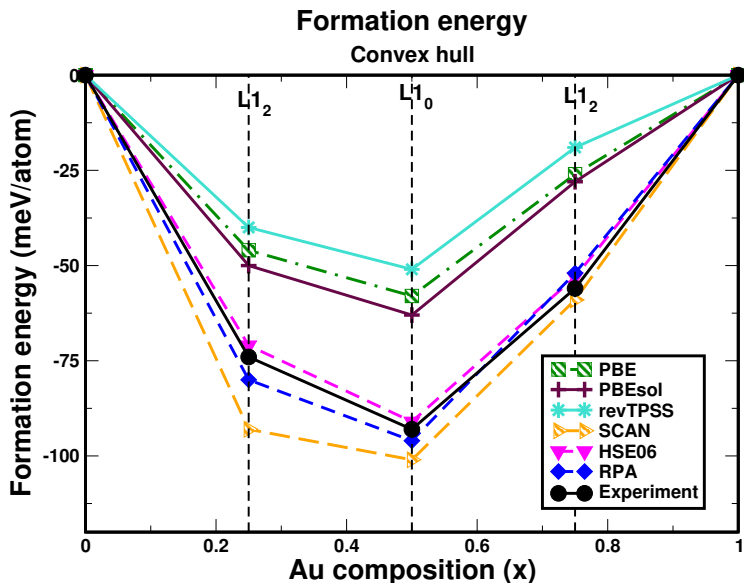
Figure 4.2: Formation energy (eV) versus volume (\AA^3). The positive formation energy refers to instability of alloys with respect to isolated bulk constituents, while negative formation energy refers to stability. Experimental formation energies are taken from References [226, 227]. The experimental volumes are indicated by ‘#’ in Figures.



4.5 Conclusions

We have explored copper-gold alloys with various levels of approximations within density functional theory, including the state-of-art random phase approximation. It is difficult to find a universal functional which can describe all of the bonding situations. Semi-local functionals can reasonably describe the transition between localized and delocalized electron densities, as manifested in the cohesive energies. On the other hand, the non-locality present in HSE and RPA can distinguish the transition between two delocalized electron densities, as seen from the formation energies of the alloys. Moreover, the performance of these functionals in describing the weakly bonded Au-Cu system depends on their potential to separately describe less-delocalized and more-delocalized electron densities of copper

Figure 4.3: Convex hull: Formation energy as a function of gold composition (x). PBE along with PBEsol and revTPSS largely underestimates the formation energy, while SCAN performs poorly on Cu-rich alloy, but improves the result as the concentration of gold increases. Formation energies predicted by non-local HSE and RPA are in close agreement with the experiment.



and gold respectively. Based on our results, we can conclude that RPA predicts accurate values for diverse properties of binary alloys, generated from metals with completely filled d-shells. It has an accuracy of semi-local functionals at the challenging situations, while consistently providing reliable results where semi-local functionals break down.

4.6 Acknowledgements

N.K.N. and A.R. acknowledge support by the National Science Foundation under Grant No. DMR-1553022. JEB was supported by the A.R. Smith Department of Chemistry and Fermentation Sciences. Computational support was provided by Temple University's HPC resources and thus was supported in part by the National Science Foundation through major research instrumentation grant number 1625061 and by the US Army Research Laboratory under contract number W911NF-16-2-0189. N.K.N., JEB, and A.R. designed the project. N.K.N. performed the calculations, and wrote the first draft. S.A. performed some of the

calculations. All authors contributed references, discussions, and revisions.

SUPPORTING INFORMATION

Table 4.5: Convergence parameters for RPA calculations; Bulk calculations: Energies for bulk calculations are converged within 1-2 meV; Atomic calculations: EXX energies are converged within 1-2 meV for both energy cutoff and cell volume. However for RPA, convergence was achieved within 1-5 meV for energy cutoff, while it is 15-20 meV for cell volume. We used PAW pseudopotentials such that the valence electron configuration includes $d^{10}s^1$ electrons for both copper and gold.

	Bulk calculations				Atomic calculations			
	EXX		RPA		EXX		RPA	
	Energy cutoff (eV)	K-mesh	Energy cutoff (eV)	K-mesh	Energy cutoff (eV)	Cell volume (\AA^3)	Energy cutoff (eV)	Cell volume (\AA^3)
Cu	1000	$16 \times 16 \times 16$	800	$16 \times 16 \times 16$	1000	$10 \times 11 \times 12$	600	$8 \times 9 \times 10$
Au	1000	$16 \times 16 \times 16$	800	$16 \times 16 \times 16$	900	$9 \times 10 \times 11$	500	$8 \times 9 \times 10$
AuCu ₃	1000	$16 \times 16 \times 16$	800	$16 \times 16 \times 16$				
AuCu	1000	$15 \times 15 \times 15$	800	$16 \times 16 \times 16$				
CuAu ₃	800	$15 \times 15 \times 15$	800	$16 \times 16 \times 16$				

Table 4.6: The equilibrium ground state properties of Au-Cu alloys using long-range dispersion corrected density functional theory (DFT), PBE+rVV10 and SCAN+rVV10. The inclusion of long-range dispersion in semilocal functionals does not significantly improve the results with respect to experiments. The rVV10 correction improves the lattice constants and bulk moduli for PBE while it slightly worsens for SCAN. However, it provides an insignificant correction to formation energies.

	Lattice constants (\AA)		Bulk moduli (GPa)		Formation Energy (eV/atom)	
	PBE+rVV10	SCAN+rVV10	PBE+rVV10	SCAN+rVV10	PBE+rVV10	SCAN+rVV10
Au	4.1328	4.0783	151.518	173.7363		
Cu	3.6155	3.5594	146.2200	162.3414		
AuCu ₃	3.7637	3.7054	148.8908	171.2157	-0.0454	-0.0940
AuCu (FCC)	3.9008	3.8405	150.4293	174.5577	-0.0450	-0.1005
AuCu (P4/mmm)	2.8258	2.7830	149.1046	171.7296	-0.0567	-0.1110
CuAu ₃	4.0240	3.9658	150.2475	172.1039	-0.0248	-0.0585
MAE	0.034	0.028	12.35	12.16		
MAPE (%)	0.90	0.78	7.30	7.88		

Table 4.7: The equilibrium ground state properties of Au-Cu alloys using the spin-orbit coupling (SOC) in DFT calculations; PBE-SOC:- PBE with SOC; SCAN-SOC:- SCAN with SOC. As expected, SOC affects the results more for Au than that of Cu. Unlike thermal correction and long-range dispersion, SOC provides a reasonable correction to formation energies obtained with semilocal DFT results. However, it does not significantly improve the results compared to experiments.

	Lattice constants (Å)		Bulk moduli (GPa)		Formation Energy (eV/atom)	
	PBE-SOC	SCAN-SOC	PBE-SOC	SCAN-SOC	PBE-SOC	SCAN-SOC
Au	4.1457	4.0791	144.3314	172.7929		
Cu	3.6345	3.5685	137.9568	157.9051		
AuCu ₃	3.7799	3.7111	141.0283	167.9038	-0.0524	-0.1026
AuCu (FCC)	3.9152	3.8438	143.1033	172.3101	-0.0554	-0.1128
AuCu (P4/mmm)	2.8364	2.7854	141.8966	169.5994	-0.0647	-0.1209
CuAu ₃	4.0374	3.9674	143.0877	170.6346	-0.0329	-0.0677
MAE	0.047	0.025	18.86	10.06		
MAPE (%)	1.25	0.69	11.32	6.47		

CHAPTER 5

FORMATION ENERGY PUZZLE IN INTERMETALLIC ALLOYS: RANDOM PHASE APPROXIMATION FAILS TO PREDICT ACCURATE FORMATION ENERGIES

5.1 Abstract

We performed density functional calculations to estimate the formation energies of intermetallic alloys. We used two semilocal approximations, the generalized gradient approximation (GGA) by Perdew-Burke-Ernzerhof (PBE) and the strongly constrained and appropriately normed (SCAN) meta-GGA. In addition, we utilized two nonlocal DFT functionals, the hybrid HSE06, and the state-of-the-art random phase approximation (RPA). The nonlocal functionals such as HSE06 and RPA yield accurate formation energies of binary alloys with completely-filled d-band metals, where semilocal functionals underperform. The accuracy at the nonlocal functionals is greatly reduced when a partially-filled d-band metal is present in an alloy, while PBE-GGA outperforms in these cases. We show that the accurate prediction of formation energies by any DFT method depends on its ability to predict the accurate electronic properties, e.g., valence d-band contribution to the density of states (DOS). The SCAN meta-GGA often corrects the PBE-DOS, however, it does not provide accurate formation energies compared to PBE. This is assumed to be due to the lack of proper error cancellation that should be expected due to the similar bulk nature of both alloys and their constituents, which may improve with the modification of meta-GGA ingredients. RPA yields too negative formation energies of alloys with partially-filled d-band metals. RPA results can be corrected by restoring the exchange-correlation kernel,

thereby improving the short-range electron-electron correlation in metallic densities.

©2020 American Physical Society

5.2 Introduction

Intermetallic alloys, composed of two or more d-band transition metals, are often interesting for applications, therefore, their application-governed aspects have been mostly explored. In most cases, alloys were classified with respect to various factors such as the radius ratio of two constituents, electronegativity, principle quantum number, ionicity, coordination number, etc. [255–258]. However, there is a scarcity of sufficient information about the chemical bonding and its relation with the equilibrium properties such as formation energy in both theory and the experiment [255]. Recently in 2014, Zhang *et.al.* [232], using DFT calculations [11, 14] for the copper-gold alloys, showed that the accurate prediction of formation energy accompanies an accurate prediction of the density of states. Here, we will generalize this result using a more diverse set of compounds.

Intermetallic alloys always have been critical tests for various approximations within density functional theory (DFT). The accurate prediction of basic equilibrium properties of intermetallic alloys and their bulk transition metal constituents with many popular DFT approximations is difficult. Semilocal approximations such as the local density approximation (LDA) [14] and various generalized gradient approximations (GGA) are unable to provide accurate formation energy (heat of formation, E_f) of weakly-bonded (WB) systems such as copper-gold alloys [84, 232–234]. Incorporating an amount of nonlocality by the kinetic energy density ($\tau(r)$), meta-GGAs slightly improve the equilibrium properties including formation energies of copper-gold alloys [84], but fail to improve beyond PBE [21] when dealing with the more strongly-bonded (SB) systems such as HfOs and PtSc [231]. Attempts at correcting the semilocal results with zero-point vibration energy, additive long-range van der Waals (vdW) interaction, and spin-orbit coupling couldn't improve

the result for copper-gold alloys [84].

In general, hybrid functionals within the generalized Kohn-Sham theory that mix the non-local exact exchange with DFT exchange do not provide accurate equilibrium properties of bulk transition metals [259]. However, surprisingly, the hybrid HSE06 [66, 67] shows some promise in the prediction of the lattice constants and formation energies of WB systems [232]. It couldn't provide a reasonable bulk modulus, which is a fundamental physical quantity describing the system in its nonequilibrium state with respect to the equilibrium one [84]. On the other hand, the random phase approximation (RPA) [74, 75, 236] within the adiabatic-connection fluctuation-dissipation theorem [169, 170] predicted excellent equilibrium properties including bulk moduli of the copper-gold alloys [84]. The accurate formation energy of WB systems by these methods may be due to the nonlocality present in them [84, 232]. On the contrary, we will later show that such nonlocality is not useful for SB systems; it improves the equilibrium volume but cannot correct the bulk moduli and formation energies.

Many of the earlier works focused mainly on the WB intermetallic alloys [84, 232–234], while a few others have included SB alloys [231, 260] using semilocal DFT approximations. In this work, we have explored a broad spectrum of binary intermetallic alloys from weakly- to strongly-bonded ones. The experimental formation energies of our test set range from 0.07 to 1.18 eV per atom. Most of the systems taken here are binary alloys that crystallize in the B2 (CsCl) phase. Table I presents the d-band metals with their electronic configurations. We have utilized one DFT approximation each from the different rungs of Perdew's Jacob ladder [190], except for LDA. The PBE-GGA (Perdew-Burke-Ernzerhof) [21], the strongly constrained and appropriately normed (SCAN) [39], the screened hybrid HSE06 (simply HSE by Heyd, Scuseria, and Ernzerhof) [66, 67], and RPA were used as the DFT approximations. In this assessment, we aim to present a broader picture regard-

Element	Sc	Cu	Zn	Y	Rh	Pd	Ag	Cd	Hf	Os	Pt	Au
Configuration	3d ¹ 4s ²	3d ¹⁰ 4s ¹	3d ¹⁰ 4s ²	4d ¹ 5s ²	4d ⁸ 5s ¹	4d ¹⁰	4d ¹⁰ 5s ¹	4d ¹⁰ 5s ²	5d ² 6s ²	5d ⁶ 6s ²	5d ⁹ 6s ¹	5d ¹⁰ 6s ¹

ing the performance of various DFT approximations on these intermetallic alloys, which is missing from earlier works.

We will later classify the alloys into three different classes purely based on the performance of different DFT functionals for predicting formation energies, as shown in Figures 5.1 and 5.2. We have a weakly-bonded (WB) region (Region I), where nonlocal HSE06 and RPA mostly perform better than semilocal PBE and SCAN. In the intermediate region (Region II), HSE06 and PBE work much better than others. Finally, there is the strongly-bonded (SB) region (Region III), where the nonlocal HSE06 and RPA severely fail to predict the accurate formation energy, while PBE-GGA outperforms them. Note that the classification performed here only refers to intermetallic alloys, and it is distinct from the classification adopted in Ref. [231] for alloys in general.

5.3 Computational details

All DFT calculations were carried out using a projector augmented wave (PAW) [206] method, as implemented in VASP [210] and GPAW [207–209]. We performed spin-polarized semilocal and HSE06 calculations using VASP, while we used GPAW to perform the RPA calculations. The semilocal calculations were initialized with the magnetic moments per site of 1.5 - 3.5 μ_B , which converged to the nonmagnetic ground-state during self-consistency. The total energy is converged with respect to plane-wave cutoff and k-mesh for all methods within 1-5 meV/atom. Besides, separate convergence tests for the EXX and correlation energies were performed for RPA. The detailed information about the plane-wave cutoff and Brillouin zone sampling are given in Supplementary Tables 5.4 and 5.5. Spin-unpolarized ground state PBE calculations were performed as inputs for the non-self-consistent RPA (for both EXX and correlation energies). We used a maximum cutoff of

350 eV to compute the response function. The correlation energies were computed as a function of the cutoff energy and extrapolated to infinity to get the RPA correlation energy as described in Refs. [85]. The gamma point ($\mathbf{q} = 0$) was skipped to avoid the possible divergent contribution and for smooth convergence with respect to k-mesh [76], as required for metallic systems. We used the recommended PBE pseudopotentials (PP) modified to include the kinetic energy density for VASP calculations [212], while 0.9.20000 data sets were utilized for GPAW calculations. The calculations include relativistic effects at the scalar level for each atom within the PAW PP.

Previously, it was showed that the spin-orbit coupling, zero-point vibrational energy, and the nonlocal vdW corrections have negligible effects on the formation energies of intermetallic alloys [84]. Therefore, we did not calculate those corrections in the present assessment. We have performed calculations for 7 volume points near the experimental equilibrium volume and fit the Birch-Murnaghan equation of state [243] to evaluate the equilibrium properties. We have used the structures from Ref. [261] and varied the lattice constants isotropically to generate structures with different volumes.

5.4 Results and Discussions

In this section, we discuss the results for ground-state equilibrium properties of various binary intermetallic alloys using DFT calculations. We present and discuss the equilibrium volumes and the bulk moduli in Supplementary Tables 5.6–5.9 separately. Here, we mainly focus on the performance of various DFT approximations in predicting formation energies. The formation energy is an important physical quantity in alloy theory as it governs the stability of that alloy. Suppose A_xB_{1-x} is a binary alloy with constituent metals A and B. Then, the formation energy per atom ΔE_f can be computed as

$$\Delta E_f(A_xB_{1-x}) = E(A_xB_{1-x}) - xE(A) - (1-x)E(B). \quad (5.4-1)$$

Table 5.1: Formation energy (eV) per atom of intermetallic alloys; the first column represents the alloys, while the second column shows the combination of the d-bands; CF is completely filled, PF is partially filled; All the compounds considered here crystallize in the B2 (CsCl) phase.

Alloys	Combination	PBE	SCAN	HSE06	RPA	Experiment
AgZn	4d(CF)-3d(CF)	-0.045	-0.017	-0.067	-0.080	-0.068 ± 0.002 [227]
AgCd	4d(CF)-4d(CF)	-0.057	-0.060	-0.083	-0.093	-0.093 ± 0.002 [227]
CuZn	3d(CF)-3d(CF)	-0.088	-0.100	-0.126	-0.110	-0.124 [227]
CuPd	3d(CF)-4d(CF)	-0.120	-0.115	-0.193	-0.168	-0.131 ± 0.008 [227]
AuCd	5d(CF)-4d(CF)	-0.169	-0.231	-0.196	-0.244	-0.196 [227]
CuY	3d(CF)-4d(PF)	-0.252	-0.295	-0.261	-0.354	-0.200 ± 0.002 [262, 263]
AuZn	5d(CF)-3d(CF)	-0.211	-0.260	-0.252	-0.290	-0.235 ± 0.043 [227]
ScAg	3d(PF)-4d(CF)	-0.282	-0.362	-0.288	-0.411	-0.272 ± 0.017 [263, 264]
AgY	4d(CF)-4d(PF)	-0.346	-0.417	-0.353	-0.467	-0.278 ± 0.033 [263, 264]
HfOs	5d(PF)-5d(PF)	-0.704	-0.754	-0.923	-0.667	-0.482 ± 0.052 [231, 265] ¹
AuSc	5d(CF)-3d(PF)	-0.812	-1.063	-0.854	-1.045	-0.789 ± 0.031 [263, 264]
RhY	4d(PF)-4d(PF)	-0.841	-0.939	-0.979	-0.943	-0.789 ± 0.035 [263, 266]
ScPd	3d(PF)-4d(CF)	-0.892	-0.992	-1.027	-1.176	-0.926 ± 0.023 [263, 267]
ScRh	3d(PF)-4d(PF)	-1.005	-1.140	-1.264	-1.172	-0.979 ± 0.016 [263, 267]
PtSc	5d(PF)-3d(PF)	-1.216	-1.455	-1.382	-1.440	-1.086 ± 0.056 [263, 267]
HfPt	5d(PF)-5d(PF)	-0.972	-1.195	-1.073	-1.058	-1.178 ± 0.068 [263, 268]

where, $E(A_xB_{1-x})$, $E(A)$, and $E(B)$ are the total bulk energies per atom of an alloy A_xB_{1-x} , metal A, and metal B respectively. x is the fractional weight of metal A in an alloy. A positive formation energy represents an instability, while the negative value depicts the stability of an alloy against its constituents.

We calculated the formation energies using various methods and tabulated the data in Table 5.1. In Table I, we compare the results for an alloy crystallized in the B2 (CsCl) phase with available experimental data. The values are tabulated by an increasing magnitude of experimental formation energies from top to bottom. Figure 5.1 illustrates the graphical representation of the values in Table 5.1. Based on the observation, we classify the results into three distinct categories (or regions) depending on the filling of d-band in metals, as shown in Figure 5.2. To understand the performance of functionals on formation energies, we plot the electronic density of states (DOS) of alloy and its constituents, because the

structural stability of an alloy is largely dependent on the density of states [255]. We show that an accurate prediction of formation energy should be accompanied by an accurate prediction of the DOS.

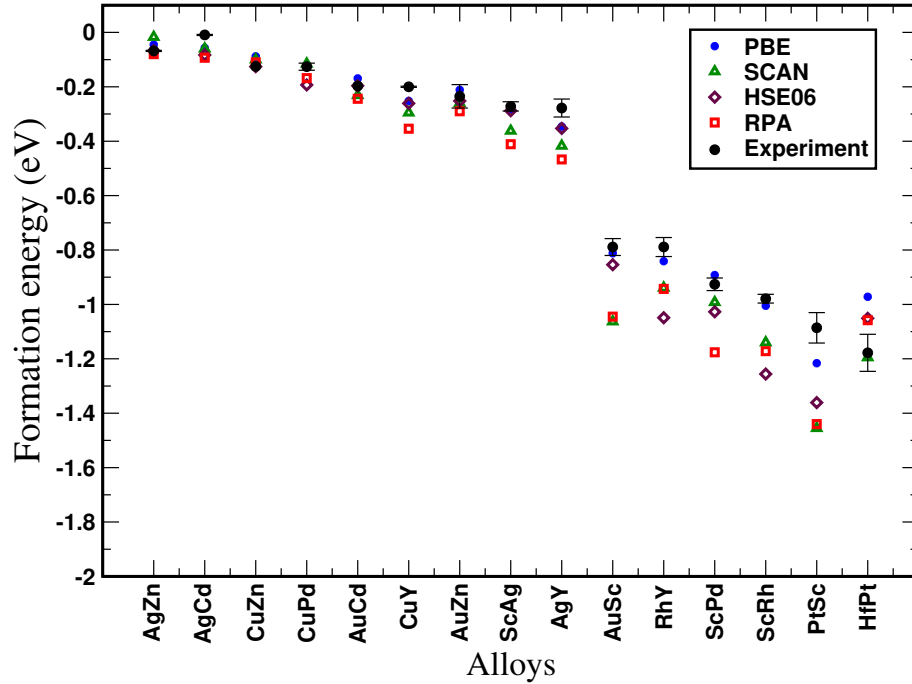
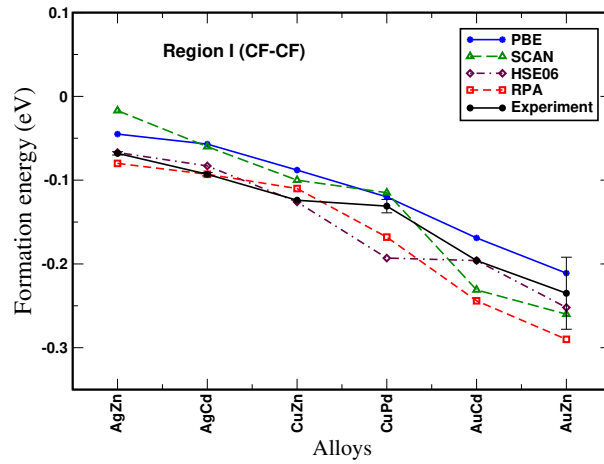


Figure 5.1: Computed formation energies compared with experimental values.

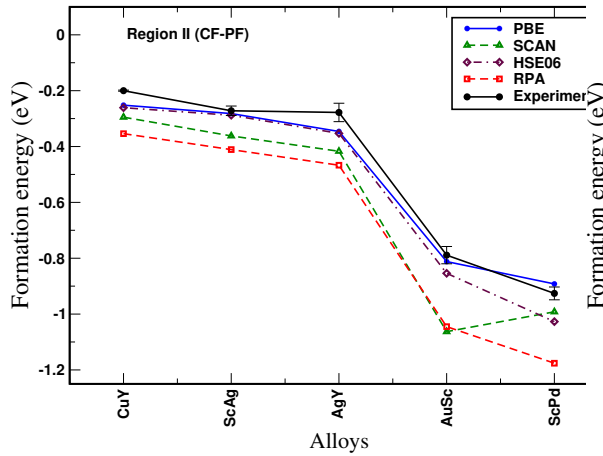
1. Completely-Filled / Completely-Filled (CF-CF)
2. Completely-Filled / Partially-Filled (CF-PF)
3. Partially-Filled / Partially-Filled (PF-PF)

5.4.1 CF-CF combination

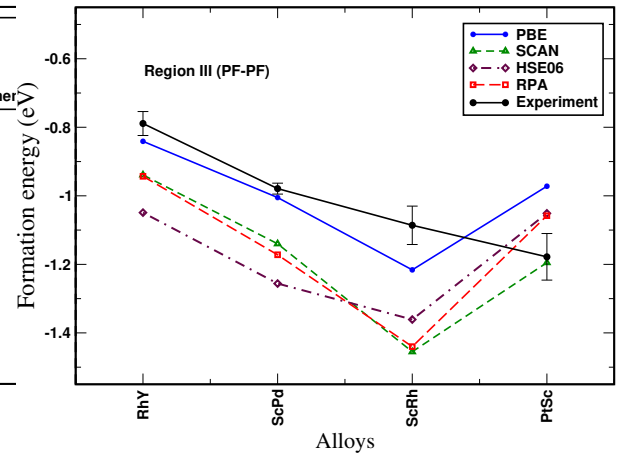
This set consists of intermetallic alloys with constituents bulk metals having completely-filled d bands such as AgZn, AgCd, CuZn, CuPd, AuCd, and AuZn (see Fig. 5.2a). These weakly-bonded alloys have lower experimental formation energies up to 200 meV, compared to other combinations. In this region, the PBE-GGA underestimates the formation energies as expected. The SCAN meta-GGA slightly improves upon PBE and yields mixed



(a) CF-CF combination



(b) CF-PF combination



(c) PF-PF combination

Figure 5.2: Formation energies with respect to three distinct classes.

results, i.e., underestimates the formation energies for systems AgZn, AgCd, CuZn, and CuPd, while overestimates them in the cases of AuCd and AuZn. In general, SCAN overestimates the experimental energies below CuPd with a formation energy larger than or equal to 130 meV. On the other hand, the hybrid HSE06 consistently predicts accurate formation energies compared to the experiment, and in agreement with the previous calculations on alloys of CF-CF combination [232]. Our results are also valid for structures other than the B2 phase, which is evident from Table 5.2 and Ref. [232]. This indicates that the phase of the crystal has an insignificant role in the performance of DFT approximations when predicting formation energies of intermetallic alloys. To describe the results, we investigate the electronic properties of the alloy and its constituent bulk metals.

We computed valence-state electronic partial density of states (PDOS) for metals having completely-filled (CF) d-bands and alloys of CF-CF combination and present them in Figures 5.3 and 5.4, respectively. The contribution from s- and p- bands near the Fermi level is negligible (not shown here) compared to that of d-band. Therefore, we only show the d-band contribution of the density of states (DOS) and compare it with the experimental PDOS of occupied states. Experimentally, one can obtain information about the valence d-band (or PDOS) from X-ray (XPS) or ultraviolet (UPS) photoemission spectra [269–280] (see section “Experimental data for valence d-band” in Supporting Information).

In Fig. 5.3, we compare the calculated d-band contribution to DOS (PDOS) with experimental d-band ranges extracted from photoemission spectra (Supplementary Table 5.10). We present the PDOS for completely-filled metals such as copper, zinc, palladium, silver, cadmium, and gold with their phase and valence d-band. The negligible density of states at the Fermi level indicates the complete filling of valence bands (3d in Cu and Zn, 4d in Ag and Cd, and 5d in Au). Besides, Zn and Cd have even lesser PDOS (more than two factors in magnitude than other completely-filled d-band metals) at the Fermi level due to the

filling of valence s-band as well. Copper has the 3d band centered around its binding energy (E_b) of 3.0–3.5 eV with a d-band width (or range) of ~ 3 eV [269, 270]. Furthermore, Zinc and Cadmium have similar PDOS with localized valence 3d and 4d bands respectively centered around the binding energies ~ 10 eV [270–272] and ~ 11 eV [273, 281] below the Fermi level with width ~ 1.5 – 2.0 eV. On the other hand, Pd, Ag, and Au have d-band ranges 0–5.5 eV (4d) [275, 276], 3.9–7.4 eV (4d) [271], and 2–8 eV (5d) [269, 272] below the Fermi level respectively. All DFT approximations agree with each other regarding the shape and width of the d-band in the PDOS plot. However, there is a discrepancy in the d-band center (E_b) among them. The PBE-GGA underestimates the binding energy (d-band center) of these metals by ~ 1 – 2 eV (maximum for Cd and Zn), whereas SCAN provides a negligible improvement of ~ 0 – 0.5 eV upon PBE. On the contrary, the hybrid HSE06 considerably improves on PBE and SCAN by increasing the binding energy (blue-shifted towards the experimental d-band range) and provides accurate results compared to experiments.

Figure 5.4 depicts the partial density of states of alloys AgZn (Fig. 5.4a), AgCd (Fig. 5.4b), CuZn (Fig. 5.4c), and AuZn (Fig. 5.4d). In AgZn, the binding energy of Ag’s 4d band increases by ~ 1 eV (onset shifts from 3.0 to 4.0 eV in PBE and SCAN, and 4.0 to 5.0 eV in HSE06) and the width also shrinks by ~ 1 eV compared to pure Ag’s 4d band. On the other hand, zinc’s 3d band is still localized around almost the same binding energy (small decrement though) as that of the pure Zn, with a negligible decrease in d-band width. These observations are consistent with the experimental results that the 4d band of Ag in AgZn decreases by 1 eV and the width shrinks by 0.7 eV with a negligible effect on the zinc’s 3d band compared to its pure constituents [271]. Similar results can be obtained for AgCd, CuZn, and AuZn. Ag’s 4d band in AgCd, Cu’s 3d band in CuZn, and Au’s 5d band in AuZn behave similarly to that of the Ag’s 4d band in AgZn. Also, Zn and Cd in these compounds behave likewise as that of Zn in AgZn. The sharp decrease in d-band widths of

Table 5.2: Formation energies (eV) per atom of alloys other than the B2 phase (CsCl, Pm-3m); CF is completely filled, PF is partially filled.

Alloys	Phase	combination	PBE	SCAN	HSE06	Expt
AuTi	CuTi (P4/nmm)	5d(CF)-3d(PF)	-0.442	-0.630	-0.430	-0.458 ± 0.015 [282]
ScRh ₃	AuCu ₃ (Pm-3m)	3d(PF)-4d(PF)	-0.610	-0.762	-0.770	-0.536 ± 0.015 [267]
YPd ₃	AuCu ₃ (Pm-3m)	4d(PF)-4d(CF)	-0.867	-0.890	-1.041	-0.819 ± 0.067 [266]
ScPt ₃	AuCu ₃ (Pm-3m)	3d(PF)-5d(PF)	-1.042	-1.263	-1.173	-0.980 ± 0.021 [283]

Cu, Ag, and Au in alloys can be attributed to the dilution (it increases the distance between two CF metal nearest neighbors which decreases its overlap with them, thereby giving localized and bound state) of these metals in alloys in presence of more localized 3d and 4d band of Zn and Cd respectively [270–273]. Also, the increase in binding energy in one of the metals and decrease in the binding energy in the other indicates some charge transfer between the constituents [270, 272]. Qualitatively, all DFT functionals PBE, SCAN, and HSE06 yield similar results in terms of the change in PDOS of alloys with respect to its constituents. However, only the nonlocal HSE06 provides an accurate binding energy in the case of both alloys and constituents, thereby predicting accurate formation energies. Also, the nonlocal RPA shows similar or better accuracy than that of semilocal functionals in predicting formation energies of CF-CF alloys. We will discuss the RPA results in detail later in a separate section “Failure of RPA and beyond RPA correction”.

5.4.2 CF-PF combination

In this section, we discuss the results for alloys with completely-filled / partially-filled (CF-PF) d-band combinations such as CuY, ScAg, AgY, AuSc, and ScPd having a B2 phase, shown as in Fig. 5.2b. We also present a few other alloys (AuTi and YPd₃) with a different structure than B2 in Table 5.2. The formation energies predicted by PBE-GGA agree well with the experiment, whereas the hybrid HSE06 concurs with PBE for lower formation energies (200–500 meV), while differs significantly from PBE and experimental results in the case of higher formation energies (e.g., YPd₃ and ScPd). On the contrary, SCAN seriously overestimates the formation energies in this region with a decrease in its

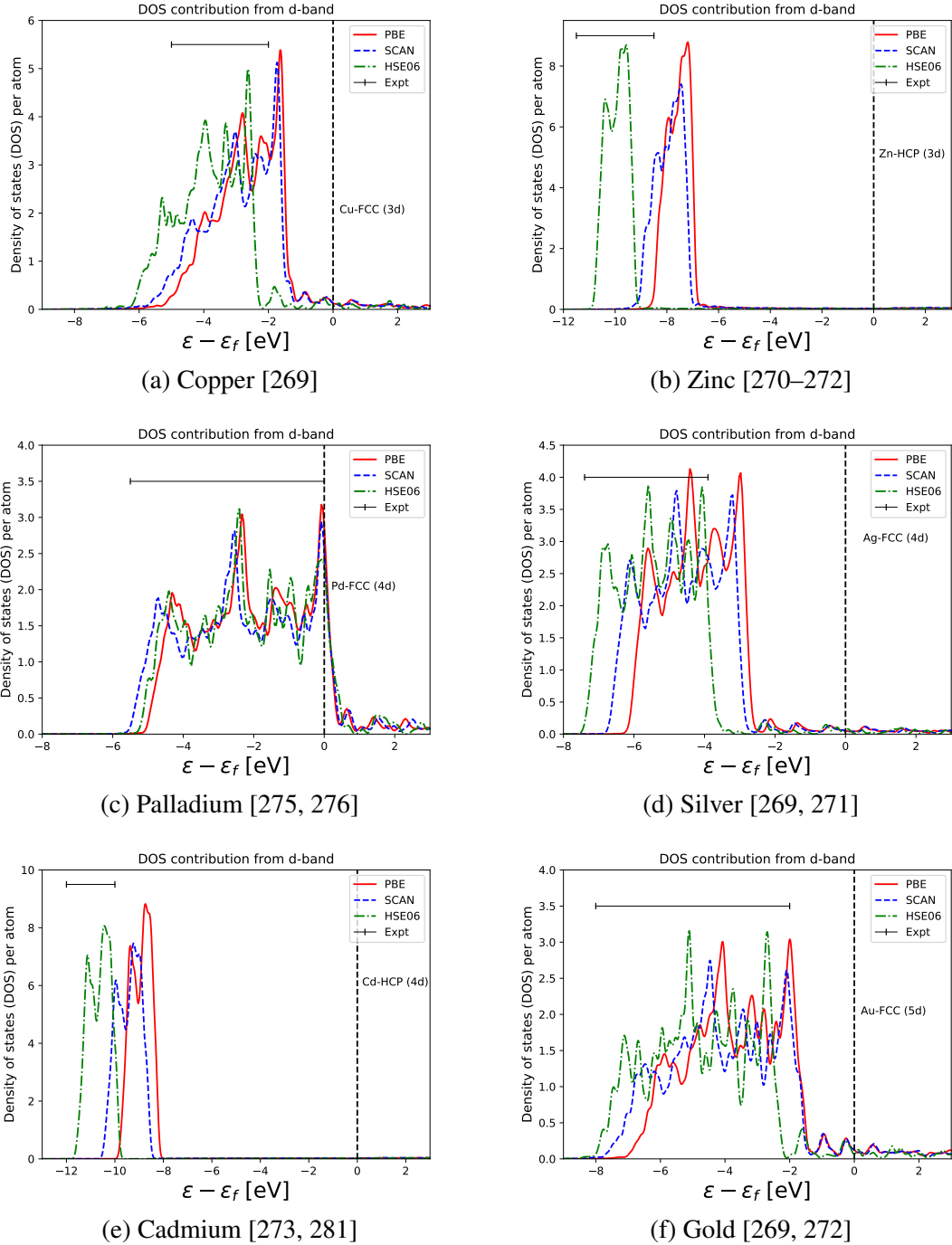


Figure 5.3: The estimated valence d-band density of states with completely-filled d configuration compared with valence d-band ranges extracted from experimental X-ray photoemission spectra or ultraviolet photoemission spectra (denoted by horizontal solid line). References are given in sub-captions. ϵ_f is the Fermi-level.

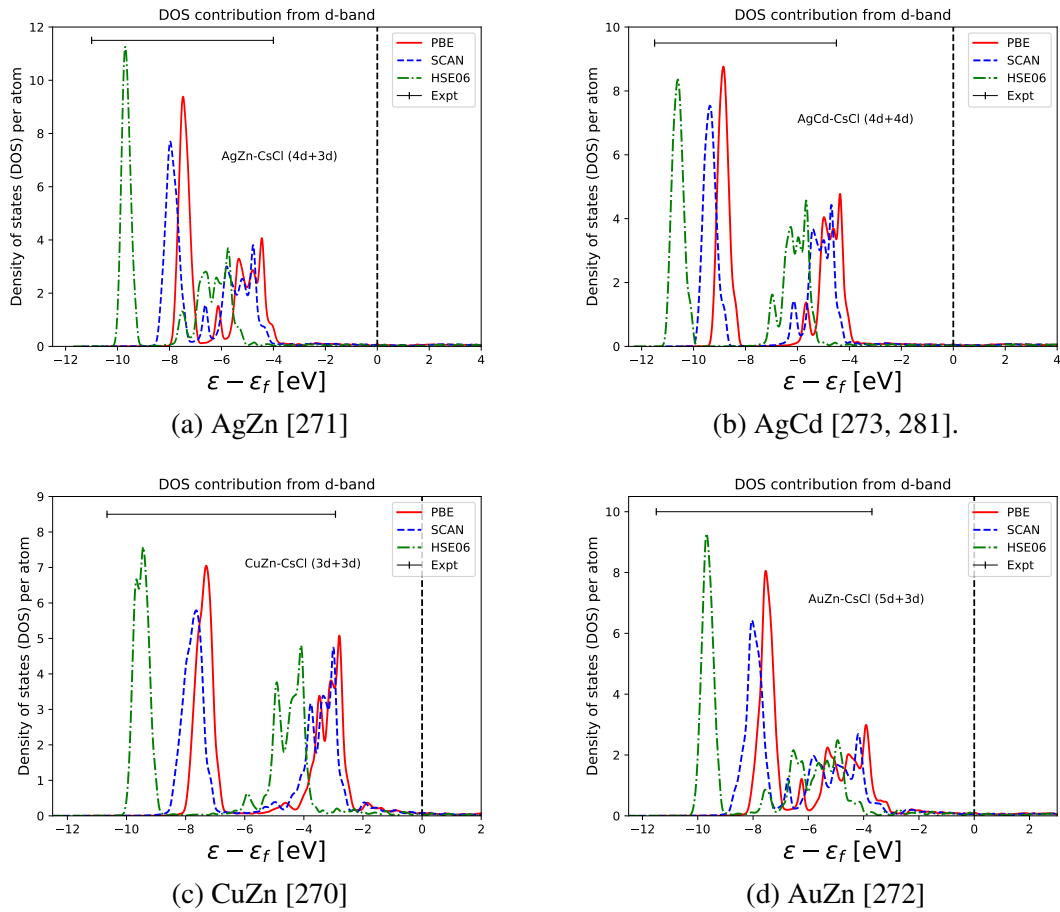


Figure 5.4: The estimated valence d-band density of states of alloys with metals having completely-filled/completely-filled d-band configuration compared with valence d-band ranges extracted from experimental X-ray photoemission spectra or ultraviolet photoemission spectra (denoted by horizontal solid line). References are given in sub-captions. ϵ_f is the Fermi-level.

deviation for alloys with increasing formation energy (YPd₃ and ScPd). The nonlocal RPA consistently overestimates the formation energies of alloys with results closer to SCAN at the best-case scenario.

Partial density of states (PDOS) of valence d-band of partially-filled (PF) metals scandium (3d), yttrium (4d), rhodium (4d), hafnium (5d), osmium (5d), and platinum (5d) are shown in Figure 5.5. Unlike the completely-filled metals, there is a significantly large density of states at the Fermi level. Experimentally, both scandium's 3d and yttrium's 4d band is localized near the Fermi level (~ 0.2 eV below for Sc) with the d-band widths of ~ 1.5 eV and 2.0 eV respectively [274, 279]. Also, rhodium's 4d band is concentrated at ~ 1.3 – 1.5 eV below the Fermi-level and has a d-band range of ~ 4.5 – 5.0 eV [277, 284]. The 5d bands of both Hf and Pt have similar localization as that of the 4d band of Rh with centroids around ~ 0.9 eV and ~ 1.6 eV respectively, with d-band widths of ~ 4 eV and ~ 8 eV [276, 278, 284] (Pt's 5d-band has two peaks, and it is the first peak). Similarly, osmium's 5d band has a peak at ~ 3.0 eV and a d-band width of ~ 8.0 eV [284]. For these alloys, the PDOS at the Fermi-level decreases as $\text{PBE} > \text{SCAN} > \text{HSE06}$, except for platinum. Also, the d-band range is blue-shifted away from the experimental valence d-band range in the order of $\text{PBE} < \text{SCAN} < \text{HSE06}$ with PBE being the closest. However, such a shift is noticeable only in the Rh's 4d and Os's 5d bands. Unfortunately, it is difficult to pinpoint the peak or a d-band centroid of DFT calculated PDOS for Rh's 4d, Os's 5d, and Pt's 5d bands, therefore, we could not compare it directly with the experimental values.

Figure 5.6 shows PDOS results for alloys AgSc, ScPd, and YPd₃. In both ScPd and ScAg, the large density of states at the Fermi-level mainly consists of the partially-filled 3d band of scandium, and its tail is slightly stretched towards larger binding energies compared to its pure counterpart (Sc in ScAg is more stretched than Sc in ScPd) [274]. Our PDOS calculated by all DFT functionals qualitatively agree with this experimental observation

(see Figures 5.6a and 5.6b). On the other hand, the completely-filled d-band of metals Ag and Pd should be red-shifted towards a lower binding energy with a decrease in its width due to similar reasons of charge-transfer and dilution as in the case of CF-CF alloys. It is the part where our DFT calculated PDOS differs from the experiment. As expected, PBE underestimates the d-band centroid of the Ag's and Pd's 4d bands, while SCAN slightly blue-shifts them. HSE06 also raises the binding energy, however, the shifted 4d band of Ag agrees with the experiment, but is overestimated in the case of Pd's 4d band. This could be the reason that the formation energy predicted by HSE06 is accurate for ScAg, but overestimates the ScPd formation energy. The calculated electronic PDOS of YPd₃ has nonseparable 4d bands of yttrium and palladium, similar to the experimental photoemission spectrum [275]. Nevertheless, it has different centroids and d-band ranges for different DFT methods. Similar to ScPd, the inaccuracy of HSE06 in the prediction of formation energy of YPd₃ is due to an incorrect prediction of the electronic PDOS of an alloy. Conversely, PBE and SCAN provide a reliable estimate of formation energies for both ScPd (Table 5.1), and YPd₃ (Table 5.2), because these functionals predict the correct electronic properties of both alloys and the bulk elements simultaneously.

5.4.3 PF-PF combination

Previously, we have observed that the inclusion of partially-filled d-band metals in alloys diminish the accuracy of the nonlocal density functionals, while the PBE-GGA consistently outperforms them. The SCAN meta-GGA indeed improves the PBE calculated electronic properties of many alloys and elemental bulks, but does not possess similar accuracy in formation energies as that of PBE. Here, we explore the alloys with both partially-filled d-band metals such as HfOs, RhY, ScRh, PtSc, HfPt, ScRh₃, and ScPt₃. In the PF-PF combination of alloys, both nonlocal functionals, HSE06 and RPA, severely overestimate the formation energies. On the other hand, semilocal functionals perform well with PBE

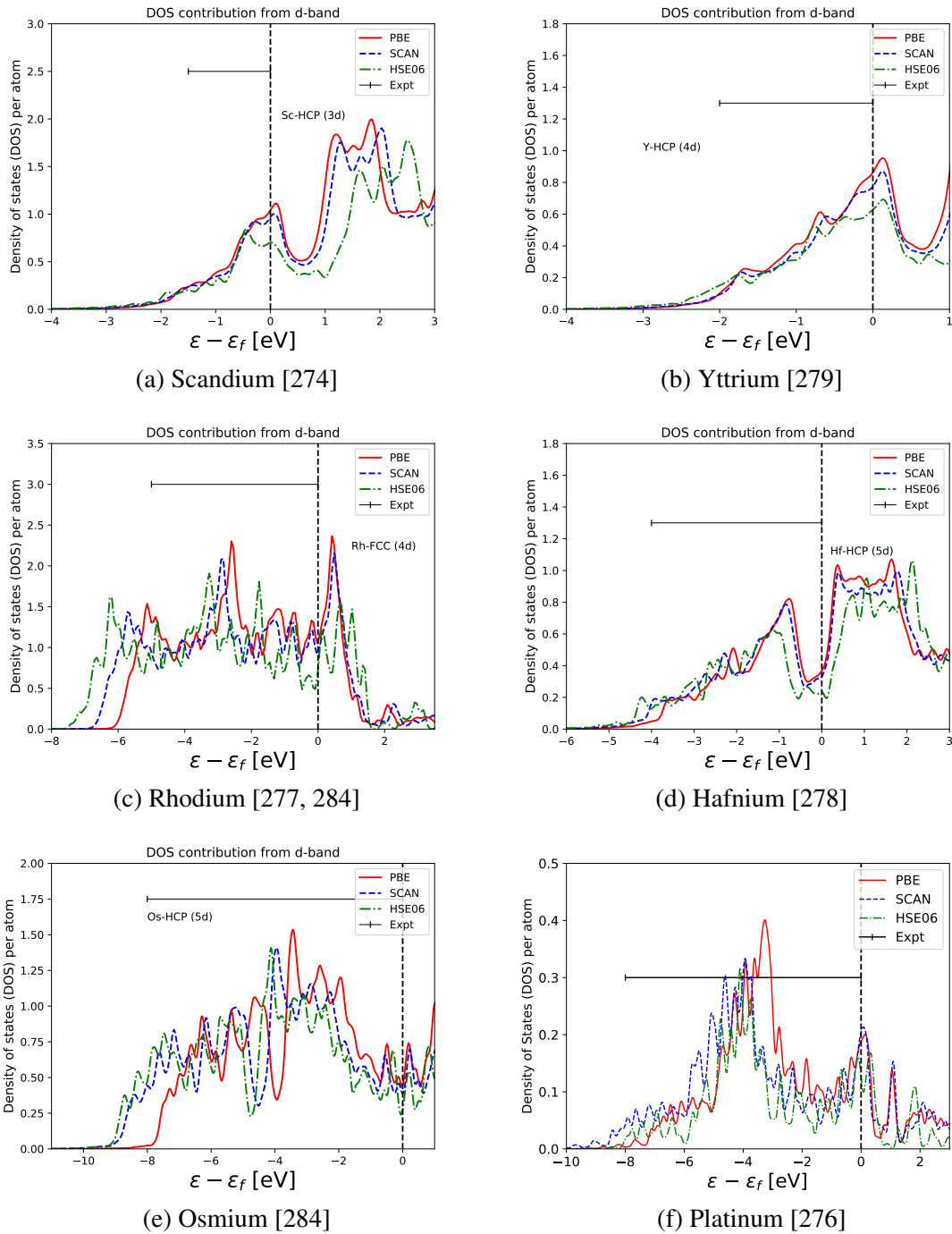
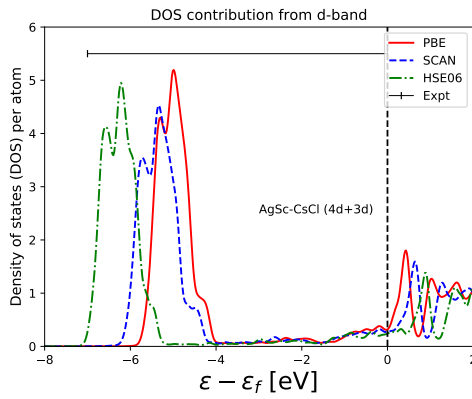
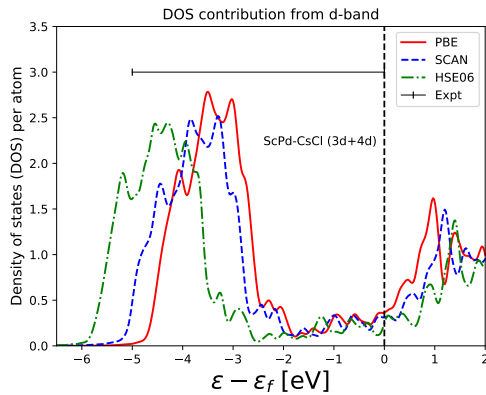


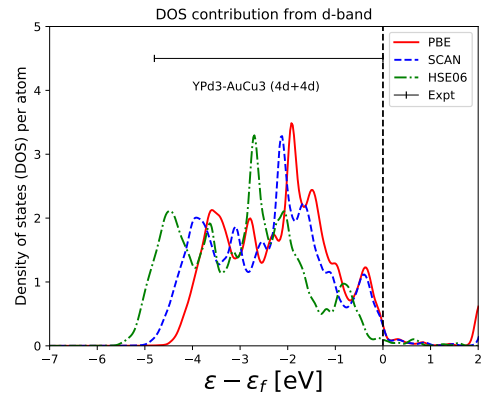
Figure 5.5: The estimated valence d-band density of states with partially-filled d configuration compared with valence d-band ranges extracted from experimental X-ray photoemission spectra or ultraviolet photoemission spectra (denoted by horizontal solid line). References are given in sub-captions. ϵ_f is the Fermi-level.



(a) AgSc [274]



(b) ScPd [274]



(c) YPd₃ [275, 285]

Figure 5.6: The estimated valence d-band density of states of alloys with metals having completely-filled / partially-filled d-band configuration compared with valence d-band ranges extracted from experimental X-ray photoemission spectra or ultraviolet photoemission spectra (denoted by horizontal solid line). References are given in sub-captions. ϵ_f is the Fermi-level.

performing much better than the SCAN except for HfPt. Our DFT results show a significant error (overestimation) in the case of HfOs, even for PBE. We suspect that there are some uncertainties in the experiment, as a few traces of $\text{Hf}_{54}\text{Os}_{17}$ and unreacted Os are also present in the sample [265].

In Figure 5.7, we compare the PDOS of HfPt (Fig. 5.7a) and ScRh₃ (Fig. 5.7b) obtained using various methods. Unfortunately, we could not obtain experimental results for HfPt for comparison. But, the XPS valence d-band spectra of ScRh₃ is available [280]. It has a d-band that ranges from the Fermi-level to around ~ 5 eV below the Fermi-level [280], and it has a shape like that of YPd₃. As expected, HSE06 PDOS is blue-shifted away from the experimental range, while PBE and SCAN yield similar PDOS compared to the experiment. However, SCAN overestimates the experimental Rh's 4d band width by ~ 1 eV, while the overestimation is only about ~ 0.5 eV in the case of PBE. This result leads to accurate formation energy for the PBE, while SCAN overshoots the experimental value by ~ 230 meV.

Though all DFT calculated d-band widths of hafnium and platinum metals are close to each other and agree with the experiment, we expect that only the SCAN calculated PDOS of HfPt should be close to that of an experimental result if available, as its formation energies are close to the experimental value.

5.5 Failure of RPA and beyond RPA correction

Earlier, we have compared the PBE and SCAN results with HSE06, and established a connection between an accurate prediction of formation energies of alloys and their electronic properties. Here, we discuss the results obtained using the nonlocal random phase approximation (RPA). The RPA calculated formation energies of binary alloys in the B2 phase are tabulated in Table 5.1 and compared with other semilocal and hybrid functionals

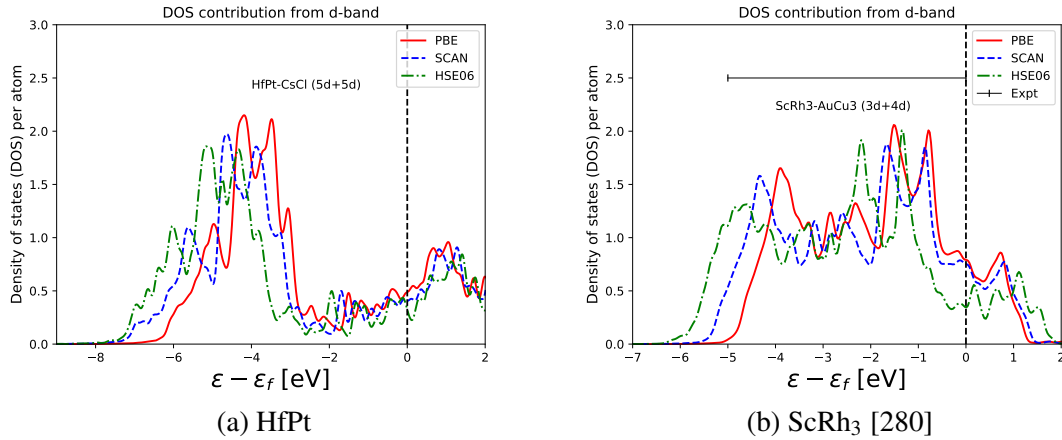


Figure 5.7: The estimated valence d-band density of states of alloys with metals having partially-filled/partially-filled d-band configuration compared with valence d-band ranges extracted from experimental X-ray photoemission spectra or ultraviolet photoemission spectra (denoted by horizontal solid line). References are given in sub-captions. ϵ_f is the Fermi-level.

as presented in Figure 5.2. RPA provides accurate formation energies of CF-CF alloys with a lower energy ($\sim < 130$ meV) such as for AgZn, AgCd, and CuZn. This is consistent with the previous results for copper-gold alloys, which have formation energies less than 100 meV [84]. Other CF-CF alloys such as CuPd, AuCd, and AuZn have deviation ranges from 35–50 meV, which is significant as compared to experimental values. Furthermore, errors in RPA enormously increase when an alloy consists of partially-filled d-band metals. In general, it overestimates the experimental formation energies up to the maximum of ~ 350 meV for PtSc.

Though RPA works reasonably well in predicting the cohesive energies of transition metal bulk comparable to PBE [83] with a mean absolute error ~ 0.25 eV, there is a notable difference in the formation energies of alloys. In contrast to formation energy, the cohesive energy of transition metal alloys is a more difficult test for DFT functionals as it involves isolated transition metal atoms [286]. Therefore, more error cancellation is expected for formation energy as both alloys and constituents have the same phase. Here, we have computed the RPA formation energies non-self-consistently using the ground-

Table 5.3: Formation energies (eV) from kernel-corrected RPA for PtSc and HfOs. Improving the short-range correlation in RPA can improve the formation energies of intermetallics where RPA fails severely.

	RPA	rALDA	rAPBE	Experiment
HfOs	-0.667	-0.642	-0.612	-0.482 ± 0.052 [231, 265] ²
PtSc	-1.440	-1.317	-1.257	-1.086 ± 0.056 [263, 267]

state PBE eigenstates and eigenvalues as reference. Therefore, we do not have RPA calculated partial density of states to compare with experiment. In RPA, the EXX energy ($E_{total} - E_c^{RPA}$) is one-electron self-interaction free, but the correlation energy E_c^{RPA} suffers from self-correlation error due to the absence of the dynamical exchange-correlation kernel ($f_{xc}(q, \omega)$) [171, 172]. RPA provides a good description of the long-range electron-electron correlation required to describe van der Waals interactions [85, 86, 92, 182]. However, the short-range electron-electron correlation is not properly described with bare RPA ($f_{xc} \rightarrow 0$) which yields too negative correlation energies (by ~ 0.4 eV/electron) for the uniform electron gas in the metallic range densities [119, 287]. Restoring the non-local exchange-correlation kernel can improve the repulsive short-range correlation, thereby giving an exact result [79, 114, 115, 119, 287]. We suspect that the too-negative formation energies (compared to experiment) by RPA for alloys with partially-filled d-band metals may be related to too-low correlation energy due to an imperfect description of the repulsive short-range electron-electron correlation. Consequently, we computed the formation energies of PtSc and HfOs using the renormalized adiabatic LDA (rALDA) [79, 114] and renormalized adiabatic PBE (rAPBE) [115] kernels and tabulated them in Table 5.3 (see Supplementary Tables 5.4 and 5.5 for input parameters of calculations).

The rALDA kernel is obtained by using a (local) truncation of ALDA kernel for wavevector $q > 2k_F$, where $k_F = (3\pi^2 * density)^{1/3}$ is the Fermi wavevector [79, 114]. Also, rAPBE is similar to rALDA, except it also includes a PBE-like gradient correction [115]. A large overestimation of formation energy from RPA can be reduced a little using rALDA. Fur-

ther, rAPBE improves the RPA formation energies by a significant amount of ~ 200 meV in the case of PtSc, closer to the experimental value. More corrections in the RPA formation energies can be expected when using a more exact uniform electron gas kernel, such as modified-CP07 (MCP07) [287].

5.6 Conclusions

We performed DFT calculations to compute the ground-state equilibrium properties of intermetallic alloys. Many of earlier studies [84, 232] argued that the nonlocality is essential for accurate formation energies. However, those studies covered only a narrow range of weakly-bonded compounds having completely-filled d-band metals. Our assessment includes a broad range of binary alloys, which also include partially-filled d-band metals. We found that the nonlocality is not always useful for formation energies. Instead, a PBE-like exchange-correlation can yield accurate results compared to the experiment, especially for strongly-bonded intermetallic alloys having partially-filled d-band metals.

Based on the observations, we classified intermetallic alloys into three categories based on their d-band filling combinations, e.g., completely-filled / completely-filled (CF-CF), completely-filled / partially-filled (CF-PF), and partially-filled / partially-filled (PF-PF). The formation energies usually increase in the order of $\text{CF-CF} < \text{CF-PF} < \text{PF-PF}$. As previously discussed, the nonlocal functionals HSE06 and RPA give accurate formation energies of CF-CF alloys, while PBE-GGA yields better results in the case of CF-PF and PF-PF alloys. Therefore, we suggest using a more PBE-like exchange-correlation for strongly-bonded alloys having a partially-filled d-band metal, while the nonlocality is necessary to capture the energy differences in the case of weakly-bonded alloys with completely-filled d-band transition metals. The difficulties to incorporate a delicate balance between the two such extreme cases make it arduous for any DFT approximation to provide the accurate equilibrium properties of a wide range of alloys. Nevertheless, a meta-GGA could be a

natural trade-off, as it contains some nonlocality due to the kinetic energy density, while it still maintains its status as a semilocal approximation.

Besides, we also established a one-to-one correspondence between formation energies and electronic properties by estimating the d-band contribution to valence density of states (DOS). In other words, the functional which predicts accurate DOS of alloys and metals simultaneously also agrees with the experimental formation energies. The PBE-GGA underestimates the d-band range of completely-filled transition metals and their alloys while it provides electronic DOS often similar or better than HSE06 in the case of partially-filled d-band metals and their alloys. Contrarily, SCAN often improves on PBE calculated d-band centroid and hence the d-band range of many alloys and bulk metals, but it does not share a similar success as that of PBE. It may be due to a lack of required error cancellation in the SCAN meta-GGA that should be expected due to the same phase of the alloy and its constituents.

The state-of-the-art RPA, which can describe different bonding situations often much better than semilocal and hybrid functionals, severely fails for the formation energies of intermetallic alloys with partially-filled d-band metals. It significantly overestimates the formation energies. This may be related to the too-negative correlation energies within the metallic densities due to the incomplete description of repulsive short-range electron-electron correlations. Restoring the nonlocal exchange-correlation kernel rAPBE improves the formation energy of PtSc by ~ 200 meV, which is substantial.

5.7 Acknowledgements

N.K.N. and A.R. acknowledge support by the National Science Foundation under Grant No. DMR-1553022. Computational support was provided by Temple University's HPC resources and thus was supported in part by the National Science Foundation through major

research instrumentation grant number 1625061 and by the US Army Research Laboratory under contract number W911NF-16-2-0189. The work of S.A. was supported by the U.S. Department of Energy, Office of Sciences, Office of Basic Energy Sciences as part of the Computational Chemical Sciences Program under Award No. DE-SC0018331. The work of B.N. was supported as part of the Center of Complex Materials from First Principles (CCM), an Energy Frontier Research Center funded by the U.S. Department of Energy (DOE), Office of Science, Basic Energy Sciences (BES), under Award No. DE-SC0012575.

SUPPORTING INFORMATION

Table 5.4: Converged parameters for elemental bulk calculations. The kernel-corrected or beyond RPA calculations were performed at RPA Ecut and a fixed K-mesh of 16x16x16. Also, the response function is computed using only one cutoff of 300 eV without extrapolation.

Elements	HSE06		EXX		RPA	
	Ecut (eV)	K-mesh	Ecut (eV)	K-mesh	Ecut (eV)	K-mesh
Sc	400	13x13x13	700	16x16x16	600	18x18x18
Cu	400	12x12x12	1000	16x16x16	800	16x16x16
Zn	400	15x15x15	800	18x18x18	800	18x18x18
Y	400	15x15x15	700	10x10x10	500	18x18x18
Rh	400	13x13x13	700	16x16x16	600	18x18x18
Pd	400	13x13x13	700	19x19x19	800	23x23x23
Ag	350	12x12x12	600	16x16x16	600	16x16x16
Cd	400	13x13x13	700	18x18x18	500	21x21x21
Hf	400	13x13x13	700	16x16x16	600	19x19x19
Os	400	15x15x15	700	19x19x19	600	20x20x20
Pt	400	14x14x14	800	18x18x18	600	20x20x20
Au	350	14x14x14	1000	15x15x15	800	16x16x16
Ti	400	13x13x13				

Equilibrium volume

In this section, we present the comparison between estimated and experimental equilibrium volumes for both elemental bulk constituents and alloys in Tables S3 and S4 respectively. As expected, PBE overestimated the equilibrium volume in most cases with excellent results for 3d and partially-filled 5d transition metals within -0.2 to 3.0 %, while the results deviate more with the experiments for 4d and completely-filled 5d elements up to 6 %. Contrary to PBE, SCAN provides accurate results for completely-filled 4d and 5d elements with an error of less than one percent. HSE06 hybrid provides more improvement keeping the trend similar to PBE, while the RPA further improves on it. For alloys, SCAN provides notable correction to PBE results, except for CuZn and HfPt where one can observe that the error is propagated from the discrepancies of their elemental bulk results: Cu (-3.8 %), Zn (-7.8 %), Hf (-4.0 %), and Pt (-4.0 %). Once again, RPA delivers accurate results for

Table 5.5: Converged parameters for alloys. The kernel-corrected or beyond RPA calculations were performed at RPA Ecut and a fixed K-mesh of 16x16x16. Also, the response function is computed using only one cutoff of 300 eV without extrapolation.

Alloys	HSE06		EXX		RPA	
	Ecut (eV)	K-mesh	Ecut (eV)	K-mesh	Ecut (eV)	K-mesh
AgZn	450	14x14x14	800	17x17x17	700	20x20x20
AgCd	450	14x14x14	800	16x16x16	800	18x18x18
CuZn	450	14x14x14	1000	20x20x20	800	19x19x19
CuPd	450	14x14x14	900	16x16x16	800	18x18x18
AuCd	450	15x15x15	800	18x18x18	700	18x18x18
CuY	450	14x14x14	900	18x18x18	700	18x18x18
AuZn	450	15x15x15	900	16x16x16	700	18x18x18
ScAg	450	14x14x14	700	18x18x18	700	18x18x18
AgY	450	14x14x14	800	19x19x19	700	18x18x18
HfOs	450	14x14x14	700	16x16x16	600	16x16x16
AuSc	450	15x15x15	900	18x18x18	700	19x19x19
RhY	450	15x15x15	700	16x16x16	600	18x18x18
ScPd	450	16x16x16	700	21x21x21	500	18x18x18
ScRh	450	14x14x14	700	16x16x16	500	18x18x18
PtSc	450	17x17x17	800	17x17x17	800	15x15x15
HfPt	450	14x14x14	700	18x18x18	600	18x18x18
AuTi	400	11x11x11				
ScRh3	400	12x12x12				
YPd3	400	14x14x14				
ScPt3	400	12x12x12				

these alloys similar to their bulk constituents mostly within two percent error compared to experiment.

We calculated the mean absolute error (MAE) and mean absolute percentage error (MAPE) for a better understanding of performances of various functionals predicting equilibrium volumes of the system considered in the present study. As expected, we can observe that the error decreases from semilocal DFT functionals to nonlocal functionals in both types of systems. The MAE for elemental bulk systems is in the order of RPA < HSE06 < PBE < SCAN, while MAPE shows a trend of RPA < HSE06 < SCAN < PBE. On the other hand, the SCAN functional performs better than HSE06 for alloy systems with MAPE in the order of RPA < SCAN < HSE06 < PBE.

Table 5.6: Equilibrium volumes for constituent elemental bulk transition metals (\AA^3).

Element	PBE	% Error	SCAN	% Error	HSE06	% Error	RPA	% Error	Experiment [261]
Sc	49.420	0.1	49.944	1.1	50.655	2.6	49.390	0.02	49.38
Cu	12.004	1.6	11.361	-3.8	12.021	1.8	11.958	1.3	11.81
Zn	30.392	-0.2	28.072	-7.8	30.406	-0.1	29.620	-2.7	30.44
Y	65.489	-0.8	67.409	2.1	67.200	1.8	64.872	-1.7	66.02
Rh	14.050	2.2	13.515	-1.7	13.54	-1.5	13.930	1.3	13.75
Pd	15.341	4.2	14.766	0.2	15.018	2.0	14.650	-0.5	14.73
Ag	17.827	4.5	17.043	-0.1	17.798	4.3	17.090	0.2	17.06
Cd	45.886	6.3	43.075	-0.2	44.631	3.4	42.410	-1.8	43.17
Hf	44.896	0.3	42.971	-4.0	44.671	-0.2	45.440	1.5	44.76
Os	28.538	2.0	27.341	-2.3	27.661	-1.1	28.060	0.3	27.98
Pt	15.610	3.0	14.537	-4.0	15.248	0.7	15.200	0.3	15.15
Au	17.961	5.8	17.103	0.7	17.595	3.7	17.868	5.2	16.98
MAE		0.62		0.69		0.53		0.4	
MAPE (%)		2.6		2.3		1.8		1.4	

Table 5.7: Equilibrium volumes for alloys (\AA^3); Alloys are presented with an increasing experimental formation energies (see Table V); % Error means percentage error.

Alloys	PBE	% Error	SCAN	% Error	HSE06	% Error	RPA	% Error	Experiment [261]
AgZn	32.346	2.6	30.428	-3.4	32.019	1.6	31.242	-0.9	31.519
AgCd	39.005	4.0	37.053	-1.2	38.405	2.4	36.886	-1.6	37.494
CuZn	26.172	1.1	24.493	-5.4	26.119	0.9	25.707	-0.7	25.882
CuPd	27.449	3.6	26.257	-0.9	27.153	2.5	26.946	1.7	26.490
AuCd	39.059	6.3	37.109	1.0	38.176	3.9	37.591	2.4	36.727
CuY	42.264	0.5	41.254	-1.9	42.692	1.6	41.663	-0.9	42.035
AuZn	32.397	4.1	30.432	-2.2	31.856	2.4	31.847	2.4	31.107
ScAg	40.703	2.5	39.335	-1.0	40.537	2.1	39.574	-0.4	39.722
AgY	48.381	2.8	46.930	-0.3	48.398	2.9	47.002	-0.1	47.046
HfOs	34.504	1.5	33.229	-2.2	33.795	-0.5	34.570	1.7	33.981
AuSc	39.525	3.3	38.014	-0.7	39.118	2.2	38.943	1.8	38.273
RhY	40.449	2.3	39.432	-0.3	39.591	0.1	40.254	1.8	39.547
ScPd	36.501	3.4	35.450	0.5	36.073	2.2	35.989	2.0	35.288
ScRh	33.775	2.7	32.850	-0.1	33.096	0.6	33.703	2.5	32.891
PtSc	36.109	3.5	34.722	-0.5	35.634	2.1	35.866	2.8	34.902
HfPt	36.846	-3.1	35.130	-7.6	36.244	-4.6	36.637	-3.6	38.011
MAE		1.06		0.62		0.74		0.59	
MAPE (%)		2.97		1.81		2.05		1.70	

Table 5.8: Bulk moduli for the constituent elemental bulk transition metals (GPa); Experimental bulk moduli are taken from Ref [259].

Element	PBE	% Error	SCAN	% Error	HSE06	% Error	RPA	% Error	Experiment [259]
Sc	53.6	-3.5	55.7	0.2	56.1	0.9	64.0	15.1	55.6
Cu	137.9	-1.7	156.2	11.3	125.8	-10.3	144.7	3.1	140.3
Zn	73.4	5.3	99.4	42.6	74.8	7.3	84.2	20.8	69.7
Y	39.9	-4.3	41.2	-1.3	40.3	-3.4	45.7	9.6	41.7
Rh	254.8	-11.8	289.5	0.3	288.2	-0.2	311.4	7.9	288.7
Pd	164.4	-15.9	206.5	5.7	171.9	-12.0	231.6	18.5	195.4
Ag	91.0	-12.3	110.5	6.5	85.8	-17.3	115.3	11.1	103.8
Cd	43.2	-19.7	59.3	10.2	52.4	-2.6	62.9	16.9	53.8
Hf	108.3	-1.3	115.1	4.9	114.2	4.1	114.1	4.0	109.7
Os	403.8	-4.9	459.6	8.2	460.7	8.5	433.2	2.0	424.6
Pt	247.3	-13.0	331.5	16.6	267.4	-5.9	298.8	5.1	284.2
Au	138.9	-20.5	166.5	-4.8	144.6	-17.3	176.7	1.1	174.8
MAE (GPa)		16.1		13.9		12.7		11.7	
MAPE (%)		9.5		9.4		7.5		9.6	

Bulk Moduli

Bulk moduli are more difficult to predict than equilibrium volumes, as they require an accurate prediction of the equation of state. We computed bulk moduli by fitting the Birch-Murnaghan equation-of-state to the energy-volume data and compared them with available experimental results in Tables S5 and S6. The PBE-GGA provides reasonably accurate bulk moduli of 3d metals, while the errors are enormous for 4d and 5d elements. On the other hand, SCAN meta-GGA significantly improves upon PBE, and it is more accurate in most cases except copper, zinc, and platinum. The error for SCAN is a maximum at about 42 % in zinc, and it is consistent with the error in its equilibrium volume. Both HSE06 and RPA have a mixed performance on bulk moduli with lower overall mean absolute error (MAE) and mean absolute percentage error (MAPE) than semilocal results. We also compared computed bulk moduli of intermetallic alloys with available experimental results. Unlike constituent elemental bulk metals, all DFT approximations studied here predict reasonable bulk moduli. For example, the estimated bulk modulus of CuZn alloy agrees with the experimental value, though, the bulk moduli of zinc significantly deviates from the experiment.

Table 5.9: Bulk moduli for the alloys (GPa); The alloys are presented in order of increasing experimental formation energies (see Table V).

BM	PBE	SCAN	HSE06	RPA	Experiment
AgZn	90.5	112.3	92.3	107.8	
AgCd	73.8	90.6	76.9	95.2	
CuZn	112.8	141.3	110.1	118.4	116 [288]
CuPd	151.6	176.8	147.8	169.3	
AuCd	90.5	110.5	98.8	116.6	100 [289, 290]
CuY	69.3	74.6	67.0	77.1	70.1 [291]
AuZn	115.6	143.6	122.6	137	131 [292]
ScAg	79.7	94.4	83.4	99.3	
AgY	66.1	75.1	66.6	79.7	70.1 [291]
HfOs	224.9	250.0	245.5	235.4	
AuSc	103.3	123.1	112.5	125.2	
RhY	108.8	121.4	117.1	121.8	
ScPd	110.7	124.8	116.5	127.6	
ScRh	138.3	154.9	152.0	154.6	
PtSc	136.4	157.7	147.5	155.1	
HfPt	179.2	209.1	192.0	191.5	

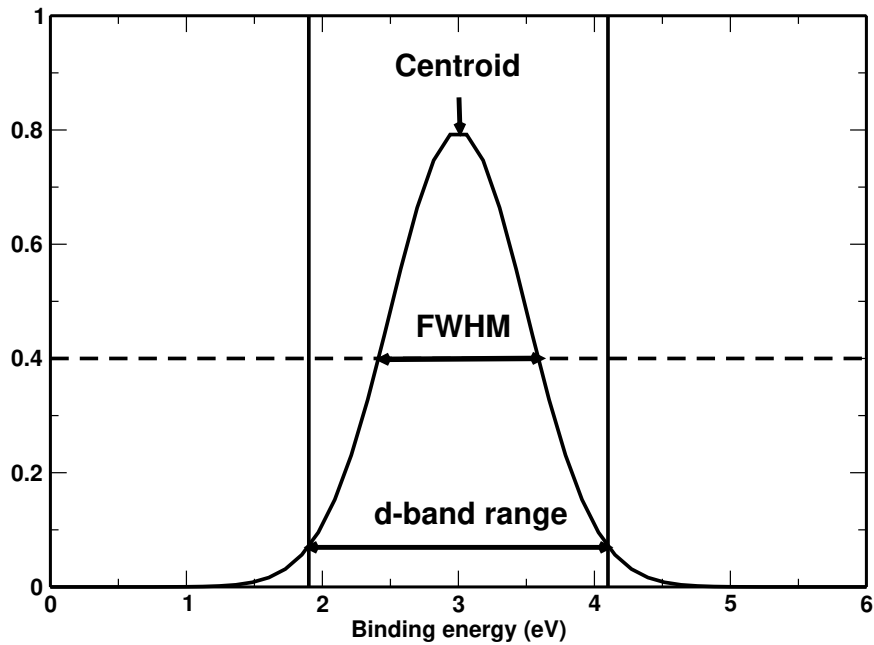


Figure 5.8: Schematic diagram for estimating the d-band range and FWHM from X-ray or ultraviolet photoemission spectra.

Experimental data for valence d-band

Both X-ray and ultraviolet photoemission spectra work via the photoelectric effect. When an atom absorbs a photon of energy $h\nu$, an electron in a core or valence state with binding energy E_b is ejected with kinetic energy E_k as

$$E_k = h\nu - E_b - \phi, \quad (5.7-2)$$

where, ϕ is the work function and E_b ($E - E_{Fermi}$) is the energy of the photoelectron with respect to the Fermi energy of the system. In principle, the photoemission spectrum can give DOS. However, one should be cautious with an exact comparison of theoretical DOS with experimental photoemission spectra (for exact features including satellite excitations and tail at high binding energy). The factors that play a crucial role in the difference between theoretical and experimental DOS could be the influence of matrix elements that govern the excitation of the photoelectrons and the photon energy itself used for the excitation process [274]. Other factors may be the instrumental resolution and electron-electron scattering processes. Here, we are not interested in the exact features of the photoemission spectra. Instead, the information about the valence d-band centroid (or binding energy) and range (or width) of the system is sufficient, as the previously-mentioned factors have an insignificant effect on it [275, 276, 279, 280]. Note that the term “d-band range” is different than the full width at half maximum (FWHM) used in several references. The d-band range is measured after removing the extra asymptotic tail, while FWHM is measured at half of the maximum intensity as shown in Supplementary Figure 5.8. We have extracted the d-band centroid and the d-band range of both alloys and its constituents from experimental photoemission spectra, and tabulated them in Supplementary Table 5.10.

Table 5.10: The d-band centroid and d-band ranges with respect to Fermi-level (or below Fermi-level) extracted from experimental photoemission spectra; unit eV.

Systems	d-band	d-band centroid	d-band range
Cu	3d	3.0–3.5	2.0–5.0 [269], 1.5–4.5 [270]
Zn	3d	10	8.5–11.5 [270–272]
Pd	4d	1	0–5.5 [275, 276]
Ag	4d		3.9–7.4 [269, 271]
Cd	4d	11	9.0–13.0 [273, 281]
Au	5d		2.0–8.0 [269, 272]
Sc	3d	0.2	0.0–1.5 [274]
Y	4d		0–2.0 [279]
Rh	4d	1.3–1.5	0–5.0 [277, 284]
Hf	5d	0.9	0–4.0 [278]
Os	5d	3	0–8.0 [284]
Pt	5d	1.6	0–8.0 [276]
AgZn	4d-3d	–	4.0–11.0 [271]
AgCd	4d-4d	–	4.5–11.5 [273, 281]
CuZn	3d-3d	–	2.9–10.7 [270]
AuZn	5d-3d	–	3.7–11.5 [272]
AgSc	4d-3d	–	0–7.0 [274]
ScPd	3d-4d	–	0–5.0 [274]
YPd ₃	4d-4d	–	0–4.8 [275, 285]
ScRh ₃	3d-4d	–	0–5.0 [280]

CHAPTER 6

UNDERSTANDING PLASMON DISPERSION IN NEARLY-FREE-ELECTRON METALS: THE RELEVANCE OF EXACT CONSTRAINTS FOR NOVEL EXCHANGE-CORRELATION KERNELS WITHIN TIME-DEPENDENT DENSITY FUNCTIONAL THEORY

6.1 Abstract

Small-wavevector excitations in Coulomb-interacting systems can be decomposed into the high-energy collective longitudinal plasmon and the low-energy single-electron excitations. At the critical wavevector and corresponding frequency where the plasmon branch merges with the single-electron excitation region, the collective energy of the plasmon dissipates into single electron-hole excitations. The jellium model provides a reasonable description of the electron-energy-loss spectrum (EELS) of metals close to the free-electron limit. The random phase approximation (RPA) is exact in the high-density limit but can capture the plasmonic dispersion reasonably even for densities with $r_s > 1$. RPA and all beyond-RPA methods investigated here, result in a wrong infinite plasmon lifetime for a wavevector smaller than the critical one where the plasmon dispersion curve runs into particle-hole excitations. Exchange-correlation kernel corrections to RPA modify the plasmon dispersion curve. There is however a large difference in the construction and form of the kernels investigated earlier. Our current work introduces recent model exchange-only and exchange-correlation kernels and discusses the relevance of some exact constraints in the construction of the kernel. We show that, because the plasmon dispersion samples a range of wavevec-

tors smaller than the range sampled by the correlation energy, different kernels can make a strong difference for the correlation energy and a weak difference for the plasmon dispersion. This work completes our understanding about the plasmon dispersion in realistic metals, such as Cs, where a negative plasmon dispersion has been observed. We find only positive plasmon dispersion in jellium at the density for Cs.

©2020 American Physical Society

6.2 Introduction

Due to its computational feasibility and relatively high accuracy, approximate Kohn-Sham density-functional theory (KS-DFT) simulations are the basis of present-day first-principles computational materials science. Particle-particle interactions can require treatment beyond semilocal KS-DFT [94]. Experimental applications heavily rely on understanding and guiding electron-electron interaction. A relevant example of electron-electron interaction is scattering resulting in electron energy loss. Experimentally the electron loss spectrum can be realized by electron energy loss spectroscopy or inelastic scattering [293, 294].

Excited states can be accurately characterized by expensive Greens function techniques. By virtue of the Runge-Gross theorem [71], DFT can be extended to time-dependent processes. Time-dependent density-functional theory (TDDFT) is becoming an attractive alternative to many-body perturbation theory and can offer, in principle, an unbiased and independent framework complementary to experimental observations, enabling the interpretation of specific experimental observations and predictions of new materials with targeted properties [295].

Plasmon excitations are collective oscillations of electrons in the absence of an external electric field, that incorporate Coulomb interaction between electrons [296, 297]. Due to the electron-electron interactions, plasmon excitations establish a high barrier when testing

ab initio theories. When the external perturbation is weak, linear response TDDFT [95] is a useful tool to describe optical excitation energies. In TDDFT the electron energy loss is quantified by the imaginary part of χ , the spatially nonlocal and dynamic density-density response function. The poles of the interacting density-density response function contain information about the optical excitation energies. The same density-density response function can deliver further information about the plasmons for a range of wavevectors.

Plasmon dispersion in nearly-free-electron alkali metals has attracted a great interest among experimentalists and theorists. The negative dispersion in the volume plasmon of the low-density alkali metals such as Rb and Cs has triggered a debate about the origin of the anomaly observed by most theoretical approximations within TDDFT and Fermi liquid theories [298]. A strong failure of approximations based on TDDFT with a static exchange-correlation kernel is the lack of a damping mechanism which results in an infinite lifetime of plasmons for a region of wavevectors smaller than the critical wavevector that separates plasmonic and particle-hole excitations [298, 299]. Such a damping mechanism is provided by time-dependent current-density functional theory (TDCDFT) [300–302] or by a frequency-dependence in the exchange-correlation kernel [287, 301]. The plasmon broadening from the frequency dependence is a very small fraction of the plasmon frequency, and the frequency dependence of the kernel has a very small effect on the plasmon dispersion [287]. The negative plasmon dispersion in low-density alkali metals can be attributed to correlation effects or band structure [303–306]. There are pros and contras for both explanations in the literature [305, 306]. In heavier alkali metals such as Cs, electron transition to the near-Fermi-level *d* bands can occur [303, 304]. The transition energy of these electrons is comparable to the plasmon energy, potentially causing a negative dispersion. Additional corrections to the interacting response function or dielectric function can originate in a weak lattice potential and core polarization effects [298].

The random phase approximation (RPA) is a method based on time-dependent Hartree theory that is often used to obtain the ground-state correlation energy of bulk and two-dimensional materials [75, 76, 78, 84, 92]. Although RPA relies on the linear response TDDFT framework, its excitation energies are inaccurate because of the overestimated short-range exchange-correlation effects [169]. The exact exchange-correlation kernel f_{xc} that would provide these effects is a functional derivative of the exchange-correlation potential. RPA is often interpreted within DFT to have roots in the adiabatic connection fluctuation dissipation theorem [170]. The bare RPA $f_{xc} = 0$ without a band structure does not yield a negative dispersion in heavy alkali metals [303]. Theoretical predictions from the late 80's in polycrystalline metals showed negative dispersion for Cs beyond RPA when the band structure was included [298]. Some investigations of the role of correlation in the plasmon dispersion discuss kernels, but most tests consider the exchange-correlation effects at the level of adiabatic local density functional approximation (ALDA) only. The work of Tatarczyk et al. [307] steps beyond this limitation to some extent by considering some more model kernels based either on the uniform electron gas paradigm or on other constraints.

In our current work we aim to fill the gap in analyzing the plasmon dispersion with recent exchange-correlation kernels, beyond the early ones developed in the 90's. Our work aims to go beyond a simple analysis of exchange-correlation effects with kernels. The major goal here is to give an *a priori* numerical analysis why kernels by themselves (without the band structure effects) can not predict negative dispersion in low density alkali metals. In this work, we rely on the jellium model. The dimensionless density parameters (r_s) for the jellium model corresponding to different metals are taken from Ref. [217]. We demonstrate that the exact constraints can lead to kernels that correctly predict a positive plasmon dispersion in jellium.

6.3 Methodology: Exchange-correlation kernels within linear response TDDFT

Nonempirical construction of density functionals has allowed widespread and successful applications of these approximations for the ground state [40]. Various exact constraints such as the uniform electron gas limit, Lieb-Oxford bound or the one-electron limit are known for the ground state [308]. According to linear response theory the interacting and noninteracting density-density response functions are coupled by the Dyson equation:

$$\chi_\lambda(q, \omega) = \chi_0(q, \omega) + \chi_0(q, \omega) \left(\lambda v_c(q) + f_{xc}^\lambda(q, \omega) \right) \chi_\lambda(q, \omega), \quad (6.3-1)$$

$\chi_\lambda(q, \omega)$ and $\chi_0(q, \omega)$ are the interacting and noninteracting response functions, respectively, $v_c(q) = \frac{4\pi\lambda}{q^2}$ and $f_{xc}^\lambda(q, \omega)$ are the Coulomb and exchange-correlation kernels. λ is the coupling constant that provides the adiabatic connection between a noninteracting Kohn-Sham ($\lambda = 0$) and the interacting real system ($\lambda = 1$) response. When Eq. 7.2-1 is applied to the uniform electron gas, $\chi_0(q, \omega)$ becomes the Lindhard function with complex frequencies [110], a basic input to our current research. In the adiabatic approximation, the exact kernel is a second functional derivative of the ground state exchange-correlation energy. In practice the exact kernel is unknown but can be modeled by satisfying exact physical constraints. Kernels are related to the “local field factors” as $G(q, \omega) = \frac{f_{xc}(q, \omega)}{-v_c(q)}$.

Many real systems have densities close to the paradigm uniform electron gas, as in alkali metals. The uniform electron gas is therefore a simple model system with physical relevance. All exchange-correlation kernels in this work model the uniform electron gas with known limiting behavior at $q \rightarrow 0$ and $q \rightarrow \infty$. The simplest approximation is known as the adiabatic local density approximation (ALDA) kernel for $\lambda = 1$ [309]:

$$f_{xc}^{ALDA}(q \rightarrow 0, \omega = 0) = -\frac{4\pi A}{k_F^2} \quad (6.3-2)$$

with $A = \frac{1}{4} - \frac{k_F^2}{4\pi} \frac{d^2(n\varepsilon_c)}{dn^2}$, where $k_F = (3\pi^2 n)^{1/3}$ is the Fermi wavevector and ε_c the correlation energy per particle of the uniform electron gas. $A = \frac{1}{4}$ belongs to the exchange-only ALDA, while the density-dependent term in A gives the correlation beyond the high-density limit.

The real-space representation of ALDA is a delta function which indicates the spatial locality of this kernel. ALDA gives reasonable accuracy for low-frequency, long-wavelength excitations, but is not the right choice for a general correction to RPA [309]. The ALDA kernel was applied to the ground state correlation energy of the uniform electron gas but makes an error of ~ 0.5 eV [119]. This error is the same in magnitude but of opposite sign to the error that RPA makes for the same system.

The ALDA kernel can be made nonlocal, by applying a cutoff that makes the exchange-correlation kernel cancel the Hartree kernel for $q > k_{cut}$. The cutoff is introduced by the renormalized ALDA (rALDA) expression [114]

$$f_{xc}^{rALDA}(n, q) = -[\theta(k_{cut} - q) \frac{4\pi}{k_{cut}^2} + \theta(q - k_{cut}) \frac{4\pi}{q^2}] \quad (6.3-3)$$

with the cutoff wavevector $k_{cut} = \frac{k_F}{\sqrt{A}}$. By construction the rALDA_{xc} kernel keeps the correct $q \rightarrow 0$ limit of ALDA, but improves the wrong $q \rightarrow \infty$ behavior of ALDA_{xc}. For inhomogeneous systems, more ingredients like the density gradient or the kinetic energy density give more flexibility for kernels, as for ground state density functional approximations. The kinetic energy density is one of the ingredients of the nonlocal energy optimized (NEO) exchange-only kernel [117].

The NEO kernel improves the ground state correlation energy and structural properties of real systems beyond RPA [117]. The NEO kernel is designed to satisfy further physical constraints beyond both ALDA or rALDA, and has the form

$$f_x^{NEO} = -\frac{4\pi}{2q^2} [1 - e^{-\beta q^2/k_F^2}] \quad (6.3-4)$$

where $\beta = \frac{1}{4\tilde{c}(1-z^2)}$. The one-electron limit is reached when the ingredient $z = \frac{\tau^w}{\tau}$ equals 1, where τ^w is the one-electron kinetic energy density [310] and τ the positive kinetic energy density constructed from the Kohn-Sham orbitals. In the uniform electron gas, z is zero. When $q \rightarrow 0$, the NEO kernel is properly independent of q for the uniform electron gas. The parameter \tilde{c} has a key relevance to the current work. In the construction of NEO, \tilde{c} is designed to give a correction to the RPA correlation energy in the high-density limit. In other words, the standard $\tilde{c} = 0.264$ parameter in NEO provides a unique fit to the exact second-order correlation energy for the spin-unpolarized electron gas. The “second-order exchange” contribution to the second-order correlation energy of the uniform gas is the correction to direct RPA from wavefunction anti-symmetry that survives in the high-density limit. It can be evaluated from explicit expressions given by von Barth and Hedin for RPA [154] and by Langreth and Perdew [169] beyond RPA.

β can be chosen to satisfy another constraint relevant to the long-wavelength ($q \rightarrow 0$) limit. This choice is also made in the ALDA, rALDA, and in the CP07 dynamic exchange-correlation kernel constructed by Constantin and Pitarke [113]. The compressibility sum rule, [311], as

$$f_{xc}(n; q \rightarrow 0, \omega = 0) = \frac{d^2}{dn^2} [n\epsilon_{xc}(n)], \quad (6.3-5)$$

is an important requirement for frequency-dependent exchange-correlation kernels. Satisfying the compressibility sum rule, β becomes

$$\beta = \frac{1}{4\tilde{c}} = -\frac{2k_F^2}{4\pi} \frac{d^2}{dn^2} [n\epsilon_{xc}(n)] = 2A \quad (6.3-6)$$

or $\tilde{c} = 0.5$ in the high-density limit.

Thus the energy optimized value of $\tilde{c} = 0.264$ in the high-density limit is different from the value $\tilde{c} = 0.5$ that yields the correct small- q kernel in the high-density limit. In the next section we will extensively discuss the impact of these physical constraints on the plasmon dispersion and provide a novel insight about the role of correlation effects. It will turn out that the difference between the ALDA and NEO kernels is important for the correlation energy, but not very important for the plasmon dispersion.

To set the scale of the problem, we plot in Fig. 6.1 three kernels as functions of wavevector q : the ALDA_{xc} kernel (exact at small q), the NEO _{xc} kernel with $\tilde{c} = 0.264$ (which we will argue later is more correct than ALDA_{xc} at larger q), and minus the Hartree kernel ($-4\pi/q^2$). Clearly, in the wavevector region $0 < q/k_F < 1$ that shapes the plasmon dispersion, the Hartree kernel (the only one present in RPA) dominates over the _{xc} kernel. This dominant effect of the Hartree kernel explains the overall good performance of RPA for plasmon dispersion. For wavevectors $q/k_F > 1$, which are important for the correlation energy, the _{xc} kernels have a larger effect. An even better _{xc} kernel might interpolate between ALDA_{xc} at small q and NEO at larger q .

6.4 Plasmon dispersion with spatially nonlocal exchange-correlation kernels in nearly-free-electron metals

The alkali metals Na and K are nearly-free-electron (NFE) systems and therefore realizations of the uniform electron gas. Correlation effects in alkali metals can be strong enough, especially for low electron densities, to impact electronic excitations. The high-resolution electron energy loss experiments indicate that the plasmon dispersion in heavy

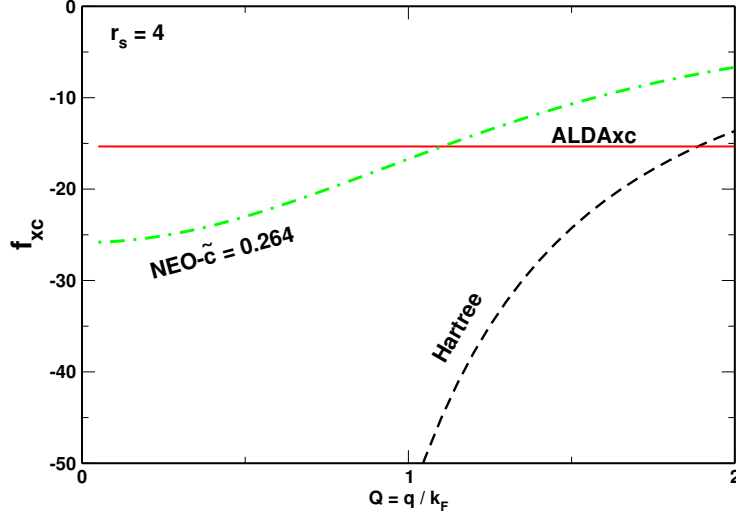


Figure 6.1: The Hartree kernel, ALDAxc kernel, and standard NEO xc kernel with $\tilde{c} = 0.264$ vs $Q = q/k_F$ for the uniform electron gas at $r_s = (\frac{3}{4\pi n})^{1/3} = 4$. For ease of comparison, it is actually minus the Hartree kernel ($-4\pi/q^2$) that is plotted here.

alkali metals such as Rb and Cs becomes negative, i.e., the plasmon frequency decreases with increasing wavevector q [298]. Since all the above experiments and calculations were performed for periodic crystals, it is difficult to decouple correlation and band structure effects [312] in the dispersion of the plasmon excitations.

Further calculations by Ku and Eguiluz in K crystal [304] indicate the relevance of band structure versus correlation and demonstrate that the exchange-correlation effects beyond RPA at the ALDA level have only a minor role in the dispersion of plasmons. A similar observation was made by Quong and Eguiluz [313] for Na crystal. Although crystal periodicity is important when modeling realistic conditions, the jellium model can offer an important way to separate the impact of many-body correlations and band structure. Within our work, we want to provide an additional theoretical and numerical insight only about the many-body correlation effects and explain why in general no beyond-RPA approximation for jellium can predict the correct plasmon dispersion and lifetime for Cs. The justification of our results is based only on exact physical constraints imposed on the construction of beyond-RPA approximations. By using the jellium model for alkali metals, we can build

upon the conclusion that ALDA gives a minor improvement beyond RPA for the plasmon dispersion. With the nonlocal exchange-correlation kernels developed since the later 90's, we can make further conclusions about how these recent approximations compare to ALDA and RPA in terms of correlation effects.

We can make two groups of assessed approximations. The first group includes exchange-only and exchange-correlation kernels based on the ALDA approximations. ALDA_x and ALDA_{xc} are both local kernels but differ in correlation contribution. rALDA_x and rALDA_{xc} are nonlocal. The second group consists of NEO exchange-only kernels [117] with the \tilde{c} parameter constructed by satisfying different physical constraints. The default version of the NEO kernel yields the exact correction to the RPA correlation energy of jellium in the high-density limit:

$$e_c^{2X} = \frac{3}{8\pi^3} \int_0^\infty dK K^2 \tilde{G}_x(K) \int_0^\infty dW \{2b(K, W)\}^2, \quad (6.4-7)$$

where $\tilde{G}_x(K)$ refers to the kernel, according to the correspondence between kernels and local-field factors. $K = \frac{q}{2k_F}$ is a dimensionless wavevector, and $W = \frac{\Omega}{2k_F^2}$ is a dimensionless frequency. The explicit expression for the second-order exchange energy e_c^{2X} comes from Langreth and Perdew [170] beyond RPA and uses the RPA correlation energy for the uniform electron gas given by von Barth and Hedin [154]. The \tilde{c} parameter that corresponds to the second-order correlation energy was found to be 0.264.

Alternatively, in the long-wavelength limit we can use the compressibility sum rule formulated as $\frac{d^2}{dn^2} [n\epsilon_{xc}(n)]$ to determine “ \tilde{c} ”. Then the \tilde{c} parameter of NEO can be estimated from the compressibility sum rule of the ALDA_{xc} expression. This fitting delivers a different $\tilde{c} = (0.43 - 0.47)$ at metallic densities considered here. While formally the NEO approximation remains an exchange-only kernel, this kind of fitting brings long-wavelength exchange-correlation effects into our NEO kernel [113].

Clearly “ \tilde{c} ” controls the correlation or screening within the NEO approximation starting from $\tilde{c} \rightarrow \infty$ in RPA. The impact of “ \tilde{c} ” as a screening parameter on ground state correlation energies was established by Bates et al in 2016 [117]. Changing “ \tilde{c} ” from its default 0.264 value was shown to yield different correlation energies in the uniform electron gas at $r_s = 4$.

The exchange-only NEO kernel can be explicitly turned into an exchange-correlation approach by replacing “ \tilde{c} ” by an electron-density-dependent parameter. This approach was tested for jellium slab correlation energies at moderate densities, and resulted in improved integrated correlation energy [116]. For a given density, the density dependence can make “ \tilde{c} ” significantly smaller than its default value. In our analysis we also investigate the effect of a low “ \tilde{c} ” parameter on the plasmon dispersion of various NFE metals. For testing purposes we choose $\tilde{c} = 0.0037$. Notice that this choice of \tilde{c} represents an unphysically low density according to Eq. (13) of Ref. [116].

At first, we discuss the plasmon dispersion up to the wavevector region where plasmons decay into single-particle excitations. We consider all the exchange-correlation kernels described above. Within the static approximation for the kernel $f_{xc}(q)$, the plasmon frequency $\omega_p(q)$ is found by solving the equation $\varepsilon(q, \omega) = 1 - (v_c(q) + f_{xc}(q)) \chi_0(q, \omega) = 0$, for $\lambda = 1$ [307], and the solutions are undamped outside the particle-hole continuum, i.e., for $q < q_c$ where $\frac{\omega_p(q_c)}{\varepsilon_F} = 2 \left(\frac{q_c}{k_F} \right) + \left(\frac{q_c}{k_F} \right)^2$. For the r_s values considered here, $q_c/k_F \approx 1 \ll k_{cut}/k_F \approx 2$, where k_{cut} is the cutoff wavevector for a kernel. Thus rALDA and ALDA kernels will yield the same plasmon dispersion.

Al is a metal with rather high density, and RPA becomes relatively exact in the high-density limit [313]. Here, we model Al by jellium with $r_s = 2.07$. The small wavevector

behavior is demonstrated by the correct plasmon energy known from an EELS experiment [314]. All ALDA and rALDA kernels return the correct long-wavelength limit of f_{xc} . The $\tilde{c} = 0.47$ NEO exchange kernel keeps the correct long-wavelength of f_{xc} . Since the compressibility sum rule delivers direct information about the long-wavelength limit, among all the approximations NEO $\tilde{c} = 0.47$ has a direct impact on the curvature of the dispersion. The fitting against this exact constraint designates that the plasmon dispersion must start out as horizontal at small wavevectors. NEO $\tilde{c} = 0.47$ exemplifies the best behavior in the long wavelength limit ($q \rightarrow 0$) that any static kernel for jellium at $r_s = 2.07$ can demonstrate.

Comparing the ALDA and rALDA kernels in the left panel of Fig. 6.2, it is apparent that the nonlocal feature of the rALDA relevant in the ground state correlation energy does not change the plasmon dispersion, and all ALDA and rALDA approximations yield the same dispersion curve. The NEO $\tilde{c} = 0.264$ and $\tilde{c} = 0.47$ methods basically agree, while the NEO $\tilde{c} = 0.0037$ is completely unphysical with low plasmon frequencies as an indication of the lack of exact constraints (See Fig. 6.2).

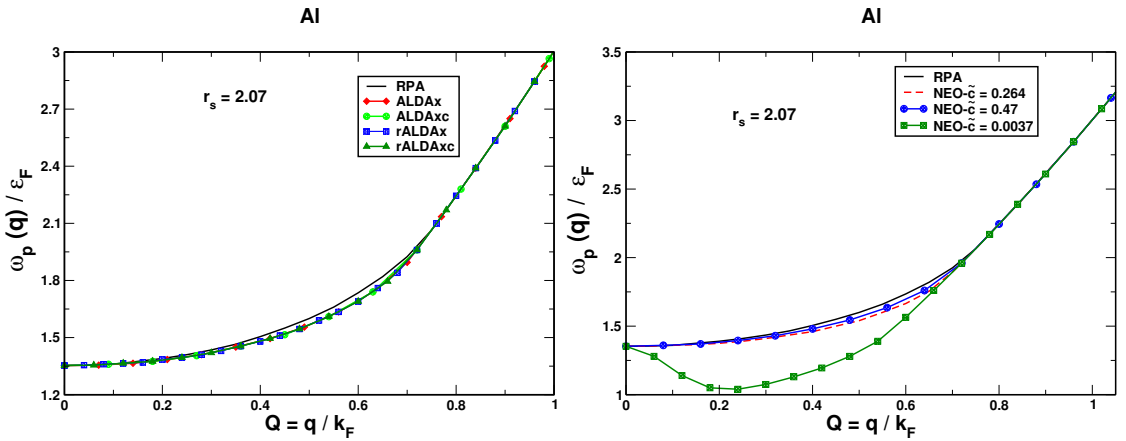


Figure 6.2: The plasmon dispersion for Al (modeled as jellium with $r_s = 2.07$) up to the critical wavevector. The left panel shows the dispersion obtained with RPA and beyond-RPA with ALDAx, ALDAxc, rALDAx and rALDAxc approximations. The right panel shows the dispersion from RPA and the three NEO approximations with the \tilde{c} parameters corresponding to different choices.

For jellium at $r_s=3.93$ (as for Na), all ALDA and rALDA dispersion curves barely dif-

fer in the left panel of Fig. 6.3. As in Al, there is no significant change coming from the nonlocal kernels. According to the right subfigure, the NEO $\tilde{c} = 0.264$ and NEO $\tilde{c} = 0.44$ kernels differ more than they do in Al for a range of ~ 0.5 for dimensionless wavevector Q . NEO $\tilde{c} = 0.0037$ leads to unphysically low plasmon frequencies.

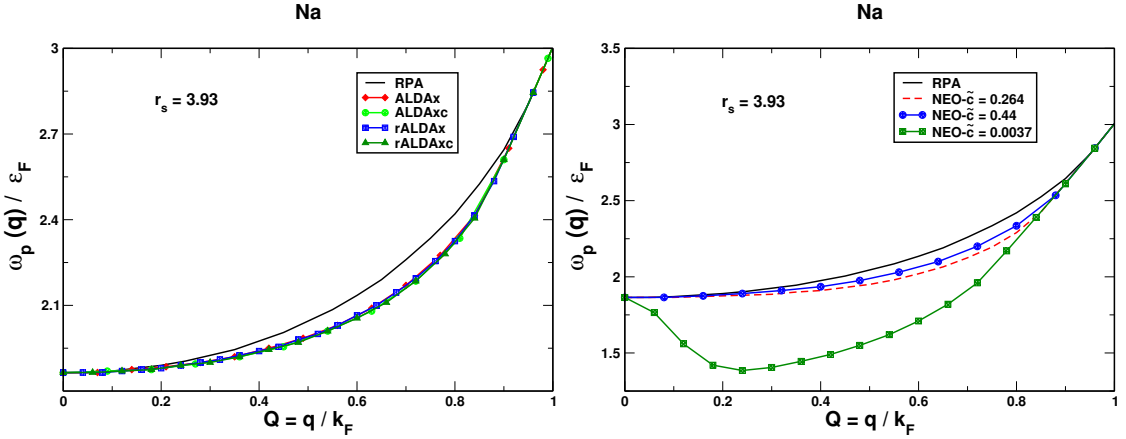


Figure 6.3: The plasmon dispersion for Na (modeled as jellium with $r_s = 3.93$), up to the critical wavevector. The left panel shows the dispersion obtained with RPA and beyond-RPA with ALDAX, ALDAXc, rALDAX and rALDAXc approximations. The right panel shows the dispersion from RPA and the three NEO approximations with the \tilde{c} parameters corresponding to different choices.

Cs is the alkali metal with the lowest density [315]. We modeled it here as jellium with $r_s = 5.62$. This characteristic manifests itself in the plasmon dispersion when comparing the approximations in the left and right panels of Fig. 6.4. Being correct at small q , the ALDAXc and rALDAXc are more suitable than ALDAX for lower densities in Cs, but the nonlocality versus locality in rALDAXc and ALDAXc does not much affect the dispersion. Comparing the NEO approximations, NEO $\tilde{c} = 0.264$ results in more correction beyond-RPA than it does in the previous two metals. Furthermore NEO $\tilde{c} = 0.264$ yields more correction in the plasmon frequencies than any of the ALDA and rALDA kernels. The exact compressibility-sum-rule-based NEO $\tilde{c} = 0.43$ behaves more like ALDAX or ALDAXc. NEO $\tilde{c} = 0.0037$ considerably lowers the plasmon dispersion. At the first glance this could be mistaken for the observed behavior for the real low-density Cs.

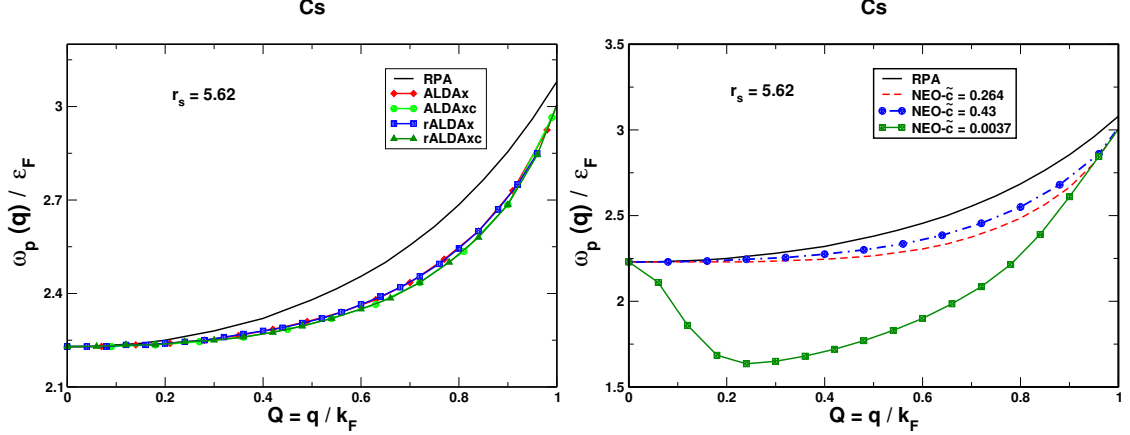


Figure 6.4: The plasmon dispersion for Cs (modeled as jellium with $r_s = 5.62$) up to the critical wavevector. The left panel shows the dispersion obtained with RPA and beyond-RPA with ALDAx, ALDAxc, rALDAx and rALDAxc approximations. The right panel shows the dispersion from RPA and the three NEO approximations with the \tilde{c} parameters corresponding to different choices.

To summarize the role of the exact constraints, we compare all the exchange and exchange-correlation models described above. Figure 6.5 displays the small wavevector behavior of all kernels and of RPA. The exact dispersion relation is known to be quadratic in the wavevector q as $E \sim q^2$. Except NEO $\tilde{c} = 0.0037$, all exchange and exchange-correlation kernels and RPA are properly horizontal at small Q wavevectors and become properly quadratic as Q increases. The horizontal line is a consequence of the exact physical constraints satisfied by these methods. NEO $\tilde{c} = 0.0037$ is not consistent with any exact constraint. While NEO $\tilde{c} = 0.264$ is based on the exact high-density limit of the correlation energy, the unphysical NEO deviates from this constraint and picks up a wrong negative quadratic dispersion.

We have also extracted the plasmon dispersion for the real metals Na and Cs by calculating the electron energy loss spectrum using the GPAW[207–209, 213] code. The results are presented in Figure 6.6. We used the projector-augmented wave (PAW)[206] pseudopotential provided with the GPAW code, an energy cutoff of 600 eV, and a $16 \times 16 \times 16$ k-point mesh to sample the Brillouin zone. Our calculations including band structure effects con-

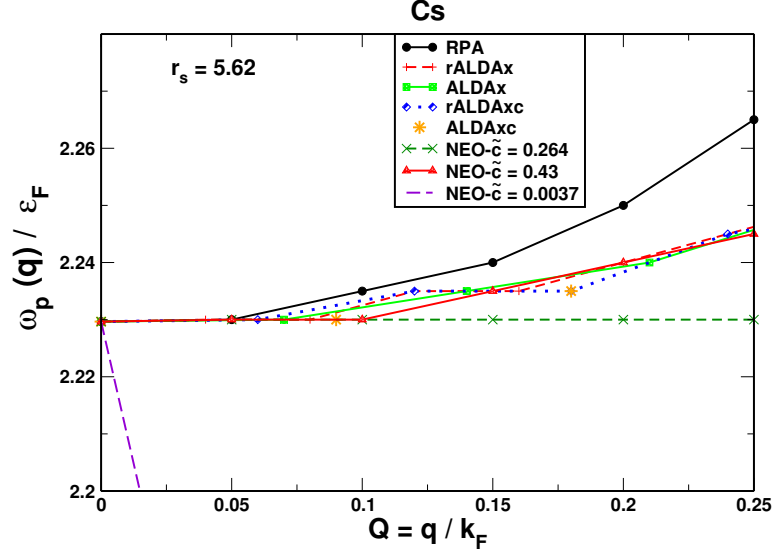


Figure 6.5: The long wavelength behavior of all approximations considered in this work.

firm that the band structure significantly alters the plasmon dispersion for Cs, while its effect is negligible for Na. The plasmon frequency at $q \rightarrow 0$ shows a 0.5 eV renormalization compared to the RPA value within the jellium model. The effect of the band structure in Cs is significantly large enough to dominate over the changes from one kernel to another.

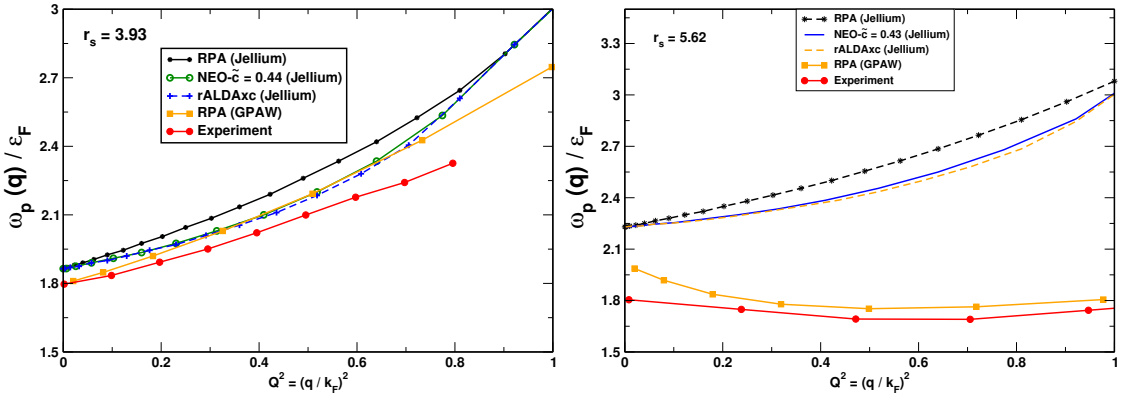


Figure 6.6: The plasmon dispersion of Na (left) and Cs (right) with RPA and some exchange-correlation kernels within the jellium model. For both Na and Cs, the dispersion with RPA is also displayed with band structure effects obtained from the GPAW code, showing results close to experiment [298]. The momentum transfer (\mathbf{q}) is in the [100] direction for bulk solids.

6.5 The dynamic structure factor within and beyond-RPA

The dynamic structure factor [170] or spectral function $S(q, \omega)$ shows the distribution of frequencies ω for density fluctuations of wavevector q in the ground state of the uniform electron gas. Although it arises from all density fluctuations of a given wavevector, the spectral function for small wavevector typically peaks around the frequency of a plasmon. The inverse frequency width of this peak, by the uncertainty principle, provides a lower bound on the decay time for such a fluctuation, while the dependence of the peak on q reflects the plasmon dispersion. Here we will investigate the effects of various model exchange-correlation kernels on the spectral function. The dynamic structure factor $S(q, \omega)$ is proportional to $\text{Im}\chi$ [316], the loss component of the dynamic density-density response function:

$$S(q, \omega) = -\frac{1}{\pi} \text{Im}\chi(q, \omega)\Theta(\omega) \quad (6.5-8)$$

This quantity has been investigated by Lewis and Berkelbach [317] using an equation-of-motion coupled cluster singles and doubles formalism, which unlike our TDDFT methods allows for plasmon decay via multi-pair electron-hole decay channels. With our real static exchange-correlation kernels, the plasmon at small finite q does not decay.

In Figure 6.7, we analyze our approximations at three wavevectors: $q = 0.1k_F$, $q = 0.5k_F$, and $q = k_F$. The latter wavevector is close to the one at which the plasmon decays into the single-pair electron-hole continuum at $r_s = 4$. To obtain a physically observable broadening for our spectral function, we have utilized a frequency $\omega - i\eta$, where ω is real, in $S(q, \omega - i\eta)$. We used $\eta = 0.032$ Hartree and $\eta = 0.063$ Hartree respectively for $r_s = 4$ and $r_s = 5.62$ (Cs). This broadening is much higher than the physical one recommended by Ref [301], but is needed to make all the plasmon peaks more visible in the figure. The first Figure 6.7 (a) compares RPA to the default NEO kernel with $\tilde{c} = 0.264$. The line shapes at $q = 0.1k_F$ and $q = 0.5k_F$ are very similar for both methods. At $q = k_F$ the line shape from

NEO becomes broader than the one from RPA, and the plasmon peak from NEO is shifted to a lower frequency. Figure 6.7.b compares three NEO kernels at $r_s = 4$ for the same three wavevectors.

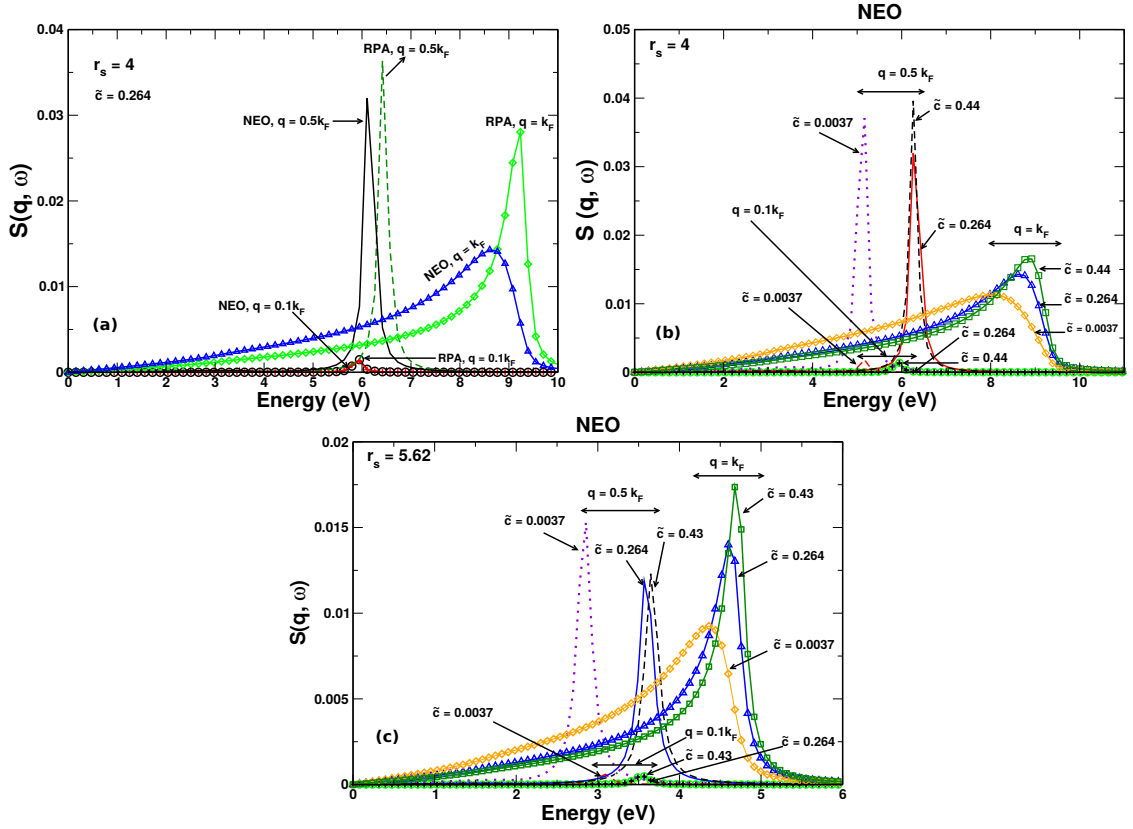


Figure 6.7: a: The jellium spectral functions for RPA and NEO $\tilde{c} = 0.264$ at $r_s = 4$. b: the spectral functions for three NEO kernels at $r_s = 4$. c: the jellium spectral functions for three NEO kernels at $r_s = 5.62$ corresponding to Cs. To make it more visible, the plasmon peak has been unphysically broadened. At $q = 0.1k_F$, we see only the plasmon peak and it is barely visible. At $q = k_F$, the plasmon peak is overlapped with the continuum of single particle-hole excitations.

The static structure factor $S(q)$ is the integral over frequency of $S(q, \omega)$, divided by the electron number N . $S(q)$ determines the well-known correlation energy of the uniform electron gas. We will now show that the range of q/k_F (less than or about equal to 4) that distributes to the correlation energy is much greater than the range of q/k_F (less than or about equal to 1) that contributes to the plasmon dispersion. In the smaller range (but not

in the larger one), the ALDxc kernel is nearly sufficient, while the default NEO kernel is nearly sufficient over the larger range. This completes our plasmon dispersion analysis with an explanation why a negative dispersion cannot exist in jellium at the density of Cs.

Exchange-correlation kernels can be applied to improve the ground state correlation energy of RPA through the adiabatic connection fluctuation dissipation theorem. This is the basis of the wavevector decomposition of the ground state exchange-correlation energy as known from Langreth and Perdew [170]:

$$E_{xc} = \int \frac{d^3q}{(2\pi)^3} \frac{1}{2} \int_0^1 \frac{d\lambda}{\lambda} \left(\frac{4\pi\lambda}{q^2} \right) N[S_\lambda(q) - 1], \quad (6.5-9)$$

where λ is the coupling constant along the adiabatic connection path and $S_\lambda(q)$ is the static structure factor found by integrating $S_\lambda(q, \omega)$ over frequency and dividing by the electron number. According to the expression given by Eq. 7.4-10, the exchange-correlation energy depends upon the dynamic structure factor. The exchange energy E_x replaces S_λ by S_0 , and the correlation energy is $E_c = E_{xc} - E_x$. Figure 6.8 shows the wavevector decomposition of the correlation energy for all exchange and exchange-correlation kernels considered here. We plot this for $r_s = 4$ and $r_s = 5.62$.

The physical basis of our analysis is the exact exchange-correlation kernel $f_{xc}(q, \omega)$ of the uniform electron gas. For the correlation energy, the static version of the kernel $f_{xc}(q, 0)$ can be applied to a good approximation [119]. Note that the frequency dependence at least qualitatively can also be ignored for $\omega \approx \omega_p$ [318, 319]. The ALDA exchange-correlation kernel $f_{xc}^{ALDA}(q, 0)$ approaches the exact kernel for the uniform electron gas at $q \rightarrow 0$. In the long wavelength limit,

$$\lim_{q \rightarrow 0} f_{xc}(q, 0) = \lim_{q \rightarrow 0} f_{xc}^{ALDA}(q, 0). \quad (6.5-10)$$

As we will see below, f_{xc}^{ALDA} breaks down for $q/k_F \geq 1$, where our constraint-based NEO kernels become less negative and more accurate. Therefore, as suggested by Fig. 6.1:

$$f_{xc}^{ALDA}(q, 0) < f_{xc}(q, 0) < 0 \quad (6.5-11)$$

The ALDA approximation becomes a lower bound to the static exact exchange-correlation kernel for the correlation energy of the uniform electron gas. Figure 6.8 visualizes the relation between ALDAxc, RPA and some other exchange-correlation kernels. The ALDAxc is shown in the left panel of Figure 6.8. The ALDAxc is very accurate for small wavevectors but starts to deviate from NEO at $q = k_F$. At $q = 2k_F$ the ALDAxc yields a strong overestimation of the correction to RPA correlation energy. All static beyond-RPA kernels make the exchange-correlation energy of RPA less negative for any density including $r_s = 5.62$. The correlation energies from NEO $\tilde{c} = 0.264$ and from the NEO kernel fitted against the compressibility sum-rule are close to each other but the unphysical NEO $\tilde{c} = 0.0037$ adds a much larger correction to the RPA correlation energy.

The constraints of Equations 6.5-10 and 7.4-12 control the plasmon dispersion and the correlation energy. The dynamic structure factor becomes a link that couples the physics in the correlation energy and plasmon dispersion. From the correlation energy, the exact uniform-electron gas-based kernel must be less negative than the ALDAxc kernel. The NEO $\tilde{c} = 0.264$ kernel is uniform electron gas-based only through its energy optimization to the high-density limit, and performs reasonably for both plasmon dispersion and correlation energy in jellium.

6.6 Conclusion

We have presented various model exchange-correlation kernels beyond-RPA for the plasmon dispersion within the jellium model for alkali metals. We have shown that the

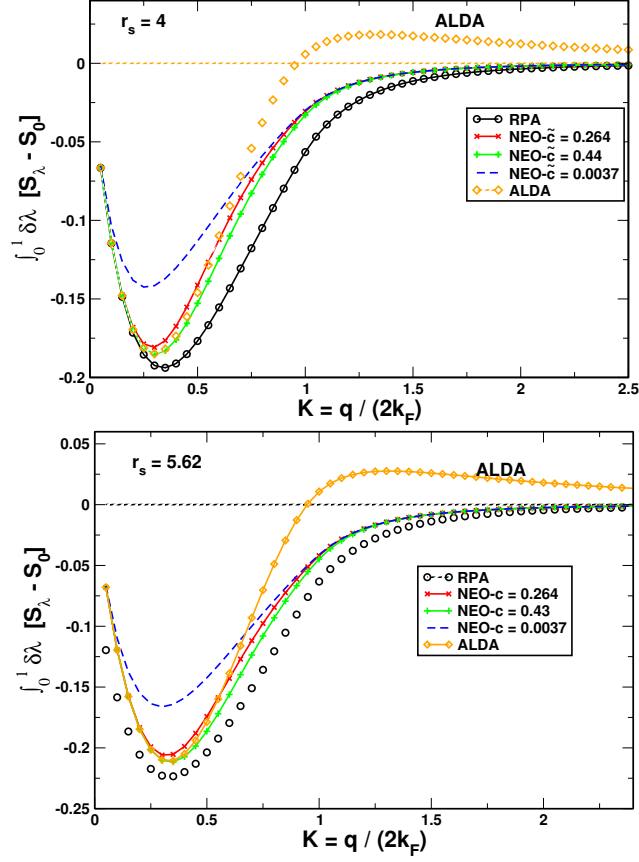


Figure 6.8: Wavevector analysis of the ground state correlation-only energy of jellium from the dynamic structure factor for reduced wavevector $K = \frac{q}{2k_F}$. The area under each curve is proportional to the correlation energy. The left figure shows the correlation-only energy for RPA, ALDA and NEO with the three choices for \tilde{c} , for $r_s=4$. The right figure shows the same for $r_s=5.62$ corresponding to Cs.

plasmon dispersion is strictly controlled by exact constraints. Additional physics beyond the ALDA kernel, such as nonlocality in space, can be unimportant for plasmon dispersion. Physical constraints such as the compressibility sum rule determine the plasmon dispersion with exchange-correlation kernels. Clearly none of our methods based on particle-hole RPA for jellium is able to predict the experimentally observed negative plasmon dispersion for the heavy alkali metal Cs which arises from band structure. The current exchange-correlation kernels do not have an explicit density dependence that could have a larger impact. For the exact exchange-correlation kernel, the ALDAxc is likely a lower bound (as suggested by Fig. 6.1). The ALDAxc is accurate for $\frac{q}{k_F} < 1$, the range of q that determines

the plasmon dispersion, even though the ALDxc kernel fails badly for $\frac{q}{k_F} \gg 1$, a range that contributes significantly to the correlation energy.

6.7 Acknowledgment

The research of N. K. N., S. R. and A. R. was supported by the National Science Foundation under Grant No.DMR-1553022. We thank John P. Perdew for comments on the manuscript.

CHAPTER 7

CONSTRAINT-BASED WAVEVECTOR- AND FREQUENCY-DEPENDENT EXCHANGE-CORRELATION KERNEL OF THE UNIFORM ELECTRON GAS

7.1 Abstract

According to time-dependent density functional theory, the exact exchange-correlation kernel $f_{xc}(n, q, \omega)$ for wavevector q and frequency ω determines not only the ground-state energy but also the excited-state energies/lifetimes and time-dependent linear density response of an electron gas of uniform density $n = 3/(4\pi r_s^3)$. Here we propose a parametrization of this function based upon the satisfaction of exact constraints. For the static ($\omega = 0$) limit, we modify the model of Constantin and Pitarke to recover at small q the known second-order gradient expansion, and to correct its approach to the large q limit. For all ω at $q = 0$, we use the model of Gross, Kohn, and Iwamoto. A Cauchy integral extends this model to complex ω . Scaling relations are identified. We then combine these ingredients, damping out the ω dependence at large q . Away from $q = 0$ and $\omega = 0$, the correlation contribution to the kernel becomes dominant over exchange, even at $r_s = 4$. The resulting correlation energies for $1 \leq r_s \leq 10$ from integration over imaginary ω are essentially exact. The plasmon pole of the density response function is found by analytic continuation of f_{xc} to ω just below the real axis, and the resulting plasmon lifetime at $r_s = 4$ is found for $q < k_F$. A static charge-density wave is found for $r_s > 69$, and shown to be associated with

softening of the plasmon mode.

©2020 American Physical Society

7.2 Introduction

In time-dependent density functional theory (TDDFT) [71, 95, 319], the exact linear density response function $\chi(\mathbf{r}, \mathbf{r}', \omega)$ of an electronic system in its ground state yields the density response $\delta n = \chi \delta v$ to a weak external scalar potential $\delta v(\mathbf{r}', \omega)$, oscillating at angular frequency ω . χ provides access to the exact ground- and excited-state energies of the system. Under the standard assumption that the ground-state and time-dependent densities for the real interacting system are the same as those of a fictitious non-interacting system in an effective scalar potential (the Kohn-Sham or KS potential in the ground-state case), the true response function χ can be constructed from the calculable non-interacting response function χ_{KS} and an exchange-correlation kernel f_{xc} . Through the adiabatic-connection fluctuation-dissipation theorem [169, 320, 321], χ yields the ground-state exchange-correlation energy from an integral along the upper half of the imaginary frequency axis. In other words, the exchange-correlation kernel f_{xc} “exactifies” the random phase approximation via an effective electron-electron interaction $\frac{1}{|\mathbf{r}'-\mathbf{r}|} + f_{xc}(\mathbf{r}', \mathbf{r}, \omega)$ just as ground-state Kohn-Sham density functional theory “exactifies” the Hartree approximation by addition of the exact density functional for the exchange-correlation energy. Under analytic continuation of f_{xc} to complex frequencies, the poles of the response functions in the lower-half complex plane are the excitation energies/inverse lifetimes.

The exact ground-state many-electron wavefunction and its total energy as an expectation value of the Hamiltonian are time-independent, but the electrons still move and their density still fluctuates around a time-independent average. TDDFT and the fluctuation-dissipation theorem provide a spectral decomposition of the exchange-correlation term of the total energy into contributions from correlations between density fluctuations at posi-

tive frequencies. The required integral over real frequencies would be challenging without a mathematical transformation by contour integration to the imaginary-frequency axis in the upper half of the complex plane

For a homogeneous electronic system, Fourier transformation leads to the simple algebraic expression

$$\chi(q, \omega) = \frac{\chi_{\text{KS}}(q, \omega)}{\tilde{\epsilon}(q, \omega)} \quad (7.2-1)$$

$$\tilde{\epsilon}(q, \omega) = 1 - \left[\frac{4\pi}{q^2} + f_{xc}(q, \omega) \right] \chi_{\text{KS}}(q, \omega). \quad (7.2-2)$$

with a wavevector of magnitude q . χ_{KS} is the Lindhard function [110], and the dependence of all functions upon the uniform density n is implicit. For a uniform density, the exchange-correlation kernel is known to be short-ranged, with a finite $q \rightarrow 0$ limit. The function $\tilde{\epsilon}$ can vanish, introducing a collective excitation or plasmon that is not present in the non-interacting KS system.

Many exact properties of the exchange-correlation kernel have been derived, and models have been constructed to satisfy those exact constraints, in much the same way that the density functional for the ground-state exchange-correlation energy, $E_{xc}[n]$, is often approximated by the satisfaction of known exact constraints. Note that the uniform-gas correlation energy from quantum Monte Carlo (QMC) calculations [322], which, as extended and parametrized in Refs. [17–19], typically serves as an input to the construction of such functionals, can be accurately predicted (not fitted) by a constraint-based interpolation [323, 324] between known high- and low-density limits.

We know of relatively few q - and ω -dependent TDDFT kernels for the uniform electron gas, essentially just the Richardson-Ashcroft [112] and Constantin-Pitarke [113] kernels.

Both are constructed only for imaginary (or zero) frequencies. The Richardson-Ashcroft kernel accurately predicts [119] the correlation energy per electron of the uniform electron gas, while the Constantin-Pitarke kernel has a parameter that fits that energy. The kernels commonly used in TDDFT calculations of excitation energies are usually adiabatic ($\omega = 0$) and often local density approximation or LDA ($q = 0$). Our kernel is designed for the uniform electron gas, and should be used with caution for other systems. An alternative would be the tensorial kernel [325] of time-dependent current density functional theory (TDCDFT), which at the LDA level is known to be more applicable than the corresponding scalar kernel of TDDFT.

In this work, we will develop a constraint-based model kernel that refines the Constantin-Pitarke 2007 (CP07) [113] q -dependent static ($\omega = 0$) kernel, and combines it with the Gross-Kohn-Iwamoto [318, 319] dynamic kernel for $q = 0$. Our kernel is developed for general complex frequencies, while that of CP07 is developed only for zero and imaginary frequencies. While many practical calculations with TDDFT for real systems use the adiabatic local density approximation based upon the uniform-gas $f_{xc}(q = 0, \omega = 0)$, we will see that there are strong dependences on both variables, and that, away from $q = 0$ and $\omega = 0$, the correlation contribution can dominate over exchange, even at the valence electron densities of metals. Our model passes several early tests: It yields very accurate correlation energies per electron for the uniform gas without fitting (while the dynamic CP07 is fitted to those energies), predicts finite lifetimes for plasmons [307] of small non-zero wavevector, and finds at about the right low density a static charge-density wave [322, 326, 327] that arises from a softening of the plasmon mode. We did not find a charge-density wave at any density with the original CP07 kernel. We hope that our model will have other applications, and that it might have implications for TDDFT in real systems.

The static kernel $f_{xc}(q, \omega = 0)$ for the uniform electron gas (jellium) has been calcu-

lated via QMC [328] and parametrized by Corradini et al. [223]. Jellium is an important model because it has a Hamiltonian with Coulomb repulsions between electrons, but with the external potential simplified from that of positive ions to that of a uniform positive-charge background. If this background is allowed to expand or contract, then jellium is only stable for an electron density $n = 3/(4\pi r_s^3)$ with $r_s \approx 4$ (in atomic units or bohr), near the valence-electron density of metallic sodium. But, by adding an appropriately-chosen short-range contribution to the external potential, a stabilized jellium model can be constructed for a better description of all simple metals and their surfaces [329]. Since the bulk electron density remains uniform, all exchange-correlation effects in bulk stabilized jellium are the same as those in bulk jellium at the same density. The book by Giuliani and Vignale [297] provides a detailed discussion of exchange and correlation in the uniform electron gas, and an explanation of the important difference between the short-range kernel of the uniform electron gas (where $f_{xc}(q, \omega)$ tends to a finite constant as $q \rightarrow 0$) and the ultra-nonlocal kernels of other systems (where in this limit f_{xc} diverges like $\frac{\alpha(\omega)}{q^2}$). For this and other reasons, kernel development has been generalized [300, 325, 330] from density to current-density functionals.

Even before TDDFT, it was known that there is a local field factor $G_{xc}(q, \omega)$, with

$$f_{xc}(q, \omega) = - \left(\frac{4\pi}{q^2} \right) G_{xc}(q, \omega), \quad (7.2-3)$$

that corrects the over-estimation of short-range correlation in the random phase approximation (RPA) for the correlation energy of a uniform electron gas. Singwi and collaborators [331] modelled a static local field factor that essentially predicted the uniform-gas correlation energy later found from QMC [322]. Lein, Gross and Perdew [119] used the Richardson-Ashcroft (RA) [112] dynamic kernel (as developed for imaginary frequencies only) to show that the static limit of a good kernel can capture most of the correction to

the RPA correlation energy, although including the frequency dependence of the RA kernel gives even more-accurate correlation energies. Here we will find that the static version of our kernel already predicts very accurate correlation energies, which are hardly changed by inclusion of our frequency dependence. But, as discussed below, the frequency dependence of the exchange-correlation kernel is needed for other applications.

7.3 Density dependence of constraint-based kernels

For simplicity, we will discuss here the density dependence of constraint-based static kernels for the uniform gas. The frequency dependence complicates the notation but does not change the conclusions. Here we will use the Fermi wavevector $k_F = (3\pi^2 n)^{1/3}$. The non-interacting response function has the simple scaling equality $\chi_{KS}(q,0) = k_F F(\frac{q}{2k_F})$, and of course the Fourier transform of the Coulomb interaction between electrons is $\frac{4\pi}{q^2} = k_F^{-2} \pi (\frac{q}{2k_F})^{-2}$.

The kernel has Coulomb-like scaling equalities only in the high-density and low-density limits

$$f_{xc}(q,0) \rightarrow k_F^{-2} G\left(\frac{q}{2k_F}\right) \quad (k_F \rightarrow \infty) \quad (7.3-4)$$

$$f_{xc}(q,0) \rightarrow k_F^{-2} H\left(\frac{q}{2k_F}\right) \quad (k_F \rightarrow 0) \quad (7.3-5)$$

Table I shows the density dependences of some of the ingredients of our kernel to be introduced later. The macroscopic or slowly-varying-density limit is achieved when $\frac{q}{2k_F} \rightarrow 0$

Thus, in the high-density limit for fixed finite $\frac{q}{2k_F}$, $\tilde{\epsilon}(q,0) \rightarrow 1 + O(k_F^{-1})$ and $\chi(q,0) \rightarrow \chi_{KS}(q,0)$. In the adiabatic connection fluctuation dissipation expression [169, 320, 321] for the exchange-correlation energy, the exchange energy per electron $\epsilon_x \sim k_F$ arises from χ_{KS} (as a function of wavevector and imaginary frequency), and the correlation energy per

Table 7.1: Density (n) dependences of key ingredients (to be defined later) of the exchange-correlation kernel $f_{xc}(\mathbf{q}, \omega)$ for a uniform electron gas with density parameter $r_s = (\frac{3}{4\pi n})^{1/3}$, and of related quantities: the Fermi wavevector $k_F = 1.9192/r_s$, the bulk plasma frequency $\omega_p = (4\pi n)^{1/2}$, and $\Delta f_0/f_0$ from Ref. [325](atomic units).

r_s	k_F	ω_p	$k^{-1/2}/k_F$	$b^{1/2}\omega_p$	$k_F^2 f_0$	$k_F^2 f_\infty$	$k_F^2 f_{xc}(\infty, \omega)$	$\Delta f_0/f_0$
0	∞	∞	1.15	∞	-3.14	-1.89	0	-
1	1.92	1.73	1.67	0.51	-3.25	-1.10	-0.39	-0.16
2	0.96	0.61	1.76	0.49	-3.36	-0.92	-0.51	-0.12
3	0.64	0.33	1.80	0.48	-3.45	-0.85	-0.57	-0.10
4	0.48	0.22	1.82	0.47	-3.53	-0.83	-0.61	-0.08
5	0.38	0.15	1.83	0.46	-3.60	-0.83	-0.63	-0.08
∞	0	0	2.06	0	-6.07	-3.65	0	-

electron ε_c from $\chi - \chi_{KS}$ (as a function of coupling constant, wavevector, and imaginary frequency). The correlation energy is much smaller than the exchange energy at high densities, but tends to about $0.9\varepsilon_x$ at very low densities. In this paper, for the ingredients of f_{xc} , we will employ the parametrization of Ref. [18] for the r_s -dependence of ε_c at zero spin polarization.

7.4 Modified CP07 static kernel

We begin with the static limit of the original CP07 kernel of Eq. (12) of Ref. [16] (in atomic units):

$$f_{xc}^{CP07}(q, 0) = \left(\frac{4\pi}{q^2}\right) B[e^{-kq^2} - 1] - \left(\frac{4\pi}{k_F^2}\right) \frac{C}{[1 + \frac{1}{q^2}]}, \quad (7.4-6)$$

$$k = \frac{A}{4\pi B}. \quad (7.4-7)$$

Here A, B, and C are positive functions of density n defined in Ref. [113]. These functions of density typically require derivatives of $\varepsilon_{xc}(r_s)$ or $\varepsilon_c(r_s)$, for which we employ the parametrizations from the appendix of Ref. [18] (numerically almost identical to those of Refs. [17] and [19]) instead of the less-accurate but simpler ones of Ref. [113]. CP07 is a constraint-based kernel that aims to reproduce the known small q and large q behaviors of

the exact kernel:

$$f_{xc}(q, 0) \rightarrow -A \quad (q \rightarrow 0) \quad (7.4-8)$$

$$f_{xc}(q, 0) \rightarrow -\left(\frac{4\pi}{k_F^2}\right) C - \left(\frac{4\pi}{q^2}\right) B \quad (q \rightarrow \infty). \quad (7.4-9)$$

Eq. (8) is the well-known compressibility sum rule; approximating f_{xc} by $-A$ is the adiabatic local density approximation. Eq. (9) is from Refs. [223, 328]. Note that C arises from correlation alone, and vanishes in the high- and low-density limits, as shown in Table I.

Eq. (7.4-6) was intended to recover Eq. (7.4-9), but does not because the $q \rightarrow \infty$ expansion of the last term of Eq. (7.4-6) is $-\frac{4\pi}{k_F^2} C \left[1 - \frac{1}{q^2}\right]$, which loses the correct $1/q^2$ contribution in Eq. (7.4-9). Thus our first change to Eq. (7.4-6) is to replace $1/q^2$ in the last term by $1/(kq^2)^2$. This substitution is needed to recover Eq. (9) and the density scalings discussed in section 2 of this article. Note that, by Table 1, kq^2 scales like $(\frac{q}{2k_F})^2$ in the high- and low-density limits.

The second change we make is to replace Eq. (8) by the more accurate and better controlled

$$f_{xc}(q, 0) \rightarrow -A + Dq^2 \quad (q \rightarrow 0), \quad (7.4-10)$$

$$D = \frac{2C_{xc}(r_s)}{n^{4/3}} \quad (7.4-11)$$

from Eqs. (25), (32), and (37) of Ref. [327], but with improved input. The $q \rightarrow 0$ limit is the limit of slowly-varying-in-space induced density, in which the second-order gradient expansion becomes exact. Thus, in Eq. (11), $C_{xc}(r_s)$ is the coefficient of the second-order

gradient expansion for the exchange-correlation energy:

$$C_{xc}(r_s) = C_x + C_c(r_s = 0) \frac{1 + 3.138r_s + 0.3r_s^2}{1 + 3.0r_s + 0.5334r_s^2}, \quad (7.4-12)$$

with $C_x = -0.00238$ [332] and $C_c(r_s = 0) = 0.00423$ [333]. Untypically, C_{xc} does not reduce to C_x as $r_s \rightarrow 0$. We have used the r_s - dependence of Eq. (36) of Ref. [334], in which C_{xc} decreases very slowly to zero as r_s increases, taking the values 0.00185, 0.00122, and 0.00015 at $r_s = 0, 4,$ and $70,$ respectively. This means that, at very low densities with $r_s \geq 70,$ D will be close to 0 and the LDA kernel will be nearly correct through order $(\frac{q}{2k_F})^2$.

A better match to the QMC kernel [328] for r_s in the metallic range and for $\frac{q}{2k_F} < \sim 1$ could be achieved by setting $D = 0$ in Eq. (10). Within its error bars, the QMC kernel can also be matched [335] by including higher-order terms in the gradient expansion of the exchange-correlation energy, although the fourth-order terms are not known for the correlation energy. In the interests of simplicity and generality, we have not included a q^4 term in Eq. (10). The goal of constraint satisfaction is not to match every detail, but to make a correct global map.

The result of these changes is the modified CP07 (MCP07) static kernel:

$$f_{xc}^{MCP07}(q, 0) = \left(\frac{4\pi}{q^2}\right) B[e^{-kq^2}(1 + Eq^4) - 1] - \left(\frac{4\pi}{k_F^2}\right) \frac{C}{[1 + \frac{1}{(kq^2)^2}]}, \quad (7.4-13)$$

$$E = \frac{D}{4\pi B} - \frac{k^2}{2}. \quad (7.4-14)$$

Its exchange-only and exchange-correlation incarnations for $r_s = 4$ are plotted in Fig. 7.1. We see that, away from $q = 0,$ correlation can be more important than exchange.

We use the name MCP07 only for the static limit of our kernel, since that is the part solely

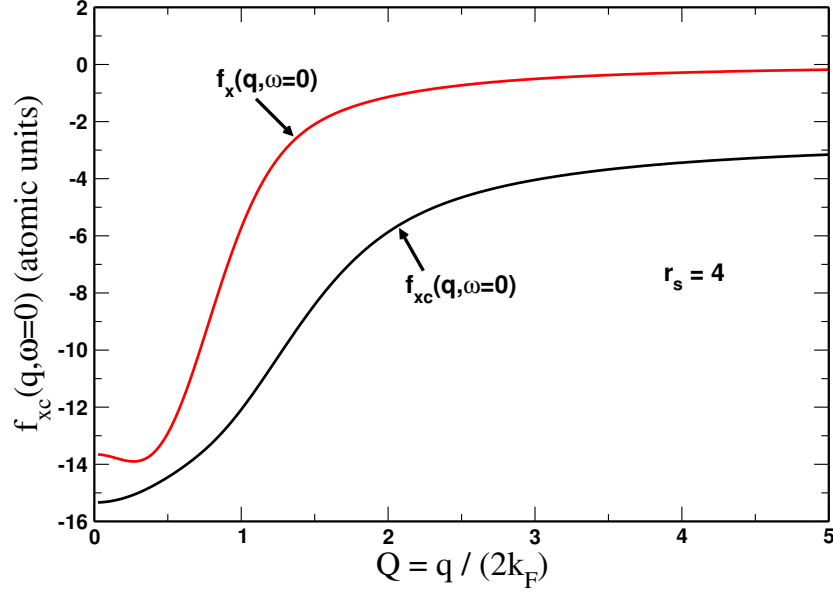


Figure 7.1: Modified CP07 (MCP07) static kernels for jellium with density parameter $r_s = 4$ at the exchange-only and exchange-correlation levels, versus reduced wavevector.

based upon a modification of the original CP07.

7.5 Static charge-density wave in jellium

Overhauser [326] proposed that periodic metals could be unstable against the formation of a static charge-density wave (CDW). Quantum Monte Carlo calculations found a CDW or incipient body-centered cubic (bcc) Wigner crystallization in spin-polarized jellium at a low critical density corresponding to $r_s = 70$ [336], or at $r_s = 85 \pm 20$ in spin-unpolarized jellium [322]. The 1980 calculation of Ceperley and Alder [322] also found that ground-state jellium remains spin-unpolarized for $r_s \leq 75 \pm 5$. In the same year, Perdew and Datta [327], using a static kernel designed to satisfy Eqs. (10) and (11), also found a CDW near this critical r_s .

Figure 7.2 of the present article, which is similar to Fig. 4 of Ref. [327], was found by fixing a value for $\frac{q}{2k_F}$ and then searching for the largest value of k_F that makes $\tilde{\epsilon}(q) = 0$ (hence a non-zero density response at wavevector q even in the absence of any perturbing

potential). This happens around $r_s = 30$ in the adiabatic local density approximation, and around $r_s = 69$ in MCP07. We could not find a charge-density wave at any density from the original CP07. All the low-density instabilities of jellium are difficult to pinpoint, because the energies of the different phases as functions of r_s are nearly the same at low densities.

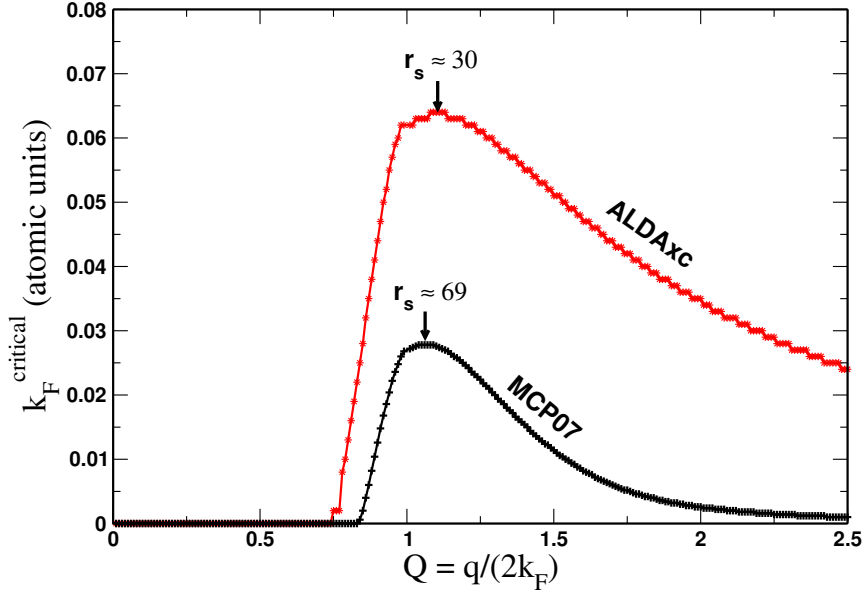


Figure 7.2: Critical Fermi wavevector for the appearance of a static charge-density wave in a low-density jellium, from the adiabatic local density approximation ($f_{xc} = f_{xc}(0,0)$) and MCP07 static ($f_{xc} = f_{xc}(q,0)$) exchange-correlation kernels, versus reduced wavevector.

The charge-density wave first appears with $\frac{q}{2k_F} \approx 1.14$, making q close to the first reciprocal lattice vector of a bcc Wigner crystal with one electron per primitive cell. For much smaller $\frac{q}{2k_F}$, the CDW is strongly suppressed by the Coulomb term $4\pi/q^2$ in Eq. (2). Later in this article, we will show that the CDW is associated with a softening of the plasmon mode.

Our Fig. 1 shows that the static MCP07 kernel $f_{xc}(q,0)$ is always more negative than its exchange-only version $f_x(q,0)$. This result confirms Overhauser’s 1968 prediction that correlation enhances the charge-density wave [326].

7.6 Frequency-dependent local kernel of Gross and Kohn

A constraint-based model for $f_{xc}(q=0, \omega)$ was proposed in 1985 by Gross and Kohn [319], and later corrected by Iwamoto and Gross [318]. It starts from a constrained interpolation for the imaginary part, evaluated at a real frequency, between known real zero- (f_0) and infinite- (f_∞) frequency limits at $q = 0$:

$$\text{Im}f_{xc}(0, \omega) = -cb^{3/4}g(b^{1/2}\omega), \quad (7.6-15)$$

$$g(x) = \frac{x}{(1+x^2)^{5/4}}, \quad (7.6-16)$$

$$b = \left\{ \left(\frac{\gamma}{c} \right) [f_\infty - f_0] \right\}^{4/3}, \quad (7.6-17)$$

$$c = 23 \frac{\pi}{15}, \quad (7.6-18)$$

$$\gamma = \frac{[\Gamma(\frac{1}{4})]^2}{(32\pi)^{1/2}} = 1.311. \quad (7.6-19)$$

Figure 7.3 shows this function of real ω for $r_s = 4$, and also its exchange-only contribution. Again the importance of correlation is manifest. Table I shows that the dimensionless quantity $b^{1/2}\omega_p$ (where $\omega_p = (4\pi n)^{1/2}$ is the bulk plasmon frequency) is nearly constant over the range of metallic densities, but not over all densities. Thus, in the metallic range, $g(b^{1/2}\omega)$ is approximately a function of $\frac{\omega}{\omega_p}$.

The next step is to use the Kramers-Kronig relations [319] between the imaginary and real parts of $f_{xc} - f_\infty$ at real frequency to find

$$\text{Re} f_{xc}(0, \omega) - f_\infty = \left(\frac{1}{\pi} \right) P \int_{-\infty}^{\infty} d\omega' \frac{\text{Im}f_{xc}(0, \omega')}{\omega' - \omega}. \quad (7.6-20)$$

As $\omega \rightarrow \infty$, $\text{Im}f_{xc}(0, \omega) \sim -c/\omega^{3/2}$ and $\text{Re}f_{xc}(0, \omega) - f_\infty \sim c/\omega^{3/2}$.

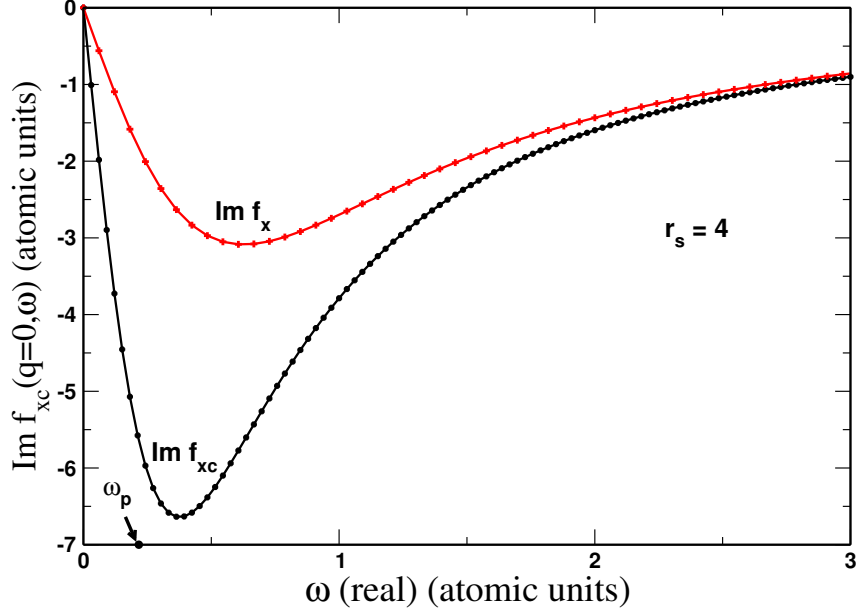


Figure 7.3: Imaginary part of the Gross-Kohn $q = 0$ dynamic kernel for jellium with density parameter $r_s = 4$, at the exchange-only and exchange-correlation levels, versus real frequency.

The principal value of the integral can be found numerically. However, the scaling relation of Eq. (15) implies the scaling relation

$$\text{Re} f_{xc}(0, \omega) - f_\infty = -c b^{3/4} h(b^{1/2} \omega), \quad (7.6-21)$$

where $h(0) = \frac{1}{\gamma}$ to recover the correct non-zero $\omega \rightarrow 0$ limit. A fair fit with the correct large- ω asymptotics is provided by the simple algebraic model

$$h_{\text{model}}(x) = \frac{\left(\frac{1}{\gamma}\right)[1 - ax^2]}{[1 + (a/\gamma)^{4/7} x^2]^{7/4}}. \quad (7.6-22)$$

with a fit parameter $a = 0.63$.

Figure 7.4 compares the real-frequency dependences of the real part of the kernel, with and without correlation, from the Kramers-Kronig relation and from the model. The model is less accurate at intermediate frequencies than at low or high frequencies. While the

Kramers-Kronig choice is the consistent one, we have found that it does not make any significant difference from the model in the applications presented here.

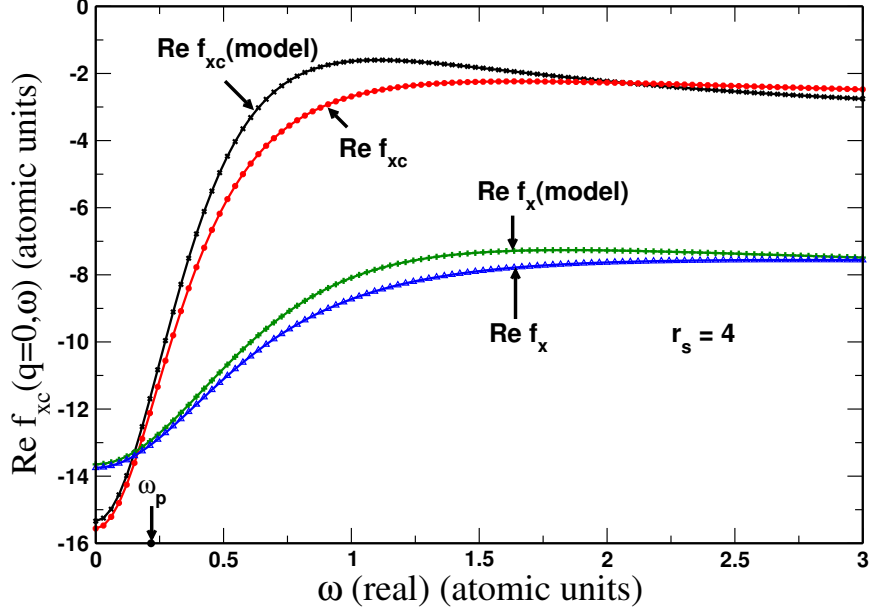


Figure 7.4: Real part of the Gross-Kohn $q = 0$ dynamic kernel for jellium with density parameter $r_s = 4$, at the exchange-only and exchange-correlation levels, versus real frequency. (From the Kramers-Kronig relation of Eq. (20) and from the model of Eq. (22).)

For calculation of the correlation energy, we will need $f_{xc}(0, \omega)$ for frequencies ω in the upper-half complex plane, where this function is analytic [319]. For this, we use the Cauchy integral over real ω' :

$$f_{xc}(0, \omega) - f_\infty = \frac{1}{2\pi i} \int_\infty^\infty d\omega' \frac{[f_{xc}(0, \omega') - f_\infty]}{\omega' - \omega}. \quad (7.6-23)$$

which follows from the residue theorem and exact properties of $f_{xc}(0, \omega) - f_\infty$ [319]. By letting ω approach the real axis from above, we can derive the Kramers-Kronig relations including Eq. (20). Figure 7.5 shows the kernel for frequencies on the upper imaginary axis, where the kernel is purely real.

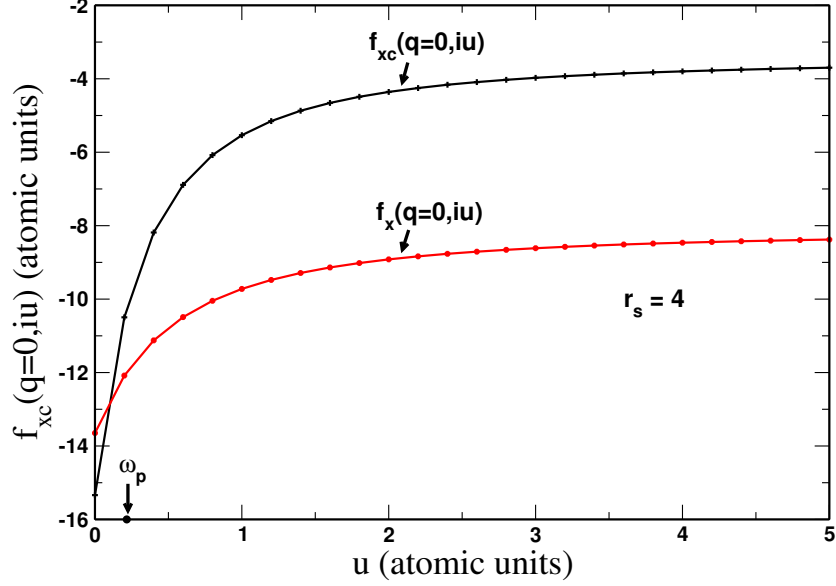


Figure 7.5: The purely-real Gross-Kohn $q = 0$ dynamic kernel for jellium with density parameter $r_s = 4$, at the exchange-only and exchange-correlation levels, versus imaginary frequency. (From the Cauchy integral of Eq. (23) and the model of Eq. (22).)

7.7 Combining the wavevector dependence of MCP07 with the frequency dependence of the Gross-Kohn kernel

An important constraint is Eq. (5.176) of Ref. [297], attributed there to Ref. [337]. It says that the ω -dependence of the kernel damps out at large q , even when the kernel itself has a non-zero large- q limit.

To avoid empiricism, we will use the same Gaussian damping factor that damps out the local density and gradient expansion terms at large q in Eq. (13):

$$f_{xc}(q, \omega) = \left[1 + e^{-kq^2} \left\{ \frac{f_{xc}(0, \omega)}{f_{xc}(0, 0)} - 1 \right\} \right] f_{xc}^{MCP07}(q, 0). \quad (7.7-24)$$

When $q = 0$, Eq. (24) properly recovers $f_{xc}(0, \omega)$. When $\omega = 0$, Eq. (24) properly recovers $f_{xc}^{MCP07}(q, 0)$. And when $q \rightarrow \infty$, Eq. (24) correctly reduces to $f_{xc}^{MCP07}(q, 0)$.

Figure 7.6 shows the q -dependence of the imaginary part of Eq. (24) for $r_s = 4$ for various real frequencies that are integer multiples of the bulk plasmon frequency. Figure 7.7 shows the same for the real part (using the model of Eq. (22)). Note that the frequency dependence is already strongly damped at $\frac{q}{2k_F} = 1$.

A viscosity correction to the compressibility value for $f_0 = f_{xc}(0,0)$ was found by Conti and Vignale [338]. It is of order 10% at metallic densities, as shown by the values of $\Delta f_0/f_0$ in Table I (based on Δf_0 values from Ref. [325]), and is not included in our Eq. (24).

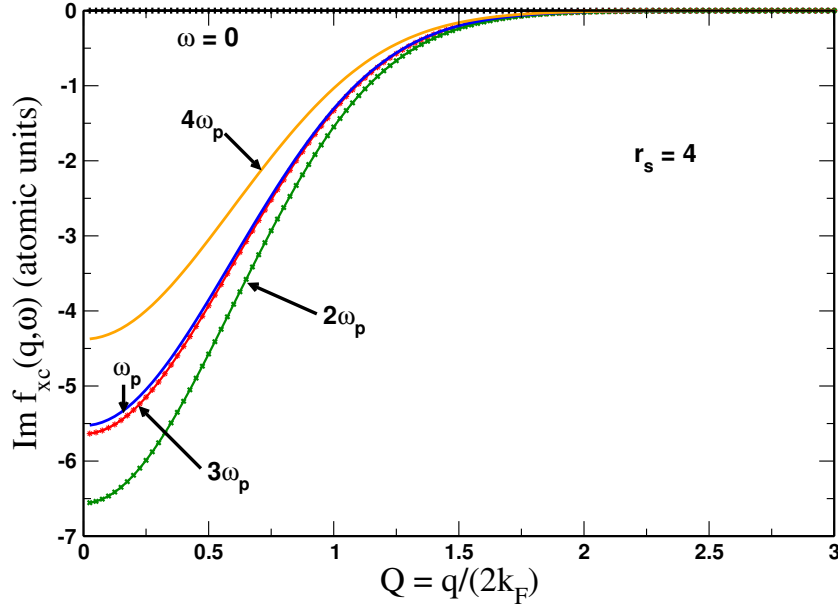


Figure 7.6: Imaginary part of the exchange-correlation kernel of Eq. (24) for jellium with density parameter $r_s = 4$, for five different real frequencies, versus reduced wavevector.

7.8 Plasmon in jellium

The plasmon is a collective long-wavelength oscillation of the electron density, at a frequency $\omega_p(q)$ that tends as $q \rightarrow 0$ to the classical limit or bulk plasmon frequency $\omega_p = (4\pi n)^{1/2}$. At q less than a critical wavevector q_c , the real part of the complex plasmon energy $\omega_p(q)$ lies above the highest energy of the continuum of single electron-hole excitations of wavevector q , which in a non-interacting picture has a highest energy of

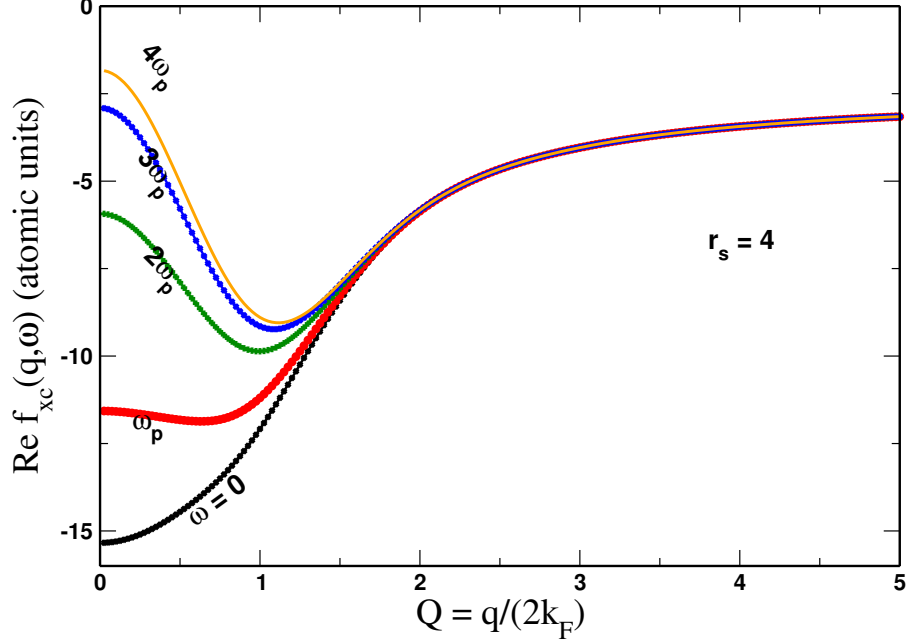


Figure 7.7: Real part of the exchange-correlation kernel of Eq. (24) for jellium with density parameter $r_s = 4$, for five different real frequencies, versus reduced wavevector. (From the model of Eq. (22).)

$\frac{(k_F+q)^2}{2} - \frac{k_F^2}{2}$. Thus

$$\frac{Re \omega_p(q_c)}{k_F^2} = \left(\frac{1}{2}\right) \left(\frac{q_c}{k_F}\right)^2 + \frac{q_c}{k_F}. \quad (7.8-25)$$

In the range $q < q_c$ (the only range we will consider here), the plasmon excitation cannot decay to a single electron-hole pair excitation, so its lifetime is infinite for any real (hence frequency-independent kernel). But a frequency-dependent kernel should yield a plasmon frequency in the lower-half complex frequency plane, where $Im \omega_p(q)$ is minus the inverse of a lifetime arising from decay of the plasmon into multiple electron-hole pairs.

We find $\omega_p(q)$ by fixing a real wavevector q and searching over complex frequencies ω for the one that zeroes out $\tilde{\epsilon}(q, \omega)$ of Eq. (2). In practice, we stop when $|\tilde{\epsilon}|$ is of order 10^{-3} . Since our Cauchy integral of Eq. (23) is only for ω in the upper-half complex plane, we find $f_{xc}(0, \omega)$ by analytic continuation or Taylor expansion from a near frequency on the real axis. The zero-th order term of this expansion almost suffices, as we confirm by

adding the first-order term, using the Cauchy-Riemann conditions on an analytic function to convert known derivatives of the real and imaginary parts of f_{xc} with respect to $\text{Re } \omega$ to derivatives with respect to $\text{Im } \omega$.

Figure 7.8 shows the resulting plasmon dispersion or $\text{Re } \omega_p(q)$ for $r_s = 4$, which would be

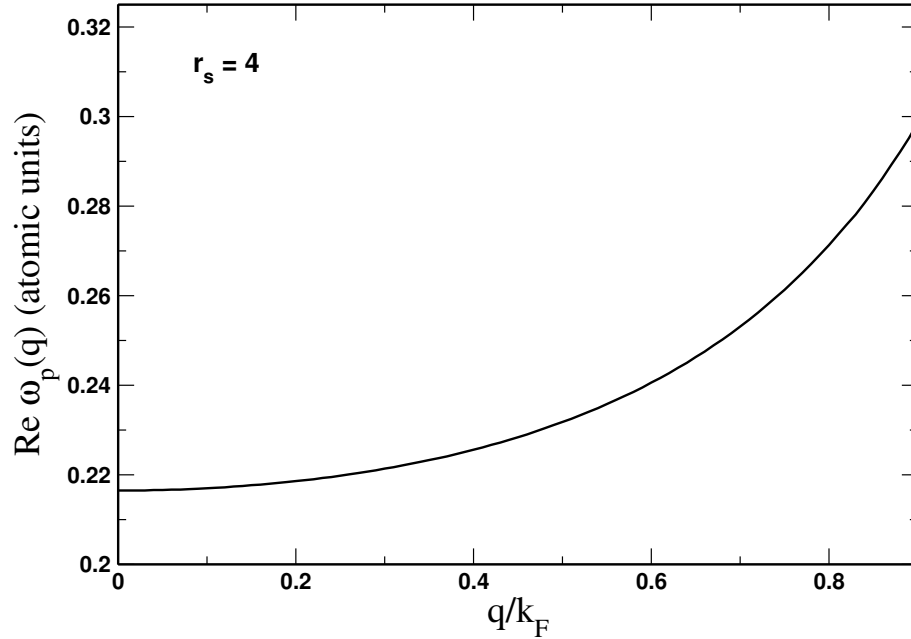


Figure 7.8: Plasmon dispersion for jellium with density parameter $r_s = 4$, from the kernel of Eq. (24), versus reduced wavevector. The real part of the plasmon frequency is plotted.

almost the same if the frequency dependence of the kernel were neglected, and not qualitatively different if the kernel were set to 0. Fig. 7.9 shows the resulting $\text{Im } \omega_p(q)$, or minus the inverse plasmon lifetime, which would equal zero without the frequency dependence. The calculated inverse lifetime grows like q^2 at small q , as expected [297, 301], but starts to decrease again as q approaches k_F , where the Gross-Kohn frequency dependence is increasingly damped out via our Eq. (24). The minimum predicted plasmon lifetime is of the order of femtoseconds.

Figure 7.10 shows $\text{Re } \omega_p(q)$ for $r_s = 69$, where the static charge density wave was found to appear in section 4. Unlike the dispersion in Fig. 8, the dispersion here is downward, and $\omega_p(q)$ appears to be heading toward zero at $q/k_F \approx 2$. Thus the static charge density

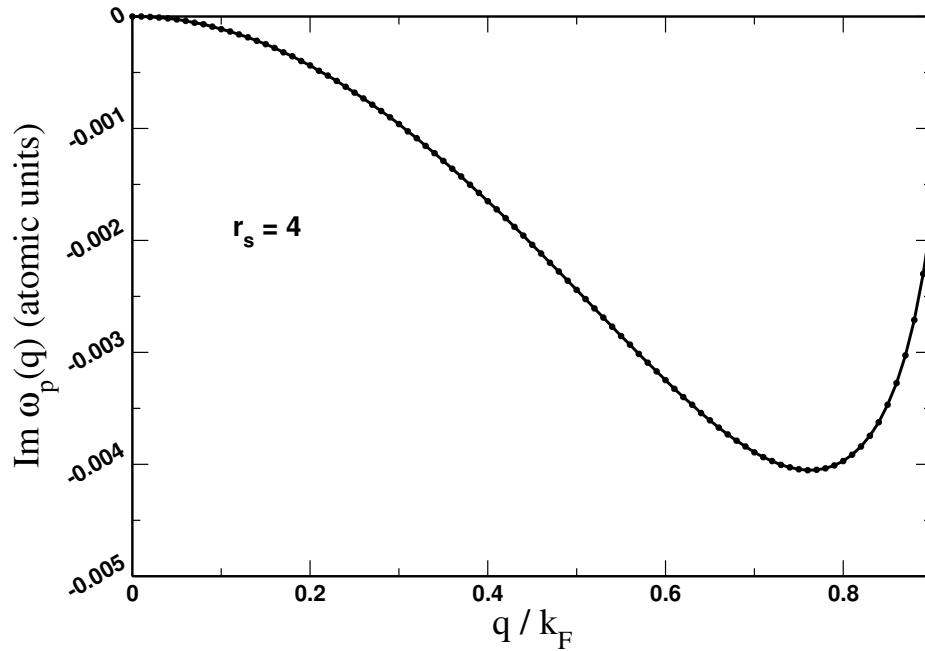


Figure 7.9: Plasmon damping for jellium with density parameter $r_s = 4$, from the kernel of Eq. (24), versus reduced wavevector. The imaginary part of the plasmon frequency is plotted.

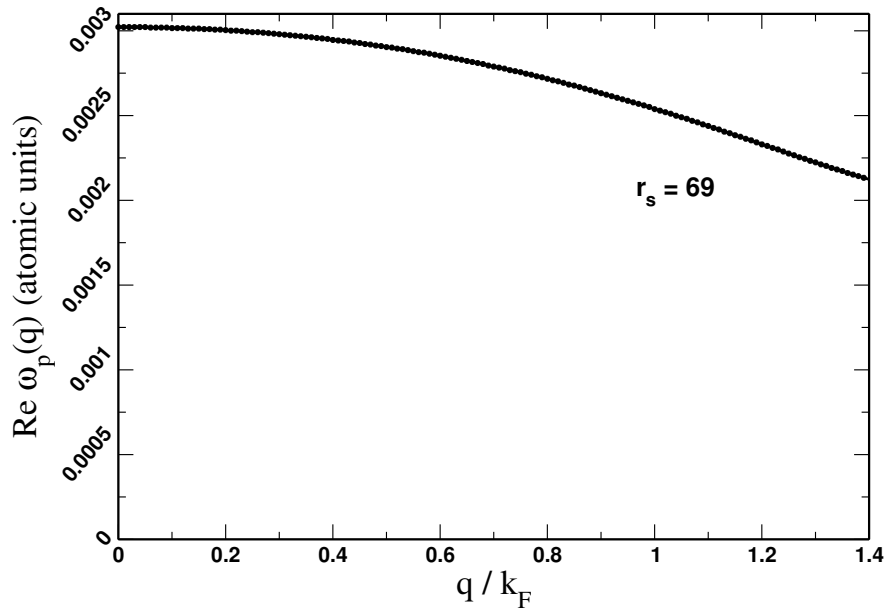


Figure 7.10: Plasmon dispersion for jellium with density parameter $r_s = 69$, from the kernel of Eq. (24), versus reduced wavevector. The softened plasmon mode may lead to the static charge-density wave.

wave can be understood to arise from a soft plasmon mode.

7.9 Correlation energy per electron in jellium

The correlation energy of the uniform electron gas has a long history, going back to the random phase approximation (RPA) ($f_{xc} = 0$) of the 1950's [320]. The formula we use here is Eq. (27) of Ref. [119]. In this equation, an integral over real frequencies from 0 to ∞ has been transformed by contour integration to an integral over imaginary frequencies in the upper half plane. This is done to avoid the plasmon pole near the real axis, and results in the smooth frequency integrand shown in Figs. 3 and 4 of Ref. [119]. The Kohn-Sham non-interacting and real interacting systems are connected adiabatically through the coupling constant λ between 0 and 1 in the Coulomb interaction $\frac{4\pi\lambda}{q^2}$. The exchange-correlation kernel must also be scaled, as in Eq. (18) of Ref. [119]:

$$f_{xc}^\lambda(n, q, \omega) = \lambda^{-1} f_{xc}\left(\frac{n}{\lambda^3}, \frac{q}{\lambda}, \frac{\omega}{\lambda^2}\right). \quad (7.9-26)$$

Figure 7.11 shows our results for the correlation energy per electron as a function of r_s in the metallic range, in comparison with the highly-accurate parametrization and extension [324] of the results of Ref. [322] by Perdew and Wang 1992 [19] (indistinguishable on the scale of the figure from the parametrization of Ref. [18]). As is well known, RPA ($f_{xc} \rightarrow 0$) makes the correlation energy per electron too low by about 0.4 eV/electron, and the adiabatic local density approximation ($f_{xc} \rightarrow f_{xc}(0,0)$) makes it too high by about the same absolute error. A good kernel $f_{xc}(q, \omega)$ should produce an accurate result, and our static MCP07 kernel does so to a remarkable extent. Adding the frequency dependence of Eq. (24) degrades the accuracy, but almost negligibly. Replacing the Gaussian in Eq. (24) by 1 (thus using the undamped Gross-Kohn frequency dependence) would degrade the accuracy significantly, correcting only about 2/3 of the RPA error.

In both this work and Ref. [119], the frequency dependence of the exchange-correlation kernel has very little effect on the correlation energy of the uniform electron gas. But the

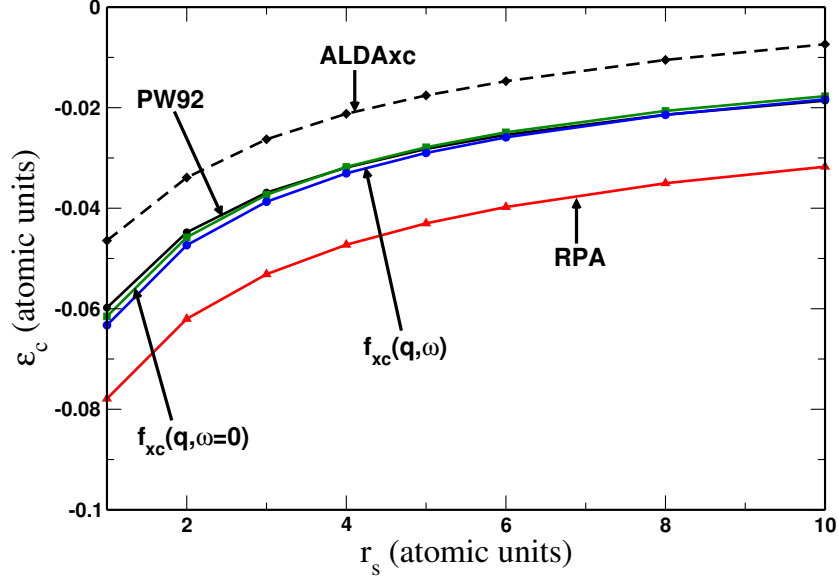


Figure 7.11: Correlation energy per electron for jellium from various kernels, and the essentially-exact Perdew-Wang 1992 (PW92) parametrization, versus density parameter r_s . The RPA has no kernel ($f_{xc} = 0$). The adiabatic local density approximation ($f_{xc} = f_{xc}(0,0)$), the static MCP07 kernel of Eq. (13) ($f_{xc} = f_{xc}(q,0)$), and the full dynamic kernel of Eq. (24) ($f_{xc} = f_{xc}(q,\omega)$) are also tested here. The wavevector dependence and frequency dependence make the kernel $f_{xc}(q, \omega)$ less negative (Figs. 1 and 5), which moves the kernel-corrected correlation energy closer to RPA, in which the kernel is zero.

frequency dependence is what produced the plasmon inverse lifetime in Fig. 9. Other properties that are or may be sensitive to the frequency dependence are listed in the Conclusions section.

7.10 Conclusions

The CP07 exchange-correlation kernel for zero frequency and the Gross-Kohn kernel for zero wavevector were constructed for the uniform electron gas via the satisfaction of exact constraints. By imposing further exact constraints, we have made an improved MCP07 static kernel and combined it with the Gross-Kohn dynamic kernel. Key added constraints include the second-order gradient expansion for the exchange-correlation energy, and the damping out of the frequency dependence with increasing wavevector. That damping out is already substantial at $q \approx k_F$.

Without any fitting, we have achieved high accuracy for all studied properties. In particular, the critical density ($r_s \approx 69$) and critical wavevector of the static charge-density wave that appears at low density are accurate. We have shown that this ground-state instability of the uniform phase is associated with a soft plasmon. We have also found that correlation enhances the instability, as Overhauser predicted in 1968 [326].

We have also studied the plasmon at the density of metallic sodium ($r_s = 4$), where our frequency dependence produces a plasmon lifetime that first decreases from infinity to a few femtoseconds and then increases, as the wavevector increases from 0 toward the Fermi wavevector k_F . Previous work [297, 301], based on a Taylor expansion for $q \ll k_F$, found a monotonic decrease in lifetime with increasing q in the latter range.

We have also calculated remarkably accurate correlation energies per electron for metallic r_s from 1 to 10. The improvement over RPA arises from the wavevector dependence of the MCP07 kernel. The frequency dependence of our kernel has almost no effect on the ground-state energy, a conclusion that might extend to real systems.

It should be noted that [118], for metallic densities, the range of wavevectors relevant to the plasmon outside the electron-hole continuum, $0 \leq q < \sim k_F$, is different from the range relevant to the correlation energy, $0 < \sim q < \sim 3k_F$. At much lower densities, the latter range is also relevant to the plasmon and charge-density wave. In the range $0 \leq q < \sim k_F$, the effective interaction $\frac{4\pi}{q^2} + f_{xc}$ in Eq. (2) is dominated by $\frac{4\pi}{q^2}$ [118], so modest deviations of f_{xc} from its RPA value 0, or better from the adiabatic local density approximation $f_{xc}(0,0)$, have almost negligible effect in that range, apart from emergent phenomena like the plasmon lifetime. Thus our applications test the kernel not only over a wide range of densities but also over a fairly wide range of $\frac{q}{2k_F}$. In the future, we hope

to find more demanding tests for the frequency dependence. Several properties of uniform or weakly-inhomogeneous densities are expected to be, unlike the correlation energy of the uniform gas, sensitive to the frequency dependence of the uniform gas kernel, including the electronic stopping power [339] and residual resistivity [340], optical absorption of a weakly-inhomogeneous electron density [341], and the peak widths of the wavevector-dependent dynamical structure factor [342].

In our uniform-gas exchange-correlation kernel, the full Gross-Kohn frequency dependence is unveiled only in the long-wavelength ($q \rightarrow 0$) limit, in which the kernel itself is overwhelmed by the Coulomb interaction $\frac{4\pi}{q^2}$. Inhomogeneous ground states [297] have ultra-nonlocal kernels with an $\frac{\alpha(\omega)}{q^2}$ variation in this limit that strongly affects optical absorption, and might quantitatively correct the qualitatively-right RPA description of long-range van der Waals interaction.

7.11 Acknowledgments

AR and NKN acknowledge support from the U.S. National Science Foundation under Grant No. DMR-1553022. JPP acknowledges support from the U.S. National Science Foundation under Grant No. DMR-1939528 (CMMT-Division of Materials Theory, with a contribution from CTMC-Division of Chemistry).

CHAPTER 8

CONCLUSIONS

In this work, we have explored exchange-correlation kernels for various ground- and excited-state properties. In the first chapter, we gave a brief introduction to ground-state density functional theory. We discussed approximations for the exchange-correlation energy that constitute the different rungs of Perdew's Jacob ladder. We briefly described several semilocal approximations with their advantages and limitations. The theoretical aspects of linear-response theory within time-dependent DFT (TDDFT) were described in Chapter 2. The random phase approximation (RPA) and various corrections to RPA were discussed. We have discussed various aspects of the exchange-correlation (XC-)kernel. Chapters 3-6 describe the performance of the XC kernels in predicting the equilibrium ground-state properties of real solids. Also, Chapters 7 and 8 discuss the construction and applications of the XC-kernel to numerous properties of the uniform electron gas (UEG). We showed that the kernel developed with the proper constraint satisfaction significantly improves both the ground-state and excited-state properties over RPA. We have developed a wavevector- and frequency-dependent XC kernel (MCP07) by modifying the static part of the CP07 kernel [287]. It satisfies all the exact-constraints that a complex-kernel can satisfy with real frequency. It provides accurate properties of the UEG, such as charge density wave (CDW), plasmonic dispersion, and the ground-state correlation energy. Besides, the kernel also describes the CDW as a soft plasmon, thereby providing a novel interpretation of the strong correlation [47].

There are several XC- kernels that can significantly improve the ground-state correla-

tion energy over RPA, where the accurate description of the short-range electron-electron correlation is crucial. However, the prediction of reliable excited-state properties such as the absorption spectra of extended systems with the TDDFT kernel is still a challenging task due to the absence of the complete knowledge of the behavior of the XC-kernel at the optical or long-wavelength limit $q \rightarrow 0$ for non-uniform electron densities. There are kernels that have the right $\sim \frac{1}{q^2}$ behavior for wavevector at the long-wavelength limit, which can predict accurate optical properties in many materials. However, the frequency-dependence is also important to capture the complete electron-hole interaction, as required for excitons. Therefore, there is still a need for further work on construction and testing of more exact-constraints in the direction of frequency-dependence for extended systems.

Our work on intermetallic alloys emphasizes the importance of a more accurate kernel that can provide accurate formation energies of intermetallic alloys, where RPA fails badly. The improvement by the rAPBE kernel is encouraging, but it is not satisfactory. The MCP07 kernel can be a good alternative for these metallic systems, as they provide accurate ground-state correlation energies over a wide range of metallic densities of the uniform electron gas. Future work may include the implementation and testing of this kernel for real solids.

BIBLIOGRAPHY

- [1] M. Born and R. Oppenheimer. Zur quantentheorie der molekeln. *Annalen der Physik*, 389(20):457–484, 1927.
- [2] D. R. Hartree. The wave mechanics of an atom with a non-coulomb central field. part ii. some results and discussion. *Mathematical Proceedings of the Cambridge Philosophical Society*, 24(1):111–132, 1928.
- [3] Vladimir Fock. Näherungsmethode zur lösung des quantenmechanischen mehrkörperproblems. *Zeitschrift für Physik*, 61(1-2):126–148, 1930.
- [4] C David Sherrill and Henry F Schaefer III. The configuration interaction method: Advances in highly correlated approaches. In *Advances in quantum chemistry*, volume 34, pages 143–269. Elsevier, 1999.
- [5] Chr. Møller and M. S. Plesset. Note on an approximation treatment for many-electron systems. *Phys. Rev.*, 46:618–622, Oct 1934.
- [6] Rodney J Bartlett. Coupled-cluster approach to molecular structure and spectra: a step toward predictive quantum chemistry. *The Journal of Physical Chemistry*, 93(5):1697–1708, 1989.
- [7] Walter Kohn. Nobel lecture: Electronic structure of matterwave functions and density functionals. *Reviews of Modern Physics*, 71(5):1253, 1999.
- [8] L. H. Thomas. The calculation of atomic fields. *Mathematical Proceedings of the Cambridge Philosophical Society*, 23(5):542–548, 1927.
- [9] Enrico Fermi. Eine statistische methode zur bestimmung einiger eigenschaften des atoms und ihre anwendung auf die theorie des periodischen systems der elemente. *Zeitschrift für Physik*, 48(1-2):73–79, 1928.
- [10] Robert G Parr and Weitao Yang. *Density-Functional Theory of Atoms and Molecules*, volume 16. OUP USA, 1994.
- [11] P. Hohenberg and W. Kohn. Inhomogeneous electron gas. *Phys. Rev.*, 136:B864, 1964.
- [12] H Englisch and R Englisch. Hohenberg-kohn theorem and non-v-representable densities. *Physica A: Statistical Mechanics and its Applications*, 121(1-2):253–268, 1983.

- [13] Mel Levy. Universal variational functionals of electron densities, first-order density matrices, and natural spin-orbitals and solution of the v -representability problem. *Proc. Natl. Acad. Sci.*, 76(12):6062–6065, 1979.
- [14] Walter Kohn and Lu Jeu Sham. Self-consistent equations including exchange and correlation effects. *Phys. Rev.*, 140(4A):A1133, 1965.
- [15] Jefferson E. Bates and Filipp Furche. Communication: Random phase approximation renormalized many-body perturbation theory. *J. Chem. Phys.*, 139(17):171103, 2013.
- [16] Xinguo Ren, Patrick Rinke, Gustavo E. Scuseria, and Matthias Scheffler. Renormalized second-order perturbation theory for the electron correlation energy: Concept, implementation, and benchmarks. *Phys. Rev. B*, 88:035120, 2013.
- [17] Seymour H Vosko, Leslie Wilk, and Marwan Nusair. Accurate spin-dependent electron liquid correlation energies for local spin density calculations: a critical analysis. *Canadian Journal of physics*, 58(8):1200–1211, 1980.
- [18] J. P. Perdew and Alex Zunger. Self-interaction correction to density-functional approximations for many-electron systems. *Phys. Rev. B*, 23:5048–5079, May 1981.
- [19] John P. Perdew and Yue Wang. Accurate and simple analytic representation of the electron-gas correlation energy. *Phys. Rev. B*, 45:13244–13249, Jun 1992.
- [20] Carlos Fiolhais, Fernando Nogueira, and Miguel AL Marques. *A primer in density functional theory*, volume 620. Springer Science & Business Media, 2003.
- [21] J. P. Perdew, K. Burke, and M. Ernzerhof. Generalized gradient approximation made simple. *Phys. Rev. Lett.*, 77:3865, 1996.
- [22] Yingkai Zhang and Weitao Yang. Comment on generalized gradient approximation made simple. *Phys. Rev. Lett.*, 80(4):890, 1998.
- [23] John P Perdew, Adrienn Ruzsinszky, Gábor I Csonka, Oleg A Vydrov, Gustavo E Scuseria, Lucian A Constantin, Xiaolan Zhou, and Kieron Burke. Restoring the density-gradient expansion for exchange in solids and surfaces. *Phys. Rev. Lett.*, 100(13):136406, 2008.
- [24] Bjørk Hammer, Lars Bruno Hansen, and Jens Kehlet Nørskov. Improved adsorption energetics within density-functional theory using revised perdew-burke-ernzerhof functionals. *Phys. Rev. B*, 59(11):7413, 1999.
- [25] Axel D Becke. Density-functional exchange-energy approximation with correct asymptotic behavior. *Phys. Rev. A*, 38(6):3098, 1988.
- [26] John P Perdew. Density-functional approximation for the correlation energy of the inhomogeneous electron gas. *Phys. Rev. B*, 33(12):8822, 1986.

- [27] Chengteh Lee, Weitao Yang, and Robert G Parr. Development of the colle-salvetti correlation-energy formula. *Phys. Rev. B*, 37(2):1, 1988.
- [28] Burkhard Miehlich, Andreas Savin, Hermann Stoll, and Heinzwerner Preuss. Results obtained with the correlation energy density functionals of becke and lee, yang and parr. *Chem. Phys. Lett.*, 157(3):200–206, 1989.
- [29] Hong Jiang. First-principles approaches for strongly correlated materials: A theoretical chemistry perspective. *International Journal of Quantum Chemistry*, 115(11):722–730, 2015.
- [30] Rex W Godby, Michael Schlüter, and LJ Sham. Self-energy operators and exchange-correlation potentials in semiconductors. *Phys. Rev. B*, 37(17):10159, 1988.
- [31] John P Perdew and Adrienn Ruzsinszky. Density-functional energy gaps of solids demystified. *The European Physical Journal B*, 91(6):108, 2018.
- [32] Jianmin Tao, John P Perdew, Viktor N Staroverov, and Gustavo E Scuseria. Climbing the density functional ladder: Nonempirical meta-generalized gradient approximation designed for molecules and solids. *Phys. Rev. Lett.*, 91(14):146401, 2003.
- [33] John P Perdew, Adrienn Ruzsinszky, Gábor I Csonka, Lucian A Constantin, and Jianwei Sun. Workhorse semilocal density functional for condensed matter physics and quantum chemistry. *Physical Review Letters*, 103(2):026403, 2009.
- [34] Jianwei Sun, Martijn Marsman, Gábor I. Csonka, Adrienn Ruzsinszky, Pan Hao, Yoon-Suk Kim, Georg Kresse, and John P. Perdew. Self-consistent meta-generalized gradient approximation within the projector-augmented-wave method. *Phys. Rev. B*, 84:035117, Jul 2011.
- [35] Jianwei Sun, Bing Xiao, and Adrienn Ruzsinszky. Communication: Effect of the orbital-overlap dependence in the meta generalized gradient approximation. *J. Chem. Phys.*, 137(5):051101, 2012.
- [36] Jianwei Sun, Robin Haunschuld, Bing Xiao, Ireneusz W Bulik, Gustavo E Scuseria, and John P Perdew. Semilocal and hybrid meta-generalized gradient approximations based on the understanding of the kinetic-energy-density dependence. *J. Chem. Phys.*, 138(4):044113, 2013.
- [37] John P Perdew, Stefan Kurth, Aleš Zupan, and Peter Blaha. Accurate density functional with correct formal properties: A step beyond the generalized gradient approximation. *Phys. Rev. Lett.*, 82(12):2544, 1999.
- [38] Yan Zhao and Donald G Truhlar. A new local density functional for main-group thermochemistry, transition metal bonding, thermochemical kinetics, and noncovalent interactions. *J. Chem. Phys.*, 125(19):194101, 2006.

- [39] Jianwei Sun, Adrienn Ruzsinszky, and John P Perdew. Strongly constrained and appropriately normed semilocal density functional. *Phys. Rev. Lett.*, 115(3):036402, 2015.
- [40] Jianwei Sun, Richard C Remsing, Yubo Zhang, Zhaoru Sun, Adrienn Ruzsinszky, Haowei Peng, Zenghui Yang, Arpita Paul, Umesh Waghmare, Xifan Wu, et al. Accurate first-principles structures and energies of diversely bonded systems from an efficient density functional. *Nat. Chem.*, 8(9):831, 2016.
- [41] Chandra Shahi, Jianwei Sun, and John P. Perdew. Accurate critical pressures for structural phase transitions of group iv, iii-v, and ii-vi compounds from the scan density functional. *Phys. Rev. B*, 97:094111, Mar 2018.
- [42] A. Patra, J. E. Bates, J. Sun, and J. P. Perdew. Properties of real metallic surfaces: Effects of density functional semilocality and van der waals nonlocality. *Proc. Nat. Acad. Sci.*, 114:E9188–E9196, 2017.
- [43] Zeng-hui Yang, Haowei Peng, Jianwei Sun, and John P Perdew. More realistic band gaps from meta-generalized gradient approximations: Only in a generalized kohn-sham scheme. *Phys. Rev. B*, 93(20):205205, 2016.
- [44] Thilo Aschebrock and Stephan Kümmel. Ultranonlocality and accurate band gaps from a meta-generalized gradient approximation. *Phys. Rev. Research*, 1:033082, Nov 2019.
- [45] Haowei Peng and John P Perdew. Synergy of van der waals and self-interaction corrections in transition metal monoxides. *Physical Review B*, 96(10):100101, 2017.
- [46] James W Furness, Yubo Zhang, Christopher Lane, Ioana Gianina Buda, Bernardo Barbiellini, Robert S Markiewicz, Arun Bansil, and Jianwei Sun. An accurate first-principles treatment of doping-dependent electronic structure of high-temperature cuprate superconductors. *Communications Physics*, 1(1):1–6, 2018.
- [47] John P. Perdew, Adrienn Ruzsinszky, Jianwei Sun, Niraj K. Nepal, and Aaron D. Kaplan. Interpretations of ground-state symmetry breaking and strong correlation in wavefunction and density functional theories, 2020.
- [48] Niraj K. Nepal, Liping Yu, Qimin Yan, and Adrienn Ruzsinszky. First-principles study of mechanical and electronic properties of bent monolayer transition metal dichalcogenides. *Phys. Rev. Materials*, 3:073601, Jul 2019.
- [49] Stefan Grimme. Accurate description of van der waals complexes by density functional theory including empirical corrections. *J. Comput. Chem.*, 25(12):1463–1473, 2004.
- [50] Stefan Grimme. Semiempirical gga-type density functional constructed with a long-range dispersion correction. *J. Comput. Chem.*, 27(15):1787–1799, 2006.

- [51] Stefan Grimme, Jens Antony, Stephan Ehrlich, and Helge Krieg. A consistent and accurate ab initio parametrization of density functional dispersion correction (dft-d) for the 94 elements h-pu. *J. Chem. Phys.*, 132(15):154104, 2010.
- [52] Stefan Grimme, Andreas Hansen, Jan Gerit Brandenburg, and Christoph Banwarth. Dispersion-corrected mean-field electronic structure methods. *Chem. Rev.*, 116(9):5105–5154, 2016.
- [53] M. Dion, H. Rydberg, E. Schröder, D. C. Langreth, and B. I. Lundqvist. Van der waals density functional for general geometries. *Phys. Rev. Lett.*, 92:246401, Jun 2004.
- [54] Oleg A. Vydrov and Troy Van Voorhis. Nonlocal van der waals density functional made simple. *Phys. Rev. Lett.*, 103:063004, 2009.
- [55] Haowei Peng, Zeng-Hui Yang, John P Perdew, and Jianwei Sun. Versatile van der waals density functional based on a meta-generalized gradient approximation. *Phys. Rev. X*, 6(4):041005, 2016.
- [56] Santosh Adhikari, Hong Tang, Bimal Neupane, Adrienn Ruzsinszky, and Gábor I Csonka. Molecule-surface interaction from van der waals-corrected semilocal density functionals: The example of thiophene on transition-metal surfaces. *Physical Review Materials*, 4(2):025005, 2020.
- [57] Mark R. Pederson, Adrienn Ruzsinszky, and John P. Perdew. Communication: Self-interaction correction with unitary invariance in density functional theory. *The Journal of Chemical Physics*, 140(12):121103, 2014.
- [58] Zeng-hui Yang, Mark R. Pederson, and John P. Perdew. Full self-consistency in the fermi-orbital self-interaction correction. *Phys. Rev. A*, 95:052505, May 2017.
- [59] Chandra Shahi, Puskar Bhattarai, Kamal Wagle, Biswajit Santra, Sebastian Schwalbe, Torsten Hahn, Jens Kortus, Koblar A. Jackson, Juan E. Peralta, Kai Trepte, Susi Lehtola, Niraj K. Nepal, Hemanadhan Myneni, Bimal Neupane, Santosh Adhikari, Adrienn Ruzsinszky, Yoh Yamamoto, Tunna Baruah, Rajendra R. Zope, and John P. Perdew. Stretched or noded orbital densities and self-interaction correction in density functional theory. *The Journal of Chemical Physics*, 150(17):174102, 2019.
- [60] Rajendra R. Zope, Yoh Yamamoto, Carlos M. Diaz, Tunna Baruah, Juan E. Peralta, Koblar A. Jackson, Biswajit Santra, and John P. Perdew. A step in the direction of resolving the paradox of perdew-zunger self-interaction correction. *The Journal of Chemical Physics*, 151(21):214108, 2019.
- [61] Puskar Bhattarai, Kamal Wagle, Chandra Shahi, Yoh Yamamoto, Selim Romero, Biswajit Santra, Rajendra R. Zope, Juan E. Peralta, Koblar A. Jackson, and John P. Perdew. A step in the direction of resolving the paradox of perdewzunger self-interaction correction. ii. gauge consistency of the energy density at three levels of approximation. *J. Chem. Phys.*, 152(21):214109, 2020.

- [62] Kamal Sharkas, Kamal Wagle, Biswajit Santra, Sharmin Akter, Rajendra R Zope, Tunna Baruah, Koblar A Jackson, John P Perdew, and Juan E Peralta. Self-interaction error overbinds water clusters but cancels in structural energy differences. *Proceedings of the National Academy of Sciences*, 117(21):11283–11288, 2020.
- [63] Santosh Adhikari, Biswajit Santra, Shiqi Ruan, Puskar Bhattarai, Niraj K Nepal, Koblar A Jackson, and Adrienn Ruzsinszky. The fermi–lödwin self-interaction correction for ionization energies of organic molecules. *J. Chem. Phys.*, 153(18):184303, 2020.
- [64] A. Seidl, A. Görling, P. Vogl, J. A. Majewski, and M. Levy. Generalized kohn-sham schemes and the band-gap problem. *Phys. Rev. B*, 53:3764–3774, Feb 1996.
- [65] Carlo Adamo and Vincenzo Barone. Toward reliable density functional methods without adjustable parameters: The pbe0 model. *J. Chem. Phys.*, 110:6158–6170, 1999.
- [66] Jochen Heyd, Gustavo E Scuseria, and Matthias Ernzerhof. Hybrid functionals based on a screened coulomb potential. *J. Chem. Phys.*, 118(18):8207–8215, 2003.
- [67] Jochen Heyd, Gustavo E Scuseria, and Matthias Ernzerhof. Erratum:hybrid functionals based on a screened coulomb potential[j. chem. phys. 118, 8207 (2003)]. *The Journal of Chemical Physics*, 124(21):219906, 2006.
- [68] Kerwin Hui and Jeng-Da Chai. Scan-based hybrid and double-hybrid density functionals from models without fitted parameters. *J. Chem. Phys.*, 144(4):044114, 2016.
- [69] Ks Kim and KD Jordan. Comparison of density functional and mp2 calculations on the water monomer and dimer. *J. Phys. Chem.*, 98(40):10089–10094, 1994.
- [70] E. Schrödinger. An undulatory theory of the mechanics of atoms and molecules. *Phys. Rev.*, 28:1049–1070, Dec 1926.
- [71] Erich Runge and Eberhard KU Gross. Density-functional theory for time-dependent systems. *Phys. Rev. Lett.*, 52(12):997, 1984.
- [72] Miguel Marques, Angel Rubio, Eberhard KU Gross, Kieron Burke, Fernando Nogueira, and Carsten A Ullrich. *Time-dependent density functional theory*, volume 706. Springer Science & Business Media, 2006.
- [73] M. Thiele, E. K. U. Gross, and S. Kümmel. Adiabatic approximation in nonperturbative time-dependent density-functional theory. *Phys. Rev. Lett.*, 100:153004, Apr 2008.
- [74] D. Bohm and D. Pines. A collective description of electron interactions: Ii. collective vs individual particle aspects of the interactions. *Phys. Rev.*, 85:338, 1952.
- [75] David Bohm and David Pines. A collective description of electron interactions: Iii. coulomb interactions in a degenerate electron gas. *Phys. Rev.*, 92:609–625, 1953.

- [76] J. Harl, L. Schimka, and G. Kresse. Assessing the quality of the random phase approximation for lattice constants and atomization energies of solids. *Phys. Rev. B*, 81:115126, 2010.
- [77] Haowei Peng and Stephan Lany. Polymorphic energy ordering of mgo, zno, gan, and mno within the random phase approximation. *Phys. Rev. B*, 87:174113, 2013.
- [78] Laurids Schimka, René Gaudoin, Jiří Klimeš, Martijn Marsman, and Georg Kresse. Lattice constants and cohesive energies of alkali, alkaline-earth, and transition metals: Random phase approximation and density functional theory results. *Phys. Rev. B*, 87:214102, Jun 2013.
- [79] Thomas Olsen and Kristian S. Thygesen. Random phase approximation applied to solids, molecules, and graphene-metal interfaces: From van der waals to covalent bonding. *Phys. Rev. B*, 87:075111, 2013.
- [80] A. M. Burow, J. E. Bates, F. Furche, and H. Eshuis. Analytical first-order molecular properties and forces within the adiabatic connection random phase approximation. *J. Chem. Theory Comput.*, 10:180–194, 2014.
- [81] Christopher E Patrick and Kristian S Thygesen. Adiabatic-connection fluctuation-dissipation dft for the structural properties of solids: The renormalized alda and electron gas kernels. *J. Chem. Phys.*, 143(10):102802, 2015.
- [82] Christopher E. Patrick and Kristian S. Thygesen. Hubbard-*u*-corrected hamiltonians for non-self-consistent random-phase approximation total-energy calculations: A study of zns, tio₂, and nio. *Phys. Rev. B*, 93:035133, 2016.
- [83] Laurids Schimka, René Gaudoin, Jiří Klimeš, Martijn Marsman, and Georg Kresse. Lattice constants and cohesive energies of alkali, alkaline-earth, and transition metals: Random phase approximation and density functional theory results. *Phys. Rev. B*, 87(21):214102, 2013.
- [84] Niraj K. Nepal, Santosh Adhikari, Jefferson E. Bates, and Adrienn Ruzsinszky. Treating different bonding situations: Revisiting au-cu alloys using the random phase approximation. *Phys. Rev. B*, 100:045135, Jul 2019.
- [85] J. Harl and G. Kresse. Cohesive energy curves for noble gas solids calculated by adiabatic connection fluctuation-dissipation theory. *Phys. Rev. B*, 77:045136, 2008.
- [86] L. Schimka, J. Harl, A. Stroppa, A. Grüneis, M. Marsman, F. Mittendorfer, and G. Kresse. Accurate surface and adsorption energies from many-body perturbation theory. *Nat. Mater.*, 9:741–744, 2010.
- [87] S Lebègue, J Harl, Tim Gould, JG Ángyán, G Kresse, and JF Dobson. Cohesive properties and asymptotics of the dispersion interaction in graphite by the random phase approximation. *Phys. Rev. Lett.*, 105(19):196401, 2010.

- [88] Henk Eshuis and Filipp Furche. A parameter-free density functional that works for noncovalent interactions. *J. Phys. Chem. Lett.*, 2(9):983–989, 2011.
- [89] Torbjörn Björkman, Andris Gulans, Arkady V Krasheninnikov, and Risto M Nieminen. van der waals bonding in layered compounds from advanced density-functional first-principles calculations. *Physical review letters*, 108(23):235502, 2012.
- [90] Adrienn Ruzsinszky, John P Perdew, and Gábor I Csonka. The rpa atomization energy puzzle. *J. Chem. Theory Comput.*, 6(1):127–134, 2010.
- [91] Niraj K. Nepal, Santosh Adhikari, Bimal Neupane, and Adrienn Ruzsinszky. Formation energy puzzle in intermetallic alloys: Random phase approximation fails to predict accurate formation energies. *Phys. Rev. B*, 102:205121, Nov 2020.
- [92] Niraj K. Nepal, Adrienn Ruzsinszky, and Jefferson E. Bates. Rocksalt or cesium chloride: Investigating the relative stability of the cesium halide structures with random phase approximation based methods. *Phys. Rev. B*, 97:115140, Mar 2018.
- [93] R. O. Jones and O. Gunnarsson. The density functional formalism, its applications and prospects. *Rev. Mod. Phys.*, 61:689–746, Jul 1989.
- [94] Giovanni Onida, Lucia Reining, and Angel Rubio. Electronic excitations: density-functional versus many-body greens-function approaches. *Rev. Mod. Phys.*, 74(2):601, 2002.
- [95] MGUJ Petersilka, UJ Gossmann, and EKV Gross. Excitation energies from time-dependent density-functional theory. *Phys. Rev. Lett.*, 76(8):1212, 1996.
- [96] Andrea Marini, Rodolfo Del Sole, and Angel Rubio. Bound excitons in time-dependent density-functional theory: Optical and energy-loss spectra. *Phys. Rev. Lett.*, 91:256402, Dec 2003.
- [97] Francesco Sottile, Valerio Olevano, and Lucia Reining. Parameter-free calculation of response functions in time-dependent density-functional theory. *Phys. Rev. Lett.*, 91:056402, Jul 2003.
- [98] S. Sharma, J. K. Dewhurst, A. Sanna, and E. K. U. Gross. Bootstrap approximation for the exchange-correlation kernel of time-dependent density-functional theory. *Phys. Rev. Lett.*, 107:186401, Oct 2011.
- [99] V. Turkowski, A. Leonardo, and C. A. Ullrich. Time-dependent density-functional approach for exciton binding energies. *Phys. Rev. B*, 79:233201, Jun 2009.
- [100] Neepa T Maitra. Perspective: Fundamental aspects of time-dependent density functional theory. *The Journal of Chemical Physics*, 144(22):220901, 2016.
- [101] Paolo E. Trevisanutto, Aleksandrs Terentjevs, Lucian A. Constantin, Valerio Olevano, and Fabio Della Sala. Optical spectra of solids obtained by time-dependent density functional theory with the jellium-with-gap-model exchange-correlation kernel. *Phys. Rev. B*, 87:205143, May 2013.

- [102] Aleksandr V. Terentjev, Lucian A. Constantin, and J. M. Pitarke. Gradient-dependent exchange-correlation kernel for materials optical properties. *Phys. Rev. B*, 98:085123, Aug 2018.
- [103] Mark S. Hybertsen and Steven G. Louie. Ab initio static dielectric matrices from the density-functional approach. i. formulation and application to semiconductors and insulators. *Phys. Rev. B*, 35:5585–5601, Apr 1987.
- [104] Carsten A Ullrich and Zeng-hui Yang. A brief compendium of time-dependent density functional theory. *Brazilian Journal of Physics*, 44(1):154–188, 2014.
- [105] CA Ullrich, UJ Gossmann, and EKV Gross. Time-dependent optimized effective potential. *Phys. Rev. Lett.*, 74(6):872, 1995.
- [106] John F Dobson, MJ Büchner, and EKV Gross. Time-dependent density functional theory beyond linear response: An exchange-correlation potential with memory. *Phys. Rev. Lett.*, 79(10):1905, 1997.
- [107] James D Talman and William F Shadwick. Optimized effective atomic central potential. *Physical Review A*, 14(1):36, 1976.
- [108] Ivan P Christov, Margaret M Murnane, and Henry C Kapteyn. High-harmonic generation of attosecond pulses in the single-cycle regime. *Physical Review Letters*, 78(7):1251, 1997.
- [109] Stuart Alan Rice, Meishan Zhao, et al. *Optical control of molecular dynamics*. John Wiley, 2000.
- [110] Jens Lindhard. On the properties of a gas of charged particles. *Dan. Vid. Selsk Mat.-Fys. Medd.*, 28:8, 1954.
- [111] Lucia Reining, Valerio Olevano, Angel Rubio, and Giovanni Onida. Excitonic effects in solids described by time-dependent density-functional theory. *Phys. Rev. Lett.*, 88(6):066404, 2002.
- [112] CF Richardson and NW Ashcroft. Dynamical local-field factors and effective interactions in the three-dimensional electron liquid. *Phys. Rev. B*, 50(12):8170, 1994.
- [113] Lucian A Constantin and JM Pitarke. Simple dynamic exchange-correlation kernel of a uniform electron gas. *Phys. Rev. B*, 75(24):245127, 2007.
- [114] T. Olsen and K. S. Thygesen. Extending the random-phase approximation for electronic correlation energies: The renormalized adiabatic local density approximation. *Phys. Rev. B*, 86:081103(R), 2012.
- [115] Thomas Olsen and Kristian S. Thygesen. Accurate ground-state energies of solids and molecules from time-dependent density-functional theory. *Phys. Rev. Lett.*, 112:203001, 2014.

- [116] Adrienn Ruzsinszky, Lucian A Constantin, and JM Pitarke. Kernel-corrected random-phase approximation for the uniform electron gas and jellium surface energy. *Phys. Rev. B*, 94(16):165155, 2016.
- [117] J. E. Bates, S. Laricchia, and A. Ruzsinszky. A non-local, energy-optimized kernel: Recovering second-order exchange in the homogeneous electron gas. *Phys. Rev. B*, 93:045119, 2016.
- [118] Niraj K. Nepal, Santosh Adhikari, Bimal Neupane, Shiqi Ruan, Santosh Neupane, and Adrienn Ruzsinszky. Understanding plasmon dispersion in nearly free electron metals: Relevance of exact constraints for exchange-correlation kernels within time-dependent density functional theory. *Phys. Rev. B*, 101:195137, May 2020.
- [119] M. Lein, E. K. U. Gross, and J. P. Perdew. Electron correlation energies from scaled exchange-correlation kernels: Importance of spatial versus temporal nonlocality. *Phys. Rev. B*, 61:13431, 2000.
- [120] Stephen L Adler. Quantum theory of the dielectric constant in real solids. *Phys. Rev.*, 126(2):413, 1962.
- [121] Nathan Wiser. Dielectric constant with local field effects included. *Phys. Rev.*, 129(1):62, 1963.
- [122] Stefan Kurth and John P. Perdew. Density-functional correction of random-phase-approximation correlation with results for jellium surface energies. *Phys. Rev. B*, 59:10461–10468, Apr 1999.
- [123] Adrienn Ruzsinszky, John P. Perdew, and Gbor I. Csonka. A simple but fully nonlocal correction to the random phase approximation. *J. Chem. Phys.*, 134(11):114110, 2011.
- [124] Filipp Furche. Molecular tests of the random phase approximation to the exchange-correlation energy functional. *Phys. Rev. B*, 64(19):195120, 2001.
- [125] Tim Gould, Adrienn Ruzsinszky, and John P Perdew. Simple self-interaction correction to random-phase-approximation-like correlation energies. *Phys. Rev. A*, 100(2):022515, 2019.
- [126] Jefferson E Bates, Niladri Sengupta, Jonathon Sensenig, and Adrienn Ruzsinszky. Adiabatic connection without coupling constant integration. *J. Chem. Theo. Comp.*, 14(6):2979–2990, 2018.
- [127] L Hedin and S Lundqvist. Solid state physics, edited by f. seitz, d. turnbull, and h. ehrenreich. *Academic Press, New York*, 23:1–180, 1969.
- [128] F Gygi and A Baldereschi. Quasiparticle energies in semiconductors: Self-energy correction to the local-density approximation. *Phys. Rev. Lett.*, 62(18):2160, 1989.

- [129] Xavier Gonze and Changyol Lee. Dynamical matrices, born effective charges, dielectric permittivity tensors, and interatomic force constants from density-functional perturbation theory. *Phys. Rev. B*, 55(16):10355, 1997.
- [130] E. E. Salpeter and H. A. Bethe. A relativistic equation for bound-state problems. *Phys. Rev.*, 84:1232–1242, Dec 1951.
- [131] Silvana Botti, Francesco Sottile, Nathalie Vast, Valerio Olevano, Lucia Reining, Hans-Christian Weissker, Angel Rubio, Giovanni Onida, Rodolfo Del Sole, and RW Godby. Long-range contribution to the exchange-correlation kernel of time-dependent density functional theory. *Phys. Rev. B*, 69(15):155112, 2004.
- [132] Xavier Gonze, Bernard Amadon, P-M Anglade, J-M Beuken, François Bottin, Paul Boulanger, Fabien Bruneval, Damien Caliste, Razvan Caracas, Michel Côté, et al. Abinit: First-principles approach to material and nanosystem properties. *Comput. Phys. Commun.*, 180(12):2582–2615, 2009.
- [133] Andrea Marini, Conor Hogan, Myrta Grüning, and Daniele Varsano. Yambo: an ab initio tool for excited state calculations. *Comput. Phys. Commun.*, 180(8):1392–1403, 2009.
- [134] Melissa J Lucero, Thomas M Henderson, and Gustavo E Scuseria. Improved semiconductor lattice parameters and band gaps from a middle-range screened hybrid exchange functional. *J. Phys. Condens. Matter*, 24(14):145504, 2012.
- [135] P. Lautenschlager, M. Garriga, L. Vina, and M. Cardona. Temperature dependence of the dielectric function and interband critical points in silicon. *Phys. Rev. B*, 36:4821–4830, Sep 1987.
- [136] P. Lautenschlager, M. Garriga, S. Logothetidis, and M. Cardona. Interband critical points of gaas and their temperature dependence. *Phys. Rev. B*, 35:9174–9189, Jun 1987.
- [137] Silvana Botti, Francesco Sottile, Nathalie Vast, Valerio Olevano, Lucia Reining, Hans-Christian Weissker, Angel Rubio, Giovanni Onida, Rodolfo Del Sole, and R. W. Godby. Long-range contribution to the exchange-correlation kernel of time-dependent density functional theory. *Phys. Rev. B*, 69:155112, Apr 2004.
- [138] Silvana Botti, Francesco Sottile, Nathalie Vast, Valerio Olevano, Lucia Reining, Hans-Christian Weissker, Angel Rubio, Giovanni Onida, Rodolfo Del Sole, and R. W. Godby. Long-range contribution to the exchange-correlation kernel of time-dependent density functional theory. *Phys. Rev. B*, 69:155112, Apr 2004.
- [139] MP Tosi and FG Fumi. Ionic sizes and born repulsive parameters in the nacl-type alkali halidesii: The generalized huggins-mayer form. *J. Phys. Chem. Solids*, 25(1):45–52, 1964.

- [140] Víctor Luaña and L Pueyo. Simulation of ionic crystals: The ab initio perturbed-ion method and application to alkali hydrides and halides. *Phys. Rev. B*, 41(6):3800, 1990.
- [141] Feiwu Zhang, J. D. Gale, B. P. Uberuaga, C. R. Stanek, and N. A. Marks. Importance of dispersion in density functional calculations of cesium chloride and its related halides. *Phys. Rev. B*, 88(5):054112, 2013.
- [142] J Narain, NK Dwivedi, GG Agrawal, and J Shanker. Structural phase transformation and the equation of state of csci, csbr, and csi crystals. *Phys. Status Solidi B*, 132(2):389–393, 1985.
- [143] W. N. Mei, L. L. Boyer, M. J. Mehl, M. M. Ossowski, and H. T. Stokes. Calculation of electronic, structural, and vibrational properties in alkali halides using a density-functional method with localized densities. *Phys. Rev. B*, 61(17):11425, 2000.
- [144] Pietro Cortona. Direct determination of self-consistent total energies and charge densities of solids: A study of the cohesive properties of the alkali halides. *Phys. Rev. B*, 46(4):2008, 1992.
- [145] J. M. Recio, A. Martín Pendás, E Francisco, M Flórez, and Víctor Luaña. Low- and high-pressure ab initio equations of state for the alkali chlorides. *Phys. Rev. B*, 48(9):5891, 1993.
- [146] Fritz London. The general theory of molecular forces. *Trans. Faraday Soc.*, 33:8b–26, 1937.
- [147] Joseph E Mayer. Dispersion and polarizability and the van der waals potential in the alkali halides. *J. Chem. Phys.*, 1(4):270–279, 1933.
- [148] Mario Tosi. Cohesive energy of the alkali halide crystals. *J. Phys. Chem. Solids*, 24(7):965–967, 1963.
- [149] K Reinitz. Elastic constants of csbr, csi, rbbr, and rbi. *Phys. Rev.*, 123(5):1615, 1961.
- [150] Jianmin Tao, Fan Zheng, Julian Gebhardt, John P. Perdew, and Andrew M. Rappe. Screened van der waals correction to density functional theory for solids. *Phys. Rev. Materials*, 1:020802, Jul 2017.
- [151] C Barrett and TB Massalski. *Structure of Metals 3rd revised edition: Crystallographic Methods, Principles, and Data, International Series on Materials Science and Technology*, 35. Pergamon Press, Oxford, New York, etc, 1987.
- [152] John F Dobson. Beyond pairwise additivity in london dispersion interactions. *Int. J. Quantum Chem.*, 114(18):1157–1161, 2014.
- [153] Anthony M Reilly and Alexandre Tkatchenko. van der waals dispersion interactions in molecular materials: beyond pairwise additivity. *Chem. Sci.*, 6(6):3289–3301, 2015.

- [154] Ulf von Barth and Lars Hedin. A local exchange-correlation potential for the spin polarized case. i. *J. Phys. Condens. Matter*, 5(13):1629, 1972. and references therein.
- [155] Oleg A Vydrov, Gustavo E Scuseria, and John P Perdew. Tests of functionals for systems with fractional electron number. *J. Chem. Phys.*, 126(15):154109, 2007.
- [156] Aron J Cohen, Paula Mori-Sánchez, and Weitao Yang. Insights into current limitations of density functional theory. *Sci.*, 321(5890):792–794, 2008.
- [157] Jeng-Da Chai and Martin Head-Gordon. Long-range corrected hybrid density functionals with damped atom–atom dispersion corrections. *Phys. Chem. Chem. Phys.*, 10(44):6615–6620, 2008.
- [158] Jianwei Sun, Bing Xiao, Yuan Fang, Robin Haunschild, Pan Hao, Adrienn Ruzsinszky, Gábor I Csonka, Gustavo E Scuseria, and John P Perdew. Density functionals that recognize covalent, metallic, and weak bonds. *Phys. Rev. Lett.*, 111(10):106401, 2013.
- [159] Yan Zhao and Donald G Truhlar. The m06 suite of density functionals for main group thermochemistry, thermochemical kinetics, noncovalent interactions, excited states, and transition elements: two new functionals and systematic testing of four m06-class functionals and 12 other functionals. *Theor. Chem. Acc.*, 120(1):215–241, 2008.
- [160] Jorge M del Campo, José L Gázquez, SB Trickey, and Alberto Vela. A new meta-gga exchange functional based on an improved constraint-based gga. *Chem. Phys. Lett.*, 543:179–183, 2012.
- [161] Y. Andersson, D. C. Langreth, and B. I. Lundqvist. van der waals interactions in density-functional theory. *Phys. Rev. Lett.*, 76:102–105, 1996.
- [162] Qin Wu and Weitao Yang. Empirical correction to density functional theory for van der waals interactions. *J. Chem. Phys.*, 116(2):515–524, 2002.
- [163] Axel D Becke and Erin R Johnson. Exchange-hole dipole moment and the dispersion interaction revisited. *J. Chem. Phys.*, 127(15):154108, 2007.
- [164] Jens Antony and Stefan Grimme. Density functional theory including dispersion corrections for intermolecular interactions in a large benchmark set of biologically relevant molecules. *Phys. Chem. Chem. Phys.*, 8(45):5287–5293, 2006.
- [165] Alexandre Tkatchenko and Matthias Scheffler. Accurate molecular van der waals interactions from ground-state electron density and free-atom reference data. *Phys. Rev. Lett.*, 102(7):073005, 2009.
- [166] Takeshi Sato and Hiromi Nakai. Density functional method including weak interactions: Dispersion coefficients based on the local response approximation. *J. Chem. Phys.*, 131(22):224104, 2009.

- [167] M. Dion, H. Rydberg, E. Schröder, D. C. Langreth, and B. I. Lundqvist. Van der waals density functional for general geometries. *Phys. Rev. Lett.*, 92:246401, 2004.
- [168] Riccardo Sabatini, Tommaso Gorni, and Stefano de Gironcoli. Nonlocal van der waals density functional made simple and efficient. *Phys. Rev. B*, 87(4):041108, 2013.
- [169] D. C. Langreth and J. P. Perdew. The exchange-correlation energy of a metallic surface. *Solid State Commun.*, 17:1425, 1975.
- [170] D. C. Langreth and J. P. Perdew. Exchange-correlation energy of a metallic surface: Wave-vector analysis. *Phys. Rev. B*, 15:2884, 1977.
- [171] H. Eshuis, J. E. Bates, and F. Furche. Electron correlation methods based on the random phase approximation. *Theor. Chem. Acc.*, 131:1084, 2012.
- [172] Xinguo Ren, Patrick Rinke, Christian Joas, and Matthias Scheffler. Random-phase approximation and its applications in computational chemistry and materials science. *J. Mater. Sci.*, 47:7447–7471, 2012.
- [173] Henk Eshuis, Julian Yarkony, and Filipp Furche. Fast computation of molecular random phase approximation correlation energies using resolution of the identity and imaginary frequency integration. *J. Chem. Phys.*, 132:234114, 2010.
- [174] Mauro Del Ben, J. Hutter, and Joost VandeVondele. Electron correlation in the condensed phase from a resolution of identity approach based on the gaussian and plane waves scheme. *J. Chem. Theory Comput.*, 9:2654–2671, 2013.
- [175] M. Kaltak, J. Klimeš, and G. Kresse. Cubic scaling algorithm for the random phase approximation: Self-interstitials and vacancies in si. *Phys. Rev. B*, 90:054115, 2014.
- [176] Mihály Kállay. Linear-scaling implementation of the direct random-phase approximation. *J. Chem. Phys.*, 142:204105, 2015.
- [177] Jan Wilhelm, Patrick Seewald, Mauro Del Ben, and J. Hutter. Large-scale cubic-scaling random phase approximation correlation energy calculations using a gaussian basis. *J. Chem. Theory Comput.*, 12:5851–5859, 2016.
- [178] B. M. Axilrod and E. Teller. Interaction of the van der waals type between three atoms. *J. Chem. Phys.*, 11:299, 1943.
- [179] D. Lu, H. Nguyen, and G. Galli. Power series expansion of the random phase approximation correlation energy: The role of third- and higher-order contributions. *J. Chem. Phys.*, 133:154110, 2010.
- [180] Menno Bokdam, Jonathan Lahnsteiner, Benjamin Ramberger, Tobias Schäfer, and Georg Kresse. Assessing density functionals using many body theory for hybrid perovskites. *Phys. Rev. Lett.*, 119(14):145501, 2017.

- [181] Marco Casadei, Xinguo Ren, Patrick Rinke, Angel Rubio, and Matthias Scheffler. Density-functional theory for f-electron systems: The α - γ phase transition in cerium. *Phys. Rev. Lett.*, 109(14):146402, 2012.
- [182] T. Björkman, A. Gulans, A. V. Krasheninnikov, and R. M. Nieminen. van der waals bonding in layered compounds from advanced density-functional first-principles calculations. *Phys. Rev. Lett.*, 108:235502, 2012.
- [183] Zidan Yan, John P Perdew, and Stefan Kurth. Density functional for short-range correlation: Accuracy of the random-phase approximation for isoelectronic energy changes. *Phys. Rev. B*, 61(24):16430, 2000.
- [184] Philipp Furche and Troy Van Voorhis. Fluctuation-dissipation theorem density-functional theory. *J. Chem. Phys.*, 122(16):164106, 2005.
- [185] Jefferson E Bates, Jonathon Sensenig, and Adrienn Ruzsinszky. Convergence behavior of the random phase approximation renormalized correlation energy. *Phys. Rev. B*, 95(19):195158, 2017.
- [186] Biswajit Santra, Jiří Klimeš, Dario Alfè, Alexandre Tkatchenko, Ben Slater, Angelos Michaelides, Roberto Car, and Matthias Scheffler. Hydrogen bonds and van der waals forces in ice at ambient and high pressures. *Phys. Rev. Lett.*, 107(18):185701, 2011.
- [187] Alberto Ambrosetti, Anthony M Reilly, Robert A DiStasio Jr, and Alexandre Tkatchenko. Long-range correlation energy calculated from coupled atomic response functions. *J. Chem. Phys.*, 140(18):18A508, 2014.
- [188] Anthony M Reilly and Alexandre Tkatchenko. Seamless and accurate modeling of organic molecular materials. *J. Phys. Chem. Lett.*, 4(6):1028–1033, 2013.
- [189] Anthony M Reilly and Alexandre Tkatchenko. Understanding the role of vibrations, exact exchange, and many-body van der waals interactions in the cohesive properties of molecular crystals. *J. Chem. Phys.*, 139(2):024705, 2013.
- [190] J. P. Perdew and K. Schmidt. Jacob’s ladder of density functional approximations for the exchange-correlation energy. In V. Van Doren, C. Van Alsenoy, and P. Geerlings, editors, *Density Functional Theory and Its Applications to Materials*, volume 577, pages 1–20. AIP Conference Proceedings, Melville, N.Y., 2001.
- [191] Jianwei Sun, Robin Haunschuld, Bing Xiao, Ireneusz W Bulik, Gustavo E Scuseria, and John P Perdew. Semilocal and hybrid meta-generalized gradient approximations based on the understanding of the kinetic-energy-density dependence. *J. Chem. Phys.*, 138(4):044113, 2013.
- [192] J. Sun, R C. Remsing, Y. Zhang, Z. Sun, A. Ruzsinszky, H. Peng, Z. Yang, A. Paul, U. Waghmare, X. Wu, M L. Klein, and J. P. Perdew. Accurate first-principles structures and energies of diversely bonded systems from an efficient density functional. *Nat. Chem.*, 8:831–836, 2016.

- [193] J. G. Brandenburg, J. E. Bates, J. Sun, and J. P. Perdew. Benchmark tests of a strongly constrained semilocal functional with a long-range dispersion correction. *Phys. Rev. B*, 94:115144, 2016.
- [194] Philipp Furche. Developing the random phase approximation into a practical post-kohnsham correlation model. *J. Chem. Phys.*, 129:114105, 2008.
- [195] Daniel Neuhauser, Eran Rabani, and Roi Baer. Expeditious stochastic calculation of random-phase approximation energies for thousands of electrons in three dimensions. *J. Phys. Chem. Lett.*, 4:1172–1176, 2013.
- [196] Jonathan E. Moussa. Cubic-scaling algorithm and self-consistent field for the random-phase approximation with second-order screened exchange. *J. Chem. Phys.*, 140:014107, 2014.
- [197] Nicola Colonna, Maria Hellgren, and Stefano de Gironcoli. Correlation energy within exact-exchange adiabatic connection fluctuation-dissipation theory: Systematic development and simple approximations. *Phys. Rev. B*, 90(12):125150, 2014.
- [198] Thomas Olsen and Kristian S Thygesen. Beyond the random phase approximation: Improved description of short-range correlation by a renormalized adiabatic local density approximation. *Phys. Rev. B*, 88(11):115131, 2013.
- [199] Thomas S. Jauho, Thomas Olsen, Thomas Bligaard, and Kristian S. Thygesen. Improved description of metal oxide stability: Beyond the random phase approximation with renormalized kernels. *Phys. Rev. B*, 92:115140, 2015.
- [200] Jefferson E Bates, Niladri Sengupta, Jonathon Sensenig, and Adrienn Ruzsinszky. Adiabatic connection without coupling constant integration. *J. Chem. Theory Comput.*, 14(6):2979–2990, 2018.
- [201] G. Jansen, R.-F. Liu, and J. G. Ángyán. On the equivalence of ring-coupled cluster and adiabatic connection fluctuation-dissipation theorem random phase approximation correlation energy expressions. *J. Chem. Phys.*, 133:154106, 2010.
- [202] János G. Ángyán, Ru-Fen Liu, Julien Toulouse, and Georg Jansen. Correlation energy expressions from the adiabatic-connection fluctuation–dissipation theorem approach. *J. Chem. Theory Comput.*, 7(10):3116–3130, 2011.
- [203] David L Freeman. Coupled-cluster expansion applied to the electron gas: Inclusion of ring and exchange effects. *Phys. Rev. B*, 15(12):5512, 1977.
- [204] A. Grüneis, M. Marsman, J. Harl, L. Schimka, and G. Kresse. Making the random phase approximation to electronic correlation accurate. *J. Chem. Phys.*, 131:154115, 2009.
- [205] Joachim Paier, Benjamin G. Janesko, Thomas M. Henderson, Gustavo E. Scuseria, Andreas Grüneis, and Georg Kresse. Hybrid functionals including random phase approximation correlation and second-order screened exchange. *J. Chem. Phys.*, 132:094103, 2010.

- [206] P. E. Blöchl. Projector augmented-wave method. *Phys. Rev. B*, 50:17953–17979, 1994.
- [207] Michael Walter, Hannu Häkkinen, Lauri Lehtovaara, Martti Puska, Jussi Enkovaara, Carsten Rostgaard, and Jens Jorgen Mortensen. Time-dependent density-functional theory in the projector augmented-wave method. *J. Chem. Phys.*, 128:244101, 2008.
- [208] J. J. Mortensen, L. B. Hansen, and K. W. Jacobsen. Real-space grid implementation of the projector augmented wave method. *Phys. Rev. B*, 71:035109, 2005.
- [209] S. R. Bahn and K. W. Jacobsen. An object-oriented scripting interface to a legacy electronic structure code. *Comput. Sci. Eng.*, 4:56–66, 2002.
- [210] Jürgen Hafner. Ab-initio simulations of materials using vasp: Density-functional theory and beyond. *J. Comput. Chem.*, 29(13):2044–2078, 2008.
- [211] Hendrik J. Monkhorst and James D. Pack. Special points for brillouin-zone integrations. *Phys. Rev. B*, 13:5188–5192, 1976.
- [212] Georg Kresse and D Joubert. From ultrasoft pseudopotentials to the projector augmented-wave method. *Phys. Rev. B*, 59(3):1758, 1999.
- [213] Jun Yan, Jens. J. Mortensen, Karsten W. Jacobsen, and Kristian S. Thygesen. Linear density response function in the projector augmented wave method: Applications to solids, surfaces, and interfaces. *Phys. Rev. B*, 83(24):245122, 2011.
- [214] Ravishankar Sundararaman and T. A. Arias. Regularization of the coulomb singularity in exact exchange by wigner-seitz truncated interactions: Towards chemical accuracy in nontrivial systems. *Phys. Rev. B*, 87:165122, 2013.
- [215] A Togo and I Tanaka. First principles phonon calculations in materials science. *Scr. Mater.*, 108:1–5, Nov 2015.
- [216] Stefano Baroni, Stefano De Gironcoli, Andrea Dal Corso, and Paolo Giannozzi. Phonons and related crystal properties from density-functional perturbation theory. *Rev. Mod. Phys.*, 73(2):515, 2001.
- [217] Neil W Ashcroft and N David Mermin. *Solid State Physics (Holt, Rinehart and Winston, New York, 1976)*. New York: Holt, Rinehart and Winston, 2005.
- [218] J Vallin, O Beckman, and K Salama. Elastic constants of csbr and csi from 4.2 k to room temperature. *J. Appl. Phys.*, 35(4):1222–1223, 1964.
- [219] RK Singh, HN Gupta, and MK Agrawal. Extended three-body-force shell model dynamics of heavier alkali-halide crystals. *Phys. Rev. B*, 17(2):894, 1978.
- [220] GK White and JG Collins. The thermal expansion of alkali halides at low temperatures. ii. sodium, rubidium and caesium halides. In *Proceedings of the Royal Society of London A: Mathematical, Physical and Engineering Sciences*, volume 333, pages 237–259. The Royal Society, 1973.

- [221] H. K. Mao, Y Wu, R. J. Hemley, L. C. Chen, J. F. Shu, L. W. Finger, and D. E. Cox. High-pressure phase transition and equation of state of csi. *Phys. Rev. Lett.*, 64(15):1749, 1990.
- [222] Linus Pauling. The nature of the chemical bond. iv. the energy of single bonds and the relative electronegativity of atoms. *J. Am. Chem. Soc.*, 54:3570–3582, 1932.
- [223] Massimiliano Corradini, Rodolfo Del Sole, Giovanni Onida, and Maurizia Palumbo. Analytical expressions for the local-field factor $g(q)$ and the exchange-correlation kernel $k_{xc}(r)$ of the homogeneous electron gas. *Phys. Rev. B*, 57(23):14569, 1998.
- [224] O Anatole von Lilienfeld and Alexandre Tkatchenko. Two- and three-body interatomic dispersion energy contributions to binding in molecules and solids. *J. Chem. Phys.*, 132(23):234109, 2010.
- [225] J. D. Hunter. Matplotlib: A 2d graphics environment. *Comput. Sci. Eng.*, 9(3):90–95, 2007.
- [226] RL Orr. Heats of formation of solid au-cu alloys. *Acta Metall.*, 8(7):489–493, 1960.
- [227] Ralph Hultgren, Pramod D Desai, Donald T Hawkins, Molly Gleiser, and Kenneth K Kelley. Selected values of the thermodynamic properties of binary alloys. Technical report, National Standard Reference Data System, 1973.
- [228] Rickard Armiento and Ann E Mattsson. Functional designed to include surface effects in self-consistent density functional theory. *Phys. Rev. B*, 72(8):085108, 2005.
- [229] Paul Ziesche, Stefan Kurth, and John P Perdew. Density functionals from lda to gga. *Comput. Mater. Sci.*, 11(2):122–127, 1998.
- [230] Jianwei Sun, Robin Haunschild, Bing Xiao, Ireneusz W Bulik, Gustavo E Scuseria, and John P Perdew. Semilocal and hybrid meta-generalized gradient approximations based on the understanding of the kinetic-energy-density dependence. *J. Chem. Phys.*, 138(4):044113, 2013.
- [231] Eric B Isaacs and Chris Wolverton. Performance of the strongly constrained and appropriately normed density functional for solid-state materials. *Phys. Rev. Mater.*, 2(6):063801, 2018.
- [232] Yongsheng Zhang, Georg Kresse, and C Wolverton. Nonlocal first-principles calculations in cu-au and other intermetallic alloys. *Phys. Rev. Lett.*, 112(7):075502, 2014.
- [233] V Ozoliņš, C Wolverton, and Alex Zunger. Cu-au, ag-au, cu-ag, and ni-au intermetallics: First-principles study of temperature-composition phase diagrams and structures. *Phys. Rev. B*, 57(11):6427, 1998.

- [234] Li-Yun Tian, Henrik Levämäki, Matti Ropo, Kalevi Kokko, Ágnes Nagy, and Levente Vitos. Exchange-correlation catastrophe in cu-au: A challenge for semilocal density functional approximations. *Phys. Rev. Lett.*, 117(6):066401, 2016.
- [235] H. Okamoto, D. J. Chakrabarti, D. E. Laughlin, and T. B. Massalski. The au-cu (gold-copper) system. *Journal of Phase Equilibria*, 8(5):454, Oct 1987.
- [236] David C. Langreth and John P. Perdew. Theory of nonuniform electronic systems. i. analysis of the gradient approximation and a generalization that works. *Phys. Rev. B*, 21:5469–5493, Jun 1980.
- [237] Charlotte L Bracey, Peter R Ellis, and Graham J Hutchings. Application of copper–gold alloys in catalysis: current status and future perspectives. *Chemical Society Reviews*, 38(8):2231–2243, 2009.
- [238] J. Mahanty and Roger Taylor. Van der waals forces in metals. *Phys. Rev. B*, 17:554–559, Jan 1978.
- [239] Alexander L Fetter and John Dirk Walecka. *Quantum theory of many-particle systems*. Courier Corporation, 2012.
- [240] Haowei Peng and John P Perdew. Rehabilitation of the perdew-burke-ernzerhof generalized gradient approximation for layered materials. *Physical Review B*, 95(8):081105, 2017.
- [241] G. Kresse and J. Furthmüller. Efficient iterative schemes for ab initio total-energy calculations using a plane-wave basis set. *Phys. Rev. B*, 54:11169–11186, Oct 1996.
- [242] Soner Steiner, Sergii Khmelevskyi, Martijn Marsmann, and Georg Kresse. Calculation of the magnetic anisotropy with projected-augmented-wave methodology and the case study of disordered fe 1- x co x alloys. *Physical Review B*, 93(22):224425, 2016.
- [243] Francis Birch. Finite elastic strain of cubic crystals. *Phys. Rev.*, 71:809–824, Jun 1947.
- [244] Andreas Grüneis, Martijn Marsman, Judith Harl, Laurids Schimka, and Georg Kresse. Making the random phase approximation to electronic correlation accurate. *The Journal of chemical physics*, 131(15):154115, 2009.
- [245] Patanachai Janthon, Sijie Luo, Sergey M Kozlov, Francesc Vines, Jumras Limtrakul, Donald G Truhlar, and Francesc Illas. Bulk properties of transition metals: A challenge for the design of universal density functionals. *Journal of chemical theory and computation*, 10(9):3832–3839, 2014.
- [246] Hillard Bell Huntington. *The elastic constants of crystals*, volume 7. Elsevier, 1958.
- [247] François Cardarelli. *Less Common Nonferrous Metals*. Springer International Publishing, Cham, 2018.

- [248] S. G. O'Hara and B. J. Marshall. Elastic constants of copper-rich alloys with gold. *Phys. Rev. B*, 3:4002–4006, Jun 1971.
- [249] Cristian Teodosiu. *Elastic models of crystal defects*. Springer Science & Business Media, 2013.
- [250] Gene Simmons. Single crystal elastic constants and calculated aggregate properties. Technical report, SOUTHERN METHODIST UNIV DALLAS TEX, 1965.
- [251] John P Perdew, Adrienn Ruzsinszky, Gábor I Csonka, Lucian A Constantin, and Jianwei Sun. Workhorse semilocal density functional for condensed matter physics and quantum chemistry. *Physical Review Letters*, 103(2):026403, 2009.
- [252] Ngoc Linh Nguyen, Nicola Colonna, and Stefano de Gironcoli. Ab initio self-consistent total-energy calculations within the exx/rpa formalism. *Phys. Rev. B*, 90:045138, July 2014.
- [253] Thomas S Jauho, Thomas Olsen, Thomas Bligaard, and Kristian S Thygesen. Improved description of metal oxide stability: Beyond the random phase approximation with renormalized kernels. *Phys. Rev. B*, 92(11):115140, 2015.
- [254] Charles Kittel, Paul McEuen, and Paul McEuen. *Introduction to solid state physics*, volume 8. Wiley New York, 1976.
- [255] Wolfgang Pfeiler. *Alloy physics: a comprehensive reference*. John Wiley & Sons, 2007.
- [256] Emmanuel Mooser and WB Pearson. On the crystal chemistry of normal valence compounds. *Acta Crystallogr.*, 12(12):1015–1022, 1959.
- [257] Frank Stein, Martin Palm, and Gerhard Sauthoff. Structure and stability of laves phases. part i. critical assessment of factors controlling laves phase stability. *Intermetallics*, 12(7-9):713–720, 2004.
- [258] Frederick E Wang. *Bonding theory for metals and alloys*. Elsevier, 2018.
- [259] Patanachai Janthon, Sijie Luo, Sergey M Kozlov, Francesc Vines, Jumras Limtrakul, Donald G Truhlar, and Francesc Illas. Bulk properties of transition metals: a challenge for the design of universal density functionals. *J Chem. Theory Comput.*, 10(9):3832–3839, 2014.
- [260] RF Zhang, SH Sheng, and BX Liu. Predicting the formation enthalpies of binary intermetallic compounds. *Chem. Phys. Lett.*, 442(4-6):511–514, 2007.
- [261] TB Massalski, Hiroaki Okamoto, Linda Kacprzak, and PR Subramanian. *Binary alloy phase diagrams, plus updates*. ASM International, Materials Park, OH, 1996.
- [262] Shunroku Watanabe and OJ Kleppa. Thermochemistry of alloys of transition metals: Part iv. alloys of copper with scandium, yttrium, lanthanum, and lutetium. *Metall. Trans. B*, 15(2):357–368, 1984.

- [263] Qiti Guo and Ole Jakob Kleppa. The standard enthalpies of formation of the compounds of early transition metals with late transition metals and with noble metals as determined by kleppa and co-workers at the university of chicagoa review. *J. Alloys Compd.*, 321(2):169–182, 2001.
- [264] K Fitzner, W-G Jung, and OJ Kleppa. Thermochemistry of binary alloys of transition metals: the me-sc, me-y, and me-la (me= ag, au) systems. *Metall. Trans. A*, 22(5):1103–1111, 1991.
- [265] Kamal Mahdouk and Jean-Claude Gachon. Calorimetric study of the hf–os and os–ti systems. *J. Alloys Compd.*, 278(1-2):185–189, 1998.
- [266] N Selhaoui and OJ Kleppa. Standard enthalpies of formation of yttrium alloys, y-me (me= ru, rh, pd, os, ir, pt), by high-temperature calorimetry. *J. Chem. Phys.*, 90:435–443, 1993.
- [267] N Selhaoui and OJ Kleppa. Standard enthalpies of formation of scandium alloys, sc+ me (me= fe, co, ni, ru, rh, pd, ir, pt), by high-temperature calorimetry. *J. Alloys Compd.*, 191(1):145–149, 1993.
- [268] Letitia Topor and OJ Kleppa. Standard enthalpies of formation of ptti, ptzr, and pthf. *Metall. Trans. A*, 19(7):1827–1831, 1988.
- [269] DE Eastman and JK Cashion. Photoemission from cu, ag, and au in the 10-to 27-ev energy range. *Phys. Rev. Lett.*, 24(7):310, 1970.
- [270] PT Andrews and LA Hisscott. X-ray photoelectron spectroscopy of some cu-zn alloys. *J. Phys. F Met. Phys.*, 5(8):1568, 1975.
- [271] RG Jordan, DM Zehner, NM Harrison, PJ Durham, and WM Temmerman. An xps investigation of the electronic structure in agzn. *Z. Phys., B, Condens. Matter.*, 75(3):291–295, 1989.
- [272] JA Leiro, K Kokko, and R Laihia. Electronic structures of aumg and auzn. *J ELECTRON SPECTROSC*, 113(2-3):167–174, 2001.
- [273] JD Riley, RCG Leckey, JG Jenkin, J Liesegang, and RT Poole. Ultraviolet photoelectron spectra of the outer d bands of ag-in and ag-cd alloys. *J. Phys. F Met. Phys.*, 6(2):293, 1976.
- [274] FL Battye, H Schulz, A Goldmann, S Hufner, D Seipler, and B Elschner. Ultraviolet photoemission from intermetallic compounds with cscl structure: Scag, scpd, scir and scr. *J. Phys. F Met. Phys.*, 8(4):709, 1978.
- [275] John C Fuggle, F Ulrich Hillebrecht, R Zeller, Zygmunt Zołnierek, Peter A Bennett, and Ch Freiburg. Electronic structure of ni and pd alloys. i. x-ray photoelectron spectroscopy of the valence bands. *Phys. Rev. B*, 27(4):2145, 1983.

- [276] H Höchst, S Hüfner, and A Goldmann. Xps-valence bands of iron, cobalt, palladium and platinum. *Phys. Lett. A*, 57(3):265–266, 1976.
- [277] Johannes W Niemantsverdriet. *Spectroscopy in catalysis: an introduction*. John Wiley & Sons, 2007.
- [278] P Steiner, H Höchst, J Schneider, S Hüfner, and C Politis. The xps valence band spectra of hf metal and $hfc_x n_y o_z$ compounds and the correlation to their superconductivity. *Z. Phys., B, Condens. Matter.*, 33(3):241–250, 1979.
- [279] Atsushi Fujimori and Louis Schlapbach. Electronic structure of yttrium hydride studied by x-ray photoemission spectroscopy. *J. Phys. C: Solid State Phys.*, 17(2):341, 1984.
- [280] Masaoki Oku, Toetsu Shishido, Takeshi Shinohara, Tsuguo Fukuda, Qiang Sun, Yoshiyuki Kawazoe, and Kazuaki Wagatsuma. Electronic structures of perovskite-type $scrh_3bx$ ($0 \leq x \leq 1$): X-ray photoelectron and nuclear magnetic resonance spectroscopies and ab initio band calculation. *J. Alloys Compd.*, 339(1-2):317–326, 2002.
- [281] G Crecelius and GK Wertheim. Effects of atomic order in α - and β -phase ag-cd alloys studied by x-ray photoelectron spectroscopy. *Phys. Rev. B*, 18(12):6525, 1978.
- [282] K Fitzner and OJ Kleppa. Thermochemistry of binary alloys of transition metals: The me-ti, me-zr, and me-hf (me= ag, au) systems. *Metall Mater Trans A*, 23(3):997–1003, 1992.
- [283] Qiti Guo and OJ Kleppa. Standard enthalpies of formation of ni_3v , ni_3hf , pd_3hf , and pt_3sc and systematics of ΔH_f for ni_3me (me. ident. la, hf, ta), pd_3me (me. ident. la, hf, ta) and pt_3me (me. ident. sc, ti, v or y, zr, nb) alloys. *J. Phys. Chem.*, 99(9):2854–2856, 1995.
- [284] CS Fadley and DA Shirley. *Electronic Densities of States from X-Ray Photoelectron Spectroscopy*. Number 323. Nat. Bur. Stand. (U.S.A.), 1971.
- [285] E Vogelzang, M Sikkens, and GA Sawatzky. Intrinsically selective absorption in alloys of early with late transition metals. *Sol. Energy Mater.*, 14(3-5):365–373, 1986.
- [286] Christopher J Cramer and Donald G Truhlar. Density functional theory for transition metals and transition metal chemistry. *Phys. Chem. Chem. Phys.*, 11(46):10757–10816, 2009.
- [287] Adrienn Ruzsinszky, Niraj K Nepal, JM Pitarke, and John P Perdew. Constraint-based wave vector and frequency dependent exchange-correlation kernel of the uniform electron gas. *Phys. Rev. B*, 101(24):245135, 2020.
- [288] David Lazarus. The variation of the adiabatic elastic constants of kcl, nacl, cuzn, cu, and al with pressure to 10,000 bars. *Phys. Rev.*, 76(4):545, 1949.

- [289] N Nakanishi, T Mori, S Miura, Y Murakami, and So Kachi. Pseudoelasticity in au-cd thermoelastic martensite. *PHILOS. MAG.*, 28(2):277–292, 1973.
- [290] Venkata Suresh Guthikonda and Ryan S Elliott. An effective interaction potential model for the shape memory alloy au-cd. *CONTINUUM. MECH. THERM.*, 21(4):269–295, 2009.
- [291] James R Morris, Yiyang Ye, Yong-Bin Lee, Bruce N Harmon, Karl A Gschneidner Jr, and Alan M Russell. Ab initio calculation of bulk and defect properties of ductile rare-earth intermetallic compounds. *Acta Mater.*, 52(16):4849–4857, 2004.
- [292] Stanley Zirinsky. The temperature dependence of the elastic constants of gold-cadmium alloys. *Acta Metall.*, 4(2):164–171, 1956.
- [293] Heinz Raether. *Excitation of plasmons and interband transitions by electrons*, volume 88. Springer, 2006.
- [294] W Schülke, JR Schmitz, H Schulte-Schrepping, and A Kaprolat. Dynamic and static structure factor of electrons in si: Inelastic x-ray scattering results. *Phys. Rev. B*, 52(16):11721, 1995.
- [295] Carsten A Ullrich. *Time-dependent density-functional theory: concepts and applications*. OUP Oxford, 2011.
- [296] D Pines. *Elementary Excitations in Solids*. Benjamin, New York, 1964.
- [297] Gabriele Giuliani and Giovanni Vignale. *Quantum theory of the electron liquid*. Cambridge university press, 2005.
- [298] A Vom Felde, J Sprösser-Prou, and J Fink. Valence-electron excitations in the alkali metals. *Phys. Rev. B*, 40(15):10181, 1989.
- [299] David Pines and Philippe Nozières. *The Theory of Quantum Liquids V. 1: Normal Fermi Liquids*. Benjamin, 1966.
- [300] Giovanni Vignale and Walter Kohn. Current-dependent exchange-correlation potential for dynamical linear response theory. *Phys. Rev. Lett.*, 77(10):2037, 1996.
- [301] Giovanni Vignale, Carsten A Ullrich, and Sergio Conti. Time-dependent density functional theory beyond the adiabatic local density approximation. *Phys. Rev. Lett.*, 79(24):4878, 1997.
- [302] Carsten A Ullrich and Giovanni Vignale. Time-dependent current-density-functional theory for the linear response of weakly disordered systems. *Phys. Rev. B*, 65(24):245102, 2002.
- [303] F Aryasetiawan and K Karlsson. Energy loss spectra and plasmon dispersions in alkali metals: Negative plasmon dispersion in cs. *Phys. Rev. Lett.*, 73(12):1679, 1994.

- [304] Wei Ku and Adolfo G Eguiluz. Plasmon lifetime in k: a case study of correlated electrons in solids amenable to ab initio theory. *Phys. Rev. Lett.*, 82(11):2350, 1999.
- [305] M Taut. Exchange-correlation correction to the dielectric function of the inhomogeneous electron gas. *J. Phys. Condens. Matter*, 4(48):9595, 1992.
- [306] M Taut and K Sturm. Plasmon dispersion constant of the alkali metals. *Solid State Commun.*, 82(4):295–299, 1992.
- [307] Krzysztof Tatarczyk, Arno Schindlmayr, and Matthias Scheffler. Exchange-correlation kernels for excited states in solids. *Phys. Rev. B*, 63(23):235106, 2001.
- [308] John P Perdew, Adrienn Ruzsinszky, Jianmin Tao, Viktor N Staroverov, Gustavo E Scuseria, and Gábor I Csonka. Prescription for the design and selection of density functional approximations: More constraint satisfaction with fewer fits. *J. Chem. Phys.*, 123(6):062201, 2005.
- [309] A Zangwill and Paul Soven. Density-functional approach to local-field effects in finite systems: Photoabsorption in the rare gases. *Phys. Rev. A*, 21(5):1561, 1980.
- [310] CF V Weizsäcker. Zur theorie der kernmassen. *Zeitschrift für Physik*, 96(7-8):431–458, 1935.
- [311] Setsuo Ichimaru. Strongly coupled plasmas: high-density classical plasmas and degenerate electron liquids. *Rev Mod. Phys.*, 54(4):1017, 1982.
- [312] KS Singwi, MP Tosi, RH Land, and A Sjölander. Electron correlations at metallic densities. *Phys. Rev.*, 176(2):589, 1968.
- [313] Andrew A Quong and Adolfo G Eguiluz. First-principles evaluation of dynamical response and plasmon dispersion in metals. *Phys. Rev. Lett.*, 70(25):3955, 1993.
- [314] E Petri and A Otto. Direct nonvertical interband and intraband transitions in al. *Phys. Rev. Lett.*, 34(20):1283, 1975.
- [315] Andrzej Fleszar, Roland Stumpf, and Adolfo G Eguiluz. One-electron excitations, correlation effects, and the plasmon in cesium metal. *Phys. Rev. B*, 55(4):2068, 1997.
- [316] E Jensen and EW Plummer. Experimental band structure of na. *Phys. Rev. Lett.*, 55(18):1912, 1985. ; P.H. Citrin et al, *ibid.* 61, 1021 (1988); B. S. Itchkawitz et al., *ibid.* 68, 2488 (1993).
- [317] Alan M Lewis and Timothy C Berkelbach. Ab initio lifetime and concomitant double-excitation character of plasmons at metallic densities. *Phys. Rev. Lett.*, 122(22):226402, 2019.
- [318] Naoki Iwamoto and EKV Gross. Correlation effects on the third-frequency-moment sum rule of electron liquids. *Phys. Rev. B*, 35(6):3003, 1987.

- [319] E. K. U. Gross and Walter Kohn. Local density-functional theory of frequency-dependent linear response. *Phys. Rev. Lett.*, 55:2850–2852, 1985.
- [320] Ph Nozières and D Pines. A dielectric formulation of the many body problem: Application to the free electron gas. *Nuovo Cimento [X]*, 9(3):470–490, 1958.
- [321] Olle Gunnarsson and Bengt I Lundqvist. Exchange and correlation in atoms, molecules, and solids by the spin-density-functional formalism. *Phys. Rev. B*, 13(10):4274, 1976.
- [322] David M Ceperley and Berni J Alder. Ground state of the electron gas by a stochastic method. *Phys. Rev. Lett.*, 45(7):566, 1980.
- [323] Jianwei Sun, John P Perdew, and Michael Seidl. Correlation energy of the uniform electron gas from an interpolation between high- and low-density limits. *Phys. Rev. B*, 81(8):085123, 2010.
- [324] Puskar Bhattarai, Abhirup Patra, Chandra Shahi, and John P Perdew. How accurate are the parametrized correlation energies of the uniform electron gas? *Phys. Rev. B*, 97(19):195128, 2018.
- [325] Zhixin Qian and Giovanni Vignale. Dynamical exchange-correlation potentials for an electron liquid. *Phys. Rev. B*, 65(23):235121, 2002.
- [326] A. W. Overhauser. Exchange and correlation instabilities of simple metals. *Phys. Rev.*, 167(3):691, 1968.
- [327] J. P. Perdew and T Datta. Charge and spin density waves in jellium. *Phys. Stat. Sol. (b)*, 102(1):283–293, 1980.
- [328] Saverio Moroni, David M Ceperley, and Gaetano Senatore. Static response and local field factor of the electron gas. *Phys. Rev. Lett.*, 75(4):689, 1995.
- [329] John P Perdew, Huy Q Tran, and Elizabeth D Smith. Stabilized jellium: Structureless pseudopotential model for the cohesive and surface properties of metals. *Phys. Rev. B*, 42(18):11627, 1990.
- [330] Carsten A Ullrich and Kieron Burke. Excitation energies from time-dependent density-functional theory beyond the adiabatic approximation. *J. Chem. Phys.*, 121(1):28–35, 2004.
- [331] K S Singwi, A Sjölander, M P Tosi, and R H Land. Electron correlations at metallic densities. iv. *Phys. Rev. B*, 1(3):1044, 1970.
- [332] P R Antoniewicz and Leonard Kleinman. Kohn-sham exchange potential exact to first order. *Phys. Rev. B*, 31(10):6779, 1985.
- [333] S. K. Ma and Keith A Brueckner. Correlation energy of an electron gas with a slowly varying high density. *Phys. Rev.*, 165(1):18, 1968.

- [334] Antonio Cancio, Guo P Chen, Brandon T Krull, and Kieron Burke. Fitting a round peg into a round hole: Asymptotically correcting the generalized gradient approximation for correlation. *J. Chem. Phys.*, 149(8):084116, 2018.
- [335] Jianmin Tao, John P Perdew, Luis Miguel Almeida, Carlos Fiolhais, and Stephan Kümmel. Nonempirical density functionals investigated for jellium: Spin-polarized surfaces, spherical clusters, and bulk linear response. *Phys. Rev. B*, **77**(24):245107, 2008.
- [336] D Ceperley. Ground state of the fermion one-component plasma: A monte carlo study in two and three dimensions. *Phys. Rev. B*, 18(7):3126, 1978.
- [337] A Holas. in *Strongly Coupled Plasma Physics, edited by F.J. Rogers and H. Dewitt, NATO Advanced Study Institute Series B:*, volume **154**. Plenum, New York, 1986.
- [338] Sergio Conti and Giovanni Vignale. Elasticity of an electron liquid. *Phys. Rev. B*, 60(11):7966, 1999.
- [339] VU Nazarov, JM Pitarke, Y Takada, Giovanni Vignale, and Y-C Chang. Including nonlocality in the exchange-correlation kernel from time-dependent current density functional theory: Application to the stopping power of electron liquids. *Phys. Rev. B*, 76(20):205103, 2007.
- [340] VU Nazarov, G Vignale, and Y-C Chang. Dynamical many-body corrections to the residual resistivity of metals. *Phys. Rev. B*, 89(24):241108, 2014.
- [341] VU Nazarov, Giovanni Vignale, and Y-C Chang. Exact dynamical exchange-correlation kernel of a weakly inhomogeneous electron gas. *Phys. Rev. Lett.*, 102(11):113001, 2009.
- [342] BC Larson, JZ Tischler, ED Isaacs, P Zschack, A Fleszar, and AG Eguiluz. Inelastic x-ray scattering as a probe of the many-body local-field factor in metals. *Phys. Rev. Lett.*, 77(7):1346, 1996.

APPENDIX

LIST OF PUBLICATIONS

- *Rocksalt or cesium chloride: Investigating the relative stability of the cesium halide structures with random phase approximation based methods.* **Niraj K. Nepal**, Adrienn Ruzsinszky, and Jefferson E. Bates, Phys. Rev. B 97, 115140 (2018).
- *First-principles study of mechanical and electronic properties of bent monolayer transition metal dichalcogenides.* **Niraj K. Nepal**, Liping Yu, Qimin Yan, and Adrienn Ruzsinszky, Phys. Rev. Materials 3 (7), 073601 (2019).
- *Treating different bonding situations: Revisiting Au-Cu alloys using the random phase approximation.* **Niraj K. Nepal**, Santosh Adhikari, Jefferson E. Bates, and Adrienn Ruzsinszky, Phys. Rev. B 100 (4), 045135 (2019).
- *Understanding plasmon dispersion in nearly free electron metals: Relevance of exact constraints for exchange-correlation kernels within time-dependent density functional theory.* **Niraj K. Nepal**, Santosh Adhikari, Bimal Neupane, Shiqi Ruan, Santosh Neupane, and Adrienn Ruzsinszky, Phys. Rev. B 101 (19), 195137 (2020).
- *Formation energy puzzle in intermetallic alloys: Random phase approximation fails to predict accurate formation energies.* **Niraj K. Nepal**, Santosh Adhikari, Bimal Neupane, and Adrienn Ruzsinszky, Phys. Rev. B 102, 205121 (2020).
- *Constraint-based wave vector and frequency dependent exchange-correlation kernel of the uniform electron gas.* Adrienn Ruzsinszky, **Niraj K. Nepal**, Jose M. Pitarke,

John P. Perdew, Phys. Rev. B 101 (24), 245135 (2020).

- *Interpretations of ground-state symmetry breaking and strong correlation in wave-function and density functional theories.* John P. Perdew, Adrienn Ruzsinszky, Janwei Sun, **Niraj K. Nepal**, Aaron D. Kaplan (submitted).
- *Stretched or noded orbital densities and self-interaction correction in density functional theory.* Chandra Shahi, Puskar Bhattarai, Kamal Wagle, Biswajit Santra, Sebastian Schwalbe, Torsten Hahn, Jens Kortus, Koblar A. Jackson, Juan E. Peralta, Kai Trepte, Susi Lehtola, **Niraj K. Nepal**, Hemanadhan Myneni, Bimal Neupane, Santosh Adhikari, Adrienn Ruzsinszky, Yoh Yamamoto, Tunna Baruah, Rajendra R. Zope, and John P. Perdew, J. Chem. Phys. 150, 174102 (2019).
- *The Fermi-Löwdin self-interaction correction for ionization energies of organic molecules.* Santosh Adhikari, Biswajit Santra, Shiqi Ruan, Puskar Bhattarai, **Niraj K Nepal**, Koblar A Jackson, Adrienn Ruzsinszky, J. Chem. Phys., 153(18):184303, 2020.

BIOGRAPHICAL SKETCH

Niraj K. Nepal was born in Nepal. After completing higher education in science in 2007, he attended Tribhuvan University, Nepal, where he received a Bachelor in Science (B.Sc.) in 2010 and a Masters in Science (M.Sc.) in 2014 in physics. Later in 2015, he attended Temple University, USA to pursue a Ph.D. degree in physics. During the following 5 years, he was involved in teaching undergraduate labs as well as in several research projects. His activities in the University were supported either by graduate teaching assistantship (GTA) or the graduate research assistantship (GRA). He received several awards during this period, CST outstanding research assistantship in 2019, Peter Havas scholarship in 2020, and the dissertation completion grant for the Fall, 2020. He defended his dissertation in November 06, 2020.